



HAL
open science

Theranostic Nanoparticles for cancer treatment using one or two-photon photodynamic therapy

Chiara Mauriello Jimenez

► **To cite this version:**

Chiara Mauriello Jimenez. Theranostic Nanoparticles for cancer treatment using one or two-photon photodynamic therapy. Other. Université Montpellier, 2016. English. NNT: 2016MONTT100 . tel-01614897

HAL Id: tel-01614897

<https://theses.hal.science/tel-01614897>

Submitted on 11 Oct 2017

HAL is a multi-disciplinary open access archive for the deposit and dissemination of scientific research documents, whether they are published or not. The documents may come from teaching and research institutions in France or abroad, or from public or private research centers.

L'archive ouverte pluridisciplinaire **HAL**, est destinée au dépôt et à la diffusion de documents scientifiques de niveau recherche, publiés ou non, émanant des établissements d'enseignement et de recherche français ou étrangers, des laboratoires publics ou privés.

THÈSE

Pour obtenir le grade de
Docteur

Délivré par l'**Université de Montpellier**

Préparée au sein de l'école doctorale Sciences Chimiques
(ED 459), et de l'unité de recherche UMR 5253 de l'Institut
Charles Gerhardt Montpellier

Spécialité : **Chimie et physico-chimie des matériaux**

Présentée par **Chiara Mauriello Jiménez**

**NANOPARTICULES À VISÉES
THÉRANOSTIQUES POUR LE
TRAITEMENT DU CANCER PAR THÉRAPIE
PHOTODYNAMIQUE À UN OU DEUX
PHOTONS**

Soutenue le 20 juillet 2016 devant le jury composé de

Mme Valérie HEITZ, Professeur, Université de Strasbourg	Rapporteur
Mr Stéphane MORNET, Chargé de recherche, CNRS Bordeaux	Rapporteur
Mme Chantal PICHON, Professeur, Université d'Orléans	Présidente du jury
Mr Damien MERTZ, Chargé de recherche, CNRS Strasbourg	Examineur
Mr Jean-Olivier DURAND, Directeur de recherche, CNRS Montpellier	Directeur de thèse
Mme Laurence RAEHM, Maître de Conférences, Université de Montpellier	Co-encadrante de thèse

« Une quête commence toujours par la chance du débutant et s'achève toujours par l'épreuve du conquérant ». Paulo Coelho

A mi familia, alla mia famiglia

Remerciements

Je voudrais tout d'abord dire un grand Merci aux personnes qui ont cru en moi et qui m'ont permis d'arriver au bout de cette thèse.

Je remercie l'ensemble des membres du jury pour avoir pris le temps de corriger cet ouvrage : Mesdames Pr. Chantal Pichon et Pr. Valérie Heitz et Messieurs Dr. Stéphane Mornet et Dr. Damien Metz.

J'exprime mes plus sincères remerciements au Dr. Jean-Olivier Durand qui a été un directeur de thèse très disponible malgré son temps fort précieux. Il a toujours été à l'écoute de mes nombreuses questions et s'est toujours intéressé à l'avancée de mes recherches. Sa capacité d'analyse, son enthousiasme et la liberté qu'il m'a laissée pour réaliser ces travaux pendant trois ans sont pour beaucoup dans ce résultat final.

Je remercie fortement le Dr. Laurence Raehm d'avoir co-encadré ce travail de thèse. Au cours duquel, elle a souvent attiré mon attention sur certains problèmes de conception et a toujours été présente pour essayer de répondre à mes questions. Aussi, ses nombreuses relectures et corrections de cette thèse ont été très appréciables. Pour tout cela merci.

Je voudrais aussi remercier les personnes qui ont collaboré de près ou de loin avec moi : le Dr. Philippe Maillard de l'Institute Curie de Paris, le Pr. Vincent Chaleix et le Pr. Vincent Sol de la Faculté de Sciences et Techniques de Limoges pour les synthèses des différentes porphyrines, le Dr. Fabienne Dumoulin de l'Université Technique de Gezbe pour la synthèse de la phthalocyanine mais aussi le Dr. Céline Frochot de l'université de Nancy pour les mesures d'oxygène singulet réalisées sur les nanoparticules.

Je tiens très particulièrement à remercier toute l'équipe du Dr. Marcel García à l'IBMM de Montpellier avec lequel j'ai eu la chance de pouvoir collaborer. Un énorme merci à au Dr. Magali Gary-Bobo et au Dr. Marie Maynadier et pour les tests *in vitro* et d'imagerie ainsi qu'au Dr. Nadir Bettache et au Dr. Dina Aggad pour les tests *in vivo*. Je les remercie tout d'abord pour leur bonne humeur et pour avoir toujours été présents pour mes questions. De plus, ils n'ont pas pris peur à chaque fois que j'amenais plein d'échantillons qui d'ailleurs remplissent en ce moment même une bonne partie de leurs tiroirs de congélateur. Je remercie aussi l'équipe du Pr. Alain Morère pour la synthèse des lectines et plus particulièrement le Dr. Elise Bouffard et le Dr. Khaled El Cheik sans lesquels une grande partie de cette thèse n'aurait pas été possible.

Au Dr. Xavier Cattöen et au Dr. Michel Wong Chi Man, un grand remerciement pour m'avoir fait découvrir le monde passionnant de la recherche pendant que je réalisais mon stage de Master 2. Merci de m'avoir toujours encouragée et enseignée, le tout dans la bonne humeur.

Je voudrais également remercier les différentes personnes, techniciens et ingénieurs, qui m'ont aidé lors des techniques de caractérisations. Tout d'abord, merci aux personnes du service commun de microscopie électronique, Franck Godiard et le Dr. Erwan Oliviero pour les mesures de TEM et d'HRTEM. Mais aussi Dominique Granier pour les mesures de DRX et Christine Biolley pour les mesures de RMN du solide. Pour les

mesures de potentiel Zéta, je remercie le Dr. Eliane Dumay et le Dr. Claire Blayo du bâtiment 15. À Serge Bertrand et Christian Curtil un grand merci pour leur aide logistique et technique et surtout pour les discussions à la paillasse et au restaurant, qui ont fait les journées et les repas plus amusants.

Je tiens à remercier fortement l'ensemble de l'équipe de SIKEMIA pour toute leur aide en matière de polymères, et plus particulièrement Adeline et Guillaume pour leur amitié.

Aussi, je remercie chaleureusement l'ensemble des personnes du laboratoire pour l'aide qu'ils m'ont apportée. Merci d'abord au Dr. Hubert Mutin et au Dr. Yannick Guari de m'avoir accueilli dans le laboratoire. Je voudrais également remercier tous les permanents et plus spécialement le Dr. Sébastien Richeter et le Dr. Sébastien Clément pour leur expertise dans le domaine des porphyrines mais aussi le Dr. Danielle Laurencin pour ses connaissances sur la RMN du solide. Je suis également reconnaissante envers le Dr. Clarence Charnay. Je remercie bien sûr tous les stagiaires, doctorants et post-docs que j'ai côtoyés au long de ces trois années. Particulièrement David et Jonas pour leurs précieux conseils à la paillasse sans lesquels une grande partie de ces recherches n'aurait pas été possible, à ma blonde et ma brune pour tous les bons moments, les rires, les thérapies de groupe et pour m'avoir amené ici un petit bout de notre chère Espagne : "Gracias chicas por todo lo que habéis hecho y por todo lo que hemos compartido". À Guillaume pour toute son optimisme et sa patience, je le remercie énormément et je remercie enfin Jeff pour ses concerts au labo et les discussions si « philosophiques » au cours des repas. Angel, Adèle et Marilyn, merci pour avoir toujours un sourire et pour nos délires si spéciaux. Merci à mes stagiaires Yolanda, Maja et Valentin qui ont participé à la réalisation des différents systèmes.

Je voudrais enfin remercier ma famille qui a fait tout son possible pour que j'arrive là où je suis en ce moment. Merci à mon père pour m'avoir transmis sa passion d'apprendre toujours de nouvelles choses. À ma mère de m'avoir transmis sa force et sa détermination sans lesquelles réaliser une thèse n'aurait pas été réalisable et je remercie mon frère pour me rappeler toujours que dans cette vie il faut aussi un grain de folie. Je tiens à remercier mes amis Bruno, Carmen, Luisa et Houda qui ont été toujours là de près ou de loin.

Je ne puis terminer sans remercier la personne qui a été à mes côtés dans les hauts et les bas pendant ces trois ans. Merci pour m'avoir aidé à me soulever à chaque obstacle avec autant de patience et d'amour. Merci de n'avoir jamais jeté l'éponge. Pour tout cette aventure et toutes celles à venir, Christophe, un très grand merci.

TABLE OF CONTENTS

ABBREVIATIONS.....	1
CHAPTER 1	3
INTRODUCTION TO PHOTODYNAMIC (CANCER) THERAPY.....	3
1.1. INTRODUCTION	4
1.2. PHOTOSENSITAZION PRINCIPLE	5
1.2.1. <i>One-photon vs Two-photon excitation</i>	7
1.3. PHOTOSENSITIZERS	8
1.3.1. <i>Photosensitizers in clinical PDT applications</i>	8
1.3.2. <i>Porphyrin and phthalocyanine description</i>	12
1.3.2.1. <i>Porphyrins</i>	12
1.3.2.2. <i>Phthalocyanines</i>	15
1.3.2.3. <i>Aggregation in porphyrins and phthalocyanines</i>	17
1.4. NANOPARTICLES FOR ENHANCED PDT	19
1.4.1. <i>Liposomal nanoparticles</i>	19
1.4.2. <i>Polymeric nanoparticles</i>	20
1.4.3. <i>Dendrimer nanoparticles</i>	21
1.4.4. <i>Gold nanoparticles</i>	22
1.4.5. <i>Magnetic nanoparticles</i>	23
1.4.6. <i>Silica nanoparticles</i>	24
1.4.7. <i>Nanoparticles as downconverting photosensitizers</i>	26
1.4.8. <i>Nanoparticles as energy transducers</i>	27
1.5. FUTURE PERSPECTIVES FOR NANOPARTICLES IN PDT	28
1.6. THESIS OUTLINE.....	28
1.7. REFERENCES	30
CHAPTER 2	35
MESOPOROUS SILICA NANOPARTICLES FOR ONE PHOTON THERAPY AND IMAGING.....	35
2.1. INTRODUCTION	36
2.1.1. <i>Brief history of mesoporous silica materials</i>	36
2.1.2. <i>Theranostics and MSN</i>	38
2.1.2.1. <i>MSNs as drug delivery systems</i>	38
2.1.2.2. <i>MSNs as gene delivery systems</i>	39
2.1.2.3. <i>MSN in photodynamic therapy</i>	40
2.1.3. <i>Chapter outline</i>	40
2.2. MESOPOROUS SILICA NANOPARTICLES FUNCTIONALIZED WITH NOVEL ANALOGUES OF MANNOSE-6-PHOSPHATE: PHOTODYNAMIC THERAPY IN LNCAP PROSTATE CANCER CELLS APPLICATIONS.....	41
2.2.1. <i>Introduction</i>	42
2.2.2. <i>Results and discussion</i>	42
2.2.3. <i>Conclusion</i>	53
2.2.4. <i>Supporting Information</i>	54
2.3. 20 NM SIZED MESOPOROUS SILICA NANOPARTICLES WITH PORPHYRIN PHOTOSENSITIZERS: TOWARDS PHOTODYNAMIC APPLICATIONS	58
2.3.1. <i>Introduction</i>	59
2.3.2. <i>Results and discussion</i>	59

2.3.3.	<i>Conclusion</i>	67
2.3.4.	<i>Supporting Information</i>	68
2.4.	GENERAL CONCLUSIONS AND PERSPECTIVES	72
2.5.	REFERENCES	73
CHAPTER 3	78
BRIDGED-SILSESQUIOXANE NANOPARTICLES: TWO-PHOTON THERAPY AND IMAGING IN CANCER CELLS		78
3.1.	INTRODUCTION	79
3.2.	VERSATILE SYNTHESIS OF BIODEGRADABLE DISULFIDE HYBRID BRIDGED-SILSESQUIOXANE NANOPARTICLES: TWO-PHOTON THERAPY AND IMAGING IN CANCER CELLS	81
3.2.1.	<i>Introduction</i>	82
3.2.2.	<i>Results and discussion</i>	83
3.2.3.	<i>Conclusion</i>	88
3.2.4.	<i>Supporting Information</i>	89
3.3.	PORPHYRIN AND PHTHALOCYANINE PHOTSENSITIZERS BASED BRIDGED-SILSESQUIOXANE NANOPARTICLES FOR TWO-PHOTON THERAPY AND IMAGING OF CANCER CELLS	99
3.3.1.	<i>Introduction</i>	100
3.3.2.	<i>Results and discussion</i>	101
3.3.3.	<i>Conclusions</i>	107
3.3.4.	<i>Supporting Information</i>	108
3.4.	GENERAL CONCLUSIONS AND PERSPECTIVES	112
3.5.	REFERENCES	113
CHAPTER 4	117
TWO-PHOTON-ACTUATED PHOTODYNAMIC THERAPY, IMAGING, DRUG AND GENE DELIVERY VIA PERIODIC MESOPOROUS ORGANOSILICA NANOPARTICLES IN CANCER CELLS		117
4.1.	INTRODUCTION	118
4.2.	USE OF FREE BASE PORPHYRIN-FUNCTIONALIZED PERIODIC MESOPOROUS ORGANOSILICA NANOPARTICLES FOR IMAGING AND SYNERGETIC GEMCITABINE DELIVERY THROUGH TWO-PHOTON THERAPY	121
4.2.1.	<i>Introduction</i>	122
4.2.2.	<i>Results and discussion</i>	123
4.2.3.	<i>Conclusions</i>	127
4.2.4.	<i>Perspectives: biodegradable EPOR PMOs nanoparticles</i>	128
4.2.5.	<i>Supporting Information</i>	130
4.3.	PORPHYRIN-FUNCTIONALIZED MESOPOROUS ORGANOSILICA NANOPARTICLES FOR TWO-PHOTON IMAGING OF CANCER CELLS AND DRUG DELIVERY	137
4.3.1.	<i>Introduction</i>	138
4.3.2.	<i>Results and discussion</i>	138
4.3.3.	<i>Conclusions</i>	143
4.3.4.	<i>Supporting Information</i>	144
4.4.	CORE-SHELL NANODIAMONDS-PERIODIC MESOPOROUS ORGANOSILICA NANOPARTICLES FOR TWO-PHOTON IMAGING, PHOTODYNAMIC THERAPY AND SYNERGISTIC pH-RESPONSIVE DRUG DELIVERY	152

4.4.1.	<i>Introduction</i>	153
4.4.2.	<i>Results and discussion</i>	154
4.4.3.	<i>Conclusions</i>	160
4.4.4.	<i>Supporting Information</i>	161
4.5.	DESIGN OF PURE PORPHYRIN MESOPOROUS ORGANOSILICA NANOPARTICLES FOR TWO-PHOTON FLUORESCENCE IMAGING, PDT AND GENE DELIVERY <i>IN VITRO</i> AND <i>IN VIVO</i>	172
4.5.1.	<i>Introduction</i>	173
4.5.2.	<i>Results and discussion</i>	174
4.5.3.	<i>Conclusions</i>	186
4.5.4.	<i>Supporting Information</i>	187
4.6.	GENERAL CONCLUSIONS AND PERSPECTIVES	195
4.7.	REFERENCES	197
5.	GENERAL CONCLUSIONS	203

NANOPARTICULES À VISÉES THÉRANOSTIQUES POUR LE TRAITEMENT DU CANCER PAR THÉRAPIE PHOTODYNAMIQUE À UN OU DEUX PHOTONS 207

ABSTRACT

RESUME

Abbreviations

Abbreviations

AcOEt: Ethyl acetate	TPE: two-photon-excited
APTES: Aminopropyl triethoxysilane	XRD: X-ray diffraction
BRB: Blood retinal barrier	
BS: Bridged silsesquioxane	
CTAB: Cetyltrimethylammonium bromide	
DIPEA: N, N- diisopropylethylamine	
DIS: Disulfide	
DMSO: Dimethyl sulphoxide	
DOX: Doxorubicin	
EtOH: Ethanol	
Hp: Hemato porphyrin	
HpD: Hematoporphyrin derivative	
FTIR: Fourier transform infrared spectroscopy	
GEM: Gemcitabine	
GFP: Green fluorescent protein	
HRTEM: High resolution transmission electron microscopy	
MSN: Mesoporous Silica Nanoparticles	
mRNA: Messenger RNA	
ND: Nanodiamonds	
NMR: Nuclear magnetic resonance	
PEG: Polyethylene glycol	
PHT: Phthalocyanine	
PDT: Photodynamic therapy	
PMO: Periodic mesoporous organosilica	
POR: Porphyrin	
PS: photosensitizer	
ROS: Reactive oxygen species	
RT: Room temperature	
siRNA: Small interfering RNA	
TEM: Transmission electron microscopy	
THF: Tetrahydrofuran	

CHAPTER 1

Introduction to photodynamic (cancer) therapy

1.1. Introduction

According to the World Health Organization statistics, cancer represents one of the first causes of death, with 8.2 million of deaths each year. In addition, it is projected that the number of cancer cases will attain 22 million cases in 2032 versus 14 million cases in 2012. The purpose of my work is focused on two types of low-size cancers: retinoblastoma, an eye cancer that usually develops in early childhood, and prostate cancer that represents 24% of all cancer in 60-80 years old men. The classical treatments for these types of cancer are chemotherapy, radiotherapy or surgery. These methods present high efficiency but low selectivity. Moreover, they may induce important adverse effects. As a result, safe, potent and cost-effective alternative treatment modality has been developed. Photodynamic therapy (PDT) or phototherapy has emerged as a highly selective technique. This medical method involves the synergistic action of a photoactivatable molecule called the photosensitizer (PS), a light source, and oxygen naturally present in the biological medium¹. After light excitation of the photosensitizer, an energy transfer to oxygen allows the formation of reactive oxygen species (ROS) that can oxidize cellular macromolecules leading to cell death (Figure 1)².

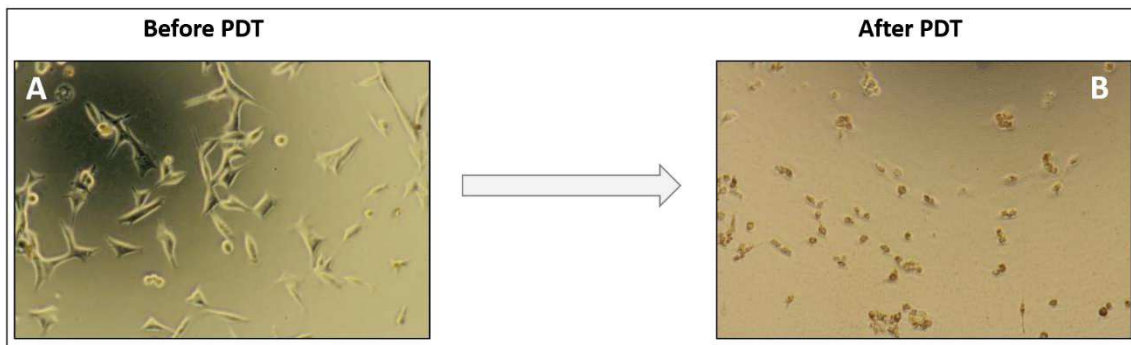


Fig. 1. Microscope images of LNCaP cells under phototherapy. A) Cells incubated with a photosensitizer, before the treatment. B) Cell apoptosis after PDT. As it can be observed most of the cells died under 20 min of light irradiation.

This technique proves to be very efficient and less invasive than surgery, but is not widely used to treat cancer today do to certain limitations as the absence of an ideal PS or the right light dosimetry for an effective treatment. However, PDT is being tested in many clinical trials and used to treat pre-cancers of the skin^{3,4}. PDT is also being tested against pre-cancers in mouth.

One of the present limitations that still remaining is the photosensitizer hydrophobicity, which promotes aggregation in biological media and limits their bioavailability. To solve this problem, encapsulation strategies have been developed. They have the advantage of increasing the tissue penetration and cellular PS and the effectiveness of PDT.

This chapter introduces the principle of the mechanism of tumour destruction done by the application of phototherapy as well as an overview of photosensitizers used in clinical applications. Two types of photosensitizers used during this work will be described in details and a description of nanoparticles that improve the photodynamic therapy will be presented.

1.2. Photosensitization principle

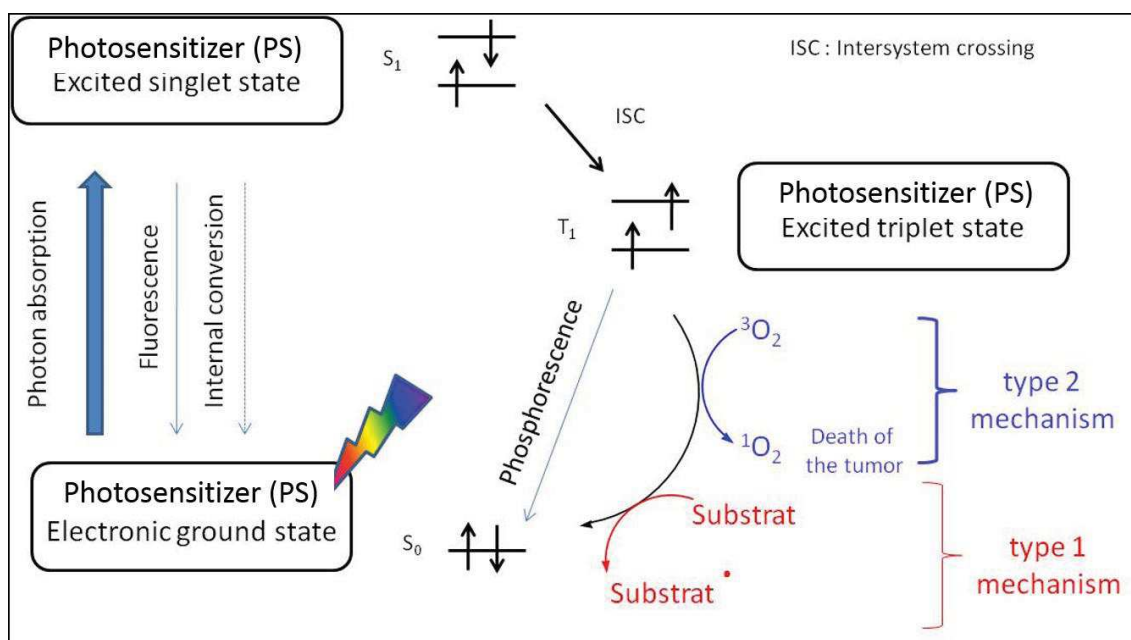
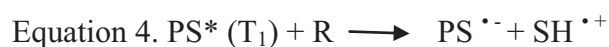
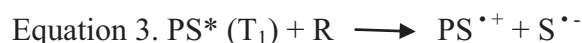
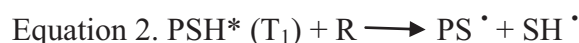
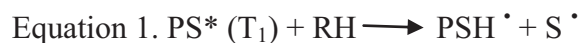
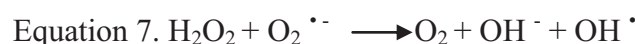
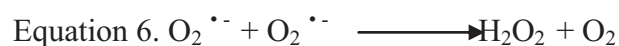
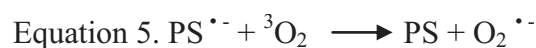


Fig. 2. Jablonski diagram representing the electronic transitions of a photosensitizer irradiated by a light source.

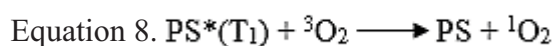
As shown in the Jablonski diagram (Figure 2), a photosensitizer (PS), when irradiated with a light source, absorbs the photon and becomes activated from the singlet fundamental state to a short-lived singlet excited state. At this point, the molecule can decay to the fundamental state emitting fluorescence or it can pass to the triplet excited state through and intersystem crossing. In the triplet excited state two reactions can happen⁵: a) A transfer of a proton (equations 1 and 2) or electron (equations 3 and 4) from the PS (T_1) or a substrate will create PS radicals^{6,7}.



Those radicals can interact with molecules of oxygen at the fundamental triplet state ($^3\text{O}_2$) and produce oxidizing agents as superoxide anion radicals ($\text{O}_2^{\bullet-}$) (equations 5) ⁸. In the presence of this anion radical and the superoxide dismutase (SOD), hydrogen peroxide (H_2O_2) is formed (equation 6). By the Fenton catalysed Haber-Weiss reaction (equation 7) the hydrogen peroxide and the superoxide anion radical generate hydroxyl radicals (HO^\bullet) which can destroy the cell membrane when they react with the polyunsaturated fatty acids. The lipid radicals obtained from this reaction can destabilize cell membranes.



b) The energy of the excited photosensitizer ($\text{PS}^*(T_1)$) is transfer directly to the molecular oxygen ($^3\text{O}_2$) which is converted to singlet oxygen ($^1\text{O}_2$) which will react with organic molecules rich in electrons as aminoacids or cholesterol (equation 8). These molecules will be oxidized and will then induce damages to vital subcellular targets (plasma membrane, organelles, and lysosomes) through oxidative stress.



The two reactions can happen simultaneously and both are responsible of the cell-killing. However, most of the photoinduced tumour destruction are due to the second process⁶.

The mechanisms of cell death (apoptosis, necrosis or autophagy) ^{9, 10} induced by PDT depends on various factors such as the concentration of the PS and its localisation, the light dosage and the tumour microenvironment¹¹. According to Agostinis and co-workers⁹, the apoptosis pathway is characterized by cell shrinkage and it happens when the PS is localized in the mitochondria or in the endoplasmic reticulum. Necrosis is often triggered when high doses of PS or light are used and when the photosensitizer is localized in plasma membrane or lysosomes¹².

As well as producing direct cell killing or vascular damages by ROS reaction, PDT has the advantage to be immune-stimulatory^{13, 14} contrary to chemotherapy, radiotherapy or surgery that are immune-depressive. The inflammatory process starts when inflammatory mediators (proteinases, cytokines, and peroxidases) originated in the treated area, stimulate white blood cell components such as macrophages. Macrophages present proteins from the tumour cells to CD4 helper T lymphocytes, which activate CD8 cytotoxic lymphocytes. These last induce necrosis and apoptosis of tumour cells.

1.2.1. One-photon vs Two-photon excitation

The principle of photosensitization described before corresponds to a one-photon excitation. One-photon excitation provides a therapy through visible light which cannot penetrate deeply in tissues and the PS activation occurs through the path of the laser beam which can cause collateral damages (Figure 3). These limitations can be reduced by two-photon irradiation (TPE) where the irradiation is limited at the focal point of the laser, allowing a resolution of the order of μm ^{15, 16}.

Indeed, two-photon photosensitizing principle, a simultaneous absorption of two photons with the same energy (or not) happens. The double absorption from the ground state to the excited singlet state pass *via* a virtual intermediary state.

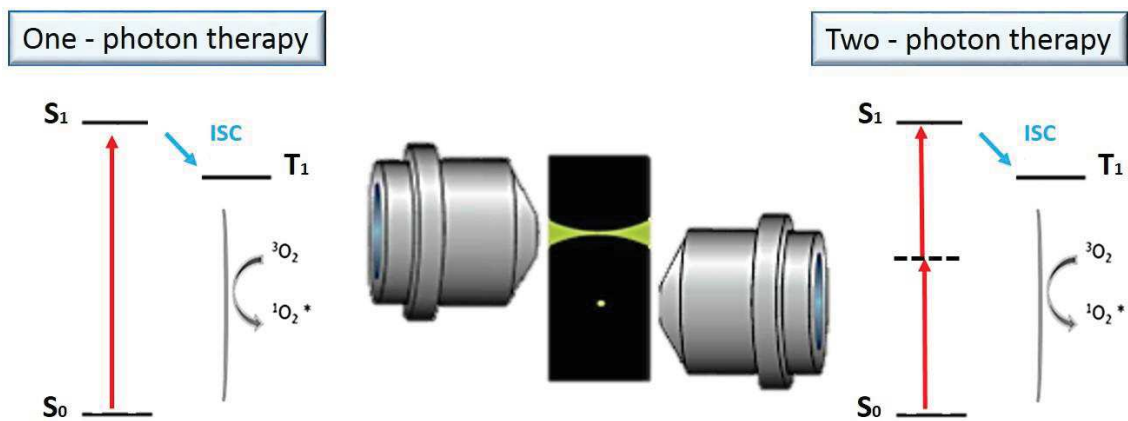


Fig. 3. One photon therapy compared with two photon therapy. The simultaneous absorption of two photons limits the irradiation therapy at the focal point of the laser. (Image adapted from the article of Ira Probohd and David Thomas Cramb: Two-Photon Excitation Photodynamic Therapy: Working Toward a New Treatment for Wet Age-Related Macular Degeneration).

Two-photon absorption requires near-infrared absorption which allows a better penetration in tissues and allows to work in the therapeutic window (700-1400 nm)

where the flow of photons is less perturbed by the absorption of biological tissues¹⁷ (parameter that affect to the fluorescence imaging).

Regarding these advantages, the use of TPE in nanomedicine appears to be relevant for cancer and other diseases therapies.

1.3. Photosensitizers

In 1912, Dr. Meyer-Betz injected to himself 200 mg of a compound named hematoporphyrin (Hp) obtained from the haemoglobin¹⁸. Under the sunlight his hands and face presented signs of photodynamic effect such erythema or oedema.

Dougherty^{19, 20} purified a derivative of the hematoporphyrin (HpD) and obtained the sodium porphyrin (Photofrin)²¹. These two compounds were the first photosensitizers to be used to clinical studies. The compounds produce long skin photosensitization and poor tissue penetration and a large amount of PS is required to obtain a good phototherapeutic effect. They are referred to as first generation PS.

A second generation of novel compounds^{22, 23} with better optical and pharmacokinetics characteristics were synthesized in the late 1980s. These compounds are porphyrin-like molecules that present high absorption coefficients and deep tissue penetration.

New studies are focused on the development of a third generation of PS²⁴ to obtain molecules that provoke shorter photosensitivity and better tumour specificity. At the present time, just a few have been used in clinical applications since their *in vitro* selectivity is not sufficiently high.

1.3.1. Photosensitizers in clinical PDT applications (approved for clinical use or under trials)

As mentioned, the second generation of photosensitizers presents good properties for clinical applications. Clinically approved photosensitizers (Table 1) include porphyrin precursors (as Levulan®, Metvixia®, Benzvix®), chlorins (Foscan®, Photolon®), texaphyrins (Lutex®, Antrin®) and phthalocyanines (Photosens®).

Sensitizer (PS)	Current Name	Indications	Current status
HpD	Photofrin	Bladder, gastric, esophageal cancer	Canada, Japan, US FDA approved
5-Aminolevulinic acid (5-ALA)	Levulan	Actinic keratosis, neck, bladder tumors	US FDA approved, Europe
5-ALA-hexylester	Hexvix	Bladder tumors	US FDA approved
5-ALA-methylester	Metvixia	Actinic keratosis, basal cell carcinoma	US FDA approved, EU, New Zealand, Australia
5-ALA-benzylester	Benzvix	Gastrointestinal cancer	Not approved
m-THPC	Foscan	Head, neck, prostate, pancreatic cancer	European Union
Sulfonated aluminium phthalocyanine	Photosens	Various cancers	Russia
Silicon phthalocyanine	Pc4	Skin cancer, actinic keratosis, non-Hodgkin lymphoma	Clinical trials USA
Lutexaphyrin	Antrin	Prostate cancer	Clinical trials USA

Table 1. Some of the PS that are approved for clinical use or under clinical trials.

Levulan® or 5-aminolaevulinic acid (ALA) is metabolized by cellular biosynthetic pathways into the protoporphyrin IX when internalised in the cells (Figure 4)²⁵. This prodrug is used, through photodynamic therapy, in the treatment of dermatological malignancies²⁶ as basal cell carcinomas, cutaneous T-cell lymphoma, and squamous cell carcinoma as well as to treat non-cancerous abnormalities (acne vulgaris)²⁷. Due to the small size of the molecule, the prodrug can penetrate the skin selectively. Used also as an imaging agent due to the fluorescence produced by the generation of the photosensitizer PpIX, this prodrug is ideal for theranostic (combination of therapy and diagnosis). The others derivatives of this molecule are the methyl ester, benzyl and hexyl derivatives known as Metvixia®, Benzvix® and Hexvix® respectively²⁸.

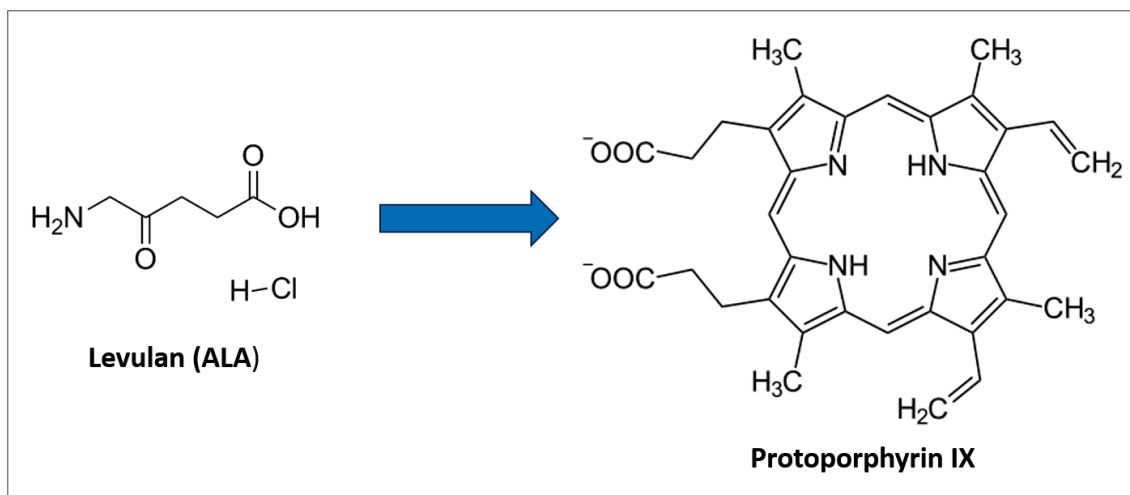


Fig. 4. The chemical structure of Levulan® which is metabolized into Protoporphyrin IX.

Lanthanide metal complexed porphyrin derivatives called texaphyrins are photosensitizers used for photodynamic therapy but also as radiosensitizers. Lutetium texaphyrin²⁹ (Lutex®) (Figure 5) is one of these lanthanide photosensitizers and present a deep red absorption. Its clinical application has been approved in USA for the treatment of breast cancer and melanoma. Its strong absorption in the average of 730-770 nm allows its use in the near-infrared (NIR). Two derivatives of the PS are the Antrin® and the Optrin®, used in the treatment in trials for the restenosis and age-related macular degeneration (AMD) respectively³⁰.

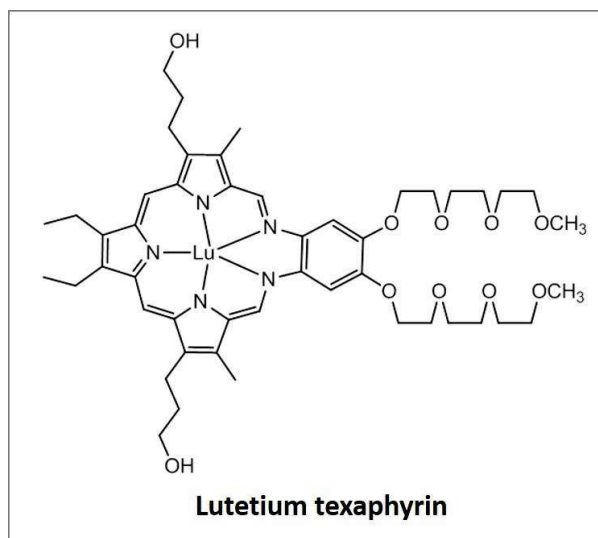


Fig. 5. The chemical structure of Lutex®.

An alternative second generation PS is the meta-tetra (hydroxyphenyl) chlorin, commercially known as Foscan®^{31, 32} (Figure 6). This photosensitizer has been approved in Europe and USA for the treatment of head and neck cancers, but also for

gastric and pancreatic cancers. The good solubility and low drug and light doses required, make it suitable for photodynamic treatment. Its liposomal and PEG-modified derivatives (Foslip® and Fospeg®) have been widely studied.

Another chlorin-based PS is the tin etiopurpurin (Purlytin®³³). The photosensitizer has been approved in USA for cutaneous metastatic breast cancer. Due to the tin atom chelated in the central cavity, the absorption band is shifted to the red (650-680 nm) which intensifies the penetration into the skin.

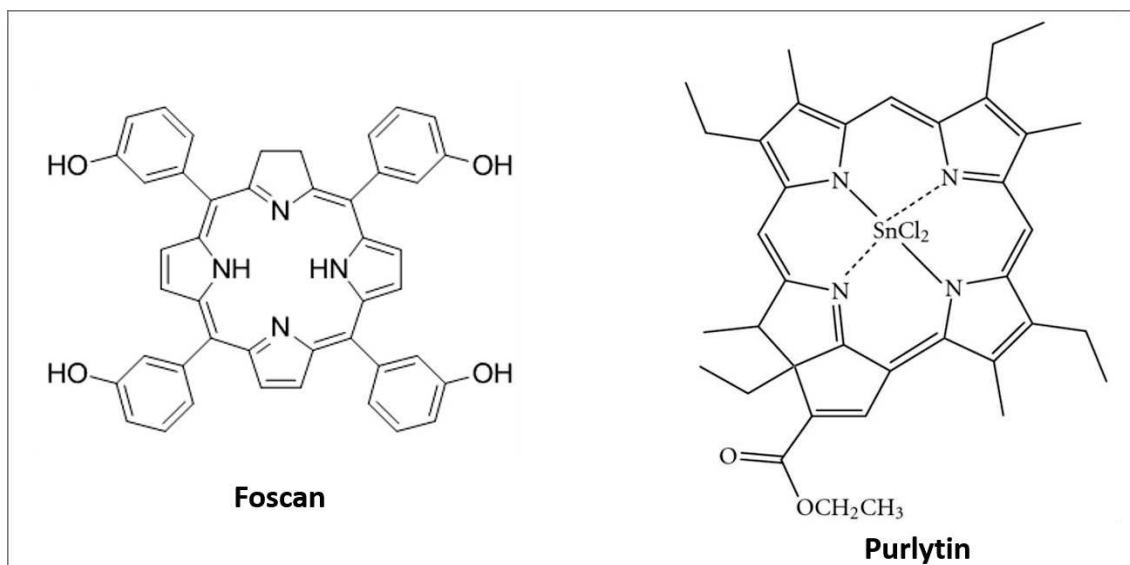


Fig. 6. The chemical structure of Foscan® and Purlytin®.

Phthalocyanines are aromatic macrocycles closely related to porphyrins but which present red-shifted bands that allow a more effective light penetration³⁴⁻³⁶. They can form coordination complexes with different metals. Depending on the metal, their capacity of production of singlet oxygen can change. With diamagnetic ions, the PS exhibit longer triplet lifetimes and higher oxygen quantum yield. Alternatively, paramagnetic ions induce minimal singlet oxygen production. The drawback of these compounds is their tendency to aggregate in aqueous solution, decreasing their photochemical activity. The sulfonated aluminium phthalocyanine (Photosens®), commercially available in Russia, is used in clinical trials against lung and gastrointestinal malignancies. The sulphonation increases the solubility in water which makes unnecessary the use of delivery vehicles. Besides, a silicon phthalocyanine was synthesized (Pc4®) to overcome the aggregation of the PS due to alkyl axial ligand (Figure 7).

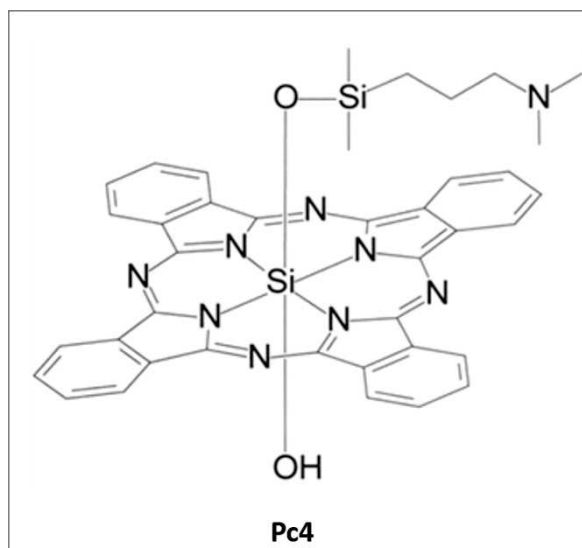


Fig. 7. The structure of the substituted silicon phthalocyanine Pc4®.

1.3.2. Porphyrin and phthalocyanine description

1.3.2.1. Porphyrins

Porphyrins^{37, 38} are heterocyclic macrocycles composed by 4 sub-pyrrole units, connecting their α carbons through methyne bridges (= CH -) (Figure 8). These compounds obey the rule of Huckel (they have $(4n + 2 \pi)$ delocalized electrons, $n = 4$) and are therefore aromatic (Figure 8).

These macrocycles are highly conjugated systems and therefore they exhibit strong absorption bands in the visible and very intense colours (normally purple).

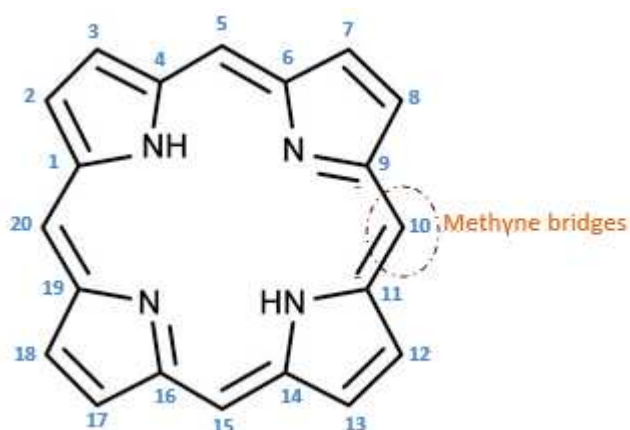


Fig. 8. Structure of the porphyrin skeleton.

Porphyrins present two different sites for electrophilic substitution: *meso* positions (5, 10, 15 and 20) and β -pyrrole positions (2, 3, 7, 8, 12, 13, 17, and 18). The chemical

substituents in these positions determine the solubility of the porphyrin in water and other solvents.

The core of porphyrins can be metallated by more several metals (*metallated porphyrins*) giving rise a square planar complex. While a non metallated core in the presence of acid or basic media leads to diacids (all the four nitrogens of the core are protonated) or dibases (metal-free porphyrins called *free-bases*).

According to the coordinated metal in the middle of the N atoms, the electrophilic substitution is done in one of two positions mentioned before. Introduction of a divalent metal an electronegative porphyrin is produced and therefore the substitution reaction will be in the *meso* positions. Metal ions with electrophilic oxidation states (Sn IV) activates the *β -pyrrole* positions for the substitution reaction.

Spectral properties

As mentioned before, porphyrins, being highly conjugated systems, exhibit a strong absorption in the visible spectrum³⁹.

For “free-base” porphyrins the absorption spectrum has a Soret band (around 420 nm) corresponding to the excitation from the ground state to the second excited state (from S₀ to S₂) and four Q bands (around 515, 550, 590 and 650 nm) corresponding to the excitation from the ground state to the singlet state (Figure 9a).

The intensity of these bands is due to the position of the substituents in the macrocyclic molecule. Based on that, porphyrins may be classified as *etio*, *rhodo*, *oxo-rhodo* and *phyllo*. The *etio* porphyrins have six or more *β -positions* substituted by groups without π electrons (i.e. alkyl groups), while if the positions are substituted by substituents with π electrons, it give rise to porphyrins of the *rhodo* type and a shift to longer wavelengths in the UV spectrum. If these groups are placed on opposite pyrroles, porphyrins *oxo-rhodo* are obtained. When the *meso* positions are occupied the *phyllo* type is obtained (Figure 9 c).

In the case of metallated porphyrins, the compound has a symmetry which produces a simplification in the UV spectrum, by reducing the number of Q bands to two (Figure 9b). These two bands are then called α and β . The intensity of the bands depends on the stability of the metal complex. When $\alpha > \beta$, the metal forms a square-planar complex

with the porphyrin (i.e. Zn (II)), whereas when $\beta > \alpha$, the metal can be easily replaced by protons (i.e. Cd (II)).

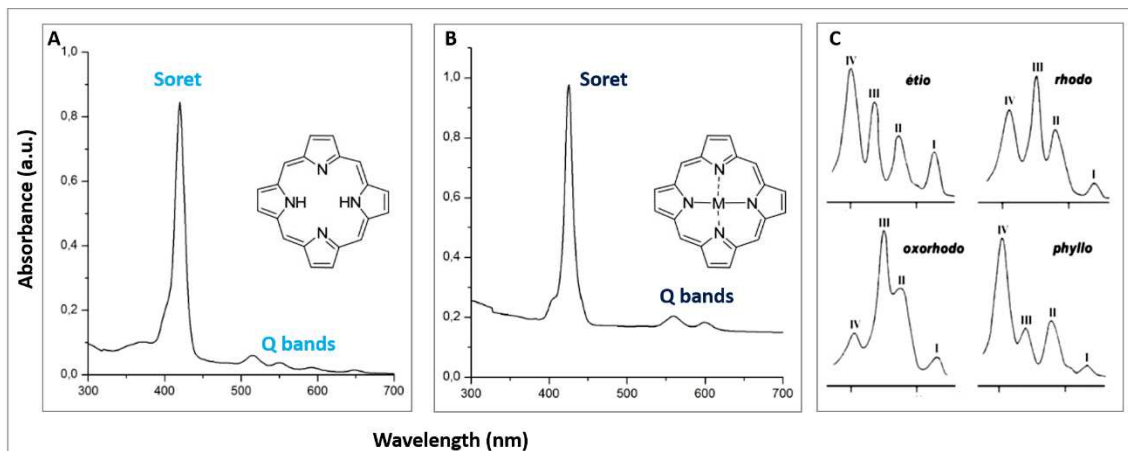


Fig. 9. UV-visible spectra of porphyrin photosensitizer. A) Spectrum of a *free base* porphyrin: four Q bands and the Soret band at 420 nm. B) A metallated porphyrin present a Soret band at 440 nm and only two Q bands. C) The intensity of Q bands depends of the position of the substituents in the macrocycle.

In infrared spectroscopy (IR), porphyrins present some characteristic bands that are presented below⁴⁰. A very intense band around $772 - 805 \text{ cm}^{-1}$ (except in *etio* porphyrins) corresponds to the off-plane bending vibration of β -hydrogens from the pyrroles rings. The band at $835-840 \text{ cm}^{-1}$ corresponds to the vibration in plane of *meso*-CH groups. This band is not present in the spectrum of *meso*-substituted compounds. At $960-990 \text{ cm}^{-1}$ appears the vibration of the in-plane deformation of the NH group, while its outside plan vibration is present at $690-710 \text{ cm}^{-1}$. For all symmetric porphyrins, a very intense band is present in the region $950-970 \text{ cm}^{-1}$, due to a ring vibration of the porphyrin skeleton. In the case of metallated porphyrins this band can be found around $1060-1010 \text{ cm}^{-1}$.

For the nuclear magnetic resonance (NMR), the current generated by the magnetic field of the apparatus induces a large magnetic anisotropy cone perpendicular to the plane of the macrocycle. In the liquid state, the proton analysis (^1H NMR) of porphyrin without substituents gives principally three singlets at -3.076 ppm and 9.74 and 10.50 ppm , which correspond to protons attached to nitrogens and to the β -pyrrole positions and the *methyne* protons respectively. These last protons are bounded to electron deficient carbons, therefore, the signal appears more deshielded than for the protons in β -pyrrole positions. The uniqueness of the signals of the β -pyrrole protons is due to the tautomerism of the internal NH protons (from HC-C=N to C=C-NH).

Three main areas are found in the carbon spectrum (^{13}C NMR): around 95-120 ppm the carbon *meso* appears, while the carbon β -pyrrole and the α -pyrrolic carbons appear at 130 and 145 ppm respectively. This signal is generally poorly defined due to the tautomerism of internal NH protons.

1.3.2.2. Phthalocyanines

Phthalocyanine (PHT), regarded as a synthetic analogue of the family of porphyrins, is a ring of 16 members with 18 π electrons (Figure 10a). This type of structure allows an extraordinary thermal and chemical stability due to its huge aromatic character. Phthalocyanines are highly versatile and are stable chromophores with unique physicochemical properties that make them ideal blocks for the molecular design of materials having electronic and special optics properties. One problem is that phthalocyanines show an inherent tendency toward aggregation. This problem is particularly important in polar media such as water, in which phthalocyanine tends to self-associate and form aggregates in solution. Therefore, hydrophilic non-aggregated phthalocyanines are of great importance and have received much attention. Dissolution in water can be achieved by the introduction of charged groups in the periphery of the macrocycle, such as sulfonatophthalocyanine (Figure 10b).

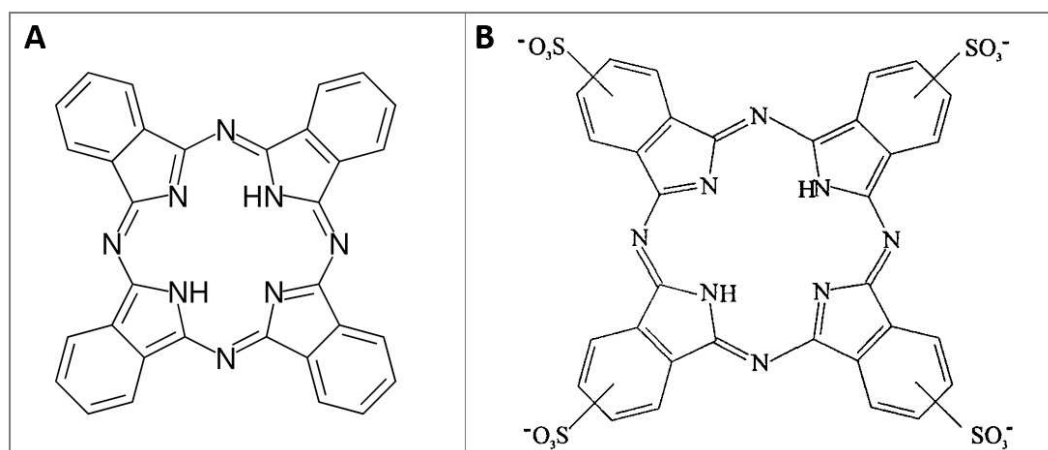


Fig. 10. A) Chemical structure of the phthalocyanine ring. B) Structure of sulfonated phthalocyanine.

The molecule is a blue-green compound formed by the union of four isoindole groups by four nitrogen atoms, leading to 16 ring atoms: eight nitrogens and eight carbons alternated with conjugated double bonds. Phthalocyanines exhibit strong electronic transitions: typically two absorption bands that give characteristic spectra.

Spectral properties

Like the porphyrin molecule the UV spectrum of phthalocyanine present some typical bands⁴¹. The Q band is very intense and is present in the visible and near infrared at around 600-800 nm. A little less intense band (also called Soret band) is found in the near ultraviolet which is located around 300-400 nm. Furthermore, a weak satellite band is observed around 600 nm (Figure 11). This faint band is attributed to higher levels of vibration relevant to the second electronic state. Both Q and Soret bands arise from the $\pi \rightarrow \pi^*$ transitions.

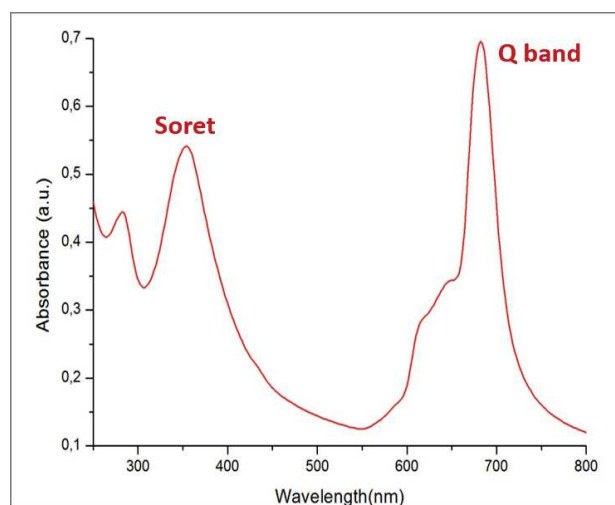


Fig. 11. UV-visible spectrum of a phthalocyanine photosensitizer, where the most intense band corresponds to the Q band.

Phthalocyanine monomers in solution generally show a strong absorption peak (Q band) around 650-700 nm with a weaker satellite band approximately at 600 nm and the Soret band between 300-400 nm. The Q band of the phthalocyanine is strongly localized in the rings of phthalocyanine and is very sensitive to the environment of the molecule. In different reference media, the Q band phthalocyanines can present 15 relative displacements. Dimerization and aggregation of phthalocyanines are accompanied by a blue shift of the Q band. This shift can be explained by the theory of molecular exciton: for a full cofacial arrangement, a blue shift of the Q absorption band appears for the spectrum of the monomer. However the Q band profile changes with different molecular forms: absorption peaks of dimers is around 640 nm while the monomer is around 680 nm, which implies a shift to the blue.

The presence of N = N bonds in the phthalocyanine molecule can be found by IR as they absorb approximately at 1400 cm^{-1} . For the dimers, the close proximity of two or

more rings may direct a dipole coupling between two identical transitions. The balance between dimers and even monomers depends strongly on the concentration and the solvent.

1.3.2.3. Aggregation in porphyrins and phthalocyanines

Aggregation has been observed in various environments for porphyrins and phthalocyanines as well as for chlorins and chlorophylls since 1937⁴². The planarity and big size of these macrocycles in solution, enhance the stacking interactions to form aggregates. Alexander was the first to study the aggregation of protoporphyrins IX in water. The study revealed that the molecules were oriented vertically face-to-face. Bergeron proved the validity of the self-assembly and self-organization of these molecules. The study revealed that the aggregation of these molecules induced several changes in their photophysical properties. The changes are easily characterized by UV-visible spectroscopy. Two kinds of aggregation are known for these compounds: the *J* aggregation and *H* aggregation³⁹.

The *J* aggregation (Figure 12) is formed when the monomeric molecules are arranged in one dimension such the transition moment of the monomers are parallel and the angle between the transition moment and the line joining the molecular center is zero (side-by-side arrangement). This kind of coupling gives an excitation at red-shifted wavelengths.

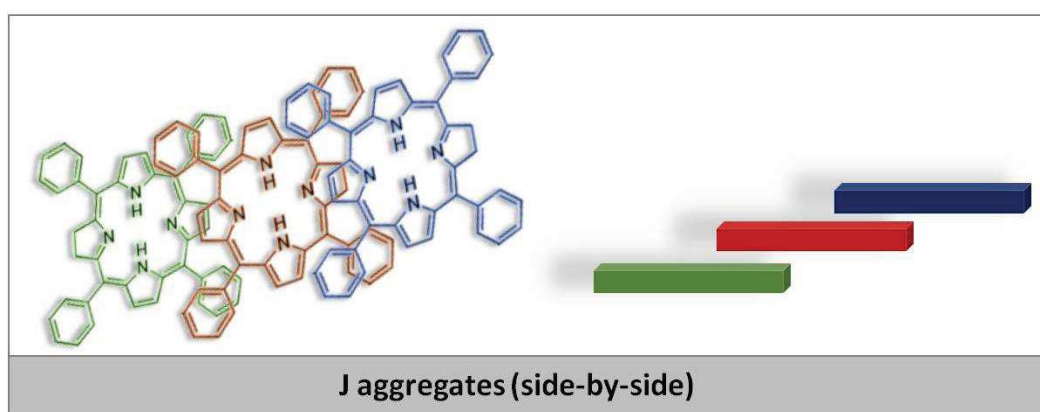


Fig. 12. Schematic illustration of J type self-assembly.

On the other hand, H aggregates (Figure 13) are also one-dimension arrangement of monomers, but the transition moments of the molecules are perpendicular to the line of centers (face-to-face arrangement).

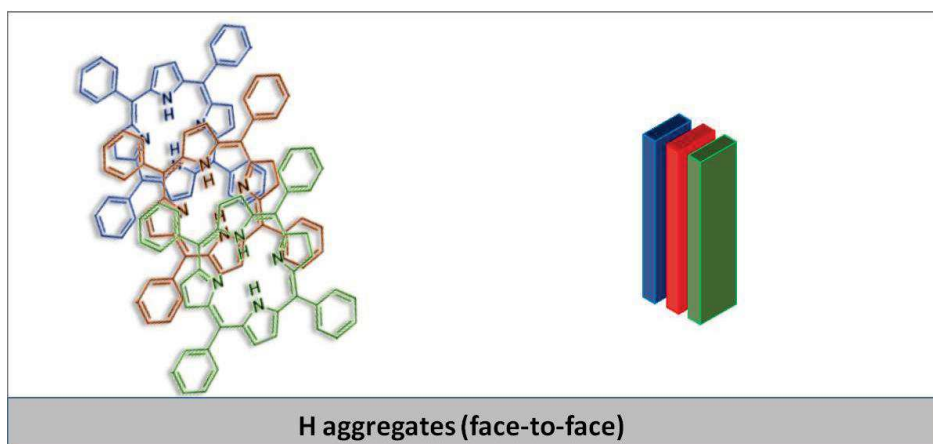
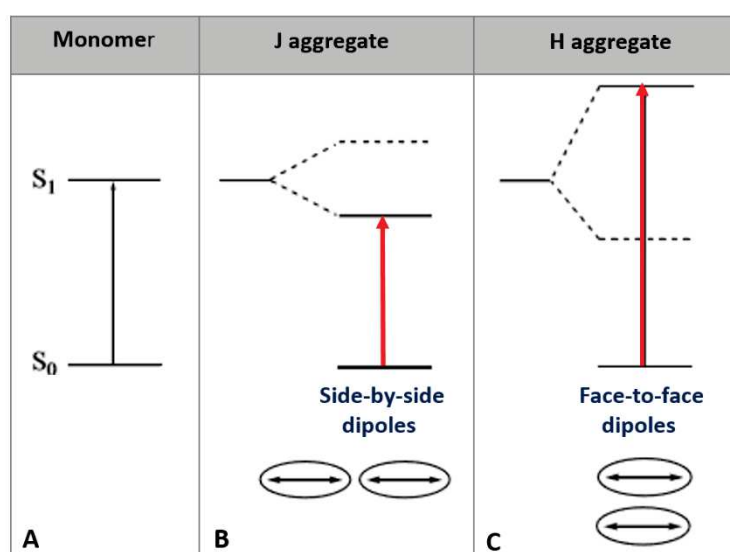


Fig. 13. Schematic illustration of H type self-assembly.

Kasha and co-workers^{43, 44} developed a model for the exciton coupling between molecules that are located in proximity. In Scheme 1B, the interaction side-by-side of the dipoles of transition of the dimer is presented. The S_1 state of the monomer is divided in two energetic level when there is coupling of dipoles. As the energetic transition to the highest level of the S_1 state is forbidden due to the symmetry, the absorption band of the dimer presents a bathochromic shift compared with the monomer. This change in the UV-visible spectra appears then when J aggregates are formed. When the molecules in solution produce a parallel interaction (face-to-face or H aggregates) of the dipoles (Scheme 1c), the energetic transition to the highest level is allowed and the absorption band of the dimer present a hypsochromic shift compared with the monomer.



Scheme 1. Schematic representation of the exciton coupling for photosensitizer dimers.

1.4. Nanoparticles for enhanced PDT

Nanoparticles have seen in last years an increasing number of applications in many fields such as catalysis (Pd nanoparticles in C-C coupling reactions⁴⁵), electronics (i.e. nanotetrapods for fuel cells), environment (i.e. iron oxide NPs to clean arsenic from water wells) or medicine. Their greater surface area per weight comparing with larger particles, make them more reactive than other materials. Those interesting physical and chemical properties, results in interesting biomedical applications such as drug delivery, imaging and therapy.

Concerning phototherapy, nanoparticles can overcome the limitations of PS because of their hydrophobicity or their rapid release from the body⁴⁶⁻⁴⁸. They can also prevent the non-specific accumulation in normal tissues, reducing the photosensitivity. The functionalization of their surface with targeting agents improves their biodistribution and pharmacokinetics.

In the field of PDT, three main use of nanoparticles can be distinguish: PS nanovehicles, nanoparticles as downconverting photosensitizers and NPs as energy transducers.

In the following chapters, the potential uses of the first family of nanoparticles will be highlighted, more particularly the use of silica and organosilica nanoparticles.

Since here, several types of nanoparticles have been described for their applications in medicine.

1.4.1. Liposomal nanoparticles

Liposomal nanoparticles are one of the first platform to be used in clinical (11 formulations are approved for clinical use) and preclinical studies due to their low systemic toxicity⁴⁹.

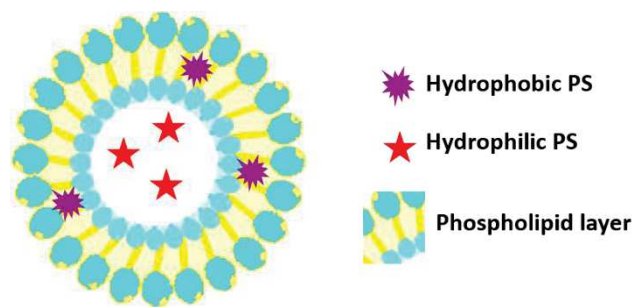


Fig. 14. Photosensitizers loaded in liposomes nanoparticles.

Liposomes (Figure 14) are microscopic vesicles of phospholipid bilayers that are able to encapsulate different drugs depending on their hydrophobicity (encapsulated in the lipid membrane) or their hydrophilicity (encapsulated in the core of the layer). The primary sites of accumulation of this type of nanoparticles are the tumours, the liver or the spleen. The development of news liposomes based on the addition of poly-ethylene glycol in the lipid layers improved their tumour delivery⁵⁰.

While presenting a high biocompatibility, their use as vehicles for PS has not emerged as the best PS delivery system. Conventional liposomes include cholesterol in their structure which reduces the permeability of the photosensitizer⁴⁹. Moreover, the exchange of lipids that occurs in the body between the HDL (high density lipoprotein) and the liposome, leads to a disintegration of the lipid bilayer of the liposome and the consequently to the premature release of the photosensitizer.

However since the year 2000, new formulations of liposomes are gaining more attention as drug carriers (liposomal carriers with triggered-release mechanism) or for theranostics (porphysomes, cerasomes). Porphysomes are supramolecular assemblies of lipids and porphyrin that show potential in imaging, photoacoustic and MRI⁵¹. Liang described the cerasome, a conjugation of porphyrin and organoalkoxysilylated lipids, which allows a high photosensitizer loading⁵².

1.4.2. Polymeric nanoparticles

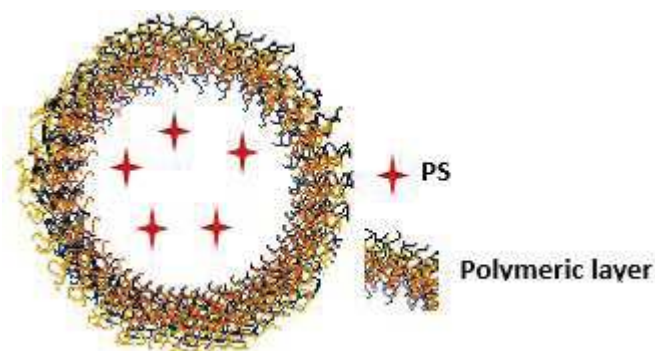


Fig. 15. Schematic illustration of polymer-based nanoparticles.

Organic polymers nanoparticles have been studied for their capacity to increase the solubility and stabilisation of the PS encapsulated inside, in aqueous environments (Figure 15). Moreover, the easily functionalization of their surface with a large variety of biomolecules has suggested their use as nanocarriers for cancer therapy⁴⁸.

Most photosensitizers entrapped into polymeric nanoparticles have been exploited and some of them such as PS encapsulated in PLGA (poly-lactic-co-glycolic acid), have been approved by the FDA for use in humans. Their encapsulation in this biodegradable polymer increase their blood-circulation time and improves the PDT efficiency. Furthermore these systems are enzymatically degraded and excreted from the body, minimising the risks of long term accumulation. The *in vitro* effects of those kinds of nanoparticles have been studied for the encapsulation of meso-tetraphenylporpholactol (a lipophilic chlorin PS) ⁵³. The incubation in glioblastoma cells for 16 h and irradiation at 650 nm caused 95% of cell cytotoxicity after irradiation.

In order to escape the removal by the phagocytic system, those nanoparticles are often modified at the surface with polyethylene glycol (PEG). This increases the circulation time in blood (around 7 h) compared to PLGA NPs (13 to 35 s). Hasan group ⁵⁴ developed PEG-PLGA nanoparticles encapsulating benzoporphyrins, which were enveloped in a liposomal formulation with the anti-angiogenic agent Avastin®. The nanoformulation enhanced the PDT activity in human pancreatic adenocarcinoma.

Multifunctional polymeric nanocarriers are gaining a particular interest in diagnostic and drug delivery. Gupta et al. ⁵⁵ described a polyacrylamide nanoplatfrom containing a NIR excitable cyanine dye and a red-light absorbing HPPH (2-(1-Hexyloxyethyl)-2-devinyl pyropheophorbide-a) for tumours imaging and photodynamic therapy. Xiang et al. developed PEG-PDLLA (polyethylene glycol-poly-lactic acid) nanoparticles loaded with doxorubicin (a chemotherapeutic agent) and with a PS (HMME, hematoporphyrin monomethyl ether) ⁵⁶. The synergetic effect between both agents led to an increased *in vivo* cell killing. The versality of those nanoplatforms represent an effective option for cancer therapeutic, diagnostic and imaging.

1.4.3. Dendrimer nanoparticles

Dendrimers have received much attention in the last years as photosensitizers nanovehicle due to their structure (three-dimensional tree-like branched molecules) that can be tailored with functional groups and targeting molecules (Figure 16) ⁵⁷. Recently, Taratula et al. ⁵⁸ described the synthesis of polypropyleneimine (PPI) dendrimers encapsulating a silicon-based phthalocyanine. The PS encapsulation efficiency was around 20 % w/w. The formulation prevented the leakage of the PS in the blood circulation and showed a high ROS production and due to the NIR absorption of the photosensitizer, efficient fluorescence imaging was obtained.

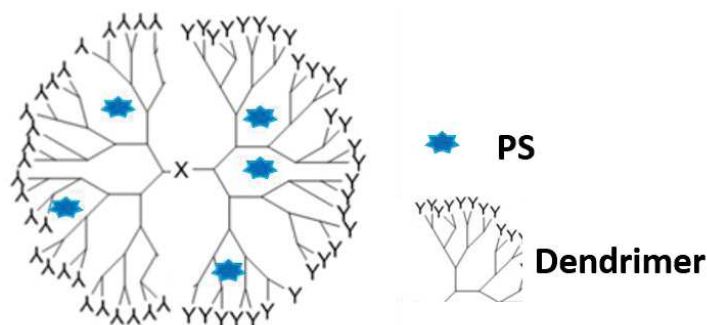


Fig. 16. PS loading scheme in dendrimers nanoparticles.

1.4.4. Gold nanoparticles

Due to their biocompatibility, easy surface functionality and size control, gold nanoparticles are of great interest in PDT (Figure 17). Their surface plasmon resonance effect (SPR) and their ability to convert light in heat make them very useful for photothermal therapy (PTT) and for plasmonic imaging⁵⁹. Their physical and optical properties of gold nanoparticles make them suitable for chemical modification with PS and effective for clinical use.

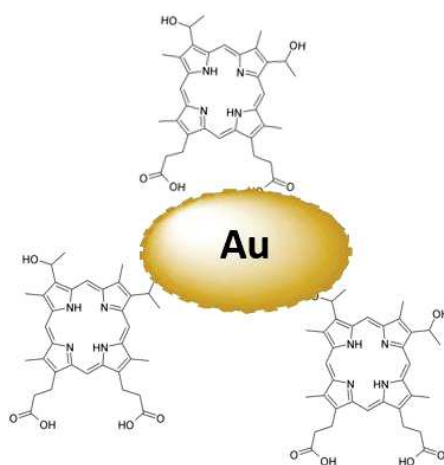


Fig. 17. Gold nanoparticles functionalized by porphyrin PS.

Russel was the first to use gold NPs for supporting a zinc phthalocyanine through a phase transfer reagent (TOAB, tetraoctylammonium bromide)⁶⁰. The $^1\text{O}_2$ oxygen quantum yield was higher than with free phthalocyanine due to the presence of the TOAB that increases the triplet energy transfer to molecular oxygen. The same system was shown to increase the PDT activity (57%) on HeLa cervical adenocarcinoma cells compared with the free PS (26%)⁶¹.

Various compositions and morphologies have been the focus of much research in recent years. Burda studied ⁶² the *in vivo* biodistribution of 5 nm PEG modified gold nanoparticles carrying a phthalocyanine photosensitizer (Pc4). NPs delivered efficiently the PS into the cytoplasm of tumour cells and were found to have a circulation half-life of 3 hours. Gold nanoparticles were found to accumulate in the liver and spleen of mice after 7 days following the intravenous tail vein administration. Nanoparticles were found in the kidneys at 4 hours after administration and spleen throughout the 7 days after administration. Biodistribution suggested that the nanoparticles were removed from the cardio-pulmonary system and the immune system and were conducted into the excretory organs where they were finally removed by renal route.

The characteristic absorption of gold nanoparticles has been used for dual photothermal-photodynamic therapies. Jang et al. described in 2011 a phthalocyanine photosensitizer conjugated with gold nanorods for PTT and PDT ⁶³. The *in vivo* studies of a subcutaneously implanted SCC7 mouse tumour model indicated that the combination of therapies was more effective at inhibiting tumour growth than the therapy alone.

1.4.5. Magnetic nanoparticles

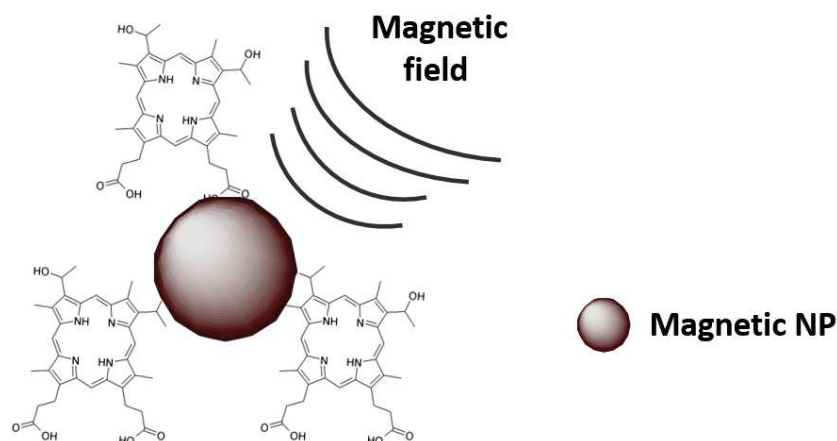


Fig. 18. A schematic illustration of multifunctional magnetic NPs.

The development of multifunctional theranostics in the field of the nanomedicine is increasing significantly. Magnetic nanoparticles are able to perform multiple functions such as Magnetic Resonance Imaging (MRI) and magnetic hyperthermal therapy (Figure 18).

Tedesco reported the use of Fe₃O₄ nanoparticles coated with zinc phthalocyanine as combined PDT-hyperthermia magnets for cancer treatment ⁶⁴. Kopelman et al.

synthesized PAA core nanoparticles encapsulating the Photofrin and iron oxide⁶⁵. The surface was functionalised by PEG and RGD peptide to enable simultaneously cancer targeting, detection and monitoring by MRI and therapy by PDT.

Prasad prepared Fe₃O₄ NPs encapsulated within PEG-coated lipid micelles containing the HPPH PS (Photochlor) to treat HeLa cervical adenocarcinoma cells⁶⁶.

Recently, the synthesis of core-shell nanoparticles with manganese oxide, terbium and gadolinium oxides have been reported as alternative material for MRI imaging and PDT applications.

1.4.6. Silica nanoparticles

Silica based nanoparticles are robust and present tuneable chemical properties that make them materials frequently used for biomedical applications. A wide range of different silica nanoparticles are prepared using a large diversity of precursors and can be synthesized through many diverse routes. Moreover their surface can be easily functionalized with targeting biomolecules for tumor-cell targeting.

For PDT applications, a wide range of photosensitizers can be encapsulated into silica nanoparticles (Figure 19), allowing the use of hydrophobic PS in aqueous environment⁶⁷.

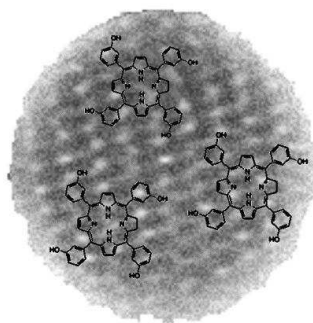


Fig. 19. Silica nanoparticle encapsulating a porphyrin photosensitizer.

ORMOSILs (organically modified silica or organically modified silicate) nanoparticles, synthesized by the Prasad group from the alkoxy organosilane in a water-oil emulsion, have seen widespread use due to their flexible hydrophobic/hydrophilic properties⁶⁸. The first ORMOSILs nanoparticles were prepared by loading the water insoluble HPPH photosensitizer into the hydrophobic core of micelles along with the triethoxyvinylsilane and aminopropyltriethoxysilane precursors. The group obtained 30 nm nanoparticles and the entrapped photosensitizer was found to generate singlet oxygen upon irradiation at levels identical to those generated by the free HPPH. The

fine pores of ORMOSILs nanoparticles (0.5-1 nm) avoided the release of the PS while allowing the generation of singlet oxygen.

Tang et al. realized a study on PDT efficiency and comparison of methylene blue PS loading in 20 nm polyacrylamide NPs⁶⁹, 190 nm-diameter nanoparticles obtained by the Stöber method (nanoparticles obtained from aqueous solutions of silicon alkoxides in the presence of ammonia catalyst) and 160 nm ORMOSILs nanoparticles. The PDT effect and the PS loading was higher in the Stöber nanoparticles due to the affinity of the positively charged methylene blue for the negatively charged Stöber NPs. Nevertheless, the determination of the production of $^1\text{O}_2$ by ADPA method (anthracene-9, 10- dipropionic acid) at 650 nm, showed a higher kinetic rate with ORMOSIL nanoparticles than with Stöber NPs.

Many studies with ORMOSILs nanoparticles embedding different PS such as Pc4, PpIX and mTHPC demonstrated the efficiency of those kinds of silica nanoparticles in PDT. On the other hand, mesoporous silica nanoparticles (MSN) are also gaining interest⁷⁰⁻⁷². To prevent the phototoxicity of the photosensitizer and its unwanted excitation by light, the strategy is to incorporate the photosensitizer into the mesoporous silica framework of the MSNs. Typically, they are synthesized by sol-gel process in the presence of a surfactant as pore agent. They possess high specific surface area and highly accessible pores which make them appropriate for drug delivery. The first study of MSNs used for PDT was reported by Mou et al.⁷³ in 2009. They incorporated a porphyrin photosensitizer into the MSNs to apply PDT in HeLa cells. Gianotti et al.⁷⁴ reported, in 2014, the synthesis of organically modified mesoporous silica nanoparticles containing rose bengal (RB) used for the treatment under green-light irradiation of skin cancer types (SK-MEL-28). Ma et al.⁷⁵ described folic acid functionalized-hollow mesoporous silica nanoparticles (HMSNs) containing 5-Aminolevulinic acid to treat as well skin cancer (B16F10).

Multifunctional MSNs have been developed in last years. Brevet et al. synthesized mannose functionalized MSN nanoparticles⁷⁶ covalently encapsulating an anionic porphyrin PS. Their use in MDA-MB-231 breast cancer cells have demonstrated the potency of carbohydrates as selective cytoadhesive molecules.

Folate conjugated, phospholipid-capped, PpIX loaded, and FTIC-sensitized MSN nanocarriers were prepared by Teng et al. for delivery of the nanovehicles in folic-acid receptor overexpressed in HeLa breast cancer cells⁷⁷. Nanoparticles decreased the dark

toxicity of the PpIX comparing to the free PS. The PDT at 630 nm in mice produced the destruction of 65% of the tumors. Cheng et al.⁷⁸ synthesized 100 nm nanoparticles encapsulating a near-infrared dye ATTO 647N and the PdTPP photosensitizer. These nanoparticles were functionalised with RGD peptides (arginine-glycine-aspartate) to target glioblastoma cells overexpressing $\alpha_v\beta_3$ integrins enabling selective binding and phototoxicity of nanoparticles.

The efficiency of silica nanoparticles as PDT and imaging agents have been demonstrated in many reports and their properties make them suitable as theranostic nanoplatforms. Nevertheless, more toxicological studies should be done concerning their systemic toxicity *in vivo*.

1.4.7. Nanoparticles as downconverting photosensitizers

Certain nanomaterials have the capacity to be a PS by themselves and generate ROS species, due to their optical absorption properties.

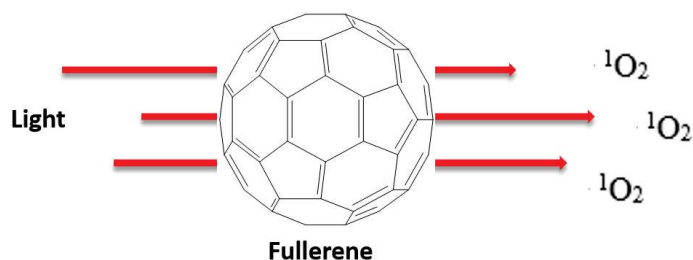


Fig. 20. Fullerene nanoparticle acting as photosensitizer.

Titanium dioxide and zinc oxide nanoparticles, known commonly as photocatalyst, have been studied as potential photosensitizing agents for PDT due to their low toxicity and excellent biocompatibility. Cai et al. used, in 1992, a colloidal suspension of TiO_2 particles to treat *in vivo* HeLa cancer cells⁷⁹. They reported an important suppression of cancer cells in mice for up to 30 days, higher than TiO_2 alone. For zinc oxide nanoparticles, Hackenberg and co-workers studied *in vitro* their effect in head and neck cell carcinoma⁸⁰. Their study revealed a great cancer cell killing through apoptosis and necrosis pathways.

Fullerenes, a carbon allotrope with a spherical shape, also represent one of these types of molecules (Figure 20). They have gained interest because of their photostability and because they are not easily susceptible to photobleach. The multifunctionalisation of fullerenes allowed their use as PDT and as MRI agents. Liu and coworkers developed a

system where DTPA (diethylenetriaminepentaacetic acid) was attached to a pegylated fullerene and mixed with a gadolinium acetate solution to obtain a Gd-chelated fullerene⁸¹. The intravenous administration in mice demonstrated their efficiency as antitumor in PDT and their accumulation could be studied by MRI.

1.4.8. Nanoparticles as energy transducers

The third type of nanoparticles can transduce energy to the PS via FRET, in order to excite the PS indirectly at wavelengths not normally absorbs. FRET (Förster resonance energy transfer) is a physical process by which energy is transferred non radiatively from an excited donor molecule to a ground state energy acceptor).

Quantum dots (QDs), semiconductor nanocrystals, are part of these materials that have taken much attention for their luminescence applications in bioimaging (Figure 21). They act as energy donors and transfer the energy to the PS that have been bound on their surface, inducing generation of ROS species. Burda's group⁸² was the first to functionalise the surface of cadmium selenide QDs with the Pc4 photosensitizer. The QDs by itself could generate $^1\text{O}_2$ but the quantum yield was really low (5% versus 40-60% by conventional photosensitizers). By conjugating the Pc4, a FRET efficiency of 77% was observed under 488 nm light. However, its insolubility in water impeded its use for biological applications.

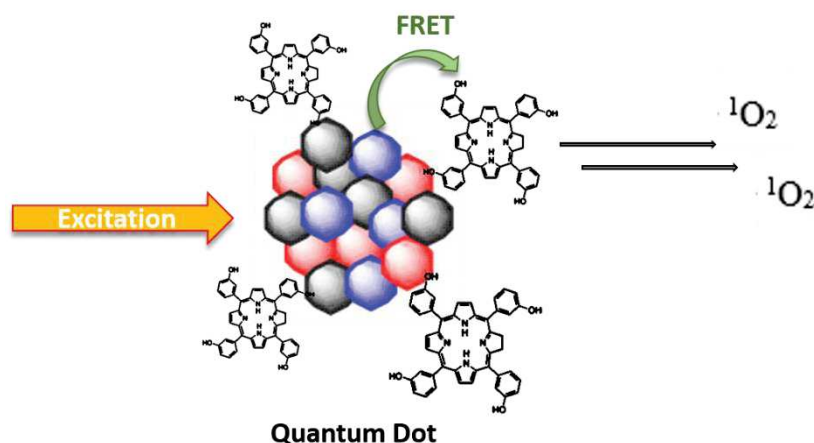


Fig. 21. Schematic diagram of the FRET-based activation from QDs to a PS bounded at the surface following direct photoexcitation of the NPs.

A new approach to treat cancer is the combination of X-ray and PDT. Chen et al. reported in 2006 the use of photoluminescent nanoparticles (BaFBr: Eu^{2+} , Mn^{2+}) functionalised with porphyrins⁸³. These nanoparticles, exposed under X-rays emit

luminescence in the visible region (for example at 400, 500 and 650 nm) allowing the activation of the Soret band of the porphyrin and the consequently efficient generation of ROS.

1.5. Future perspectives for nanoparticles in PDT

Photodynamic therapy is a promising therapeutic technique in the treatment of cancer. Its high selectivity compared to common techniques such as chemotherapy and the minimal invasive character compared with surgery make this therapy very attracting. Nevertheless, it has still not gained the acceptance as first treatment probably due to the disadvantages presented by the classical photosensitizers. Nanoparticles can improve current PDT modalities, by transporting hydrophobic PS to tumours through biofunctionality and targeted therapy. However, most of the reported studies of the use of nanotechnology for PDT applications did not pass initial stages of *in vitro* and *in vivo* experiments. Further studies of their long term physiological effects, safety protocols and standardized procedures to assess *in vivo* biodistribution, are required to achieve homogeneous nanoparticles before translation in clinical practice. However, the development of nanotechnologies in combination with PDT, bioimaging and drug delivery still stay very promising.

1.6. Thesis outline

This dissertation contains a number of experiments that demonstrates the efficacy of using silica or organosilica nanoparticles for drug and gene delivery and PDT treatment. Each potential nanopatform encapsulates a different photosensitizer of the porphyrin or phthalocyanine family.

First, mesoporous silica nanoparticles (MSN) will be described for use for fluorescence imaging and one-photon photodynamic therapy (PDT). Phosphonate and carbohydrate analogues of mannose-6 phosphate ligands were explored as potential targeting ligands for phototherapy in prostate cancer cells. In the beginning, MCM-41 nanoparticles covalently encapsulating a porphyrin photosensitizer were synthesized. Their surface was then functionalized with four different analogues and nanoparticles were tested *in vitro* in LNCaP prostate cancer cells. Then, mesoporous silica nanoparticles containing three different porphyrin photosensitizers were synthesized and tested *in vitro* for one-

photon therapy. These nanoparticles were designed to treat retinoblastoma. To pass through the blood-retinal barrier (BRB), one of the parts of the blood-ocular barrier, these nanoparticles had to present a size under 20 nm.

Furthermore, two alternative new nanomaterials were designed for two-photon therapy and fluorescence imaging: bridged silsesquioxane (BS) on the one hand and periodic mesoporous organosilica (PMOs) nanoparticles on the other. These nanomaterials are exclusively synthesized from organoalkoxysilanes that provide nanoparticles with many interesting characteristics compared to silica nanoparticles.

First of all, non-porous bridged silsesquioxane nanoparticles were synthesized from a metallated porphyrin or phthalocyanine photosensitizer. These nanoparticles were tested *in vitro* with breast cancer cells for two-photon therapy. To add biodegradability to the system, BS were synthesized from a disulphide precursor plus the metallated porphyrin. The biodegradability was assessed in near-physiological conditions and NPs were used for efficient *in vitro* phototherapy.

Finally, drug-delivery PMOs nanoparticles were synthesized. Four different kinds of these nanoparticles are presented. First, PMOs formed from bis-silylated ethane precursor and free-base porphyrin precursor were described and tested for *in vitro* two-photon fluorescence imaging and therapy. These nanoparticles were also used to deliver gemcitabine. The high drug loading and the synergistic effect between the delivery and the application of PDT treatment demonstrated their promising efficiency in the nanomedicine field. Secondly, nanoparticles made with bis-silylated ethylene and octasilylated porphyrin were presented for doxorubicin delivery and two-photon-actuated fluorescence imaging. Thirdly, nanodiamonds used as PS were encapsulated in ethane and ethylene PMOs. Fluorescence imaging, doxorubicin delivery and PDT effect were obtained *in vitro*. Finally, pure porphyrin porous organosilica nanoparticles were synthesized from a metallated porphyrin. PDT was tested *in vitro* in MCF-7 breast cancer cells. Due to their big porosity, gene delivery could be performed *in vitro* and *in vivo*. Fluorescence imaging was also performed successfully *in vitro* and *in vivo* in zebrafish.

1.7. References

1. B. W. Henderson and T. J. Dougherty, *Photochem. Photobiol.*, 1992, 55, 145-157.
2. N. L. Oleinick, R. L. Morris and I. Belichenko, *Photochem. Photobiol. Sci.*, 2002, 1, 1-21.
3. D. Fayter, M. Corbett, M. Heirs, D. Fox and A. Eastwood, *Health Technology Assessment*, 2010, 14, 129.
4. M. Horn, P. Wolf, H. C. Wulf, T. Warloe, C. Fritsch, L. E. Rhodes, R. Kaufmann, M. De Rie, F. J. Legat, I. M. Stender, A. M. Solér, A. M. Wennberg, G. A. E. Wong and O. Larkö, *British Journal of Dermatology*, 2003, 149, 1242-1249.
5. M. Ochsner, *Journal of Photochemistry and Photobiology B: Biology*, 1997, 39, 1-18.
6. A. P. Castano, T. N. Demidova and M. R. Hamblin, *Photodiag. Photodyn. Ther.*, 2004, 1, 279-293.
7. A. P. Castano, T. N. Demidova and M. R. Hamblin, *Photodiag. Photodyn. Ther.*, 2005, 2, 1-23.
8. O. Buchardt, *John Wiley & Sons Inc.*, 1976.
9. P. Agostinis, K. Berg, K. A. Cengel, T. H. Foster, A. W. Girotti, S. O. Gollnick, S. M. Hahn, M. R. Hamblin, A. Juzeniene, D. Kessel, M. Korbelik, J. Moan, P. Mroz, D. Nowis, J. Piette, B. C. Wilson and J. Golab, *CA: A Cancer Journal for Clinicians*, 2011, 61, 250-281.
10. E. Buytaert, M. Dewaele and P. Agostinis, *Biochimica et Biophysica Acta (BBA) - Reviews on Cancer*, 2007, 1776, 86-107.
11. P. Mroz, A. Yaroslavsky, G. B. Kharkwal and M. R. Hamblin, *Cancers*, 2011, 3, 2516.
12. C. Zhou, *Journal of Photochemistry and Photobiology B: Biology*, 1989, 3, 299-318.
13. E. Reginato, P. Wolf and M. R. Hamblin, *World journal of immunology*, 2014, 4, 1-11.
14. A. P. Castano, P. Mroz and M. R. Hamblin, *Nature reviews. Cancer*, 2006, 6, 535-545.
15. S. Brown, *Nat Photon*, 2008, 2, 394-395.
16. O. Kazuya and K. Yoshiaki, *Anti-Cancer Agents in Medicinal Chemistry*, 2008, 8, 269-279.
17. B. Liu, C. Li, Z. Cheng, Z. Hou, S. Huang and J. Lin, *Biomaterials Science*, 2016.
18. M. H. Gold, in *Photodynamic Therapy in Dermatology*, ed. H. M. Gold, Springer New York, New York, NY, Editon edn., 2011, pp. 1-4.
19. T. J. Dougherty, *Photochem. Photobiol.*, 1983, 38, 377-379.
20. T. J. Dougherty, C. J. Gomer, B. W. Henderson, G. Jori, D. Kessel, M. Korbelik, J. Moan and Q. Peng, *J. Nat. Cancer Inst.*, 1998, 90, 889-905.
21. J. Golab, G. Wilczynski, R. Zagozdzon, T. Stoklosa, A. Dabrowska, J. Rybczynska, M. Wasik, E. Machaj, T. Oldak, K. Kozar, R. Kaminski, A. Giermasz, A. Czajka, W. Lasek, W. Feleszko and M. Jakobisiak, *British Journal of Cancer*, 2000, 82, 1485-1491.
22. D. Wöhrle, A. Hirth, T. Bogdahn-Rai, G. Schnurpfeil and M. Shopova, *Russian Chemical Bulletin*, 1998, 47, 807-816.

23. A. Ormond and H. Freeman, *Materials*, 2013, 6, 817.
24. L. B. Josefsen and R. W. Boyle, *British Journal of Pharmacology*, 2008, 154, 1-3.
25. M. g. Wachowska, A. Muchowicz, M. g. Firczuk, M. Gabrysiak, M. Winiarska, M. g. WaÅ„czyk, K. Bojarczuk and J. Golab, *Molecules*, 2011, 16, 4140.
26. B. Zhao and Y.-Y. He, *Expert. Rev. Anticancer Ther.*, 2010, 10, 1797-1809.
27. M. H. Gold, *Lasers Med. Sci.*, 2007, 22, 67-72.
28. R. F. V. Lopez, N. Lange, R. Guy and M. V. r. L. B. Bentley, *Adv. Drug. Deliv. Rev.*, 2004, 56, 77-94.
29. J. L. Sessler and R. A. Miller, *Biochemical Pharmacology*, 2000, 59, 733-739.
30. T. C. Zhu, J. C. Finlay and S. M. Hahn, *Journal of Photochemistry and Photobiology B: Biology*, 2005, 79, 231-241.
31. C. Hopper, C. Niziol and M. Sidhu, *Oral Oncology*, 2004, 40, 372-382.
32. C. S. Betz, W. Rauschnig, E. P. Stranadko, M. V. Riabov, V. Albrecht, N. E. Nifantiev and C. Hopper, *Lasers Surg. Med.*, 2008, 40, 300-311.
33. I. Yoon, J. Z. Li and Y. K. Shim, *Clinical Endoscopy*, 2013, 46, 7-23.
34. C. Anderson, S. Hrabovsky, Y. McKinley, K. Tubesing, H.-P. Tang, R. Dunbar, H. Mukhtar and C. A. Elmets, *Photochem. Photobiol.*, 1997, 65, 895-901.
35. J. Huang, N. Chen, J. Huang, E. Liu, J. Xue, S. Yang, Z. HUANG and J. Sun, *Science in China Series B: Chemistry*, 2001, 44, 113-122.
36. N. Brasseur and T. Patrice, in *Photodynamic Therapy*, The Royal Society of Chemistry, Editon edn., 2003, vol. 2, pp. 105-118.
37. E. B. Fleischer, *Acc. Chem. Res.*, 1970, 3, 105-112.
38. K. W. Wooburn, N. J. Vardaxis, J. S. Hill, A. H. Kaye, J. A. Reiss and D. R. Phillips, *Photochem. Photobiol.*, 1992, 55, 697-704.
39. R. Giovannetti, *Macro to Nano Spectroscopy*, 2012.
40. J. O. Alben, S. S. Choi, A. D. Adler and W. S. Caughey, *Annals of the New York Academy of Sciences*, 1973, 206, 278-295.
41. N. E. Galanin, E. V. Kudrik and G. P. Shaposhnikov, *Russian Journal of Organic Chemistry*, 2008, 44, 225-230.
42. A. E. Alexander, *Journal of the Chemical Society (Resumed)*, 1937, 1813-1816.
43. E. G. McRae and M. Kasha, *The Journal of Chemical Physics*, 1958, 28, 721-722.
44. H. Kano and T. Kobayashi, *The Journal of Chemical Physics*, 2002, 116, 184-195.
45. A. Balanta, C. Godard and C. Claver, *Chem. Soc. Rev.*, 2011, 40, 4973-4985.
46. W.-T. Li, in *Handbook of Biophotonics*, Wiley-VCH Verlag GmbH & Co. KGaA, Editon edn., 2013.
47. S. S. Lucky, K. C. Soo and Y. Zhang, *Chemical Reviews*, 2015, 115, 1990-2042.
48. D. Bechet, P. Couleaud, C. I. Frochot, M.-L. Viriot, F. o. Guillemain and M. Barberi-Heyob, *Trends Biotechnol.*, 2008, 26, 612-621.
49. A. S. L. Derycke and P. A. M. de Witte, *Adv. Drug. Deliv. Rev.*, 2004, 56, 17-30.
50. F. Moret, D. Scheglmann and E. Reddi, *Photochem. Photobiol. Sci.*, 2013, 12, 823-834.
51. E. Huynh and G. Zheng, *Nano Today*, 2014, 9, 212-222.
52. X. Liang, X. Yue, Z. Dai and J.-i. Kikuchi, *Chem. Commun.*, 2011, 47, 4751-4753.
53. J. R. McCarthy, J. M. Perez, C. BrÄ¼ckner and R. Weissleder, *Nano Lett.*, 2005, 5, 2552-2556.

54. P. Rai, S. K. Chang, Z. Mai, D. Neuman and T. Hasan, 2009.
55. A. Gupta, S. Wang, P. Pera, K. V. R. Rao, N. Patel, T. Y. Ohulchanskyy, J. Missert, J. Morgan, Y.-E. Koo-Lee, R. Kopelman and R. K. Pandey, *Nanomedicine : nanotechnology, biology, and medicine*, 2012, 8, 941-950.
56. G.-H. Xiang, G.-B. Hong, Y. Wang, D. Cheng, J.-X. Zhou and X.-T. Shuai, *Int. J. Nanomedicine*, 2013, 8, 4613-4622.
57. B. Klajnert, M. Rozanek and M. Bryszewska, *Curr. Med. Chem.*, 2016, 19, 4903-4912.
58. O. Taratula, C. Schumann, M. A. Naleway, A. J. Pang, K. J. Chon and O. Taratula, *Mol. Pharm.*, 2013, 10, 3946-3958.
59. M.-C. Daniel and D. Astruc, *Chemical Reviews*, 2004, 104, 293-346.
60. D. C. Hone, P. I. Walker, R. Evans-Gowing, S. FitzGerald, A. Beeby, I. Chambrier, M. J. Cook and D. A. Russell, *Langmuir*, 2002, 18, 2985-2987.
61. M. E. Wieder, D. C. Hone, M. J. Cook, M. M. Handsley, J. Gavrilovic and D. A. Russell, *Photochem. Photobiol. Sci.*, 2006, 5, 727-734.
62. Y. Cheng, J. D. Meyers, A.-M. Broome, M. E. Kenney, J. P. Basilion and C. Burda, *J. Am. Chem. Soc.*, 2011, 133, 2583-2591.
63. B. Jang, J.-Y. Park, C.-H. Tung, I.-H. Kim and Y. Choi, *ACS Nano*, 2011, 5, 1086-1094.
64. F. L. Primo, M. M. A. Rodrigues, A. R. Simioni, M. V. L. B. Bentley, P. C. Morais and A. C. Tedesco, *J. Magn. Magn. Mater.*, 2008, 320, e211-e214.
65. R. Kopelman, Y.-E. Lee Koo, M. Philbert, B. A. Moffat, G. Ramachandra Reddy, P. McConville, D. E. Hall, T. L. Chenevert, M. S. Bhojani, S. M. Buck, A. Rehemtulla and B. D. Ross, *J. Magn. Magn. Mater.*, 2005, 293, 404-410.
66. L. O. Cinteza, T. Y. Ohulchanskyy, Y. Sahoo, E. J. Bergey, R. K. Pandey and P. N. Prasad, *Mol. Pharm.*, 2006, 3, 415-423.
67. P. Couleaud, V. Morosini, C. Frochot, S. Richeter, L. Raehm and J. O. Durand, *Nanoscale*, 2010, 2, 1083-1095.
68. I. Roy, T. Y. Ohulchanskyy, H. E. Pudavar, E. J. Bergey, A. R. Oseroff, J. Morgan, T. J. Dougherty and P. N. Prasad, *J. Am. Chem. Soc.*, 2003, 125, 7860-7865.
69. W. Tang, H. Xu, R. Kopelman and M. A. Philbert, *Photochem. Photobiol.*, 2005, 81, 242-249.
70. M. Gary-Bobo, Y. Mir, C. Rouxel, D. Brevet, O. Hocine, M. Maynadier, A. Gallud, A. Da Silva, O. Mongin, M. Blanchard-Desce, S. Richeter, B. Loock, P. Maillard, A. Morere, M. Garcia, L. Raehm and J.-O. Durand, *Int. J. Pharm.*, 2012, 432, 99-104.
71. O. Hocine, M. Gary-Bobo, D. Brevet, M. Maynadier, S. Fontanel, L. Raehm, S. Richeter, B. Loock, P. Couleaud, C. Frochot, C. Charnay, G. Derrien, M. Smaïhi, A. Sahmoune, A. Morere, P. Maillard, M. Garcia and J.-O. Durand, *Int. J. Pharm.*, 2010, 402, 221-230.
72. M. Perrier, M. Gary-Bobo, L. Lartigue, D. Brevet, A. Morere, M. Garcia, P. Maillard, L. Raehm, Y. Guari, J. Larionova, J.-O. Durand, O. Mongin and M. Blanchard-Desce, *J. Nanopart. Res.*, 2013, 15, 1602.
73. S.-H. Cheng, C.-H. Lee, M.-C. Chen, J. S. Souris, F.-G. Tseng, C.-S. Yang, C.-Y. Mou, C.-T. Chen and L.-W. Lo, *Journal of Materials Chemistry*, 2010, 20, 6149-6157.
74. E. Gianotti, B. Martins Estevão, F. Cucinotta, N. Hioka, M. Rizzi, F. Renò and L. Marchese, *Chemistry – A European Journal*, 2014, 20, 10921-10925.
75. X. Ma, Q. Qu and Y. Zhao, *ACS Appl. Mater. Interfaces.*, 2015, 7, 10671-10676.

76. D. Brevet, M. Gary-Bobo, L. Raehm, S. Richeter, O. Hocine, K. Amro, B. Looock, P. Couleaud, C. Frochot, A. Morere, P. Maillard, M. Garcia and J. O. Durand, *Chem. Commun.*, 2009, 1475-1477.
77. I. T. Teng, Y.-J. Chang, L.-S. Wang, H.-Y. Lu, L.-C. Wu, C.-M. Yang, C.-C. Chiu, C.-H. Yang, S.-L. Hsu and J.-a. A. Ho, *Biomaterials*, 2013, 34, 7462-7470.
78. S.-H. Cheng, C.-H. Lee, C.-S. Yang, F.-G. Tseng, C.-Y. Mou and L.-W. Lo, *Journal of Materials Chemistry*, 2009, 19, 1252-1257.
79. R. Cai, Y. Kubota, T. Shuin, H. Sakai, K. Hashimoto and A. Fujishima, *Cancer Res.*, 1992, 52, 2346-2348.
80. S. Hackenberg, A. Scherzed, M. Kessler, K. Froelich, C. Ginzkey, C. Koehler, M. Burghartz, R. Hagen and N. Kleinsasser, *International Journal of Oncology* 2010, 37, 1583-1590.
81. J. Liu, S.-i. Ohta, A. Sonoda, M. Yamada, M. Yamamoto, N. Nitta, K. Murata and Y. Tabata, *J. Control. Release*, 2007, 117, 104-110.
82. A. C. S. Samia, X. B. Chen and C. Burda, *J. Am. Chem. Soc.*, 2003, 125, 15736-15737.
83. W. Chen and J. Zhang, *Journal of Nanoscience and Nanotechnology*, 2006, 6, 1159-1166.

CHAPTER 2

Mesoporous silica nanoparticles for one photon therapy and imaging

2.1. Introduction

Nanomedicine,^{1, 2} application of nanotechnology to the medical science, is emerging as the best technique for diagnostic and therapeutic applications^{3, 4}. The main purpose of this field is the development of tools for the diagnosis, the prevention and the treatment of diseases. Nanomedicine studies the nanoscale interactions and for it, uses nanodevices that are capable to interactuate at the molecular scale, interconnect at micro level and interact at the cellular level. One of the greatest challenges in this process, is the development of « personalized » nanotherapies⁵, offering targeted therapies avoiding the damage to the healthy cells surrounding the diseased organs and avoiding the feared secondary side effects of current treatments.

Several nanodevices have been suggested to provide a selective treatment and to carry, retain and deliver drug molecules to specific tissues or cells. Mesoporous Silica Nanoparticles (MSNs) are one of the nanodevices that have emerged in the medical field and have grown during the last decade⁶. These particles present several advantages such as tuneable size and shape, high pore volume and surface area that allow a high drug load, and a versatile functionalization that allow the circumvention of unwanted biological interactions and facilitate the cellular uptake. All these advantages make them very promising for the diagnostic by fluorescence imaging or MRI, as drug delivery systems⁷, and for the treatment of cancer through different therapies such as photodynamic therapy⁸.

2.1.1. Brief history of mesoporous silica materials

The first monodispersed silica particles were synthesized by Stöber¹⁵ et al. in 1968, using tetraalkyl silicates as silica precursor and a mixture of water-alcohol and ammonia as a catalyst. Synthetic mesoporous silica materials, obtained by the hydrolysis and condensation of tetraorthosilicate (TEOS) in the presence of a cationic surfactant, were first patented by Chiola et al. in 1971⁹.

Until 1990, the mesoporous silica materials were almost unknown. It was during that year, that the group of Kuroda published for the first time the synthesis of this kind of materials. In 1992, Mobil Oil Corporation studied and described in details the synthesis of a novel mesoporous silica material family, the M41S including MCM (Mobil Corporation of Matter). MCM materials (Figure 1) including MCM-41 (with hexagonal

structure), MCM-48 (with cubic structure) and MCM-50 (with lamellar structure). Modifying the Stöber method, Grun¹⁶ obtained micrometer-scaled MCM-41 spherical particles. In 2000, a new kind of mesoporous silica known as SBA-15, was described by Stucky et al.¹⁰ Since then, different mesoporous materials, dependent of the kinetics of sol-gel chemistry, were obtained by changing the ratio alcohol-water, the pH, the catalyser or the silica source.

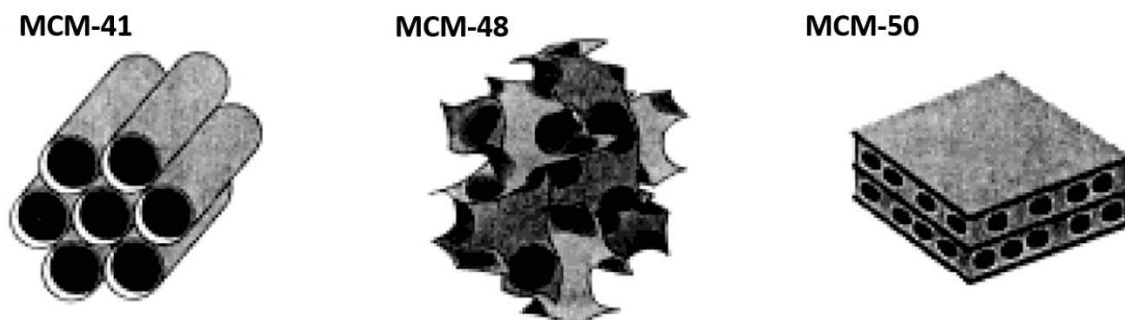


Fig. 1. MCM materials synthesized by Mobil Oil Corporation.

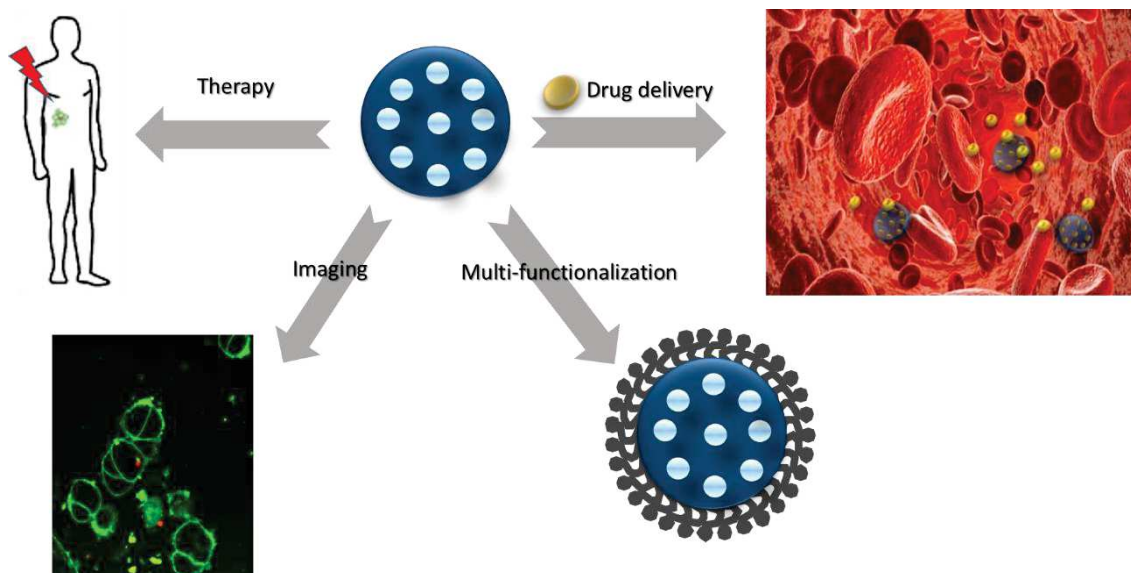
Nano-sized MCM-41 were first successfully synthesized and reported in 2002 by the groups of Cai¹¹, Mann¹² and Ostafin¹³. Then MSN were popularized by Victor Lin¹⁴ (2003) whose team reported the synthesis of mesoporous silica nanospheres used as drug delivery nanocarriers. Changing the methanol-water ratio, Yano¹⁷ et al. synthesized mono-dispersed MSNs with radial structure of the mesopores. The size of MSNs was expanded by Nakamura¹⁸, adding an additional silica source. Varying the TEOS-surfactant ratio, spherical MSNs presenting a wide range of diameters (65-740 nm) were obtained by Nooney et al.¹³

Typically, MSN, obtained after the removal of the surfactant, present a versatile size (15-1000 nm), a tuneable high surface area (600-1000 m²/g) and high pore volume (0.6-1.0 ml/g) that allow high levels of drug loading (from 3 to 30 wt %). Hence, the surface-chemistry of the MSNs can be tuned to optimize the cellular uptake, to attach imaging agents for application in diagnosis or to minimize the nanoparticle opsonization.

Nowadays, MSN with various morphologies, size and pore structures have been synthesized and reported. Controlling the kinetics of sol-gel chemistry, it is possible to tune properties that make them highly promising platforms for medical applications in drug or gene delivery systems, antibiotic systems and as treatment of tuberculosis, hepatitis, cancer and other diseases.

2.1.2. Theranostics and MSN

The development of mesoporous silica nanoparticles as theranostics nanocarriers have attracted considerable interest in the last years. The platform properties and their easily multi-functionalization, make them useful in drug delivery, gene delivery, cellular imaging and photodynamic therapy (Scheme 1).



Scheme 1. Use of mesoporous silica nanoparticles.

2.1.2.1. MSNs as drug delivery systems

Poor chemical and biological properties of many drugs (poor solubility, drug instability, poor cellular uptake) narrow their therapeutic window. Mesoporous silica nanoparticles are suited to deliver small molecules with the advantage of being able to carry a high load of poorly soluble drugs such as doxorubicin (DOX), camptothecin (CMPT) or paclitaxel. Doxorubicin has been used in the majority of the studies. In 2010, Lee¹⁹ et al. delivered DOX to the tumour sites and generated apoptosis *ex vivo* 48 hours post-injection. Meng²⁰ et al. injected intravenously DOX-loaded MSN coated with PEG-PEI, and tumour regression was significantly higher as compared with the free drug.

Camptothecin also possess remarkable anticancer activity but poor solubility. Zink and Tamanoi²¹ used drug-loaded MSNs which were injected intravenously in the tail vein of mice bearing MCF-7 breast cancer cells. Tumour growth was effectively suppressed.

To provide a sustained and proportionated release of the drugs, different approaches were designed. Huang et al. provided MSNs with DOX conjugated with pH-sensitive

linkers, hydrazone bonds. The intratumour injection of the nanoparticles induced significant apoptosis of MES-SA/DOX-resistant cancer cells. He et al.²² designed a MSN system where the DOX-loaded carrier still contained the surfactant (CTAB) used as chemosensitizer. This system presented higher drug efficiencies *in vitro* compared with the free drug. Tamanoi et al.²³ published, in 2008, the synthesis of azobenzene nanoimpellers incorporated in the silica mesopores in order to entrap CMPT and released it through light-induced photoisomerization in PANC-1 and SW480 cancer cells (Figure 2).

Those results confirm MSN as excellent candidates for drug delivery.

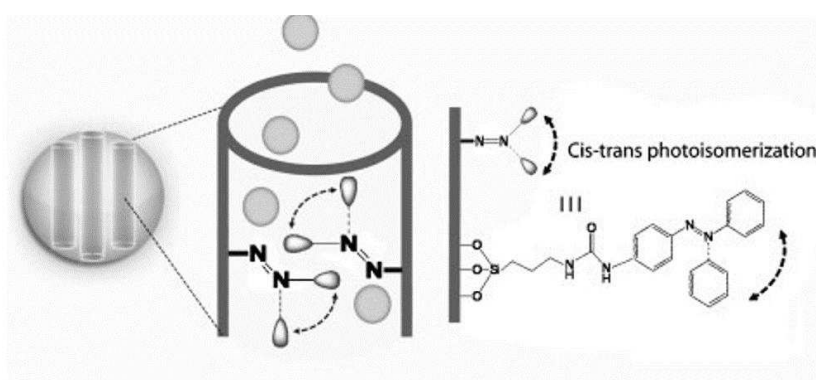


Fig. 2. Azobenzene nanoimpellers synthesized by Tamanoi and delivering CMPT through light.²³

2.1.2.2. MSNs as gene delivery systems

DNA, si-RNA or m-RNA based drugs also present poor bioavailability and poor cellular uptake due to their negative charge. Nowadays, mainly liposomes systems are used as carriers of these drugs but MSNs exhibit several characteristics as an efficient protection for cargo that can be beneficial for the gene-delivery.

Nel et al.^{24, 25} designed siRNA-adsorbed MSNs coated with a layer of polyethyleneimine (PEI). Efficient gene transfection was observed *in vitro*. To protect the cargo into the mesopores and to increase the loading, Gu et al.²⁶ synthesized in 2011 MSN with larger mesopores. The maximum loading capacity was reported to be 121.6 mg DNA/g of MSN which is higher than the amount of gene adsorbed in the mesopores of conventional MSN nanoparticles (48.3 mg DNA/g of MSN).

Gao and co-workers²⁷ were able to adsorb up to 150 $\mu\text{g/g}$ of MSN of firefly luciferase plasmid DNA using amino-functionalized MSNs containing larger cage-like pores (20

nm of diameter). Kim et al.²⁸ reported MSN with a mean mesopore of 23 nm, increasing the loading levels of luciferase plasmid DNA.

Recent works also exploit the possibilities of simultaneous co-delivery of chemotherapeutic drugs and gene as siRNA. Chen et al.²⁹ described MSNs carrying DOX and siRNA that increased the cytotoxicity of DOX close to 132-fold when compared to the free drug.

2.1.2.3. MSN in photodynamic therapy

As described in Chapter 1, photodynamic therapy (PDT) is an interesting alternative to radio- and chemotherapy. It involves the use of photosensitizers (PS) that, upon irradiation at specific wavelengths, induce the formation of reactive oxygen species that lead to cell death.

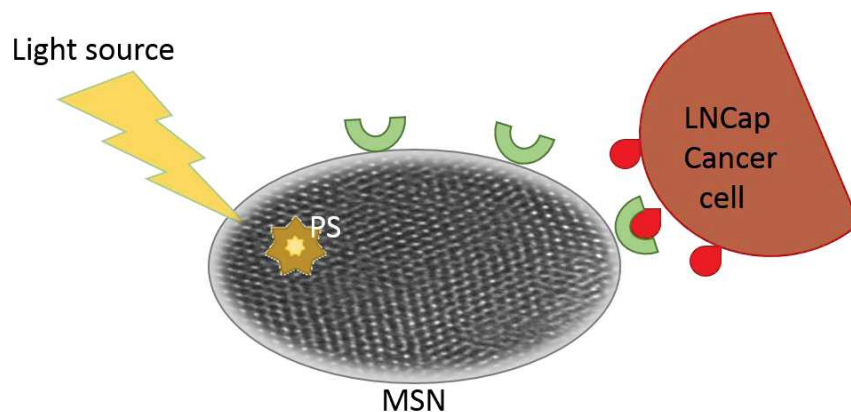
2.1.3. Chapter outline

In this chapter, the synthesis of mesoporous silica nanoparticles and their application in one-photon therapy and imaging for the treatment of prostate cancer and retinoblastoma will be described.

In the first part of the chapter, the synthesis of MCM-41 nanoparticles containing a porphyrin PS is presented. Those nanoparticles were functionalized by four novel analogues of the mannose-6-phosphate ligand and tested *in vitro* in LNCaP prostate cancer cells. One-photon PDT efficiency and imaging were demonstrated.

In the second part, the synthesis of small mesoporous silica nanoparticles, measuring 20 nm, used to treat retinoblastoma are reported. Three kinds of porphyrin photosensitizers were covalently encapsulated in MSNs and tested *in vitro* in MCF-7 breast cancer cells.

2.2. Mesoporous silica nanoparticles functionalized with novel analogues of Mannose-6-Phosphate: photodynamic therapy in LNCaP prostate cancer cells applications



Abstract

New targeting biomolecules combined with nanodevices contribute to the development of a personalized and non-invasive therapy. In the present study, MCM-41 mesoporous silica nanoparticles encapsulating a porphyrin photosensitizer (PS), were successfully prepared by sol-gel method. New analogues of mannose-6-phosphate (membrane lectin overexpressed in prostate cancer cells) were synthesized in our group and used as targeting biomolecules for the treatment of prostate cancer. One photon therapy was applied in LNCaP prostate cancer cells and the effect of these biomarkers in the kinetic internalization and PDT was studied.

Interdisciplinary collaboration

Nanomaterial synthesis, physic-chemical characterizations and applications in solution: C. Mauriello Jimenez, D. Warther, L. Raehm, J-O. Durand.

Synthesis of the porphyrin photosensitizer: P. Maillard

Synthesis of new ligands: E. Bouffard, K. El Cheikh, A. Morère.

Cell studies: A. Gallud, M. Maynadier, M. Gary-Bobo, M. Garcia.

2.2.1. Introduction

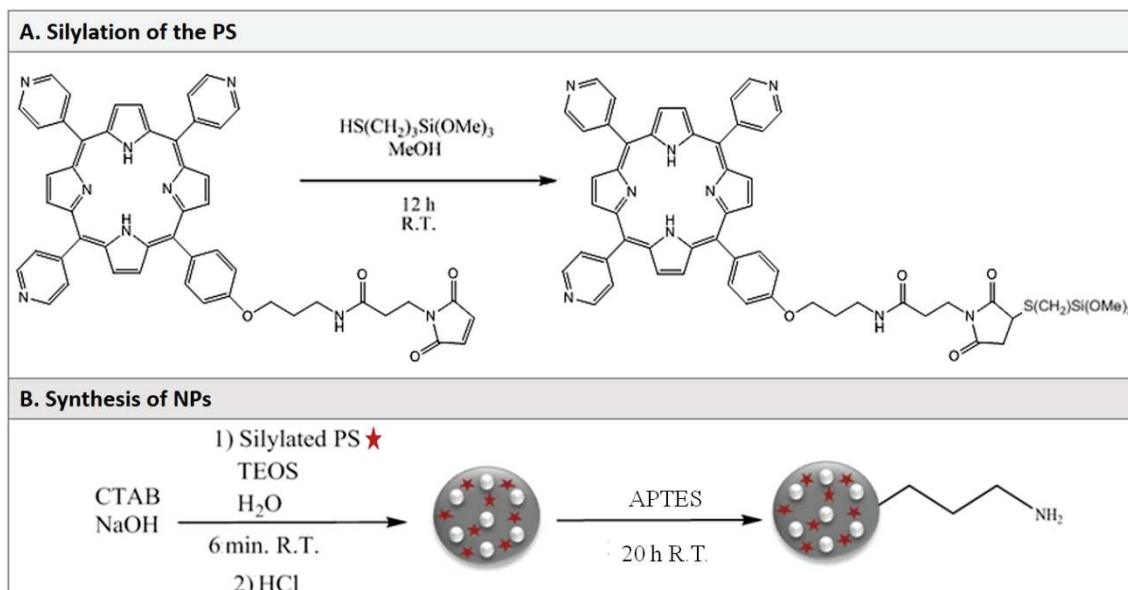
In the last decade, according to the World Health Organization, cancer represented one of the first causes of death in the world and the number of low size cancers is also increasing. For this type of small cancers, nanoparticles have been developed as a new alternative therapy. As described in the general introduction, mesoporous silica nanoparticles (MSNs) have great potential for use in cancer treatment since they are biocompatible and safe and can be used as drug and gene delivery systems but also in imaging and therapies as photothermal or photodynamic therapy. In the course of our work,³³⁻³⁷ mesoporous silica nanoparticles containing different photosensitizers were developed to treat breast, colon, retina or prostate cancer by photodynamic therapy. Recently, our group published the synthesis of mesoporous silica nanoparticles functionalized by a new carbohydrate ligand (M6C)³⁸ analogue of mannose-6 phosphate ligand to target the corresponding prostate cancer membrane receptor. The treatments *in vitro* and *ex vivo* in prostate cancer cells lines and human primary cells obtained from tissues biopsies were described. It was demonstrated that untargeted nanoparticles produced only 25% of cell death and targeted M6C-MSNs induced 75% cell death. In view of these results, our group developed new di-carbohydrate and the correspondent phosphonate analogues. Their capacity to target the membrane receptors of prostate cancer cells has been demonstrated through the functionalization of MCM-41 nanoparticles encapsulating a porphyrin photosensitizer.

This study demonstrates the usefulness of these new ligands, especially the phosphonate analogue, in LNCaP prostate cancer cells. The use of MSN functionalized with those analogues provided an efficient targeted one-photon therapy. In addition, the encapsulated porphyrin allowed the localization of targeted nanoparticles in lysosomes after active endocytosis through the fluorescence imaging.

2.2.2. Results and discussion

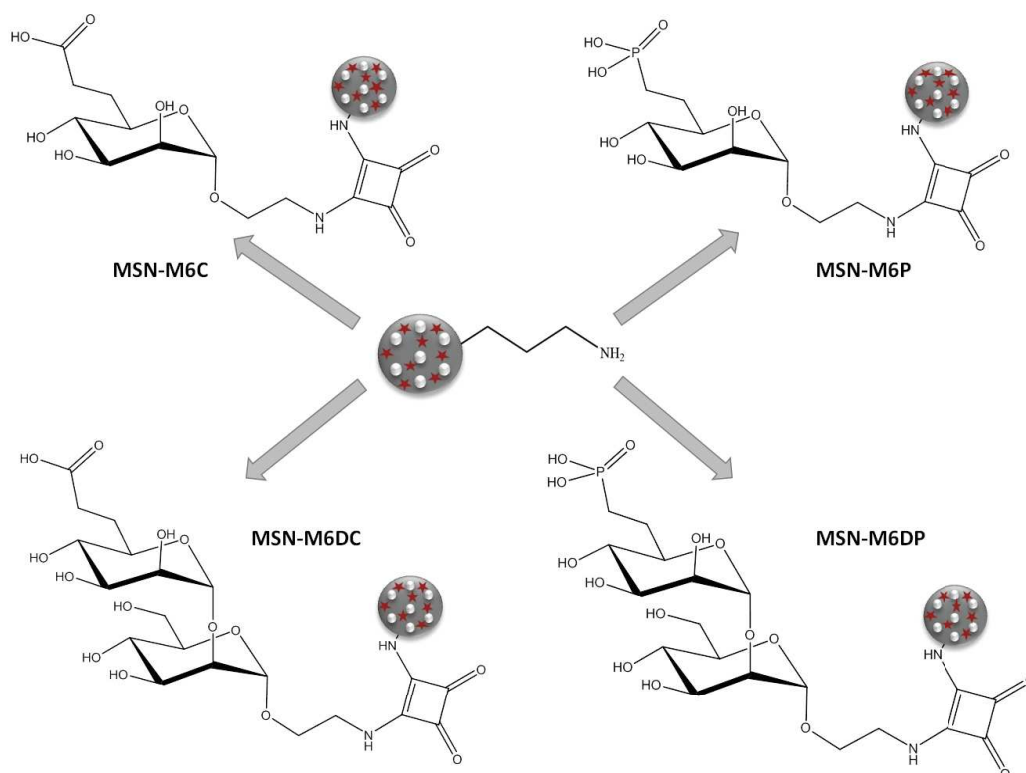
The porphyrin photosensitizer (PS) and corresponding mesoporous silica nanomaterials were initially prepared. Firstly, the PS was silylated overnight at room temperature with mercaptopropyltrimethoxysilane in methanol (Scheme 1a; Supp. Inf. S2). Secondly, the synthesis of the mesoporous silica nanoparticles (MSN) encapsulating the PS was carried out (Supp. Inf. S3). The sol-gel process described by Brevet et al.³⁹ was

performed. The reaction between TEOS (silica source) and PS was carried out in water with sodium hydroxide catalysis at room temperature. The presence of a surfactant, cetyltrimethylammonium bromide (CTAB), was necessary to obtain a MCM-41 structure type (Scheme 1b). As described by Brevet et al.³⁹ functionalization with aminopropyltriethoxysilane (APTES) was required to functionalize the surface *a posteriori* with the different ligands (Supp. Inf. S4). The reaction was carried out in water at pH 6 at room temperature for 20 hours (MSN-NH₂).



Scheme 1. Silylation of the porphyrin PS (a) and synthesis of MSNs and their surface functionalization with amino groups (b).

Then, the post-functionalization with the analogues of the mannose-6-phosphate ligand, the M6C (monocarbohydrate analogue), M6DC (dicarbohydrate analogue), M6P (monophosphonate analogue) and M6DP (the diphosphonate analogue) were performed (Scheme 2; Supp. Inf. S5-S8). For the reactions, all the ligands were taken with the same molarity. For the first three target molecules the same protocol was used. A solution of the ligand and water was added to a solution of MSN-NH₂ in ethanol. The reaction was carried out at 50°C during 12 hours. For the diphosphonate analogue the reaction was carried out at room temperature for 24 h in the presence of triethylamine catalysis.



Scheme 2. Functionalization of MSNs with the analogues of the mannose-6-phosphate.

The morphology and composition of the unfunctionalized (MSN and MSN-NH₂) and targeting (MSN-M6C, MSN-M6DC, MSN-M6P and MSN-M6DP) nanomaterials were then characterized *via* various techniques. Number-averaged Dynamic Light Scattering (DLS) revealed MSN with a hydrodynamic diameter around 226 nm (Figure 1). The diameter is increasing with the solvation layer around the nanoparticle caused by the grafted biomolecules.

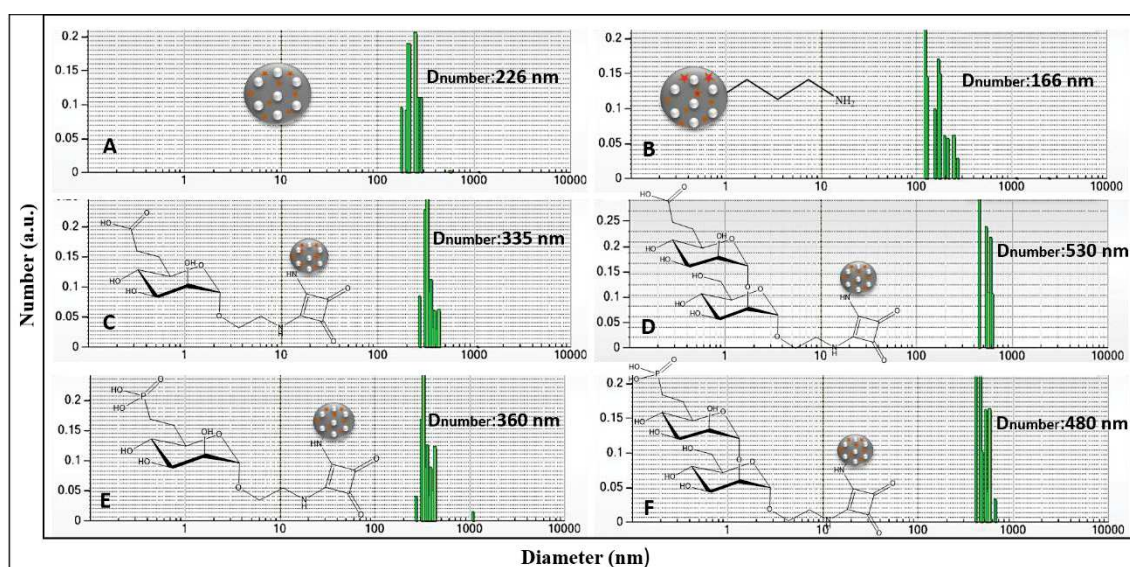


Fig. 1. Number-averaged Dynamic Light Scattering of a-b) MSN and MSN-NH₂; c-d) NPs functionalized with carboxylates analogues and e-f) NPs functionalized with phosphonate analogues.

Transmission electron microscopy (TEM), showed 130 nm diameter MSN nanoparticles (Figure 2a). This was confirmed by the study of the distribution size of nanoparticles. The Gaussian analysis gave a mean size at 138 nm. Furthermore, MCM-41 nanoparticles present a typical hexagonal structure type. (Figure 2b). Post-functionalization with the analogues didn't change the size, as demonstrated by the distribution size with a mean size at 139 nm, and didn't change the pore structure of the materials. (Figure 2c)

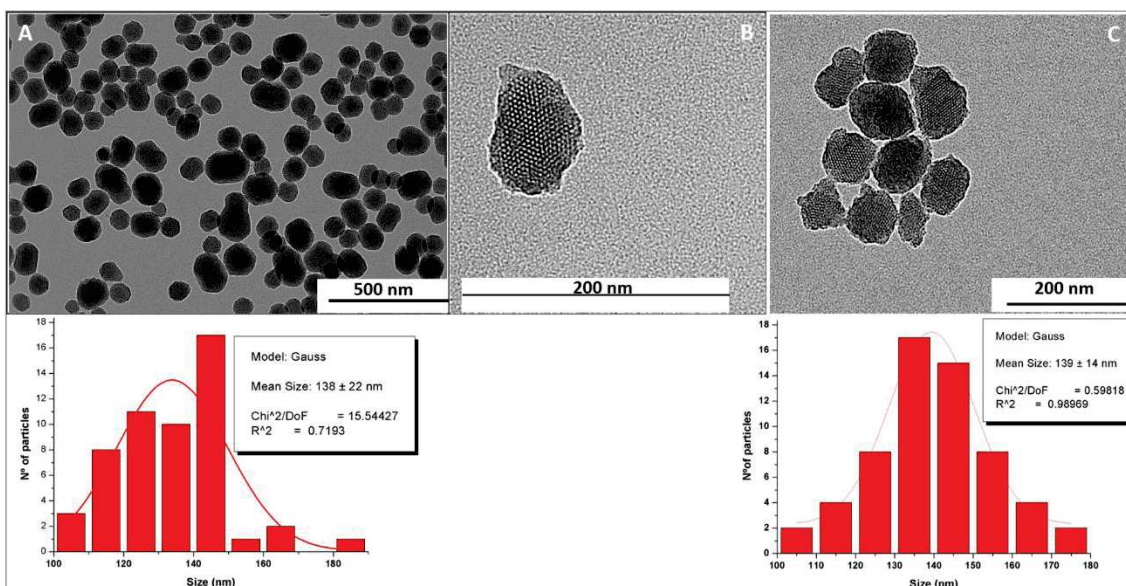


Fig. 2. a) TEM image (scale bar: 500 nm) of MSN nanoparticles and their size distribution. 138 nm nanoparticles were obtained. b) The hexagonal structure of the porosity, characteristic of MCM-41 NPs. c) TEM image and size distribution of functionalized nanoparticles. (Scale bar: 200 nm).

The IR spectra (Figure 3) showed bands at 1050 cm^{-1} and 480 cm^{-1} that correspond at the asymmetric and bending vibration of the Si-O-Si bonds. The broad band around 3500 cm^{-1} may be due to the surface silanols and adsorbed water molecules indicating that the silica framework is hydrophilic. The absence of three bands between 2850 and 2950 cm^{-1} indicates that the surfactant was successfully removed.

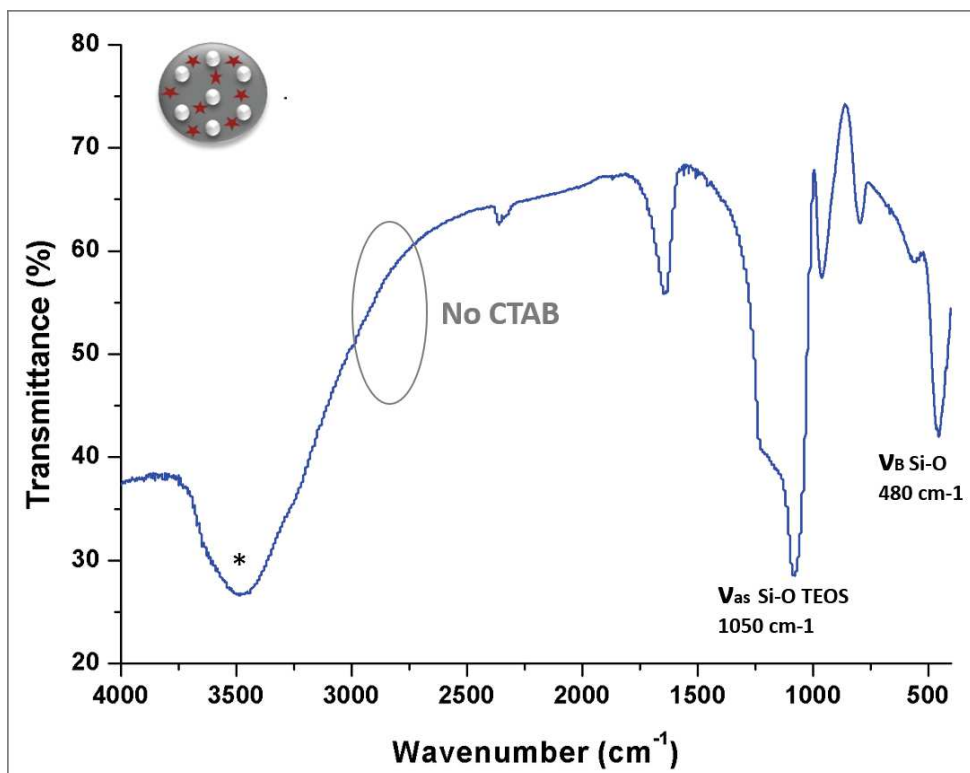


Fig. 3. FTIR spectra of MSN NPs. * Indicates the vibration modes of water.

Solid State NMR ^{29}Si spectra of MSN (Figure 4a) showed the presence of the siloxane network with the Q^2 (-95 ppm), Q^3 (-100 ppm) and Q^4 (-110 ppm) bands. NMR ^{13}C cross-polarization magic angle spinning (CP-MAS) displayed the carbons corresponding to carbons found in the TEOS moiety (Figure 4b). At 15 and 59 ppm, two bands corresponding to the CH_3 and the CH_2 respectively, were observed. They belong to the siloxane network that is not completely condensed.

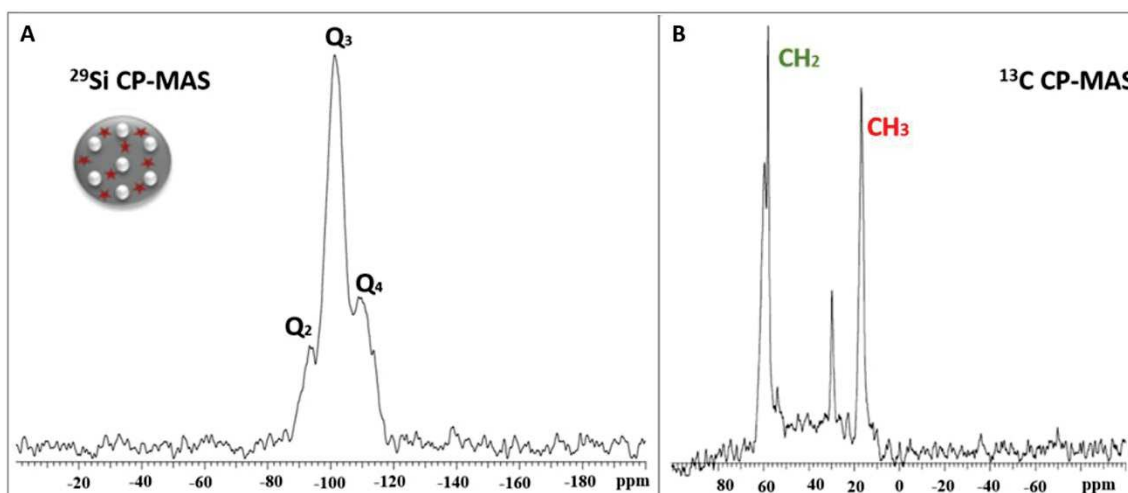


Fig. 4. a) ^{29}Si solid state NMR. b) ^{13}C solid state NMR.

Nitrogen-adsorption-desorption analysis calculated a surface area of $1109 \text{ m}^2 \cdot \text{g}^{-1}$ for POR-MSN, with 2 nm BJH pore diameters (Figure 5b). As shown in Figure 5a nanoparticles present a typical IV isotherm with a defined step at a relative pressure at 0.35. The size and the porosity of POR-MSN make them suitable nanocarriers for nanomedicine.

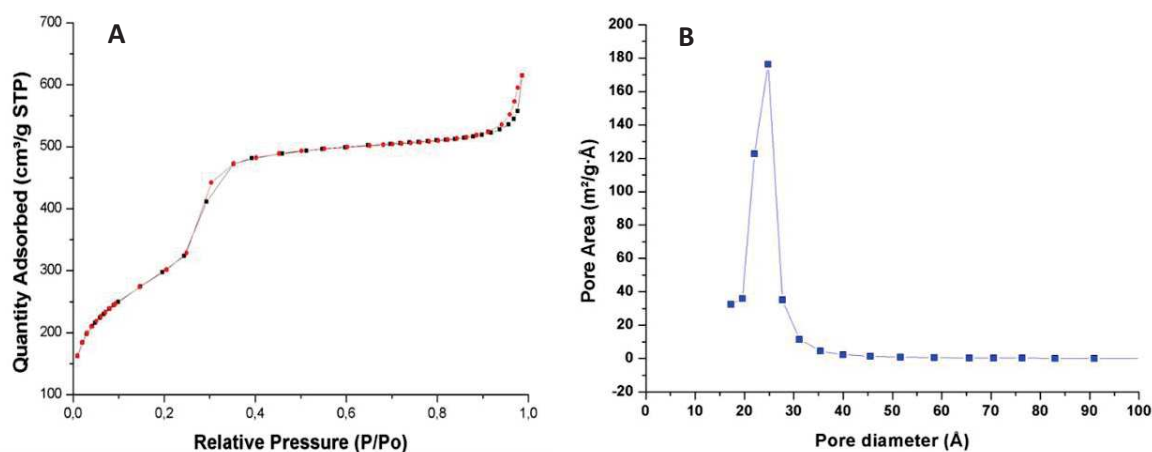


Fig. 5 a) Nitrogen-adsorption-desorption curve. b) BJH analysis of pore diameter.

UV-visible spectroscopy of solutions of the nanoparticles in EtOH (Figure 6), confirmed the successful encapsulation of the PS in the MSN as shown respectively by the absorption of the Soret band at 415 nm and the presence of the four Q bands at 520, 556, 593 and 650 nm (Figure 6a-b). The surface functionalization by the different ligands was confirmed by the presence of a band at 290 nm (with a shift at 300 nm for the di-phosphonate analogue), corresponding to the bond created between the NH_2 present at the surface of MSN-NH_2 and the squarate unit present in all the ligands (Figure 6c).

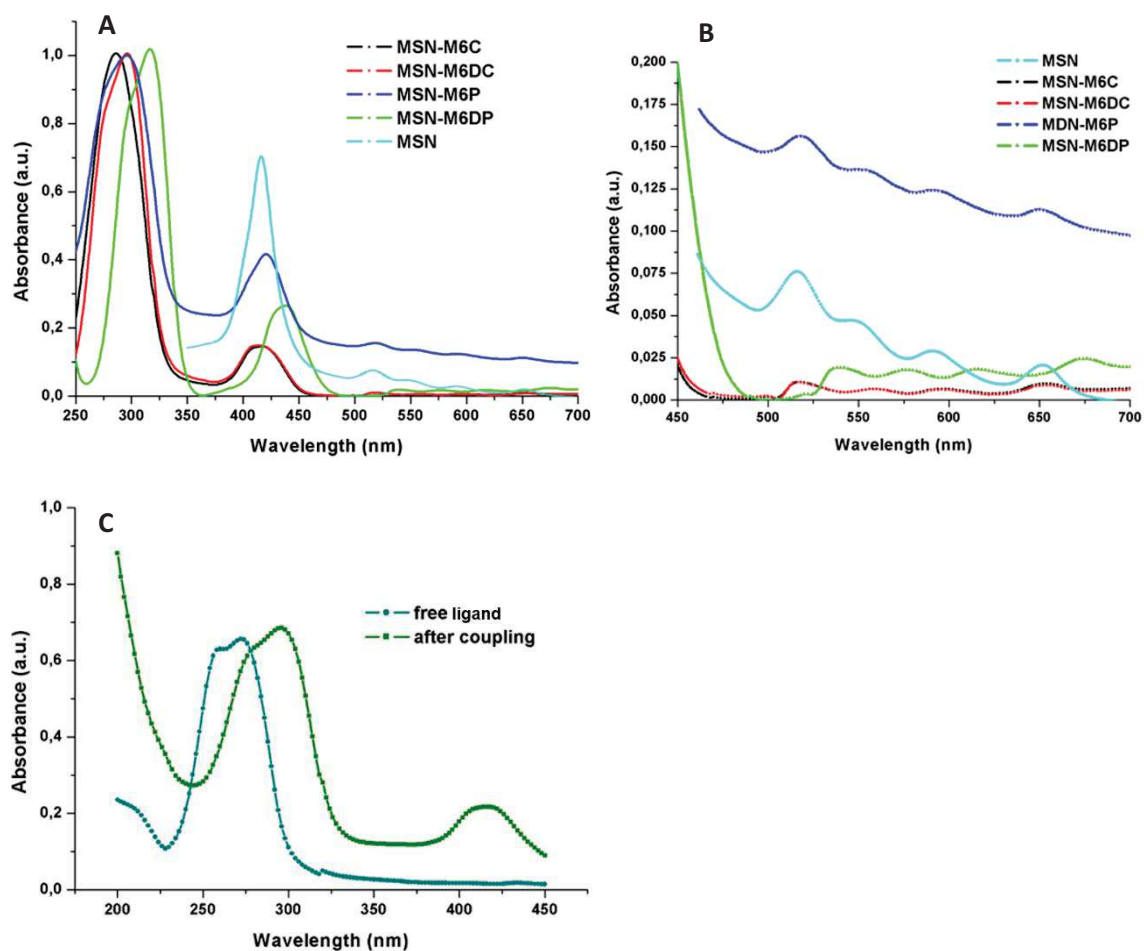
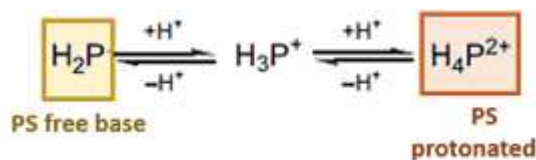


Fig. 6. A) UV-Visible absorption spectra of untargeted and targeted NPs. B) UV-Vis spectra representing the Q bands of MSN and their targeted nanoparticles. C) Confirmation of the shift of the target band after functionalization.

The Soret and Q bands of the porphyrin are not shifted when the nanoparticles are functionalized with the carboxylates analogues resulting in a Soret band at 415 nm and Q bands at 516, 554, 593, 650 nm. Comparing the spectra in the presence of phosphonate analogues with UV spectra of MSN-carboxylates analogues, we observed a slight red shift of the Soret band at 419 nm for the monophosphonate analogue. The shift is more important in the presence of the corresponding di-analogue. In this case the Soret band is shifted at 436 nm and the Q bands are shifted at 537, 575, 614 and 671 nm. This phenomenon can be explained by the pK_a of the analogues (Figure 7). If we compare one phosphonate and one carboxylate compound with similar structure to our mono-analogues, we observe that the phosphonate, presenting two pK_a at almost 2 and 6.6, is more acid than the carboxylic analogue presenting a pK_a of 4-5. As it is known the core of a tetraphenyl porphyrin molecule (Scheme 3) can be protonated and presents

a pK_a of 4.35 (pK_a for the monoprotonated and bisprotonated species are almost the same). Many studies demonstrated that a protonation of the porphyrin core induces a change in its photophysical properties and specially induces changes in the UV-visible spectra (i.e. red shift, changes in the number of Q bands).



Scheme 3. Protonation of a free base porphyrin.

The acidity contributed by the phosphonate analogue on the surface of the nanoparticles in water solution could induce a protonation of the porphyrins moieties that are located near to the surface of the nanoparticles and consequently induce a red shift of the Soret and Q bands. As it is also known, upon addition of acid (protonation of the porphyrin core) the symmetry of porphyrin changed from a D_{2h} to a D_{4h} symmetry comprising changes in Q bands from four bands to two bands. In the case of the addition of phosphonate analogues, there is not a decrease of number of Q bands but there is a red shift on the spectrum. This could be explained by a mixture of porphyrins moieties: protonated porphyrins near to the surface and free base porphyrins inside the nanoparticle.

The amounts of PS and targeting biomolecules were determined by quantitative analysis of the intensity of the absorption spectra bands. The quantity of porphyrin was determined in unfunctionalized MSNs and calculated from the absorption of the Soret band at 420 nm. The quantity of ligand was determined at 290 nm, using the Lambert law. (Table 1). For the same concentration of ligand added to the reaction (3.33 μmol), we obtained almost the same quantity of M6C and M6P grafted onto the nanoparticles. The quantity of ligands grafted onto the surface of NPs decreased for di-analogues, especially for M6DP analogue, may be due to the steric hindrance caused by the volume of the biomolecules.

Nanoparticles	Porphyin [C] $\mu\text{mol/g}_{\text{NPs}}$	Ligand [C] $\mu\text{mol/g}_{\text{NPs}}$
MSN	11	-
MSN-M6C	11	352
MSN-M6DC	11	329
MSN-M6P	11	354
MSN-M6DP	11	167

Table 1. Quantitative determination of the concentration of photosensitizers and target biomolecules in nanoparticles.

Different concentrations of MSN were first incubated with MCF-7 breast cancer cells, to determine the optimal quantity of nanoparticles for one photon PDT treatment (Figure 8a). The best concentration with an optimal PDT effect / cytotoxicity relation was fixed at $80 \mu\text{g. mL}^{-1}$ under irradiation at 650 nm for 20 min. Then, nanoparticles functionalized with the different ligands were incubated for 6 hours and 18 hours in LNCaP prostate cancer cells. For carboxylates analogues (M6C and M6DC), we obtained a better effect after 18 hours of incubation but for phosphonate analogues we obtained a better effect after only 6 hours. This, can be explained by a fast turn-over of the M6P receptor which induced a faster internalisation (Figure 8b and c). The study of the internalisation kinetics was done and a better endocytosis was obtained after 6 hours. In the case of phosphonate ligands an exocytosis started since 9 hours (Figure 8d). Regarding the percent of cell death at 6 hours of incubation, we obtained as expected, better results with the dicarboxylate ligand (MSN-M6DC) in the family of the carboxylates analogues with a 73% of cell death and with 74 % of cell death the di-phosphonate (MSN-M6DP) in the family of phosphonate analogues. This can be explained because of the similarity of the structure of the *di*-ligands to the prostate cancer receptor and a phosphonate group is better recognized by a phosphate receptor.

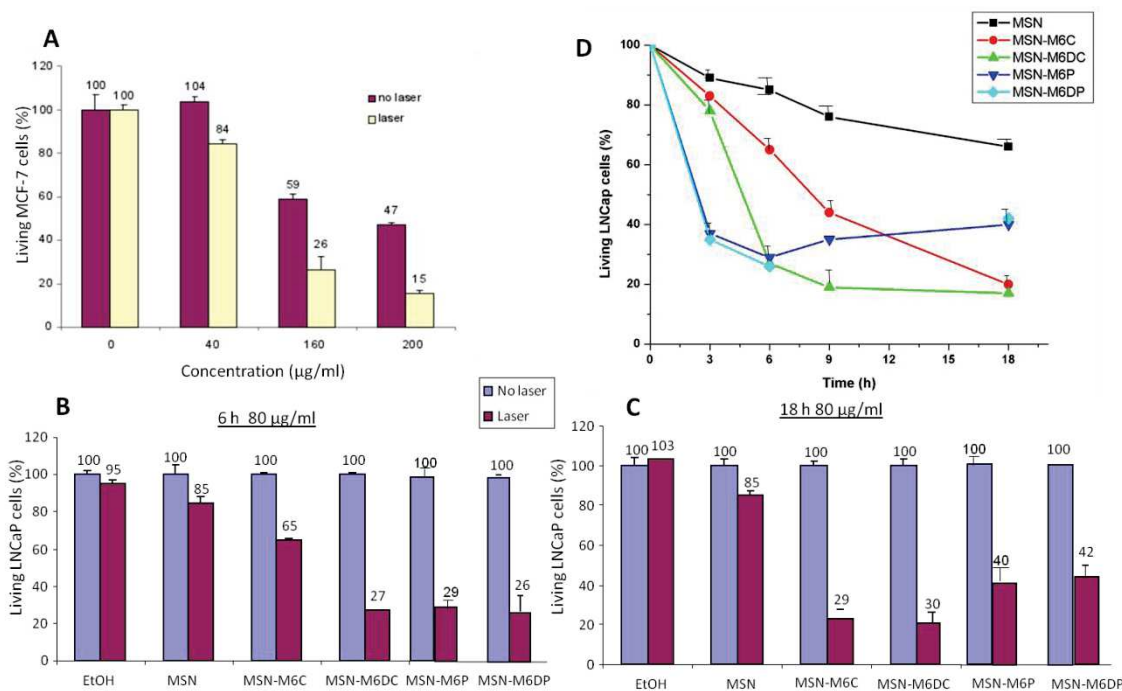


Fig. 8. In-vitro one hv PDT effect and kinetic internalisation studies on cancer cells. a) PDT on different concentrations of MSN in MCF-7 breast cancer cells. b-c) PDT effect of MSN and targeted MSN after 6 and 18 hours in LNCaP prostate cancer cells. d) Internalisation kinetic studies of MSN and targeted nanoparticles in LNCaP prostate cancer cells.

The endocytosis of the unfunctionalized MSN as well as the functionalized MSN was clearly seen with the confocal microscopy merged images in MCF-7 breast cancer cells and in LNCaP prostate cancer cells (Supp. Inf. S9-S10). Nanoparticles were incubated 24 hours and 5 hours for MCF-7 and LNCaP cells respectively and irradiated at 750 nm. An important quantity of nanoparticles functionalized with the mono-ligands were present in the membranes comparing to the naked MSN. With the di-ligands, nanoparticles were present in the membranes but an important quantity was internalized at 5 hours. The efficiency of the targeting for prostate cancer is clearly visible by fluorescence imaging as the quantity of internalized NPs is in fact more important in LNCaP cells than in MCF-7 cells (Figure 9). As it can be noted, the endocytosis of “naked” nanoparticles (MSN) is not really important compared with functionalized nanoparticles. Between the different ligands is confirmed that phosphonate ligands are better recognized by cancer receptors and more nanoparticles (MSN-M6P and MSN-M6DP) are easily internalized into the cancer cells compared with carboxylate-functionalized nanoparticles (MSN-M6C and MSN-M6DC).

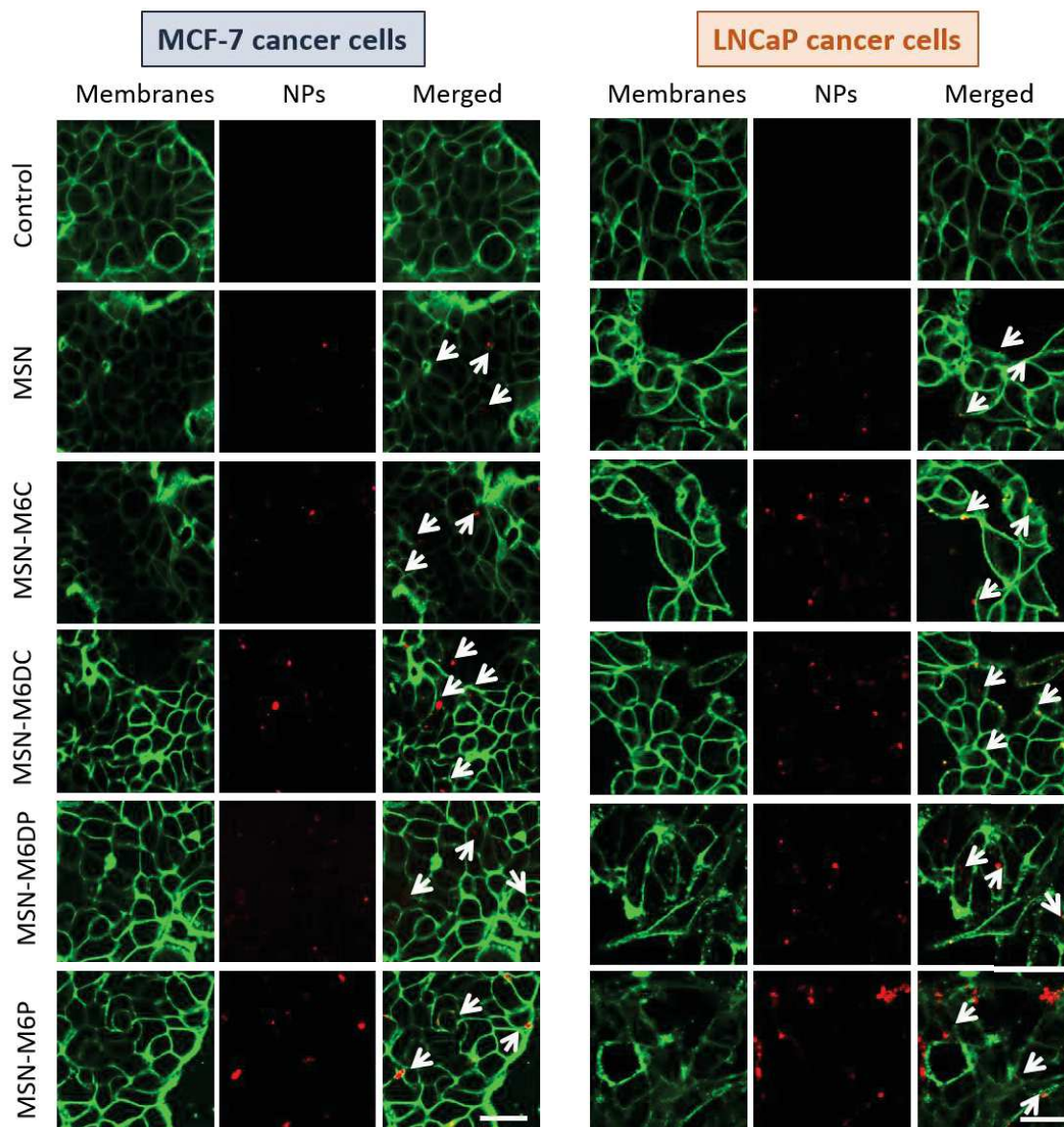


Fig. 9. Fluorescence imaging (5% of laser power) of MCF-7 breast and LNCaP prostate cancer cells. Cell membranes were stained with Cell Mask. Nanoparticles were incubated for 24 hours and 5 hours for MCF-7 and LNCaP cells respectively and irradiated at 750 nm. Arrows indicate NPs in cells. Scale bar 10 μm .

2.2.3. Conclusion

In summary, we have designed MCM-41 nanoparticles encapsulating a porphyrin photosensitizer. Their morphology and composition were fully characterized by various techniques, which showed the encapsulation of the PS. Then, the surface was functionalized by four different targeting ligands, analogues of the mannose-6-phosphate. Two families of analogues were studied: carboxylates and phosphonates and each family included a mono and a di-ligand. Their presence was confirmed by UV-visible spectroscopy. Besides, the nanoparticles cellular uptake was demonstrated by TPE-fluorescence imaging *in vitro* in LNCaP prostate cancer cells. One-photon therapy was applied to all nanoparticles and lead to 40 % to 75 % of cancer cell killing. The best effect was obtained for the di-ligands specially the phosphonate analogue after only 9 hours. The data demonstrated that the therapeutic strategy using M6DP as a target for prostate cancer is strongly effective. It is envisioned that such ligand-functionalized nanomaterial could be a new promising nanovector for applications in prostate cancer treatment.

2.2.4. Supporting Information

Experimental section

2.2.4. S1. Materials and general procedures

ACS reagents grade starting materials and solvents were used as received without further purification.

3-(2,5-dioxo-2,5-dihydro-1H-pyrrol-1-yl)-N-(3-(4-(10,15,20-tri(pyridin-4-yl)porphyrin-5-yl) phenoxy) propyl) propanamide was synthesized as described [51].

Cetyltrimethylammonium bromide (CTAB) was purchased from Alfa Aesar, tetraethyl orthosilicate (TEOS), amino-propyltriethoxy silane (APTES), (3- mercapto propyl)trimethoxysilane (MPS) and sodium hydroxide were purchased from Sigma-Aldrich. Ultrapure water was obtained with a Barnstead™Easypure™RoDi from Thermo Scientific. DLS measurements were performed on a Vasco Particle Size Analyzer DL135 from Cordouan Technologies and analyzed with nanoQ software. ¹HNMR spectra was recorded on a Bruker AC-300 spectrometer. Chemical shifts (in δ units, ppm) are referenced to TMS using DMSO-d₆ ($\delta = 2.50$ ppm) as the internal standard. IR spectra were recorded on a Perkin-Elmer 100 FT spectrophotometer. UV-visible spectra were obtained using a Perkin-Elmer spectrometer (molar extinction coefficient value is given in L mol⁻¹cm⁻¹). ²⁹Si and ¹³C solid state NMR sequences were recorded with a VARIAN VNMRS300, using Q8MH8 and adamantane references respectively. BET analyses were performed using a TRISTAR 3000 gas adsorption analyzer instrument. TEM analyses were performed on a JEOL 1200 EXII instrument.

Nanomaterial synthesis

2.2.4. S2. Silylation of PS precursor

PS [51] precursor was silylated overnight at room temperature following the procedure already described. Briefly, 5.31 mg (6.31 μ mol) of the porphyrin precursor were dissolved in 1 mL of MeOH and 4.3 μ L (21.8 μ mol) of (3-mercaptopropyl) trimethoxysilane were added. The reaction was stirred at room temperature for 12 h.

2.2.4. S3. Synthesis of mesoporous silica nanoparticles (MSN)

A mixture of 343 mg of CTAB (9×10^{-4} mol) and 20 mL of a freshly prepared solution of NaOH 0.12 M was stirred at 25°C for 2 hours at 400 rpm in a 500 mL three neck round bottom flask. Then, the photosensitizer PS (1 mL, 6.31×10^{-3} mmol) was added to the aforementioned solution. After 3 min, 1.75 mL (0.78×10^{-2} mmol) of TEOS were added dropwise. After 40 s, the mixture was diluted with 130 mL of deionized H₂O at 25°C and the stirring was increased at 750 rpm. The reaction was stirred for 6 minutes then rapidly neutralized to pH 7 by the addition of 0.2M HCl (about 20 mL). Afterwards, MSN were obtained after centrifugation (20 min. 20000 turns/min.). CTAB was extracted by sonication with 30 mL of a solution of NH₄NO₃ in EtOH (6g /L) at 40°C. After centrifugation, the extraction procedure was repeated two times, and then MSN were put in suspension in EtOH and centrifugated for three times. They were dried under vacuum for few hours. MSN were characterized by UV-visible spectra, with $\epsilon = 62921 \text{ M}^{-1} \cdot \text{cm}^{-1}$ for the Soret band ($\lambda = 415 \text{ nm}$). 108 mg of product were obtained.

2.2.4. S4. Surface functionalization: NH₂ - MSN

75.6 mg of MSN were put in suspension in 1.8 mL H₂O for 20 min. Then 756 μL of EtOH and 118 μl of APTES were added. The suspension was neutralized to pH 6 by addition of HCl 0.2M. The reaction was stirred at RT for 20h, and MSN-NH₂ were centrifuged for 15 min. at 20000 turns/min. The nanoparticles were washed by EtOH (dispersion with ultrasounds followed by centrifugation). They were dried under vacuum for few hours. 63.4 mg of product were obtained.

2.2.4. S5. Surface functionalization by ligand M6C (MSN-M6C)

9.4 mg of nanoparticles MSN-NH₂ were put in suspension in 2.4 mL of EtOH for 10 min in sonication. 1.3 mg (3.3×10^{-3} mmol) of M6C were dissolved in 2 mL of H₂O. This solution was added dropwise to the suspension of MSN-NH₂ in EtOH. The suspension was stirred at 50°C and 500 rpm overnight. After centrifugation (12 min., 10000 turns/min) the nanoparticles were redispersed in water (ultrasounds) and centrifuged again (3 cycles). Then MSN-M6C were redispersed in EtOH and centrifuged (two cycles). They were dried under vacuum for few hours. MSN-M6C were characterized by UV-visible spectra, with $\epsilon = 16000 \text{ M}^{-1} \cdot \text{cm}^{-1}$ for the ligand band ($\lambda = 290 \text{ nm}$). 7 mg of product were obtained.

2.2.4. S6. Surface functionalization by ligand *M6DC* (MSN-M6DC)

9.2 mg of nanoparticles MSN-NH₂ were put in suspension in 2.4 mL of EtOH for 10 min in sonication. 1.83 mg (3.3×10^{-3} mmol) of M6DC were dissolved in 2 mL of H₂O. This solution was added dropwise to the suspension of MSN-NH₂ in EtOH. The suspension was stirred at 50°C and 500 rpm overnight. After centrifugation (12 min., 10000 turns/min) the nanoparticles were redispersed in water (ultrasounds) and centrifuged again (3 cycles). Then MSN-M6C were redispersed in EtOH and centrifuged (two cycles). They were dried under vacuum for few hours. MSN-M6DC were characterized by UV-visible spectra, with $\epsilon = 16000 \text{ M}^{-1} \cdot \text{cm}^{-1}$ for the ligand band ($\lambda = 290 \text{ nm}$). 6.7 mg of product were obtained.

2.2.4. S7. Surface functionalization by ligand *M6P* (MSN-M6P)

9.2 mg of nanoparticles MSN-NH₂ were put in suspension in 2.4 mL of EtOH for 10 min in sonication. 1.75 mg (3.3×10^{-3} mmol) of M6P were dissolved in 2 mL of H₂O. This solution was added dropwise to the suspension of MSN-NH₂ in EtOH. The suspension was stirred at 50°C and 500 rpm overnight. After centrifugation (12 min., 10000 turns/min) the nanoparticles were redispersed in water (ultrasounds) and centrifuged again (3 cycles). Then MSN-M6C were redispersed in EtOH and centrifuged (two cycles). They were dried under vacuum for few hours. MSN-M6P were characterized by UV-visible spectra, with $\epsilon = 3147 \text{ M}^{-1} \cdot \text{cm}^{-1}$ for the ligand band ($\lambda = 290 \text{ nm}$). 7.5 mg of product were obtained.

2.2.4. S8. Surface functionalization by ligand *M6DP* (MSN-M6DP)

9.5 mg of nanoparticles MSN-NH₂ were put in suspension in 2.4 mL of EtOH for 10 min in sonication. 1.86 mg (3.3×10^{-3} mmol) of M6P were dissolved in 2 mL of H₂O. This solution was added dropwise to the suspension of MSN-NH₂ in EtOH. 50 μL of Et₃N were added and the suspension was stirred at RT for 18h. After centrifugation (12 min., 10000 turns/min) the nanoparticles were redispersed in water (ultrasounds) and centrifuged again (3 cycles). Then MSN-M6C were redispersed in EtOH and centrifuged (two cycles). They were dried under vacuum for few hours. MSN-M6DP were characterized by UV-visible spectra, with $\epsilon = 19174 \text{ M}^{-1} \cdot \text{cm}^{-1}$ for the ligand band ($\lambda = 290 \text{ nm}$). 6.6 mg of product were obtained.

***In vitro* studies**

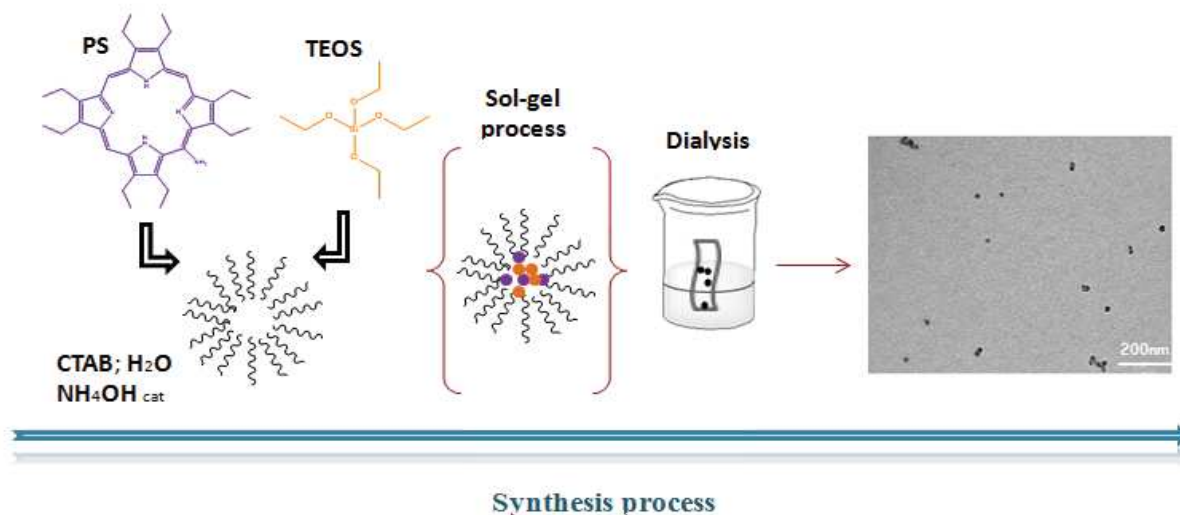
2.3.4. S9. *In vitro* one-photon photodynamic therapy (PDT) experimental settings

MCF-7 human breast cancer cells were cultured in Dulbecco's modified Eagle's medium (DMEM) supplemented with 10% foetal bovine serum and 50 $\mu\text{g}\cdot\text{mL}^{-1}$ gentamycin. All cells were allowed to grow in humidified atmosphere at 37°C under 5% CO_2 . For *in vitro* phototoxicity, MCF-7 cells were seeded into a 384 multiwell glass-bottomed plate (thickness 0.17 mm), with a black polystyrene frame, 2000 cells per well in 50 μL of culture medium, and allowed to grow for 24 h. NPs were then dispersed under ultrasounds in PBS at a concentration of 1 $\text{mg}\cdot\text{mL}^{-1}$ and cells were then incubated for 24 h with or without nanoparticles at a final concentration of 80 $\mu\text{g}\cdot\text{mL}^{-1}$ in supplemented DMEM. After incubation with NPs, cells were washed twice, maintained in fresh culture medium, and then submitted (or not) to laser irradiation. After 2 days, the MTT assay was performed.

2.3.4. S10. *In vitro* fluorescence imaging experimental settings

The day prior to the experiment, MCF-7 cells were seeded onto bottom glass dishes (World Precision Instrument, Stevenage, UK) at a density of 10^6 $\text{cells}\cdot\text{cm}^{-2}$. Adherent cells were then washed once and incubated in 1 ml culture medium containing NPs at a concentration of 80 $\mu\text{g}\cdot\text{mL}^{-1}$ for 5 h or 24 h. Fifteen min before the end of incubation, cells were loaded with Cell Mask TM Orange Plasma Membrane Stains (Invitrogen, Cergy Pontoise, France) for membrane staining at a final concentration of 5 $\mu\text{g}\cdot\text{mL}^{-1}$. Before visualization, cells were washed gently with phenol red-free DMEM. Cells were then scanned with LSM 780 LIVE (Carl Zeiss, Le Pecq, France), at 750 nm with a slice depth (Z stack) of 0.62 μm .

2.3. 20 nm sized mesoporous silica nanoparticles with porphyrin photosensitizers: towards photodynamic applications



Abstract

We report the synthesis of 20 nm sized mesoporous silica nanoparticles encapsulating three different porphyrin photosensitizers (PS). Synthesized by the sol-gel method, in the presence of cetyltrimethylammonium bromide surfactant and tetraorthosilicate as silica source, we developed those nanoparticles with the aim of treating cancer cells using photodynamic therapy (PDT). The colloidal stability, due to the PEG-silane chain grafted on the surface, was demonstrated at 37°C in cell culture medium. Then, nanoparticles were functionalized by silylated squarate mannose and used in MCF-7 breast cancer cells for one-photon therapy. Promising results were obtained after 5 hours of incubation.

Interdisciplinary collaboration

Nanomaterial synthesis, physico-chemical characterizations and applications in solution: C. Mauriello Jimenez, Y. Galán, V. Saunier, D. Warther, L. Raehm, J-O. Durand.

Synthesis of the porphyrin photosensitizer a and b: P. Maillard

Cell studies: A. Gallud, M. Maynadier, M. Gary-Bobo, M.Garcia.

Determination of oxygen quantum yield: C. Frochot, P. Arnoux

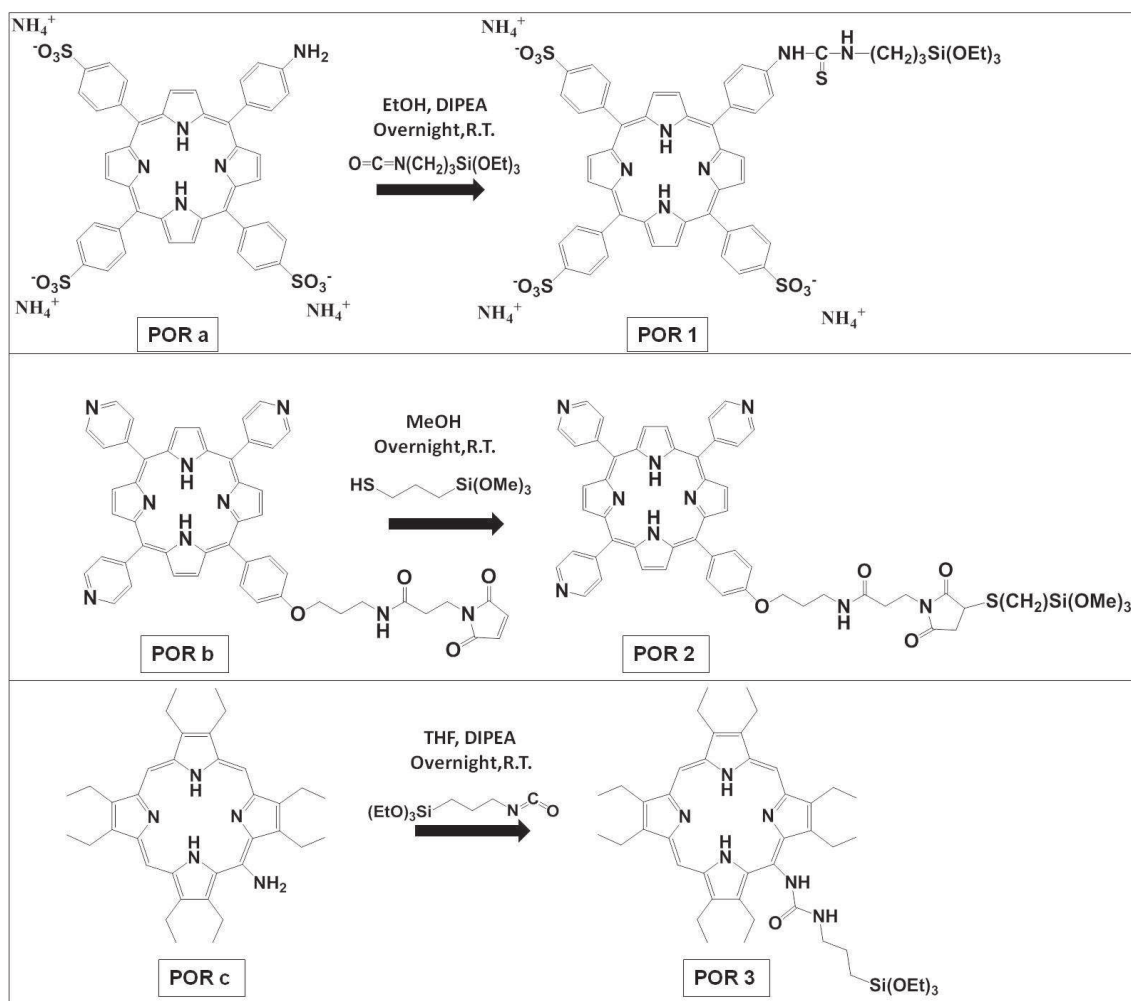
➤ *J. Sol-gel Sci. Technol.*, 2016, 1-10, DOI: 10.1007/s10971-016-3991-6

2.3.1. Introduction

Mesoporous Silica Nanoparticles (MSN) have attracted much attention in different fields in the last decade and particularly for biological applications. The field has been extensively reviewed.⁴⁰⁻⁶⁸ Indeed their tuneable pore size, flexible functionalization, and high specific surface area^{69, 70} allowed the use of MSN in many different applications such as antireflective coatings⁷¹, catalysis,⁷² sensors⁷³ and biology.⁷⁴ The usual size of MSN obtained from classical synthetic methods leads to diameters of about 100 nm. However the size reduction of MSN with diameters below 50 nm has been the subject of much effort over the last 6 years. Indeed small-sized MSN are particularly attractive for applications in material science⁷⁵ or biology,⁷⁶ and the mechanism of their synthesis has been recently investigated.⁷⁷ The pioneering works in down-sizing MSN diameter were performed by the groups of Kuroda, Huo, Mou, in 2009⁷⁸⁻⁸⁰ and by the group of Wiesner who reached diameter below 10 nm.^{81, 82} Small-sized MSN were used by Shi and co-workers^{83, 84} and others⁸⁵ for cancer applications. These nanoparticles conjugated with TAT peptide were able to target the nuclei of cells *in vitro* and *in vivo* and very efficient photodynamic therapy application⁸⁶ was described. In the course of our work on photodynamic therapy with silica-based particles,^{39, 87} we were interested in small-sized MSN in order to cross biological membranes. We performed the synthesis of mannose-functionalized 20 nm diameter MSN but as the outer specific surface area increased, the colloidal stability of the particles was difficult to achieve.⁸⁸ Finally we managed to image retinoblastoma cells. In the continuation of this work, we present here the syntheses and characterizations of mannose-functionalized small-sized MSN possessing porphyrin photosensitizers in the walls of the MSN towards photodynamic therapy applications.

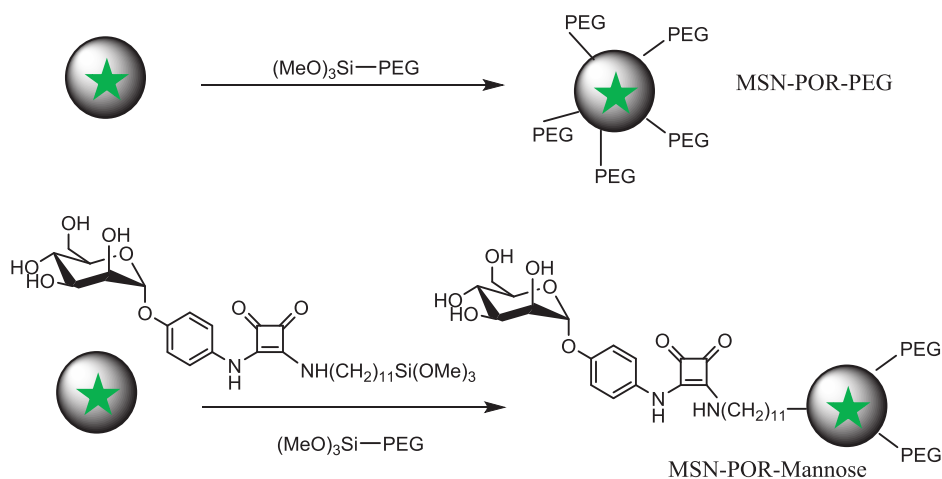
2.3.2. Results and discussion

First of all, the silylation of the three porphyrin (a, b and c) photosensitizers was performed overnight at room temperature under different conditions (Scheme 1 and Supp. Inf. S2).



Scheme 1. Silylation of the POR precursors.

Then, nanoparticles were synthesized (Supp. Inf. S3) by the sol-gel procedure at 50°C overnight in the presence of TEOS and silylated porphyrins POR 1-3 (*solution 1*). In order to stabilize the colloidal surface of the nanoparticles, 10 mL of the solution were stirred overnight with PEG-Si at 50°C and then were dialyzed for 6 days in order to remove the surfactant. MSN-POR-PEG were obtained (Scheme 2 and Supp. Inf. S4)



Scheme 2. Surface functionalization of MSN following ref⁸⁸.

Number-averaged DLS, size distribution and TEM of MSN-POR-PEG are depicted in Figure 1. Dynamic light scattering (DLS) of MSN-POR-PEG (in EtOH) showed nanoparticles with a hydrodynamic diameter of 20-22 nm. The PEG-Si allowed the colloidal stabilization of nanoparticles as is shown in Figure 1 (a-c). We obtained monodisperse solutions of nanoparticles with a hydrodynamic diameter of 20-22 nm. TEM image showed mesoporous nanoparticles measuring around 19 nm. The size was confirmed by the study of the size distribution. The resulting Gaussian analysis of 100 nanoparticles demonstrated the agreement between TEM and DLS analysis giving as size 20 nm for the POR1 (Figure 1d) and POR3 (Figure 1f) and 18 nm for POR2 (Figure 1e). Following these results any separation method had to be applied to the nanoparticles solution.

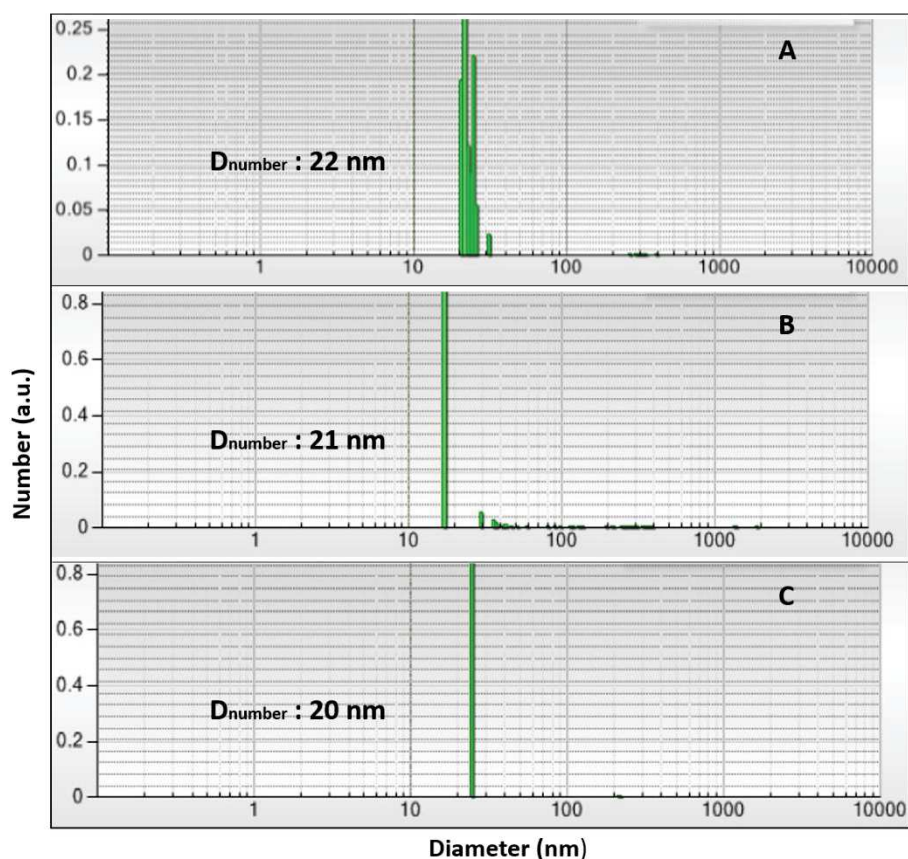


Fig. 1. a-c Number-averaged DLS in EtOH of MSN-POR1-PEG, MSN-POR2-PEG and MSN-POR3-PEG after dialysis.

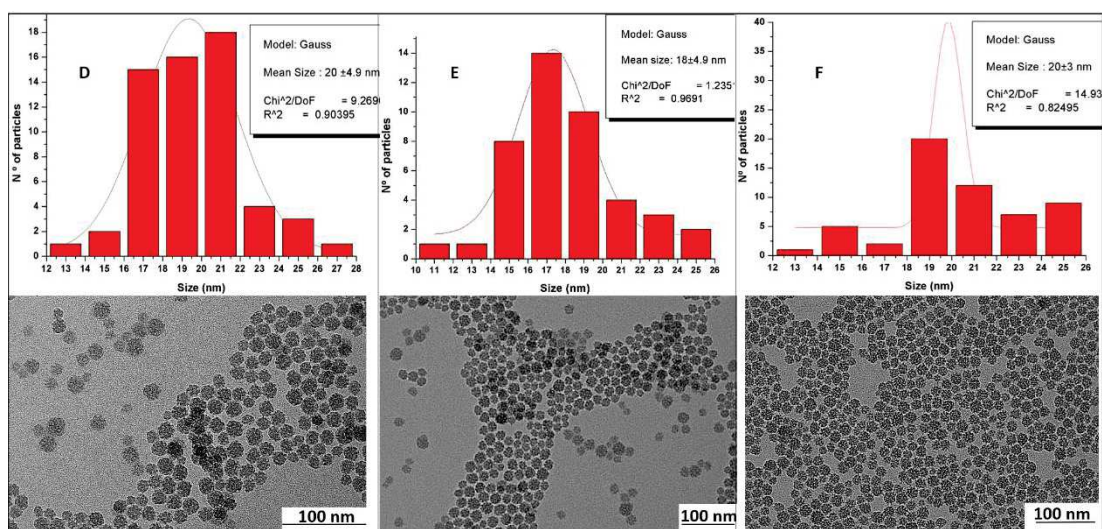


Fig. 1.d-f) Distribution size and TEM images of the corresponding MSN-POR-PEG nanoparticles. Images showed a homogenous size of nanoparticles (scale bar: 100 nm).

The MSN were also functionalized with PEG and silylated α -D-mannose following a procedure recently described (Supp. Inf. S5).⁸⁸ The MSN-POR2-Mannose were analysed by Dynamic Light Scattering (DLS) at 25°C and at 37 °C, to study their stability at physiologic temperature (Figure 2). On the left, nanoparticles were first

tested in saline conditions with PBS at 25 °C and then at 37°C for 40 min. Therefore 1 mL of a solution of MSN-POR2-Mannose (10 mg of nanoparticles/mL of EtOH) were added to 1 mL of PBS and the suspension was homogenized by sonication and allowed to stay for 24 hours at room temperature.

On the right, their stability was studied in a mixture of cell culture medium (GIBCO) with 20% foetal bovine serum, 100 U mL⁻¹ of penicillin and 100 gmL⁻¹ of streptomycin. According to that, 500 µL of the nanoparticles solution were diluted in 500 µL of the cell culture medium and treated as mentioned before. As it can be observed, the size distribution is similar at 25°C and 37°C and the prepared MSN were stable in the cell culture medium.

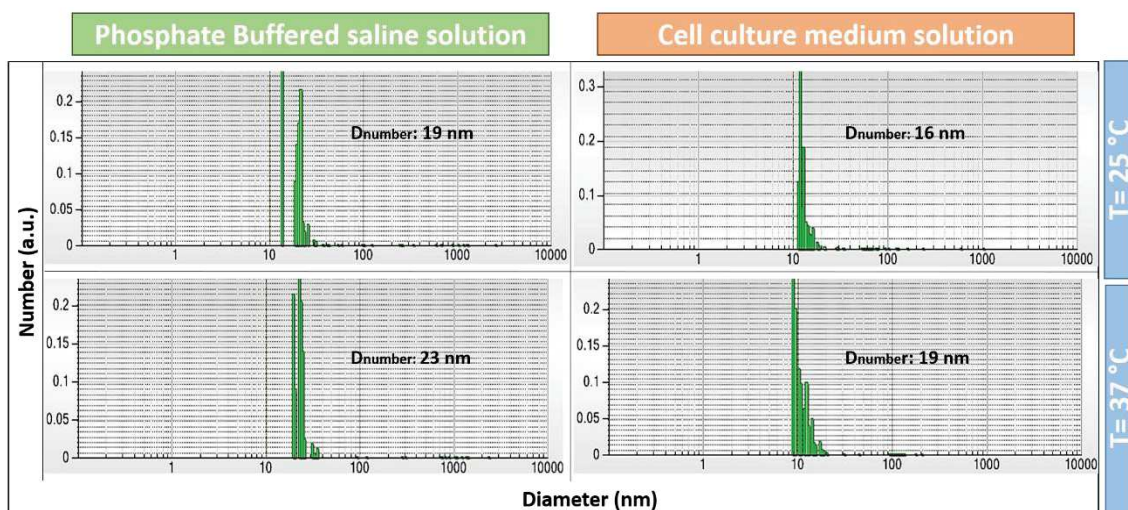


Fig. 2. DLS of MSN-POR2-Mannose. On the left side, measurements in PBS at 25°C and 37°C. On the right, measurements in cell culture medium at 25°C and 37°C.

The specific surface area and pore characteristics of MSN-POR2 after dialysis were examined using the nitrogen adsorption-desorption measurements. As shown in Figure 3a, NPs present typical IV isotherm characteristics with defined step at a relative pressure of 0.4. An hysteresis at 0.8 corresponding to the interparticle aggregates can be observed. This phenomenon is confirmed by BJH analysis of pore size (Figure 3b). The first band at 2.5 nm corresponds to the pore size and the second and third band at 5 nm and 9.6 nm respectively, correspond to the space between nanoparticles. The specific surface area was 840 m²/g and the pore volume was 1.28 cm³/g.

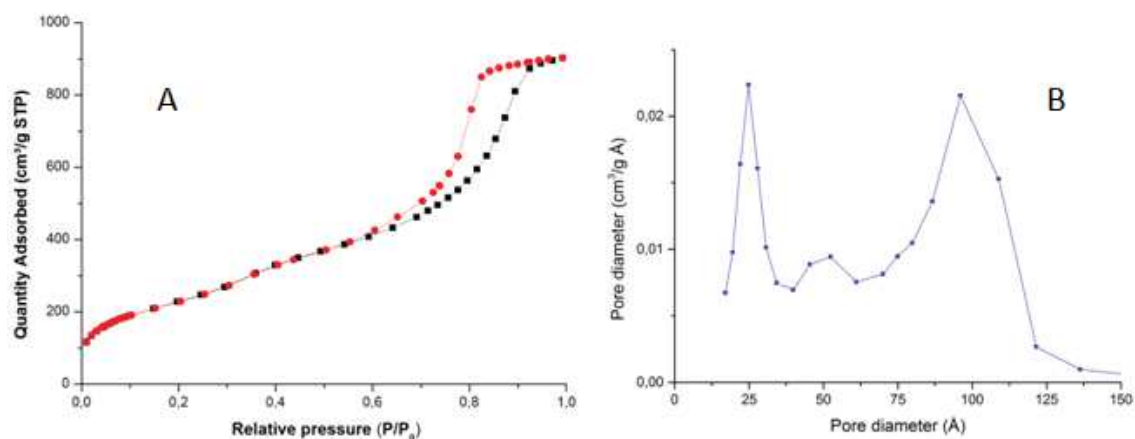


Fig. 3. a) The N₂ adsorption-desorption isotherms and b) the pore distribution of NPs.

The amount of encapsulated photosensitizer and grafted targeting biomolecule was determined by quantitative analysis of the intensity of the absorption spectra bands. The UV-Visible absorption spectra of 1 mL of MSNs solutions (1 mL in EtOH contains 10 mg of MSN) and POR are shown in Figure 4. The quantity of porphyrin was determined using the intensity of the Soret band at 420 nm and the quantity of mannose was determined at 340 nm, using the Beer-Lambert law (Table 1). The first spectra of anionic porphyrin POR 1, MSN-POR1-PEG and MSN POR1-Mannose are presented Figure 4a. We observed that the Soret and Q bands of POR1 are not shifted after encapsulation in agreement with well dispersed and non-aggregated POR1 in MSN. UV-Vis spectra of POR2, MSN-POR2-PEG, and MSN-POR2-Mannose are presented Figure 4b. A modification of the Q bands was observed when comparing the spectra of MSN-POR2 with the porphyrin precursor. This is probably due to the formation of aggregates of POR2 inside the nanoparticles. The concentration of POR2 in MSN is three times more important than POR1 in MSN. In Figure 4c, UV-Vis spectra of POR 3 and the corresponding MSNs are depicted. At 420 nm, a red shift of the Soret band was observed and it can be also observed that the four Q bands of POR3 are changed in two Q bands when POR3 was encapsulated in MSN. The disparition of two Q bands is due to the formation of the dication of the porphyrin by the treatment with AcOH during the dialysis process (Fig. 4d). With the addition of acid, the symmetry of porphyrin is changed from a D_{2h} which is corresponding to a free-base porphyrin, to a D_{4h} symmetry which corresponds to the attachment of protons to the two imino nitrogens of the pyrrole rings of the porphyrin.

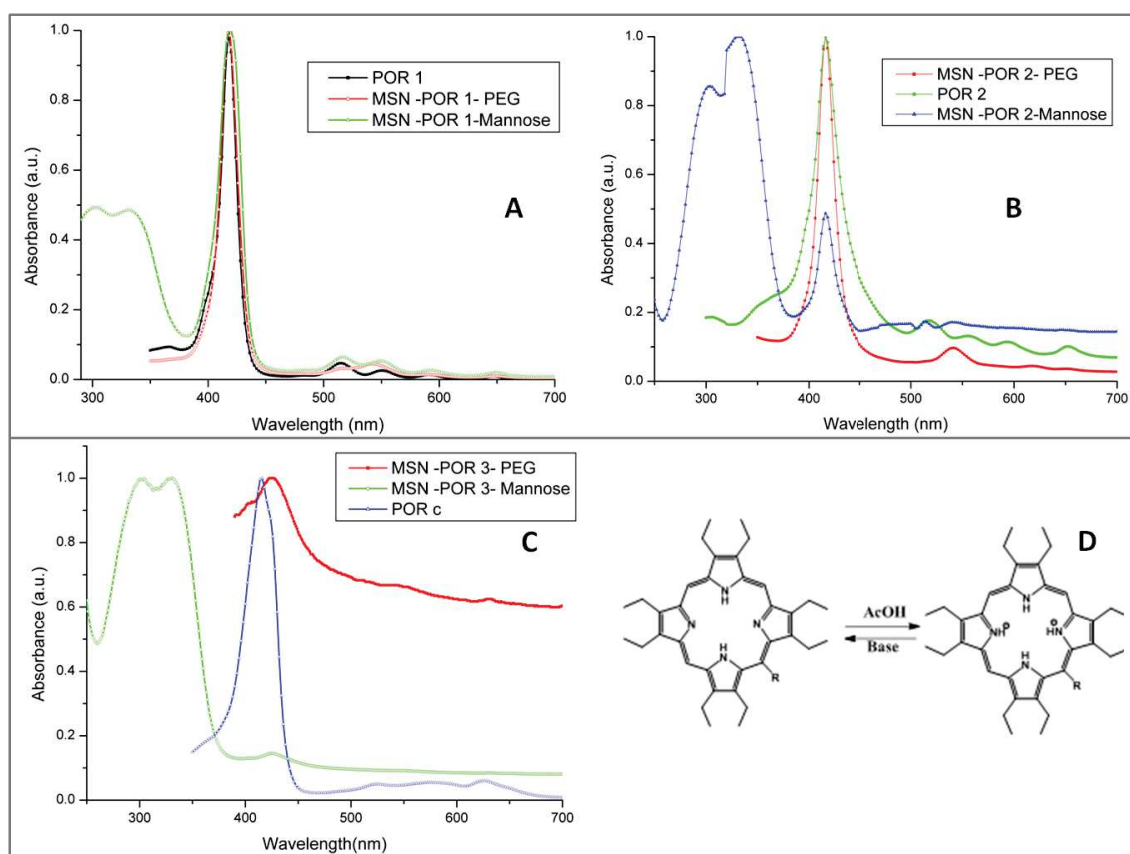


Fig. 4. a-b-c) UV-vis absorbance spectra in EtOH of the different porphyrins and the corresponding NPs and d) scheme of protonation of the free base porphyrin c under acidic conditions.

	Porph. [c] ($\mu\text{mol/g NPs}$)	Mannose [c] ($\mu\text{mol/g NPs}$)
MSN-POR 1-Mannose	1	14
MSN-POR 2-Mannose	3	11
MSN-POR 3-Mannose	0.1	5

Table 1. Quantification of porphyrin and mannose in NPs.

The quantum yield of singlet oxygen production obtained by $^1\text{O}_2$ phosphorescence measurements in EtOH (Supp. Inf. S6), with Rose Bengal used as standard reference, was calculated to be 43% for MSN-POR1-Mannose and 47% for MSN-POR2-Mannose (Figure 5). Therefore, MSN-POR2-Mannose were subsequently used for PDT of MCF-7 breast cancer cells.

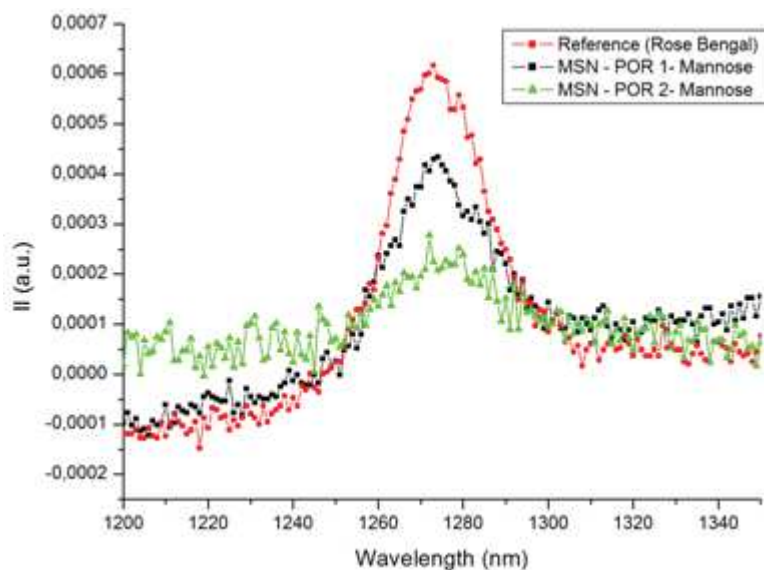


Fig. 5. $^1\text{O}_2$ Phosphorescence spectra and determination of singlet oxygen production of MSN-POR1-Mannose and MSN-POR2-mannose ($\lambda_{\text{ex}} = 422 \text{ nm}$) using Rose Bengal as reference in EtOH.

Breast cancer cells (MCF-7) were incubated with the photo-activable MSN-POR2-Mannose at $80 \mu\text{g mL}^{-1}$ for various times at 37°C (Supp. Inf. S7). Then, they were irradiated for 10 min at a laser wavelength of 420 nm which corresponds to the Soret band wavelength. The colorimetric assay with MTT (a yellow tetrazole reduced to a purple formazan in living cells) was then performed after two days to assess the cytotoxicity of the nanoparticles (Figure 6). The nanoparticles were not cytotoxic at $80 \mu\text{g mL}^{-1}$ without a specific irradiation as is shown in blue columns. However, under excitation at 420 nm, MSN-POR2-Mannose showed photocytotoxicity which is in agreement with $^1\text{O}_2$ formation. A significant cell death was observed after only 3 hours incubation and reached 33% after 5 hours. This result confirmed a rapid cellular uptake of the MSN.

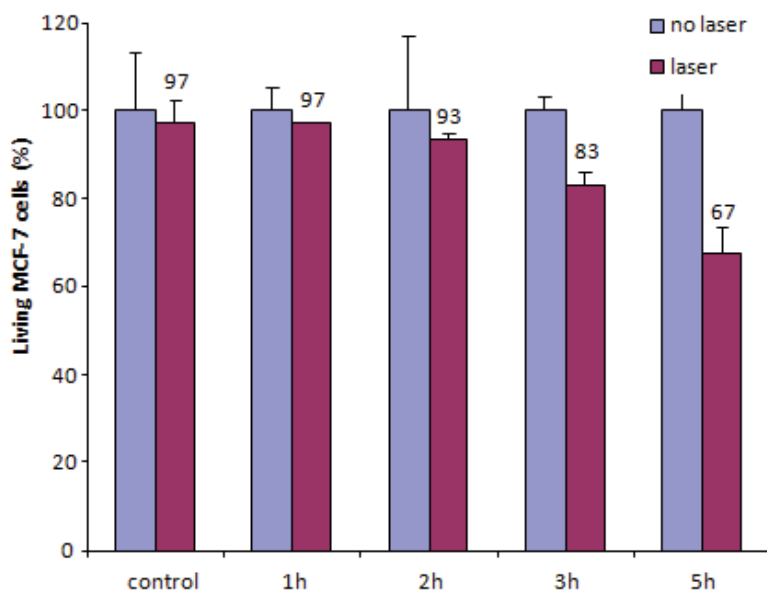


Fig. 6. *In vitro* PDT effect of MSN-POR2-Mannose on human breast cancer cells. MCF-cells were incubated during different times, rinsed and then irradiated at 420 nm during 10 min using a fluorescence microscope equipped.

2.3.3. Conclusion

20 nm mesoporous silica nanoparticles covalently encapsulating porphyrin photosensitizers have been successfully prepared by the sol gel procedure in presence of CTAB and TEOS. The surface of the nanoparticles was functionalized with PEG-silane or PEG and silylated squarate mannose. The stability of the prepared nanoparticles was demonstrated by DLS analyses at 25°C and 37°C in PBS and in cell culture medium. MSN-POR1-Mannose and MSN-POR2-Mannose were able to produce singlet oxygen and preliminary *in vitro* PDT experiments with MSN-POR2-Mannose were successfully performed on breast cancer cells.

2.3.4. Supporting Information

Experimental section

2.3.4. S1. Materials and general procedures

ACS reagents grade starting materials and solvents were used as received without further purification.

Ammonium 4,4',4''-(20-(4-aminophenyl) porphyrin-5, 10,15-triyl)tribenzenesulfonate (**POR a**) and 3-(2,5-dioxo-2,5-dihydro-1H-pyrrol-1-yl)-N-(3-(4-(10,15,20-tri(pyridin-4-yl)porphyrin-5-yl) phenoxy) propyl) propanamide (**POR b**) were synthesized as described [51,49]. 5-(amino)-2, 3, 7, 8, 12, 13, 17, 18-(octaethyl) porphyrin was purchased from Pophychem (**POR c**).

3-(((4-(((2R, 3S, 4S, 5S, 6R)-3, 4, 5-trihydroxy-6-(hydroxymethyl) tetrahydro-2H-pyran-2-yl) oxy) phenyl) amino)-4-((3-(trimethoxysilyl) propyl) amino) cyclobutane-1, 2-dione (*silylated squarate mannose, Mannose-Si*)) was obtained from a reported procedure by D. Warther et al. (RSC Adv. **2014**, 4, 37171-37179).

Cetyltrimethylammonium bromide (CTAB) was purchased from Alfa Aesar, tetraethyl orthosilicate (TEOS), amino-propyltriethoxy silane (APTES), isocyanatopropyltriethoxy silane (IPTS), (3- mercapto propyl)trimethoxysilane (MPS) and ammonium hydroxide were purchased from Sigma-Aldrich. (6-[2-(2-[2-Methoxyethoxy]-ethoxy)-ethoxy] hexyl) trimethoxysilane (PEG-Si) and 11-amino-undecyltrimethoxysilane (NH₂-Si) were purchased from SiKEMIA. Ultrapure water was obtained with a Barnstead™Easypure™RoDi from Thermo Scientific. DLS measurements were performed on a Vasco Particle Size Analyzer DL135 from Cordouan Technologies and analyzed with nanoQ software. ¹H NMR spectra was recorded on a Bruker AC-300 spectrometer. Chemical shifts (in δ units, ppm) are referenced to TMS using DMSO-d₆ (δ = 2.50 ppm) as the internal standard. IR spectra were recorded on a Perkin-Elmer 100 FT spectrophotometer. UV-visible spectra were obtained using a Perkin-Elmer spectrometer (molar extinction coefficient value is given in L mol⁻¹ cm⁻¹). TEM images were taken on a JEOL 1200 EXII, 120 kV.

Nanomaterial synthesis and characterizations

2.3.4. S2. Preparation of POR1 - POR2 - POR3

PORa and **PORb** precursors were silylated overnight at room temperature following the procedure already described. **PORc** was silylated with isocyanatopropyltriethoxysilane. Briefly, 3.1 mg (5.45 μmol) of the photosensitizer were dissolved in 1 mL of tetrahydrofuran, 4.2 μL (3 eq.) of isocyanatopropyltriethoxysilane and 4.4 μL (5 eq.) of diisopropylethylamine were added. The reaction was stirred at room temperature for 12 h. The yield for the three reactions was 97-98 %.

^1H NMR POR3 (300 MHz, DMSO): δ 7.31(s, 1H, pyr-CH-pyr), 7.09(s, 1H, pyr-CH-pyr), 6.05(s, 1H, pyr-CH-pyr), 5.75(s, 1H, CO-NH-CH₂), 4.36(s, 1H, CO-NH-porh), 3.75 (q, $^3J = 6.8$ Hz, 6H, O-CH₂-CH₃), 3.60 (t, $^3J = 6.0$ Hz, 16H, CH₃-CH₂-porph), 1.76 (t, $^3J = 6.4$ Hz, 24H, CH₃-CH₂-porph), 1.66 – 1.54 (m, 4H, CH₂-CH₂-CH₂-Si), 1.15 (t, $^3J = 7.0$ Hz, 9H, O-CH₂-CH₃), 0.66 – 0.54 (t, $^3J = 7.0$ Hz, 2H, CH₂.Si).

2.3.4. S3. Synthesis of 20 nm sized mesoporous silica nanoparticles: Intermediary solution (I)

A mixture of 816 mg of CTAB (2.24 mmol; 0.5 eq.), ultrapure water (100 mL) and 1 mL of a freshly prepared solution of NH₄OH 0.2 M (0.2 mmol; 0.04 eq.) was stirred at 50°C for 2 hours at 500 rpm in a 250 mL three neck round bottom flask. Then, the photosensitizer POR (0.3mL, $1.63 \cdot 10^{-3}$ mmol) was added to the aforementioned solution. After 30 seconds, tetraorthoethylsilicate (1mL) was fast added to the mixture and the condensation process was conducted overnight. Afterwards, the solution was cooled at room temperature and stored without purification.

2.3.4. S4. Surface stabilization: PEG-Si chain (MSN-POR-PEG)

10 mL of the solution aforementioned (*solution I*) was stirred at 50°C at 500 rpm in a Schlenck. Then, 126 mg of PEG-Si was added and the mixture was stirred overnight at the same temperature. Once the solution was cooled, purification and extraction of the surfactant (CTAB) were done by dialysis process (cut off 12 kDa) in a mixture of EtOH/H₂O/AcOH: 1/1/0.07 for 24 hours. The operation was renewed two times. The suspension was then dialyzed in EtOH for three times for 24 hours and stored at room

temperature in EtOH. The multiples dialysis allowed the removal of the directing agent and of any non-grafted compound.

2.3.4. S5. Surface stabilization and functionalization by Mannose-Si (MSN-POR-Mannose)

MSN-POR-Mannose were functionalized on the surface as described [50]. Briefly, 10 mL of the solution aforementioned (*solution I*) was stirred at 50°C at 500 rpm in a Schlenck. Then, 126 mg of PEG-Si was added along with a solution of Mannose-Si in DMSO (13 mg in 0.4 mL of DMSO) and the mixture was stirred overnight at the same temperature. Extraction and purification process was done as mentioned before.

2.3.4. S6. Determination of singlet oxygen quantum yield [$\phi(^1\text{O}_2)$]

$^1\text{O}_2$ luminescence spectra were recorded on a Horiba Jobin Yvon Fluorolog-3 (FL3-222) spectrofluorimeter equipped with a 450 W Xenon lamp, a thermostated cell compartment (25°C), a R928 (HAMAMATSU Japan) UV-visible photomultiplier and a liquid nitrogen cooled InGaAs infrared detector (DSS-16A020L Electro-Optical System Inc., Phoenixville, PA, USA). The excitation spectrometer is a SPEX double grating monochromator (1200 grating/mm blazed 330 nm). $^1\text{O}_2$ production was measured by the IR detector through a SPEX double grating monochromator (600 grating/mm blazed 1 μm). All spectra were recorded using four optical faces quartz cells. Rose Bengal was chosen as reference solutions thanks to its high $^1\text{O}_2$ quantum yields in ethanol ($\Phi_{\Delta} = 0.68$)⁵³. The absorbance value at the excitation wavelength of the reference and the sample solutions were set to around 0.2.

***In vitro* studies**

2.3.4. S7. *In vitro* one-photon photodynamic therapy (PDT) experimental settings

MCF-7 human breast cancer cells were cultured in Dulbecco's modified Eagle's medium (DMEM) supplemented with 10% foetal bovine serum and 50 $\mu\text{g.mL}^{-1}$ gentamycin. All cells were allowed to grow in humidified atmosphere at 37°C under 5% CO_2 . For *in vitro* phototoxicity, MCF-7 cells were seeded into a 384 multiwell glass-bottomed plate (thickness 0.17 mm), with a black polystyrene frame, 2000 cells per well in 50 μL of culture medium, and allowed to grow for 24 h. NPs were then dispersed

under ultrasounds in PBS at a concentration of 1 mg.mL^{-1} and cells were then incubated for 5 h with or without nanoparticles at a final concentration of $80 \text{ }\mu\text{g.mL}^{-1}$ in supplemented DMEM. After incubation with NPs, cells were washed twice, maintained in fresh culture medium, and then submitted (or not) to laser irradiation. After 2 days, the MTT assay was performed.

2.4. General conclusions and perspectives

Different porphyrin photosensitizers were covalently encapsulated in mesoporous silica nanoparticles and used for *in vitro* one photon therapy and imaging. First, MCM-41 nanoparticles were synthesized by sol-gel process at room temperature and functionalized by four novel analogues of the membrane lectin overexpressed in prostate cancer cells, the mannose-6-receptor. Two novel carboxylated and phosphonated analogues were tested. Their kinetic internalisation was tested at 3, 6, 9 and 18 hours and phosphonate analogues presented a faster internalisation and exocytosis. Their PDT effect was studied under irradiation at 650 nm in LNCaP prostate cancer cells, and better results were obtained for di-substituted analogues with almost 75% of death. Imaging results at 750 nm were also reported for the four nanoparticles.

Second, 20 nm-sized MSNs were synthesized at 50 °C under ammonium hydroxide catalysis. Three different porphyrins were encapsulated and the resulting nanoparticles were analysed by different techniques. The production of singlet oxygen for two of them make them useful for photodynamic therapy. Nanoparticles produced 30% of death after only 5 hours of incubation.

In a near future drug delivery of camptothecin or doxorubicin could be envisaged for the first type of nanoparticles. Test in zebrafish will be done to demonstrate the capacity of these targeted nanoparticles for *in vivo* imaging and PDT. For the second type of nanoparticles, another type of powerful photosensitizers have to be tested to obtain a high percent of death. New targeting biomolecules have also to be tried to improve their internalisation.

2.5. References

1. D. F. Emerich, *Expert Opin. Biol. Ther.*, 2005, **5**, 1-5.
2. L. Y. Rizzo, B. Theek, G. Storm, F. Kiessling and T. Lammers, *Curr. Opin. Biotechnol.*, 2013, **24**, 1159-1166.
3. J. L. Markman, A. Rekechenetskiy, E. Holler and J. Y. Ljubimova, *Adv. Drug Delivery Rev.*, 2013, **65**, 1866-1879.
4. E. M. B. Brown, 2015.
5. T. Lammers, L. Y. Rizzo, G. Storm and F. Kiessling, *Clin. Cancer Res.*, 2012, **18**, 4889-4894.
6. J. M. Rosenholm, C. Sahlgren and M. Linden, *Nanoscale*, 2010, **2**, 1870-1883.
7. J. Zhang and J. M. Rosenholm, *Ther. Delivery*, 2015, **6**, 891-893.
8. V. Mamaeva, C. Sahlgren and M. Linden, *Adv. Drug Delivery Rev.*, 2013, **65**, 689-702.
9. C. Vincent, R. J. E and V. C. D, Google Patents, Editon edn., 1971.
10. D. Margolese, J. A. Melero, S. C. Christiansen, B. F. Chmelka and G. D. Stucky, *Chemistry of Materials*, 2000, **12**, 2448-2459.
11. Q. Cai, Z.-S. Luo, W.-Q. Pang, Y.-W. Fan, X.-H. Chen and F.-Z. Cui, *Chemistry of Materials*, 2001, **13**, 258-263.
12. C. E. Fowler, D. Khushalani, B. Lebeau and S. Mann, *Advanced Materials*, 2001, **13**, 649-652.
13. R. I. Nooney, D. Thirunavukkarasu, Y. Chen, R. Josephs and A. E. Ostafin, *Chemistry of Materials*, 2002, **14**, 4721-4728.
14. C.-Y. Lai, B. G. Trewyn, D. M. Jeftinija, K. Jeftinija, S. Xu, S. Jeftinija and V. S. Y. Lin, *J. Am. Chem. Soc.*, 2003, **125**, 4451-4459.
15. W. Stober, A. Fink and E. Bohn, *Journal of Colloid and Interface Science*, 1968, **26**, 62-69.
16. M. Grün, I. Lauer and K. K. Unger, *Advanced Materials*, 1997, **9**, 254-257.
17. K. Yano and Y. Fukushima, *Journal of Materials Chemistry*, 2004, **14**, 1579-1584.
18. T. Nakamura, M. Mizutani, H. Nozaki, N. Suzuki and K. Yano, *The Journal of Physical Chemistry C*, 2007, **111**, 1093-1100.
19. J. E. Lee, N. Lee, H. Kim, J. Kim, S. H. Choi, J. H. Kim, T. Kim, I. C. Song, S. P. Park, W. K. Moon and T. Hyeon, *Journal of the American Chemical Society*, 2010, **132**, 552-557.
20. H. Meng, M. Xue, T. Xia, Z. Ji, D. Y. Tarn, J. I. Zink and A. E. Nel, *Acs Nano*, 2011, **5**, 4131-4144.
21. J. Lu, M. Liong, Z. Li, J. I. Zink and F. Tamanoi, *Small*, 2010, **6**, 1794-1805.
22. Q. He, Y. Gao, L. Zhang, Z. Zhang, F. Gao, X. Ji, Y. Li and J. Shi, *Biomaterials*, 2011, **32**, 7711-7720.
23. J. Lu, E. Choi, F. Tamanoi and J. I. Zink, *Small (Weinheim an der Bergstrasse, Germany)*, 2008, **4**, 421-426.
24. T. Xia, M. Kovochich, M. Liong, H. Meng, S. Kabehie, S. George, J. I. Zink and A. E. Nel, *ACS Nano*, 2009, **3**, 3273-3286.
25. H. Meng, M. Liong, T. Xia, Z. Li, Z. Ji, J. I. Zink and A. E. Nel, *ACS Nano*, 2010, **4**, 4539-4550.
26. X. Li, J. Zhang and H. Gu, *Langmuir*, 2011, **27**, 6099-6106.
27. F. Gao, P. Botella, A. Corma, J. Blesa and L. Dong, *The Journal of Physical Chemistry B*, 2009, **113**, 1796-1804.

28. M.-H. Kim, H.-K. Na, Y.-K. Kim, S.-R. Ryoo, H. S. Cho, K. E. Lee, H. Jeon, R. Ryoo and D.-H. Min, *Acs Nano*, 2011, **5**, 3568-3576.
29. A. M. Chen, M. Zhang, D. G. Wei, D. Stueber, O. Taratula, T. Minko and H. X. He, *Small*, 2009, **5**, 2673-2677.
30. S.-H. Cheng, C.-H. Lee, M.-C. Chen, J. S. Souris, F.-G. Tseng, C.-S. Yang, C.-Y. Mou, C.-T. Chen and L.-W. Lo, *Journal of Materials Chemistry*, 2010, **20**, 6149-6157.
31. E. Gianotti, B. Martins Estevão, F. Cucinotta, N. Hioka, M. Rizzi, F. Renò and L. Marchese, *Chemistry – A European Journal*, 2014, **20**, 10921-10925.
32. X. Ma, Q. Qu and Y. Zhao, *ACS Applied Materials & Interfaces*, 2015, **7**, 10671-10676.
33. M. Gary-Bobo, Y. Mir, C. Rouxel, D. Brevet, I. Basile, M. Maynadier, O. Vaillant, O. Mongin, M. Blanchard-Desce, A. Morere, M. Garcia, J.-O. Durand and L. Raehm, *Angewandte Chemie-International Edition*, 2011, **50**, 11425-11429.
34. M. Gary-Bobo, O. Hocine, D. Brevet, M. Maynadier, L. Raehm, S. Richeter, V. Charasson, B. Looock, A. Morere, P. Maillard, M. Garcia and J.-O. Durand, *International Journal of Pharmaceutics*, 2012, **423**, 509-515.
35. M. Gary-Bobo, Y. Mir, C. Rouxel, D. Brevet, O. Hocine, M. Maynadier, A. Gallud, A. Da Silva, O. Mongin, M. Blanchard-Desce, S. Richeter, B. Looock, P. Maillard, A. Morere, M. Garcia, L. Raehm and J.-O. Durand, *International Journal of Pharmaceutics*, 2012, **432**, 99-104.
36. O. Hocine, M. Gary-Bobo, D. Brevet, M. Maynadier, S. Fontanel, L. Raehm, S. Richeter, B. Looock, P. Couleaud, C. Frochot, C. Charnay, G. Derrien, M. Smaïhi, A. Sahmoune, A. Morere, P. Maillard, M. Garcia and J.-O. Durand, *Int. J. Pharm.*, 2010, **402**, 221-230.
37. M. Gary-Bobo, P. Nirde, A. Jeanjean, A. Morere and M. Garcia, *Current Medicinal Chemistry*, 2007, **14**, 2945-2953.
38. O. Vaillant, K. El Cheikh, D. Warther, D. Brevet, M. Maynadier, E. Bouffard, F. Salgues, A. Jeanjean, P. Puche, C. Mazerolles, P. Maillard, O. Mongin, M. Blanchard-Desce, L. Raehm, X. Rebillard, J.-O. Durand, M. Gary-Bobo, A. Morere and M. Garcia, *Angew. Chem., Int. Ed.*, 2015, **54**, 5952-5956.
39. D. Brevet, M. Gary-Bobo, L. Raehm, S. Richeter, O. Hocine, K. Amro, B. Looock, P. Couleaud, C. Frochot, A. Morere, P. Maillard, M. Garcia and J. O. Durand, *Chemical Communications*, 2009, 1475-1477.
40. N. Z. Knezevic and J.-O. Durand, *Nanoscale*, 2015, **7**, 2199-2209.
41. N. Z. Knezevic and J.-O. Durand, *ChemPlusChem*, 2015, **80**, 26-36.
42. Y. Zhang, J. Yan and S. Liu, *Biointerface Research in Applied Chemistry*, 2014, **4**, 767-775, 769.
43. K.-N. Yang, C.-Q. Zhang, W. Wang, P. C. Wang, J.-P. Zhou and X.-J. Liang, *Cancer Biology & Medicine*, 2014, **11**, 34-43.
44. P. Nadrah, O. Planinsek and M. Gaberscek, *Journal of Materials Science*, 2014, **49**, 481-495.
45. Q. He and J. Shi, *Advanced Materials (Weinheim, Germany)*, 2014, **26**, 391-411.
46. P. N. Dave and L. V. Chopda, *Materials Science Forum*, 2014, **781**, 17-24, 19 pp.
47. C. Argyo, V. Weiss, C. Braeuchle and T. Bein, *Chemistry of Materials*, 2014, **26**, 435-451.
48. W. X. Mai and H. Meng, *Integr. Biol.*, 2013, **5**, 19-28.

49. K. T. Mody, A. Popat, D. Mahony, A. S. Cavallaro, C. Yu and N. Mitter, *Nanoscale*, 2013, **5**, 5167-5179.
50. V. Mamaeva, C. Sahlgren and M. Linden, *Advanced Drug Delivery Reviews*, 2013, **65**, 689-702.
51. R. Duan, F. Xia and L. Jiang, *Acs Nano*, 2013, **7**, 8344-8349.
52. D. Douroumis, I. Onyesom, M. Maniruzzaman and J. Mitchell, *Critical Reviews in Biotechnology*, 2013, **33**, 229-245.
53. Y. Chen, H. Chen and J. Shi, *Advanced Materials*, 2013, **25**, 3144-3176.
54. P. Yang, S. Gai and J. Lin, *Chemical Society Reviews*, 2012, **41**, 3679-3698.
55. J. L. Vivero-Escoto, R. C. Huxford-Phillips and W. B. Lin, *Chemical Society Reviews*, 2012, **41**, 2673-2685.
56. F. Tang, L. Li and D. Chen, *Advanced Materials*, 2012, **24**, 1504-1534.
57. Y.-S. Lin, K. R. Hurley and C. L. Haynes, *Journal of Physical Chemistry Letters*, 2012, **3**, 364-374.
58. Z. Li, J. C. Barnes, A. Bosoy, J. F. Stoddart and J. I. Zink, *Chemical Society Reviews*, 2012, **41**, 2590-2605.
59. T. Asefa and Z. Tao, *Chemical Research in Toxicology*, 2012, **25**, 2265-2284.
60. Y.-W. Yang, *Medchemcomm*, 2011, **2**, 1033-1049.
61. A. Popat, S. B. Hartono, F. Stahr, J. Liu, S. Z. Qiao and G. Q. Lu, *Nanoscale*, 2011, **3**, 2801-2818.
62. Q. He and J. Shi, *Journal of Materials Chemistry*, 2011, **21**, 5845-5855.
63. J. L. Vivero-Escoto, I. I. Slowing, B. G. Trewyn and V. S. Y. Lin, *Small*, 2010, **6**, 1952-1967.
64. K. K. Coti, M. E. Belowich, M. Liong, M. W. Ambrogio, Y. A. Lau, H. A. Khatib, J. I. Zink, N. M. Khashab and J. F. Stoddart, *Nanoscale*, 2009, **1**, 16-39.
65. I. I. Slowing, J. L. Vivero-Escoto, C.-W. Wu and V. S. Y. Lin, *Adv. Drug. Deliv. Rev.*, 2008, **60**, 1278-1288.
66. B. G. Trewyn, I. I. Slowing, S. Giri, H.-T. Chen and V. S. Y. Lin, *Accounts of Chemical Research*, 2007, **40**, 846-853.
67. B. G. Trewyn, S. Giri, I. I. Slowing and V. S. Y. Lin, *Chemical Communications* 2007, 3236-3245.
68. I. I. Slowing, B. G. Trewyn, S. Giri and V. S. Y. Lin, *Advanced Functional Materials*, 2007, **17**, 1225-1236.
69. S.-H. Wu, C.-Y. Mou and H.-P. Lin, *Chemical Society Reviews*, 2013, **42**, 3862-3875.
70. I. I. Slowing, J. L. Vivero-Escoto, B. G. Trewyn and V. S. Y. Lin, *Journal of Materials Chemistry*, 2010, **20**, 7924-7937.
71. Y. Hoshikawa, H. Yabe, A. Nomura, T. Yamaki, A. Shimojima and T. Okubo, *Chemistry of Materials*, 2010, **22**, 12-14.
72. S. Huh, H.-T. Chen, J. W. Wiench, M. Pruski and V. S. Y. Lin, *Angewandte Chemie, International Edition*, 2005, **44**, 1826-1830.
73. J. Lei, L. Wang and J. Zhang, *Chemical Communications (Cambridge, United Kingdom)*, 2010, **46**, 8445-8447.
74. L. Mondragon, N. Mas, V. Ferragud, C. de la Torre, A. Agostini, R. Martinez-Manez, F. Sancenon, P. Amoros, E. Perez-Paya and M. Orzaez, *Chemistry-a European Journal*, 2014, **20**, 5271-5281.
75. E. Yamamoto, M. Kitahara, T. Tsumura and K. Kuroda, *Chem. Mater.*, 2014, **26**, 2927-2933.
76. L. Pan, J. Liu, Q. He, L. Wang and J. Shi, *Biomaterials*, 2013, **34**, 2719-2730.

77. Z. Yi, L. F. Dumege, C. J. Garvey, C. Feng, F. She, J. E. Rookes, S. Mudie, D. M. Cahill and L. Kong, *Langmuir*, 2015, **31**, 8478-8487.
78. C. Urata, Y. Aoyama, A. Tonegawa, Y. Yamauchi and K. Kuroda, *Chemical Communications*, 2009, 5094-5096.
79. Z.-A. Qiao, L. Zhang, M. Guo, Y. Liu and Q. Huo, *Chemistry of Materials*, 2009, **21**, 3823-3829.
80. F. Lu, S. H. Wu, Y. Hung and C. Y. Mou, *Small*, 2009, **5**, 1408-1413.
81. K. Ma, U. Werner-Zwanziger, J. Zwanziger and U. Wiesner, *Chemistry of Materials*, 2013, **25**, 677-691.
82. K. Ma, H. Sai and U. Wiesner, *Journal of the American Chemical Society*, 2012, **134**, 13180-13183.
83. M. Wu, Q. Meng, Y. Chen, Y. Du, L. Zhang, Y. Li, L. Zhang and J. Shi, *Adv. Mater. (Weinheim, Ger.)*, 2015, **27**, 215-222.
84. L. Pan, J. Liu, Q. He and J. Shi, *Adv. Mater. (Weinheim, Ger.)*, 2014, **26**, 6742-6748.
85. Z.-Y. Li, Y. Liu, J.-J. Hu, Q. Xu, L.-H. Liu, H.-Z. Jia, W.-H. Chen, Q. Lei, L. Rong and X.-Z. Zhang, *ACS Appl Mater Interfaces*, 2014, **6**, 14568-14575.
86. L. Pan, J. Liu and J. Shi, *Advanced Functional Materials*, 2014, **24**, 7318-7327.
87. P. Couleaud, V. Morosini, C. Frochot, S. Richeter, L. Raehm and J. O. Durand, *Nanoscale*, 2010, **2**, 1083-1095.
88. D. Warther, C. M. Jimenez, L. Raehm, C. Gerardin, J.-O. Durand, A. Morere, K. El Cheikh, A. Gallud, M. Gary-Bobo, M. Maynadier and M. Garcia, *RSC Adv.*, 2014, **4**, 37171-37179.

CHAPTER 3

Bridged-silsesquioxane nanoparticles: Two-photon therapy and imaging in cancer cells

3.1. Introduction

Bridged silsesquioxanes (BS) are emerging as a new generation of organosilica nanomaterials. They are hybrid materials with silicon-oxide networks and organic bridging groups, obtained through a sol-gel process from organo (R) bridged-poly-trialkoxysilanes where R serves as a spacer between two Si-O_{1.5} linkages^{1,2}. Due to the difficulty to control the growth of nanoparticles from a molecular precursor, the kinetics of the sol-gel process still remain a challenge since the absence of a silica source such as tetraethoxysilane (TEOS), leads to the generation of a crystalline bulk or micro-sized nanoparticles. As they possess a high content of organic groups (between 40% and 60%) their chemical, thermal and photophysical properties will depend on the organic groups present in the organoalkoxysilane precursors.

The first bridged silsesquioxane nanoparticles (BS) were reported by Shea and co-workers in 2006³. They described a material composed by an aggregation of 100 nm particles based on coumarin dimer precursors. This material was used for photovoltaic applications. Shea and Khiterer also prepared BS nanoparticles by an emulsion method for applications as component in a solid state electrochromic device⁴.

Concerning the biomedical applications few studies are reported. In 2011, Lin's group synthesized platin-based BS nanoparticles for cancer treatment⁵. In the same year, Wong Chi Man et al. reported the first imprinted BS NPs as drug delivery system (Figure 1), based on a silylated triazine precursor that allowed the association of cyanuric acid through hydrogens bonds⁶.

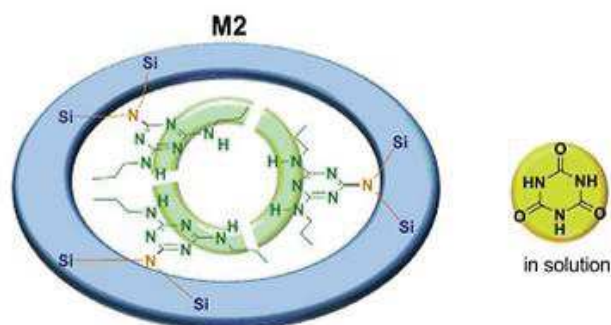


Fig. 1. Bridged silsesquioxane nanoparticles synthesized by Wong Chi Man et al. (figure obtained with the authorisation of the authors).

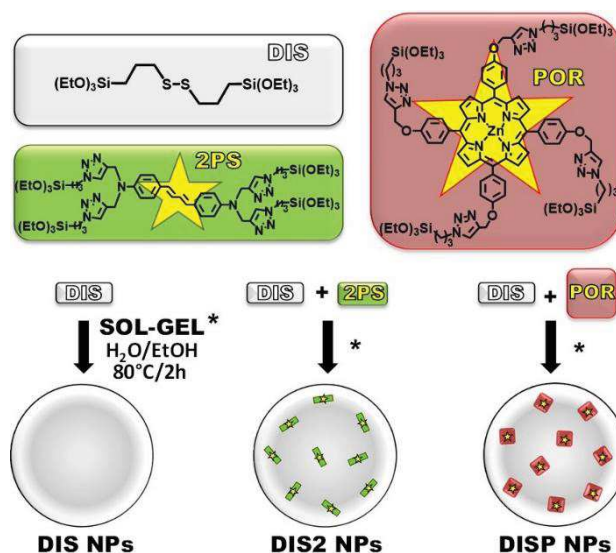
In 2012, Shea and co-workers reported the synthesis of bridged silsesquioxane nanoparticles for antibody release through light-triggered charge⁷. Sun et al. described

enzyme-responsive MSNs capped with bridged silsesquioxanes containing azo-groups for colon-drug delivery ⁸. The release of ibuprofen was achieved by the reductive cleavage of the azo bonds done by the azo-reductase present in the colonic fluid.

In this chapter, biodegradable BS nanoparticles are presented first. Non porous nanoparticles were synthesized from a tetrasilylated Zn metallated porphyrin photosensitizer, obtained by click chemistry and a bistriethoxysilyl disulfide precursor. 100 nm and 50 nm diameter non porous nanoparticles were obtained by switching the concentration of the disulfide precursor. Their biodegradability was assessed in near-physiological conditions and the cleavage of disulfide bonds in free thiols was demonstrated by different techniques. Their PDT capacity and imaging effect were tested in cancer cells.

In the second part, the syntheses of porphyrin and phthalocyanine pure BS nanoparticles are presented. 50 nm non porous BS nanoparticles were synthesized from the tetrasilylated Zn metallated porphyrin mentioned before and a tetrasilylated phthalocyanine precursor. The silylation was realized through CuAAC click-reaction from a tetraalkyne porphyrin or phthalocyanine photosensitizer and azido-propyl triethoxysilane as silylation agent. The resulting nanoparticles were used for two-photon therapy and fluorescence imaging at low laser power in MCF-7 breast cancer cells.

3.2. Versatile synthesis of Biodegradable Disulfide Hybrid Bridged-silsesquioxane nanoparticles: Two-photon therapy and imaging in cancer cells



Abstract

We describe for the first time biodegradable bridged silsesquioxane (BS) nanomaterials for two-photon-excited (TPE) photodynamic therapy (PDT) and imaging in breast cancer cells. A versatile synthesis was developed to design monodisperse disulfide-photosensitizer (i.e. tetra-alkoxysilylated diaminoalkyl-diphenylbudiene and Zn-porphyrin) nanospheres of 30 to 50 nm.

Interdisciplinary collaboration

Nanomaterial synthesis, physic-chemical characterizations and applications in solution: C. Mauriello Jimenez, J. Croissant, X. Cattöen, M. Wong Chi Man, L. Raehm, J-O. Durand.

Synthesis of the porphyrin photosensitizer: P. Maillard.

Two photon photophysical characterizations: O. Mongin, V. Hughes, M. Blanchard-Desce.

Cell studies: M. Maynadier, M. Gary-Bobo, M.Garcia.

➤ *Chem. Commun.*, 2015,**51**, 12324-12327

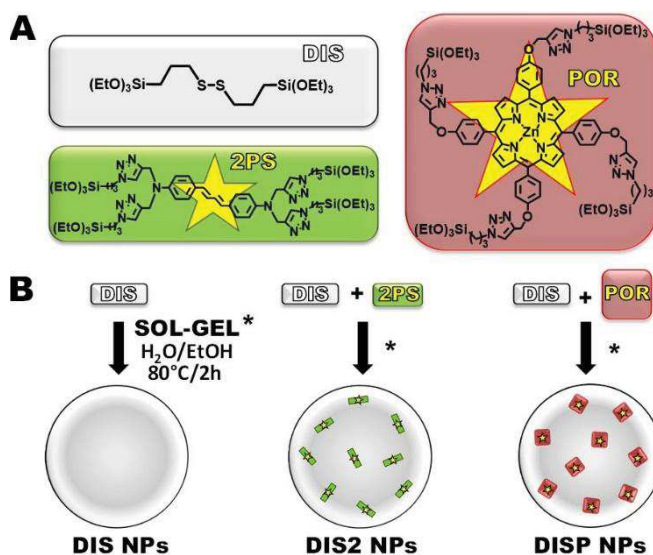
3.2.1. Introduction

Two-photon nanomedicine is emerging as an excellent strategy to fulfill the spatiotemporal requirements of cancer therapy.⁹⁻¹⁵ Near-infrared (NIR) two-photon-sensitive nanodevices benefit the three-dimensional resolution and the low scattering losses of the irradiation in biological tissues, and thus safer and more selective treatments.¹⁶⁻¹⁹ Biodegradable nanoparticles (NPs) are of particular interest since they favor a safe and efficient excretion of the nanodevice.²⁰⁻²² Biodegradable nanomaterials have been reported various polymeric NPs²³⁻²⁵ amongst which are poly(lactic-co-glycolic acid) (PLGA) and poly- ϵ -caprolactone (PCL) aliphatic polyesters,^{21, 25} and with inorganic and hybrid NPs such porous silicon,²⁰ periodic mesoporous organosilica,²⁶ magnesium and manganous phosphate,²⁷ and calcium phosphate²⁸.

Bridged silsesquioxane (BS) NPs are an emerging nanomaterial category for applications in nanotechnology.^{7, 18, 19, 29, 30} BS compounds are produced from sol-gel processes of bis- or multi-organoalkoxysilane precursors so as to maximize the organic content of the resulting material (~40-70%).^{7, 31} Up to now, very few studies have been reported on BS NPs since it is generally challenging to control the sol-gel process towards the nanoscale without the addition of silica precursors (e.g. tetraethoxysilane). Shea and co-workers pioneered BSNPs with photoresponsive,^{7, 32} electrochemical,³³ and electrochromic properties,³⁴ while Hammers *et al.* used a modified Stöber synthesis to elaborate BS NPs from perylene diimide fragments as photovoltaic material.³⁵ Only one study has been reported on biodegradable BS NPs with gadolinium(III)-disulfide-based material as *in-vitro* contrast agents via magnetic resonance imaging (MRI).³⁶ BS NPs releasing cis-platin for targeted cancer chemotherapy were also reported.⁵ We recently studied the first BS NPs for two-photon excited (TPE) photodynamic therapy (PDT) on cancer cells from a tetraalkoxysilylated diphenylbutadiene two-photon photosensitizer (2PS).¹⁸

In this communication we describe a versatile synthesis to obtain biodegradable BS nanomedical devices based on disulfide linkers. A novel tetra-alkoxysilylated porphyrin photosensitizer precursor (POR) was developed via click chemistry and fully characterized.^{18, 37} 2PS and POR precursors were then co-condensed with bis (propyl) disulfide to design two-photon-sensitive biodegradable BS NPs for nanomedical applications (Scheme 1). The proof of concept of the biodegradability was

demonstrated, and the designed hybrid BS NPs were biocompatible. Furthermore, these NPs were applied for TPE-fluorescence imaging and TPE-PDT on cancer cells.



Scheme 1. Bis(3-triethoxysilylpropyl)disulfide (DIS), multi-alkoxysilylated two-photon photosensitizer (2PS) and porphyrin (POR) sol-gel precursors (A). Versatile synthetic process to design disulfide-based (DIS), and hybrid DIS/2PS (DIS2) or DIS/POR (DISP) BS NPs (B).

3.2.2. Results and discussion

The POR precursor and following BS nanomaterials were initially prepared. Firstly, the POR photosensitizer was designed from 5,10,15,20-tetra(propargyloxyphenyl)Zn porphyrin³⁸ then alkoxy-silylated via a copper-catalyzed azide-alkyne cycloaddition (CuAAC) click coupling (see Scheme S2).³⁸ The POR precursor was fully characterized via ¹H and ¹³C nuclear magnetic resonance (NMR), Fourier transform infrared (FTIR), and mass spectroscopies (Supp. Inf. S2). Secondly, the elaboration of the disulfide- and photosensitizer-disulfide-based biodegradable BS NPs was carried out. A versatile sol-gel process was used for three types of material, the disulfide (DIS), the disulfide-2PS photosensitizer (DIS2), and the disulfide-POR photosensitizer (DISP) hybrid BS NPs (see Scheme 1). The reaction was carried out in a water/ethanol (5:2, v:v) mixture with sodium hydroxide catalysis at 80°C (Supp. Inf. S3-S4). Note that, the presence a cetyltrimethylammonium bromide was found to be necessary for the control of the NPs condensation.

The morphology and composition of the BS nanomaterials were then characterized via various techniques. Transmission electron microscopy (TEM) revealed DIS and DIS2 nearly monodisperse nanospheres of 30 nm and 40 nm respectively (See Figure 1a and b). Besides, this synthetic route could be used to tune the size of the NPs with the variation of the alkoxy silane concentrations. Consequently, DISP NPs of 200 and 50 nm could be prepared (Figure 1c and d respectively) by decreasing the disulfide precursor concentration of a quarter (Supp. Inf. S5-S6).

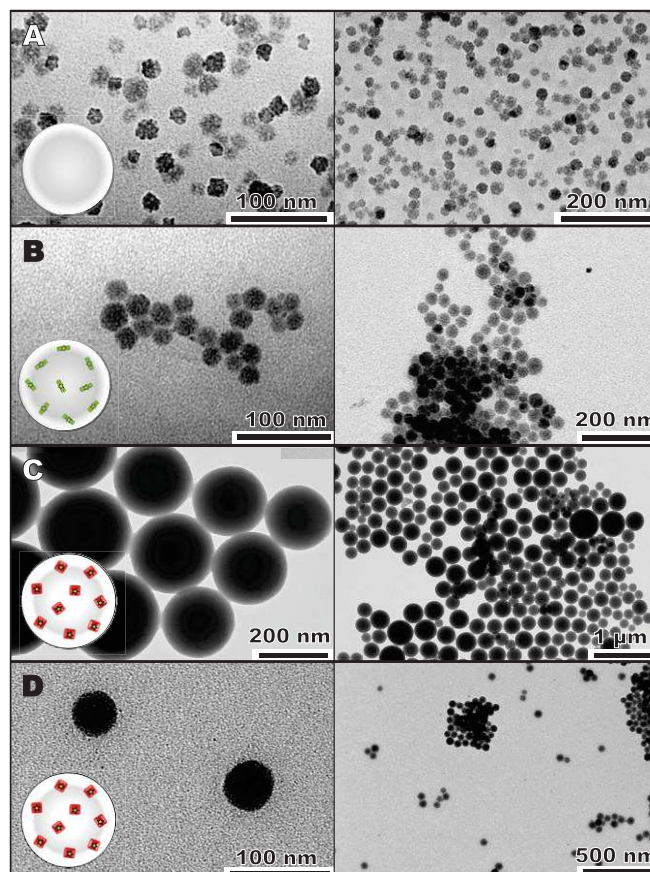
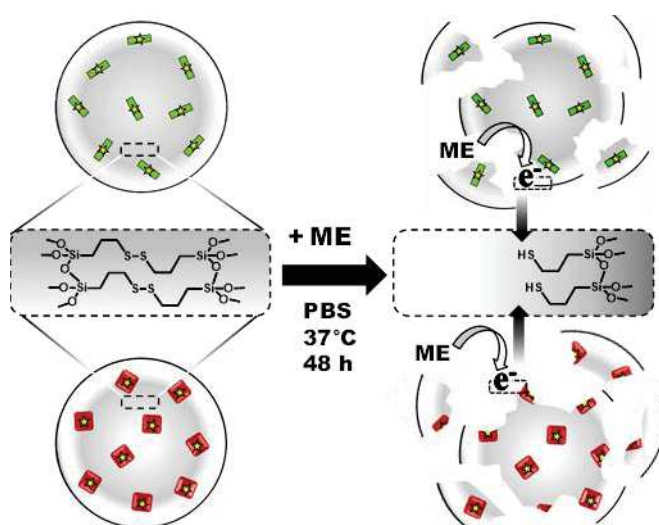


Fig. 1. TEM micrographs of as prepared DIS (A), DIS2 (B), 200 nm DISP (C), and 50 nm DISP NPs (D).

UV-Visible spectroscopy confirmed the successful encapsulation of 2PS and POR photosensitizers in BS frameworks as shown respectively by the absorption peak maximum at 390 nm (Figure S8a), and the Soret bands from 403 to 461 nm along with the Q bands at 569 and 607 nm (Fig. S8b). In light of the fact that the Soret band at 425 nm in the precursor was split into three bands at 403, 431, and 461 nm, it can be asserted that the aggregation of the POR moieties occurred in the DISP NPs, according to the type H (blue shift at 403) and J aggregates (red shift at 461 nm).^{39, 40}

The presence of the disulfide and photosensitizers functions is also supported by the FTIR spectra of the DIS and DIS2 NPs composed of the $\nu_{\text{C-H}}$ and $\nu_{\text{Si-C}}$ stretching vibration modes of the disulfide group at 3000-2870 and 1140 cm^{-1} respectively, and the 2PS butadiene $\nu_{\text{C=C}}$ at 1610 cm^{-1} with the aromatic $\nu_{\text{C-H}}$ and para-disubstituted bending modes at 3140-3020 and 797 cm^{-1} respectively (Fig. S8 and S9). Similar observations were made from FTIR spectra of DISP NPs depicting the $\nu_{\text{C=C}}$ (1612 cm^{-1}) and $\nu_{\text{C-H}}$ (797 cm^{-1}) typical of such porphyrin derivatives.⁴¹ Moreover, solid state NMR ^{13}C and ^{19}Si cross-polarization magic angle spinning (CPMAS) spectra of the DIS, DIS2, and DISP NPs showed both the presence of the siloxane network by the T_3 silicon environments at -67 ppm (Fig. S10a,c, and e), with the three types of carbon of the DIS moiety at 10, 27, and 47 ppm, and the photosensitizers carbon local environments (see Fig. S10d and f). The 2PS content in the DIS2 NPs was determined to be of 28 weight percent (wt %) via elemental analysis of nitrogen atoms (14 per 2PS molecule, see Table S11). Similarly, the POR contents were respectively of 10 and 14 wt% for DISP NPs of 50 and 200 nm (16 nitrogen atoms per POR molecule, Table S11).

The biodegradability of the BS NPs was then assessed in near-physiological conditions. The nanomaterials were dispersed in PBS at 37°C, and an equivalent of the intracellular concentration of glutathione was added (2 nM of mercaptoethanol: ME) in order to cleave disulfide linkers in the BS frameworks (see Scheme 2). The proof of concept of this phenomenon was validated by TEM micrographs before and after 48 h of chemical degradation depicted degraded particle fragments (Figure 2).



Scheme 2. Representation of the chemical degradation of BS NPs.

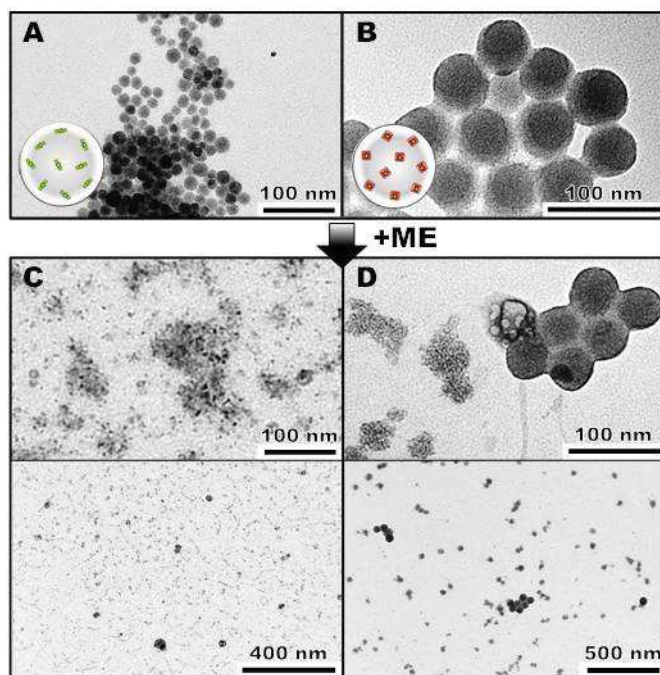


Fig. 2. TEM micrographs of DIS 2 (a, c) and DISP NPs (b, d) before (a-b) and after 48 h of near-physiological chemical reduction (c-d).

Accordingly, dynamic light scattering (DLS, Fig. S12) analyses measured decreased hydrodynamic diameters after degradation. Besides, the proposed mechanism is supported by FTIR analyses of degraded DIS2 (Fig. S13) and DISP NPs (Fig. S14) which displayed the appearance of the thiol stretching mode at 2554 cm^{-1} .

As-prepared BS biodegradable nanomaterials were then applied for TPE biomedical applications. Importantly, both DIS2 and DISP BS nanospheres did not display any significant cytotoxicity up to $125\text{ }\mu\text{g}\cdot\text{mL}^{-1}$ (see Figure 3a). Hence, two-photon confocal in-vitro studies were led on MCF-7 breast cancer cells incubated 20 h with $40\text{ }\mu\text{g}\cdot\text{mL}^{-1}$ of biocompatible BS NPs. TPE-fluorescence was performed with irradiation at low-laser power on DIS2 and DISP NPs (760 and 800 nm respectively). The endocytosis of DIS2 as well as the DISP nanospheres was clearly seen with the confocal microscopy merged images (see Figure 3b, c). Besides, the DIS2 material displayed powerful two-photon fluorescence particularly efficient for intracellular NPs tracking.

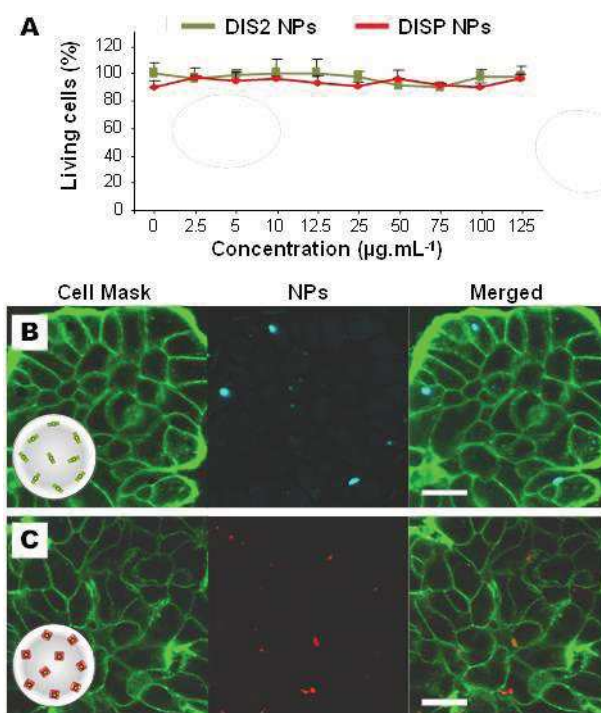


Fig. 3. Cytotoxicity study of DIS2 and 50 nm DISP NPs with MCF-7 cancer cells (A). Two-photon confocal microscopy images of cells NPs incubated during 20 h with 40 µg.mL⁻¹ of DIS2 (B) and DISP (C). Scale bars of 10 µm.

Two-photon-triggered PDT was eventually conducted on cancer cells incubated with DIS2 and 50 nm DISP NPs irradiated at maximum power. Figure 4 demonstrates the harmlessness of the two-photon laser on the one hand (see white bars), and the great potential of the photosensitizer-disulfide-based NPs on the other (red bars). Indeed, 40% of selective cell death was obtained with irradiated DIS2 while DISP NPs caused up to 54%, which make them particularly interesting nanomedical devices for cancer therapy. Similar 2PS molecules have been reported to produce electrons under irradiation.^{42, 43} Concerning DISP NPs, the surprising two-photon sensitivity of the DISP NPs arose from the H and J POR aggregates, as reported in the literature.¹⁷ The disulfide framework is thus well-suited for the preservation of the TPE-PDT effect and the design of biodegradable nanomedical tools.

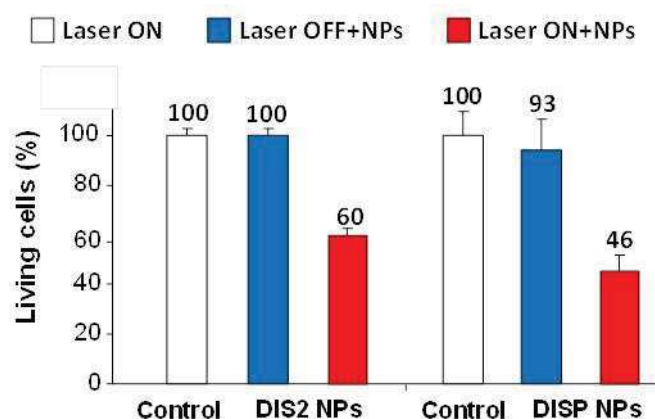


Fig. 4. TPE-triggered cancer cell killing on DIS2 (irradiated at 760 nm) and 50 nm DISP NPs (irradiated at 800 nm).

3.2.3. Conclusion

In summary, we have designed photosensitizer-disulfide-based bridged silsesquioxane NPs via a versatile synthetic process. A novel porphyrin photosensitizer was reported and used for the preparation of hybrid BS NPs. The morphology, compositions, and functionalities of the nanomaterials were fully characterized by various techniques, which showed the encapsulation of photosensitizers in the disulfide matrices. Besides, the POR molecules were found to be aggregated in the BS NPs, which produced two-photon sensitivity for biomedical applications. The DIS2 and DISP BS NPs were both biodegradable in near-physiological media, and biocompatible in MCF-7 cancer cells. Furthermore, TPE-fluorescence imaging *in vitro* was performed to demonstrate the NPs cellular uptake, and TPE-PDT lead to 40 to 60% of spatiotemporally-controlled cancer cell killing. It is envisioned that such organic-inorganic hybrid material could be efficient biodegradable theranostic for cancer treatment.

3.2.4. Supporting Information

Experimental section

3.2.4. S1. Materials and procedures

Cetyltrimethylammonium bromide (CTAB) and sodium hydroxide were purchased from Sigma-Aldrich. Absolute ethanol was purchased from Fisher Chemicals. R. Norma Pure. Bis(3-triethoxysilylpropyl)disulfide were purchased from ABCR. (3-azidopropyl)-trimethoxysilane was obtained from a reported procedure by M. Ortega-Muñoz et al (*Adv. Synth. Catal.* **2006**, 348, 2410).

^1H and ^{13}C NMR spectra were recorded with a Bruker AC 400 spectrometer. Chemical shifts (in δ units, ppm) are referenced to TMS using CHCl_3 ($\delta = 7.26$ ppm) and CDCl_3 ($\delta = 77.0$ ppm) as the internal standards, respectively, for ^1H and ^{13}C NMR spectra. IR spectra were recorded on a Perkin-Elmer 100 FT spectrophotometer. Absorption spectra were recorded on a Hewlett-Packard 8453 spectrophotometer and fluorescence data were collected on a Perkin-Elmer LS55 fluorimeter. Mass spectrometry was carried out at the Laboratoire de Mesures Physiques (Montpellier, France) with a Thermo-Finnigan MAT95 apparatus in electronic impact ionization mode. Dynamic light scattering analyses were performed using a Cordouan Technologies DL 135 Particle size analyzer instrument. ^{29}Si and ^{13}C CPMAS solid state NMR sequences were recorded with a VARIAN VNMRS300, using Q8MH8 and adamantane references respectively. TEM analysis performed on a JEOL 1200 EXII instrument. SEM analysis performed on a FEI Quanta FEG 200 instrument.

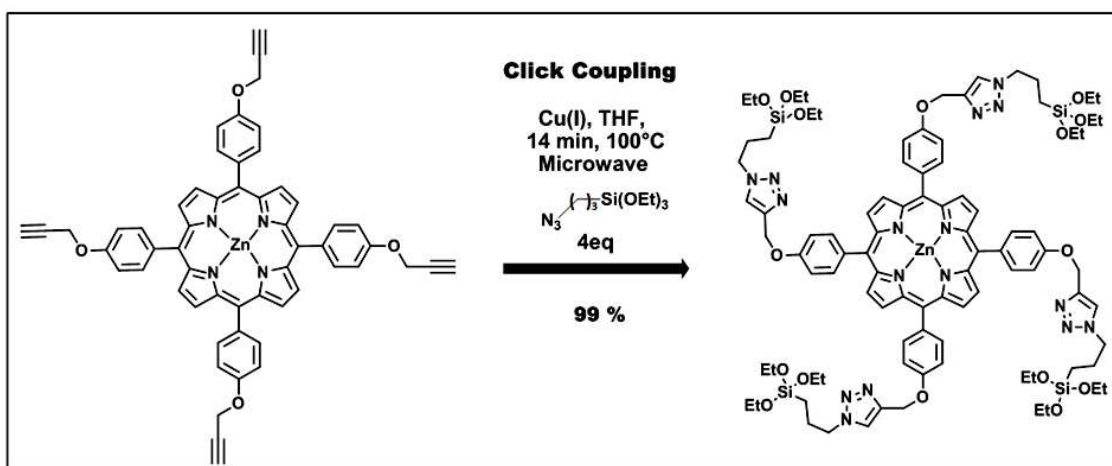
Nanomaterial synthesis and characterization

3.2.4. S2. Silylation of POR precursor

A mixture of the tetrapropargyld porphyrine derivative (100 mg, $1.12 \cdot 10^{-1}$ mmol), bromotris(triphenylphosphine)copper(I) ($[\text{CuBr}(\text{PPh}_3)_3]$, 10 mg, $1 \cdot 10^{-2}$ mmol), and anhydrous THF (3 mL) was placed in a 10 mL microwave sealable reactor, and (3-azidopropyl)triethoxysilane (150 mg, 0.6 mmol) was added. Then, the tube was flushed with argon and the microwave process was conducted 20 min at 100°C at 200 mW.

After evaporation of the solvents, the POR precursor was quantitatively obtained as a purple solid (210 mg, 1.12×10^{-1} mmol). The yield of the reaction was 100 %.

^1H NMR (300 MHz, $\text{DMSO-}d_6$): δ 8.81 (s, 8H, $\text{H}_{\text{pyrrole}}$), 8.41 (s, 4H, triazole), 8.09 (d, $^3\text{J} = 8.4$ Hz, 8H, $\text{H}_{\text{ph-pyrrole}}$), 7.44 (d, $^3\text{J} = 8.2$ Hz, 8H, $\text{H}_{\text{ph-triazole}}$), 5.43 (s, 8H, $\text{N-CH}_2\text{-riazole}$), 4.45 (t, $^3\text{J} = 7.0$ Hz, 8H, triazole- CH_2), 3.77 (q, $^3\text{J} = 7$ Hz, 24H, $\text{O-CH}_2\text{-CH}_3$), 1.99 (t, $^3\text{J} = 7.8$ Hz, 8H, triazole- $\text{CH}_2\text{-CH}_2$), 1.16 (t, $^3\text{J} = 6.9$ Hz, 36H, $\text{O-CH}_2\text{-CH}_3$), 0.60 (t, $^3\text{J} = 7.7$ Hz, 8H, $\text{CH}_2\text{-Si}$). ^{13}C NMR (400MHz, DMSO): δ 158.8, 149.9, 143.19, 135.5, 131.8, 129, 125, 120, 113.1, 58.2, 53.3, 52.14, 24.3, 18.5, 7.3. ^{29}Si NMR (400MHz, DMSO): δ -46.4. FTIR (neat KBr) $\nu_{\text{max}}/\text{cm}^{-1} = 3116, 3032, 2977, 2932, 2882, 1596, 1563, 1502, 1435, 1391, 1346, 1296, 1268, 1240, 1174, 1107, 1068, 996, 945, 840, 789, 712, 684, 533, 422$. UV/Vis λ_{max} (EtOH): 426, 561, 604 nm. Emission (EtOH): $\lambda_{\text{max}} = 607, 660$ nm ($\lambda_{\text{excitation}} = 432$ nm). MALDI-TOF: calcd for $\text{C}_{92}\text{H}_{120}\text{N}_{16}\text{O}_{16}\text{Si}_4\text{Zn}$: 1880.690, found 1880.720.



Scheme S2. Design of the POR precursor via click CuAAC coupling.

3.2.4. S3. Synthesis of DIS NPs

A mixture of CTAB (250 mg), distilled water (120 mL), and sodium hydroxide (875 μL , 2 M) was stirred at 80°C during 50 minutes at 700 rpm in a 250 mL three neck round bottom flask. Then, bis(3-triethoxysilylpropyl)disulfide (2.4 mL) was added to the aforementioned solution, and the condensation process was conducted for 2 h. Afterwards, the solution was cooled to room temperature while stirring; fractions were gathered in propylene tubes and collected by centrifugation during 15 minutes at 21 krpm. The sample was then washed three times with ethanol, water, and ethanol. Each

washing was followed by centrifugation collection of the sample in the same manner. The as-prepared material was dried under vacuum for few hours.

3.2.4. S4. Synthesis of DIS2 NPs

A mixture of CTAB (250 mg), distilled water (120 mL), and sodium hydroxide (875 μL , 2 M) was stirred at 80°C during 50 minutes at 700 rpm in a 250 mL three neck round bottom flask. Then, bis (3-triethoxysilylpropyl) disulfide (2.4 mL) was added to the aforementioned solution along with the two-photon photosensitizer (177 mg dried in 1 mL of absolute ethanol), and the condensation process was conducted for 2 h. Afterwards, the solution was cooled to room temperature while stirring; fractions were gathered in propylene tubes and collected by centrifugation during 15 minutes at 21 krpm. The sample was then washed three times with ethanol, water, and ethanol. Each washing was followed by centrifugation collection of the sample in the same manner. The as-prepared material was dried under vacuum for few hours.

3.2.4. S5. Synthesis of 200 nm DISP NPs

A mixture of CTAB (125 mg), distilled water (60 mL), and sodium hydroxide (437 μL , 2 M) was stirred at 80°C during 50 minutes at 700 rpm in a 250 mL three neck round bottom flask. Then, bis(3-triethoxysilylpropyl)disulfide (400 μL) was added to the aforementioned solution along with the two-photon photosensitizer (20 mg in 800 μL of absolute ethanol), and the condensation process was conducted for 2 h. Afterwards, the solution was cooled to room temperature while stirring; fractions were gathered in propylene tubes and collected by centrifugation during 15 minutes at 21 krpm. The sample was then washed three times with ethanol, water, and ethanol. Each washing was followed by centrifugation collection of the sample in the same manner. The as-prepared material was dried under vacuum for few hours. 86.3 mg of product were obtained.

3.2.4. S6. Synthesis of 50 nm DISP NPs

A mixture of CTAB (125 mg), distilled water (60 mL), and sodium hydroxide (437 μL , 2 M) was stirred at 80°C during 50 minutes at 700 rpm in a 250 mL three neck round bottom flask. Then, bis (3-triethoxysilylpropyl) disulfide (300 μL) was added to the aforementioned solution along with the two-photon photosensitizer (20 mg in 800 μL of absolute ethanol), and the condensation process was conducted for 2 h. Afterwards, the

solution was cooled to room temperature while stirring; fractions were gathered in propylene tubes and collected by centrifugation during 15 minutes at 21 krpm. The sample was then washed three times with ethanol, water, and ethanol. Each washing was followed by centrifugation collection of the sample in the same manner. The as-prepared material was dried under vacuum for few hours. 68.6 mg of product were obtained.

3.2.4. S7. Biodegradability studies

A mixture of NPs (1.5 mg), PBS (500 μ L), and mercaptoethanol (50 μ L) was stirred two days at 37°C in an eppendorf tube. Then, aliquots were taken directly to perform the TEM and DLS analyses.

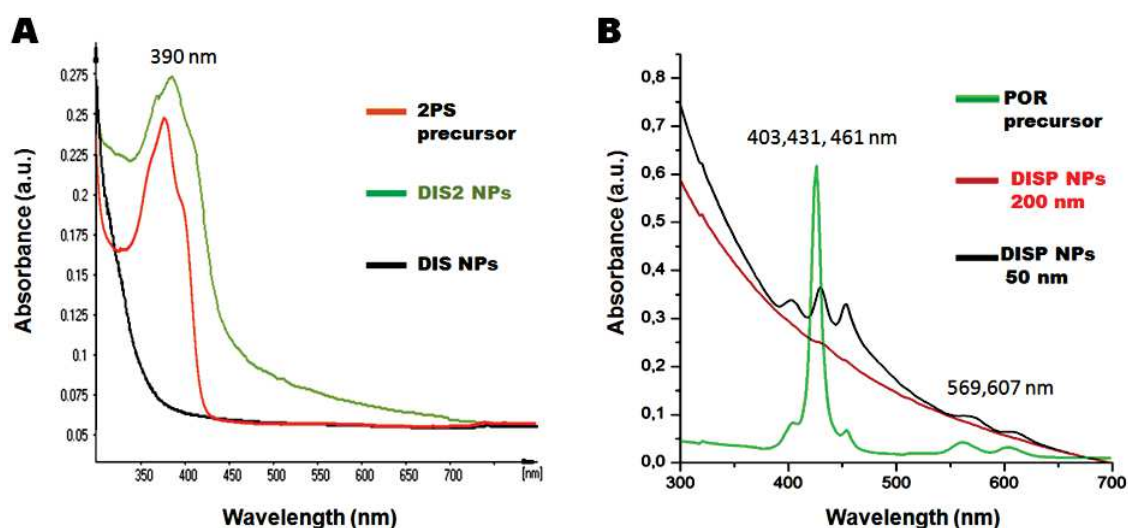


Figure S8. UV-Visible spectra of the 2PS precursor, DIS, and DIS2 NPs (A), and of the POR precursor, 50 nm DISP and 200 nm DISP NPs (B), demonstrating the incorporations of both the 2PS and POR photosensitizers.

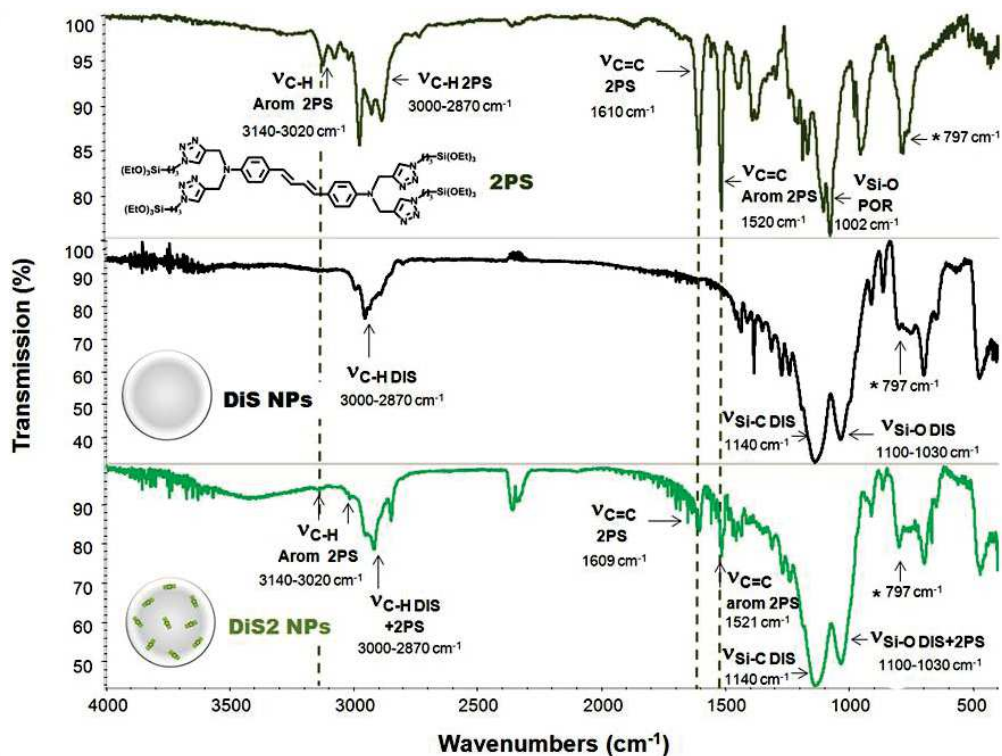


Figure S9. FTIR spectra of the 2PS precursor, DIS, and DIS2 NPs confirming the presence of the DIS and 2PS moieties in the nanomaterials framework. *Out of plan bending of para-disubstituted aromatic rings in the 2PS.

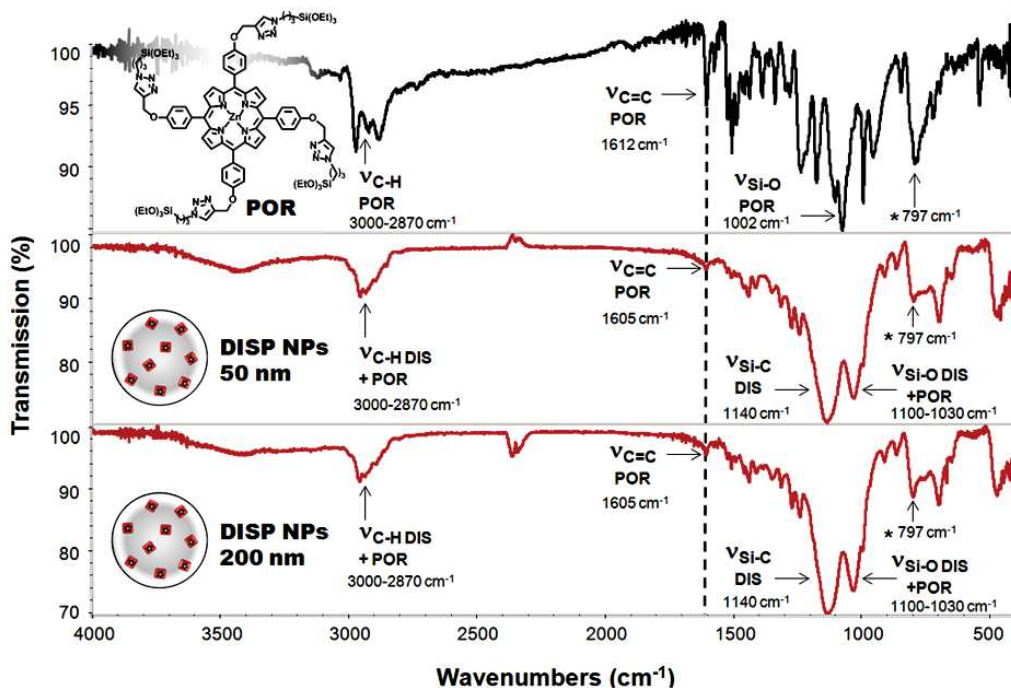


Figure S10. FTIR spectra of the POR precursor, DIS, and DISP NPs confirming the presence of the DIS and POR moieties in the nanomaterials framework. *Out of plan bending of para-disubstituted aromatic rings in the POR.

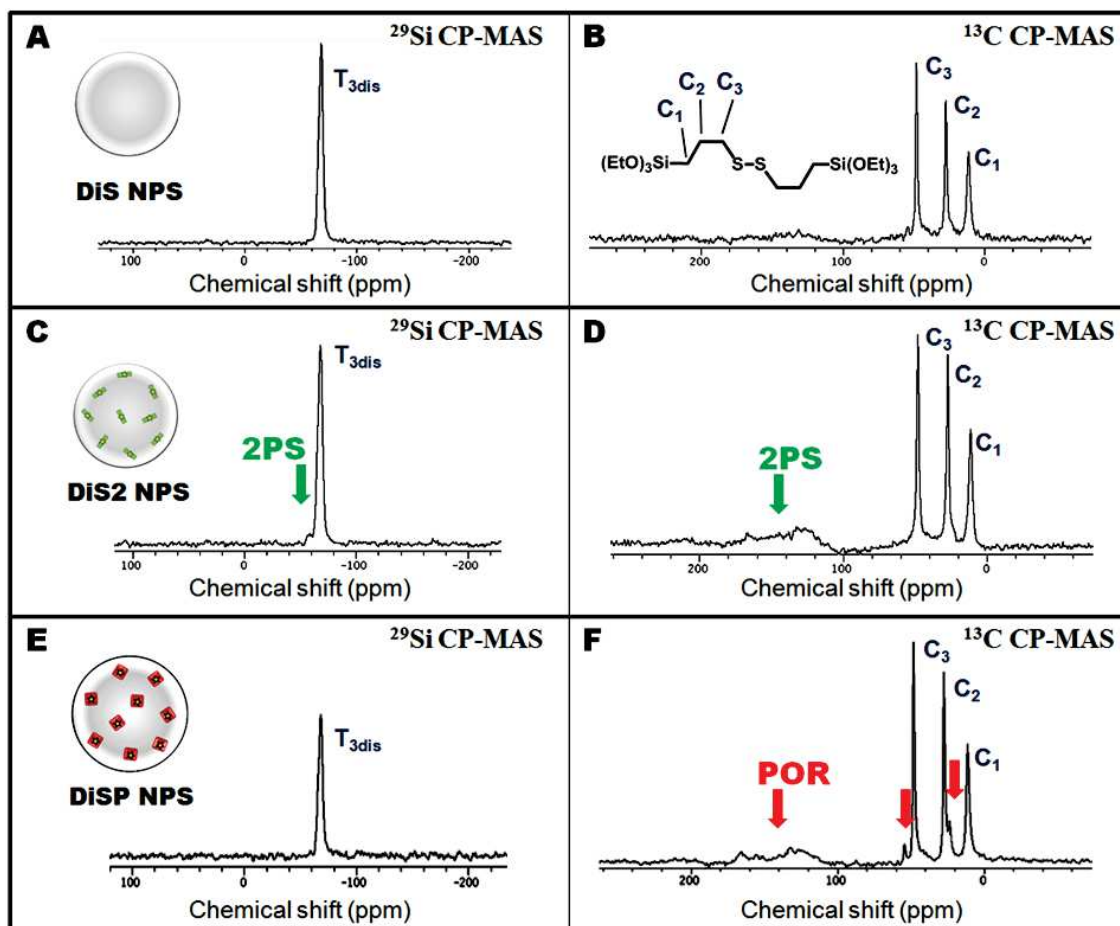


Figure S11. Solid state NMR ^{29}Si and ^{13}C CP-MAS spectra of DIS (A-B), DIS2 (C-D), and DISP (E-F).

Table S12. Photosensitizers weight percent determination in the NPs.

Sample	NPs N wt% ^[a]	NPs 2PS or POR wt% ^[b]
DIS2 NPs	5.88	28
50 nm DISP NPs	1.62	10
200 nm DISP NPs	2.25	14

[a] Elemental analysis by combustion measurements of the NPs.

[b] Determination based on the nitrogen wt% in the 2PS and POR molecules.

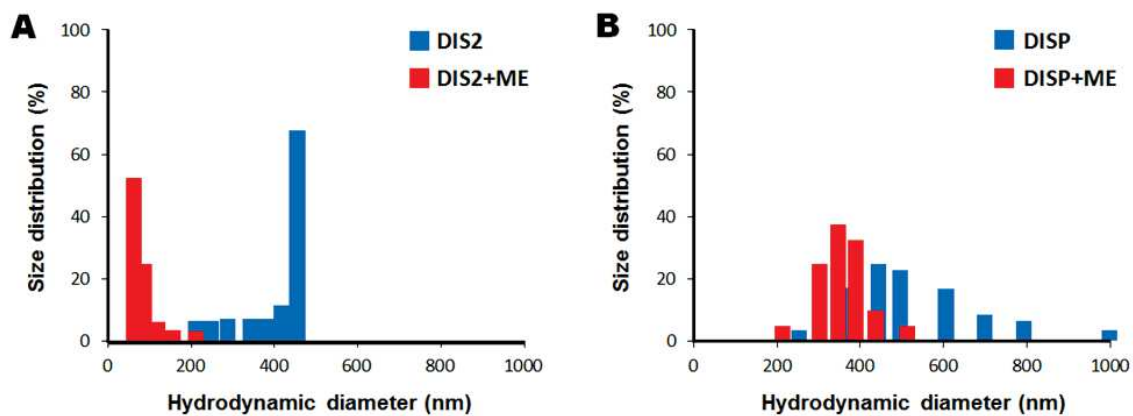


Figure S13. DLS size distributions of DIS2 (A) and DISP NPs (B) before and after mercaptoethanol addition in near-physiological conditions for 48 h, consistent with the expected decrease of particle sizes. The initial large sizes of BS NPs arise from: (a) aggregates of NPs, and (b) the hydration layer around particles.

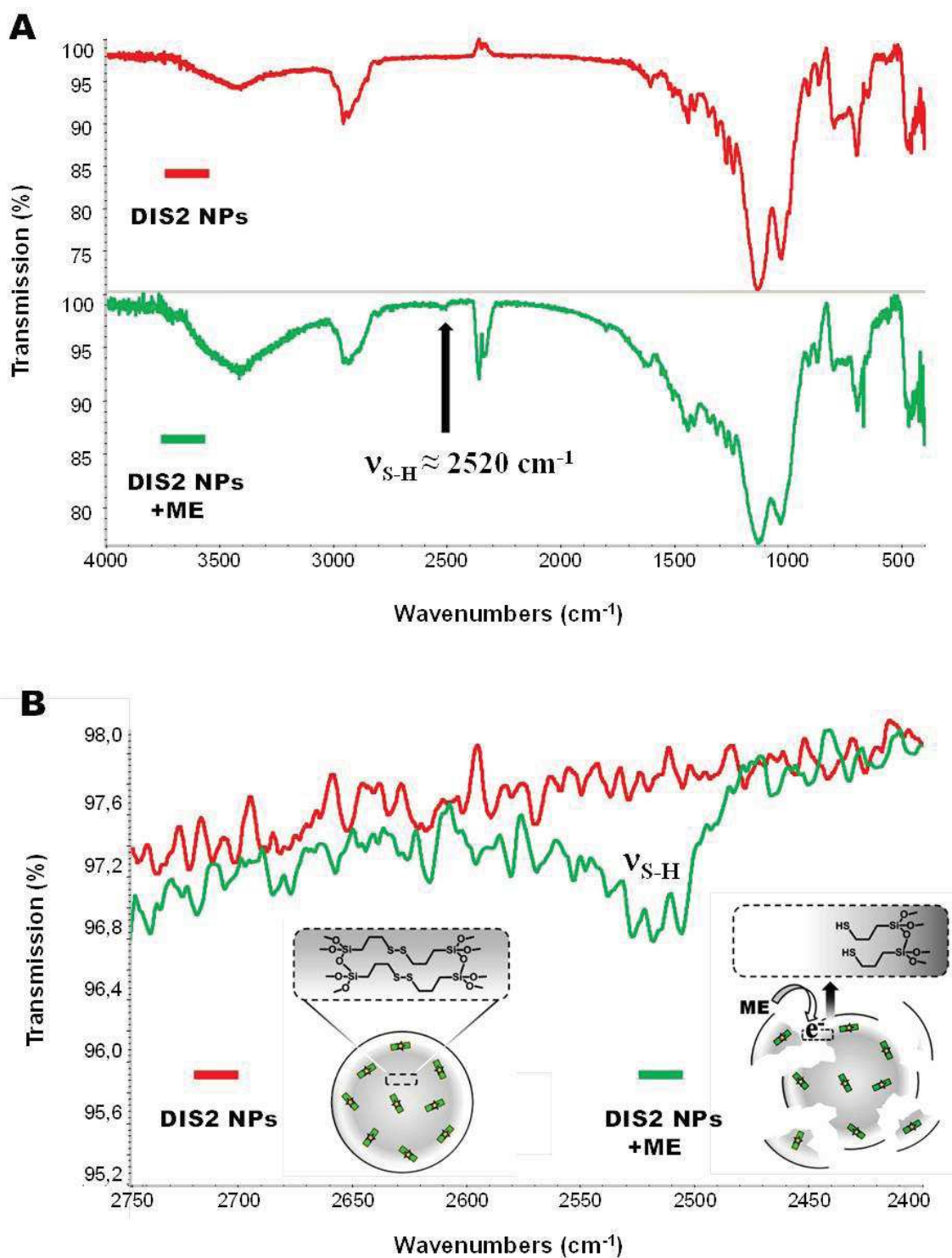


Figure S14. FTIR spectra of DIS2 NPs before and after mercaptoethanol addition (A), confirming the degradation of the disulfide framework with the appearance of the thiol stretching band (B).

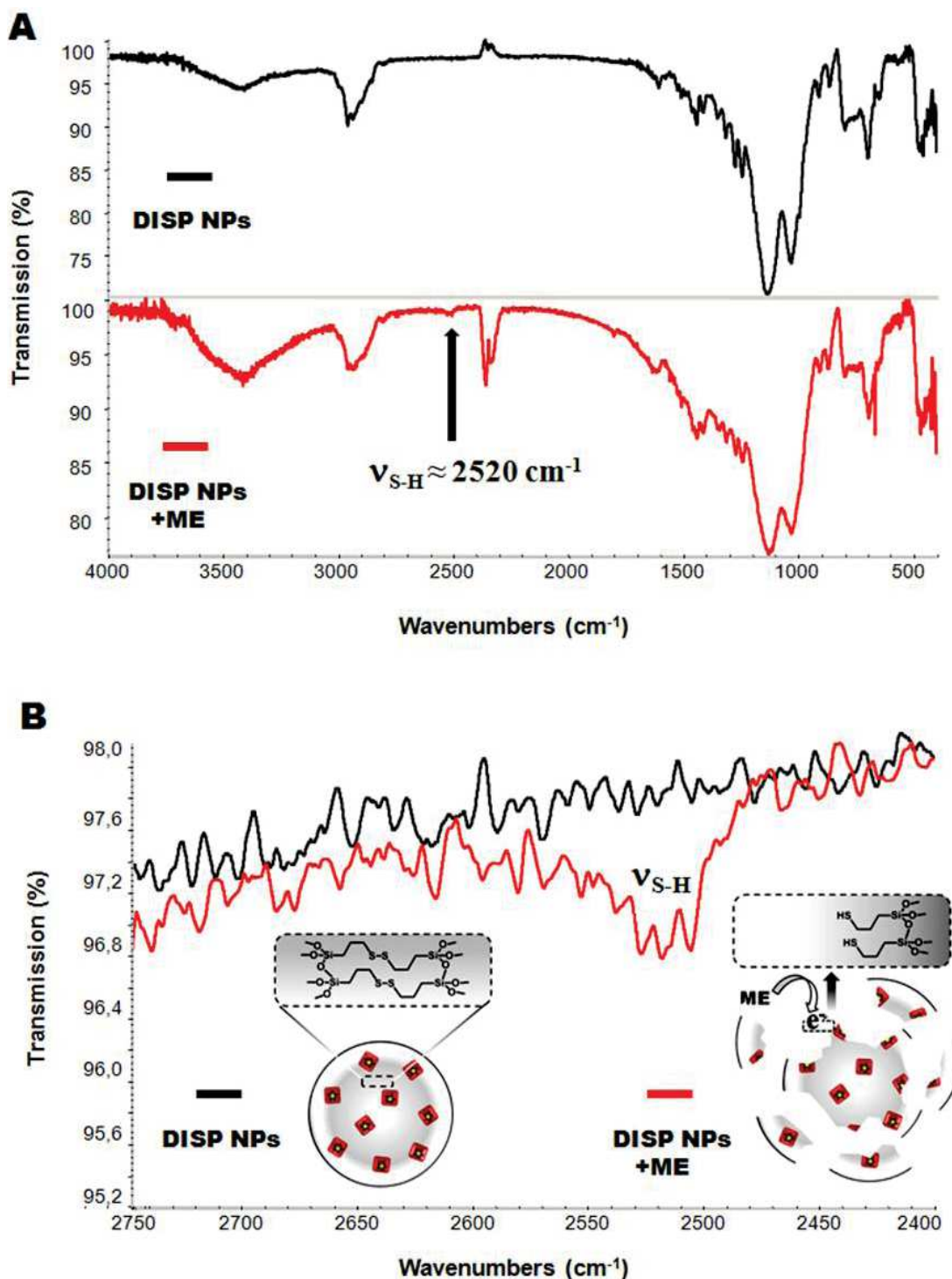


Figure S15. FTIR spectra of DISP NPs before and after mercaptoethanol addition (A), confirming the degradation of the disulfide framework with the appearance of the thiol stretching band (B).

***In vitro* studies**

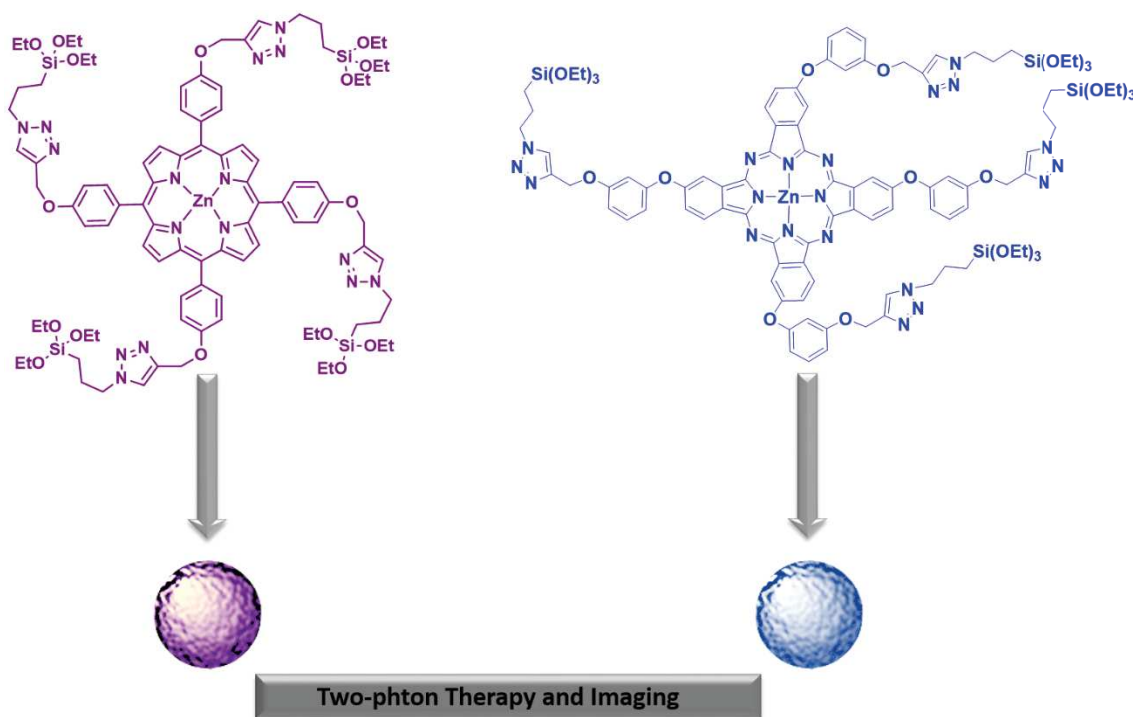
3.2.4. S16. Two-photon fluorescence imaging

The day prior to the experiment, MCF-7 cells were seeded onto bottom glass dishes (World Precision Instrument, Stevenage, UK) at a density of 10^6 cells.cm⁻². Adherent cells were then washed once and incubated in 1 mL culture medium containing NPs at a concentration of 40 $\mu\text{g.mL}^{-1}$ for 20 h. Fifteen min before the end of incubation, cells were loaded with Cell Mask TM Orange Plasma Membrane Stains (Invitrogen, Cergy Pontoise, France) for membrane staining at a final concentration of 5 $\mu\text{g.mL}^{-1}$. Before visualization, cells were washed gently with phenol red-free DMEM. Cells were then scanned with a LSM 780 LIVE confocal microscope (Carl Zeiss, Le Pecq, France), at 760 or 800 nm with a slice depth (Z stack) of 0.62 μm .

3.2.4. S17. TPE-therapy

MCF-7 human breast cancer cells were cultured in Dulbecco's modified Eagle's medium (DMEM) supplemented with 10% fetal bovine serum and 50 $\mu\text{g.mL}^{-1}$ gentamycin. All cells were allowed to grow in humidified atmosphere at 37°C under 5% CO₂. For *in vitro* phototoxicity, MCF-7 cells were seeded into a 384 multiwell glass-bottomed plate (thickness 0.17 mm), with a black polystyrene frame, 2000 cells per well in 50 μL of culture medium, and allowed to grow for 24 h. NPs were then dispersed under ultrasounds in PBS at a concentration of 1 mg.mL^{-1} and cells were then incubated for 20 h with or without nanoparticles at a final concentration of 40 $\mu\text{g.mL}^{-1}$ in supplemented DMEM. After incubation with NPs, cells were washed twice, maintained in fresh culture medium, and then submitted (or not) to laser irradiation; with the Carl Zeiss Microscope LSM 780 LIVE confocal microscope (laser power input 3W). Half of the well was irradiated at 760 or 800 nm by three scans of 1.57 s duration in 4 different areas of the well. The laser beam was focused by a microscope objective lens (Carl Zeiss 10x, NA 0.4). After 2 days, the MTT assay was performed and was corrected.

3.3. Porphyrin and phthalocyanine photosensitizers based bridged-silsesquioxane nanoparticles for two-photon therapy and imaging of cancer cells



Abstract

We report the synthesis of two different bridged silsesquioxane nanoparticles produced on the one hand from a metallated porphyrin (BSPOR), and from the other hand with a metallated phthalocyanine (BSPHT). Both precursors were tetrasilylated by click chemistry under CuAAC catalysis. Their efficiency for intracellular tracking was demonstrated by the *in vitro* imaging at 750 nm in MCF-7 cancer cells and their efficiency for photodynamic therapy was demonstrated with two-photon therapy.

Interdisciplinary collaboration

Nanomaterial synthesis, physic-chemical characterizations and applications in solution: C. Mauriello Jimenez, L. Raehm, J-O. Durand.

Synthesis of the porphyrin and phthalocyanine photosensitizer: P. Maillard, F. Dumoulin.

Cell studies: M. Maynadier, M. Gary-Bobo, M. Garcia.

3.3.1. Introduction

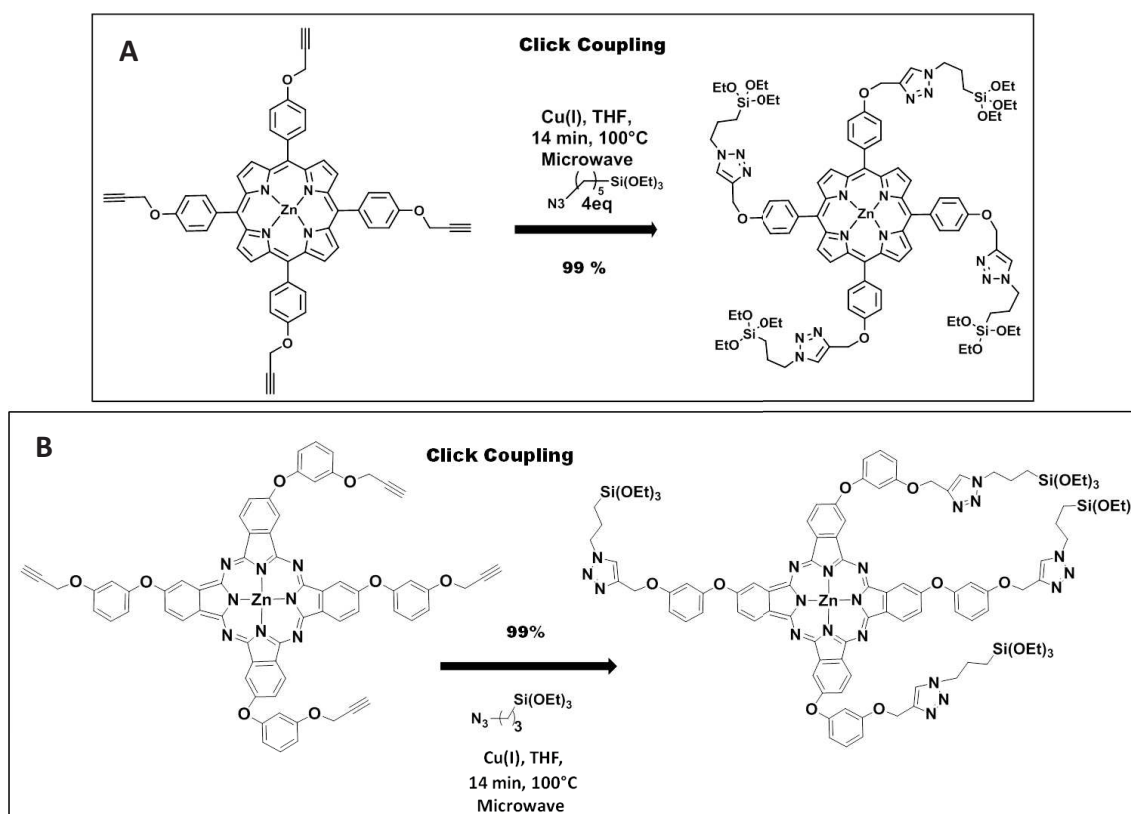
The field of nanomedicine has been growing in the last years as a new tool for the diagnostic practices such as medical images and therapeutic applications. MRI and fluorescence complementary imaging techniques offer poor tissue penetration and low resolution *in vivo* images, using ultraviolet and visible light. Near-infrared (NIR) imaging solves these problems since the irradiation at 700-900 nm allows a deeper penetration and a minimal autofluorescence in tissues⁴⁴. Porphyrins and phthalocyanines, as photosensitizer molecules, are suited for this type of imaging, since they present emission wavelengths in the NIR region. They are also suited for therapeutic applications with their photodynamic properties⁴⁵. In 2008, Yeh et al. described, using two-photon fluorescence imaging, the subcellular localization determined by the differences in porphyrin fluorescence lifetime properties in the cell membrane and the cytosol⁴⁶.

The poor water solubility and toxicity of those photosensitizers make their use difficult for theranostics. Nanoparticles encapsulating the photosensitizer (PS) reduce these problems. We studied in the second chapter, the synthesis of mesoporous silica nanoparticles encapsulating different porphyrin photosensitizers for applications in one-photon PDT and imaging^{47, 48}. Herein, we report the cell killing effects via two-photon PDT and near-infrared fluorescence imaging *via* pure photosensitizer BS nanoparticles. MSNs contain around 10% of the PS whereas these BS nanoparticles¹⁸ are synthesized from pure photosensitizer precursor. This amount of PS and the aggregation of photosensitizer molecules in the nanoparticles that produces a red shift of the UV visible spectra, make them suitable for imaging and two-photon PDT.

Two novel tetraalkoxysilylated two-photon photosensitizers (2PS) were developed via CuAAC click-reaction^{29, 49} and were fully characterized. Sol-gel process was achieved by auto-condensation of the photosensitizers. The arrangement of the molecules into the nanoparticles leads to the formation of photosensitizer aggregates that allows the NIR-fluorescence imaging in cancer cells. Therefore, 2 hv PDT was applied at 800 nm and lead to good results in MCF-7 cancer cells.

3.3.2. Results and discussion

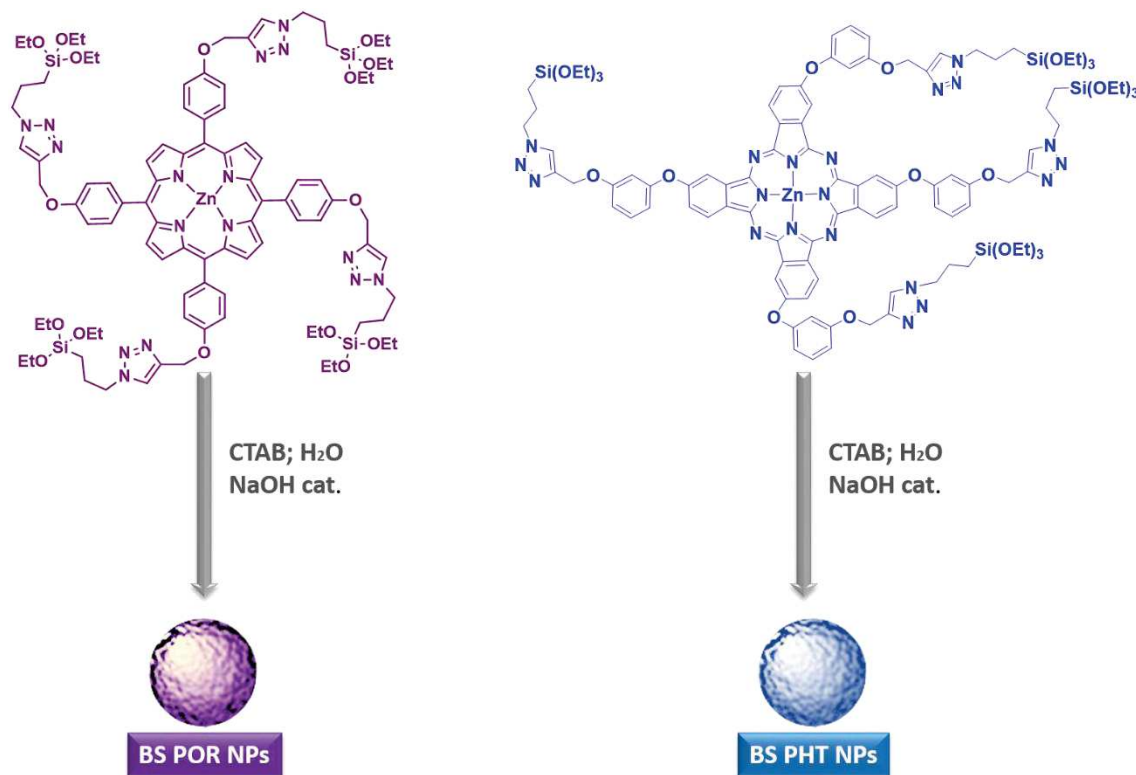
The porphyrin (POR) and the phthalocyanine (PHT) precursors and corresponding NPs nanoparticles were initially prepared (Scheme 1). First, the PHT and the POR photosensitizer were alkoxy-silylated via a copper-catalyzed azide-alkyne cycloaddition (CuAAC) click coupling in microwave during 15 min at 100°C. Silylated precursors were fully characterized via ^1H and ^{13}C nuclear magnetic resonances (NMR), Fourier transform infrared (FTIR), UV-visible (UV) and mass spectroscopy (MALDI) (Supp. Inf. S2-S3). Then, elaboration of BS nanoparticles was carried out.



Scheme 1. Tetra-alkoxysilylated two-photon photosensitizer porphyrin (A) and tetra-alkoxysilylated two-photon phthalocyanine PHT (B) sol-gel precursors.

The nanomaterial elaboration of porphyrin-based BS (BSPOR) was achieved first (Scheme 2). The synthesis started with the formation of micelles using cetyltrimethylammonium bromide in water and sodium hydroxide as catalyst at 80°C at 750 rpm during 2 hours. Then, a solution of the silylated POR precursor in a mixture of DMSO/EtOH was added quickly to the solution mentioned before. The reaction was stirred for 2 hours at 80°C and 750 rpm (Supp. Inf. S4).

Secondly, the synthesis of phthalocyanine based BS nanoparticles (BSPHT) was performed (Supp. Inf. S5). The formation of micelles was elaborated as for the first nanoparticles. After 2 hours, a solution of the silylated phthalocyanine precursor in EtOH was added and the sol-gel process was conducted for two hours at 80°C at 750 rpm.



Scheme 2. Synthetic process to design BSPOR and BSPHT nanoparticles.

The morphology and the composition of both nanomaterials were then characterized via various techniques. Transmission electron microscopy (TEM) images showed non porous NPs of polydispersed BSPOR (150-250 nm diameter) (Figure 1a) and 106 nm diameter aggregated BSPHT nanoparticles (Figure 1e). Number-averaged Dynamic Light Scattering (DLS) revealed solutions of BS nanoparticles in EtOH with a hydrodynamic diameter measuring around 263 nm and 93 nm for BSPOR (Figure 1b) and BSPHT (Figure 1f) respectively. The size distribution of 100 nanoparticles was studied and a Gaussian analysis revealed a diameter of 102 nm and 106 nm for BSPOR and BSPHT NPs respectively (Figure 1 c and d).

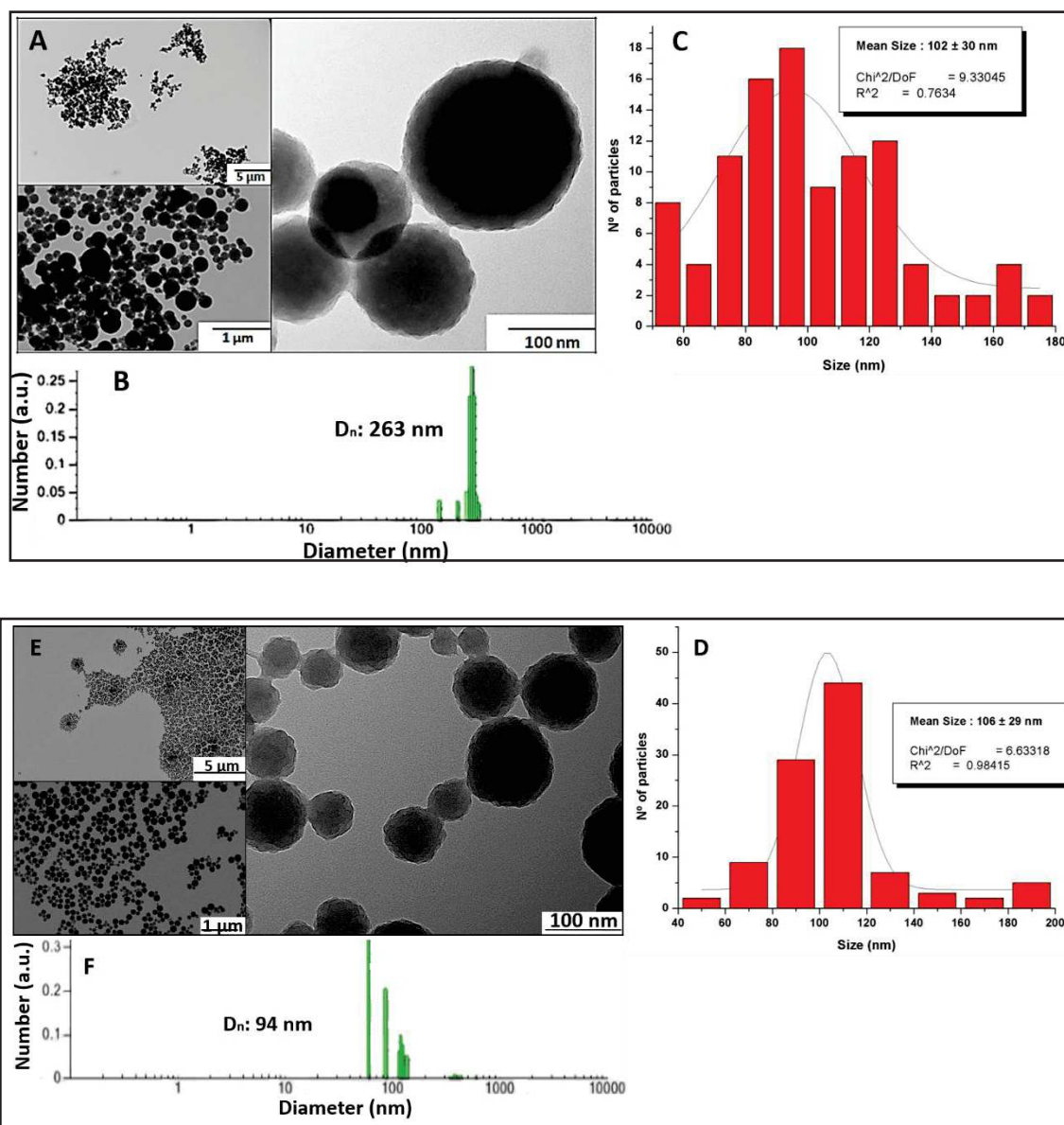


Fig. 1. TEM micrographs of as prepared BSPOR (a), BS PHT NPs (e). Number-averaged dynamic light scattering gave 263 nm BSPOR (b) and 94 nm BSPHT nanoparticles (f). Their size distribution was studied by the Gaussian analysis (c for BSPOR and d for BSPHT).

The FTIR spectrum of the BSPOR nanoparticles (Figure 2) presents the absorption bands for C-H and C-H aromatic stretching in the 3000 and 2800 cm^{-1} region. The C=C aromatic stretching at 1596 cm^{-1} and the porphyrin ring vibration and deformation at 1068 cm^{-1} and 712 cm^{-1} confirmed the presence of the photosensitizer precursor into the nanoparticles.

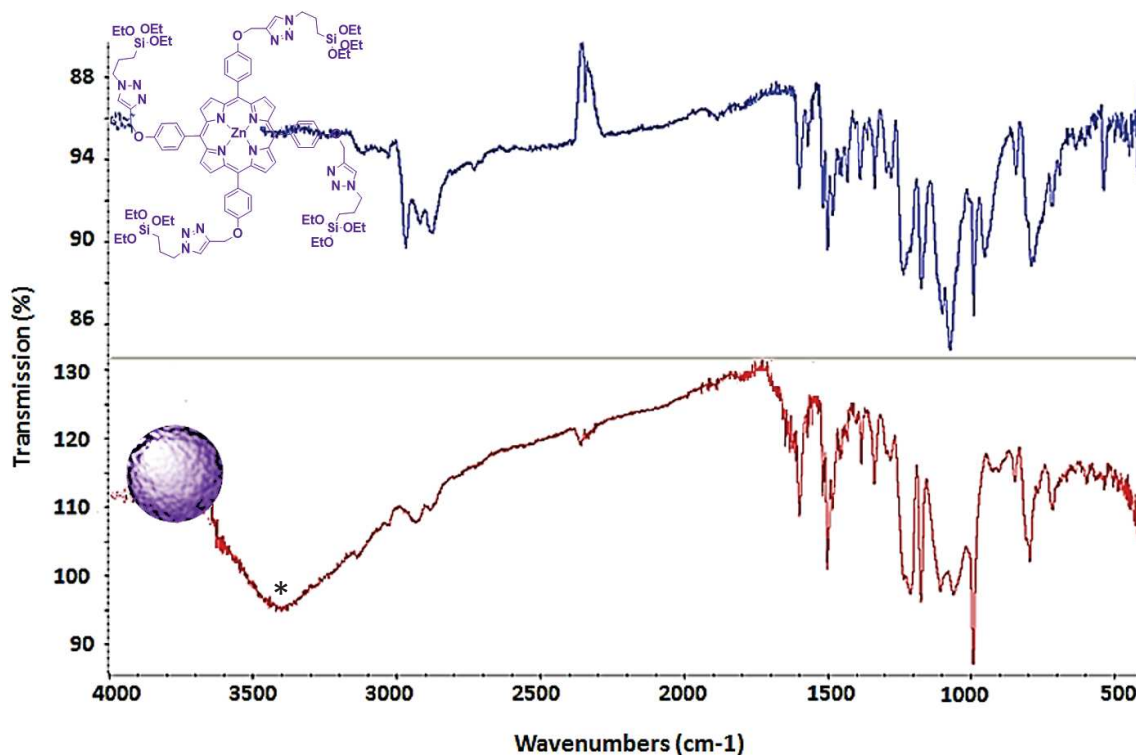


Fig. 2. FTIR spectra of BSPOR NPs.* Indicates the vibration modes of water.

Solid state NMR ^{29}Si cross-polarization (Fig. 3A) spectrum depicted the presence of the T_2 and T_3 environment at -58 and -65 ppm respectively for BSPOR. Solid state ^{13}C NMR displayed the carbons corresponding to the porphyrin precursor (Figure 3b).

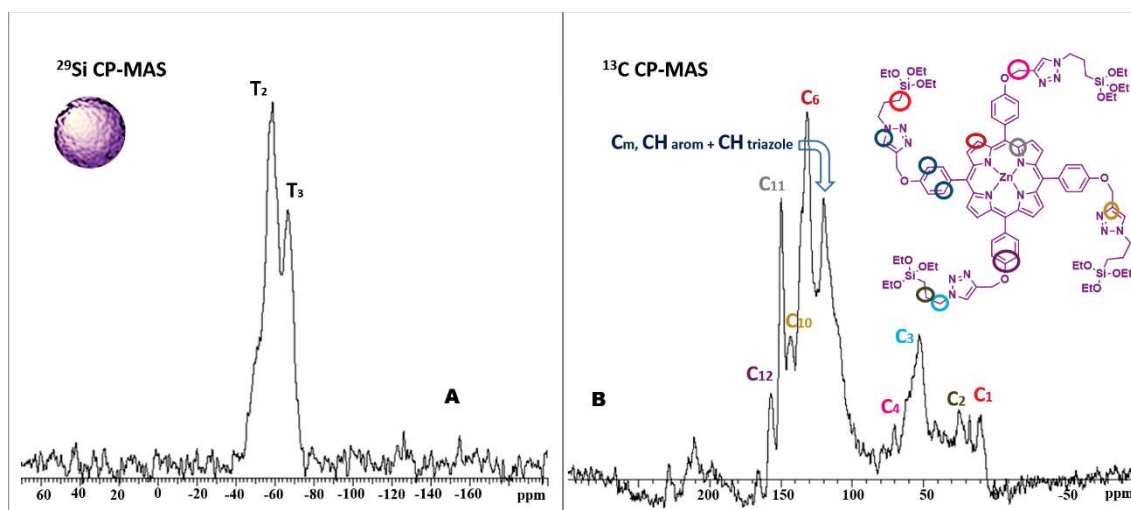


Fig. 3. A) ^{29}Si solid state NMR. B) ^{13}C solid state NMR.

UV-visible spectroscopy of solutions of nanoparticles in EtOH, confirmed the presence of metallated PS precursors. BS made with the porphyrin precursor (Figure 4a) present the typical spectrum of a metallated porphyrin with a large Soret band at 451 nm and two Q bands at 566 and 610 nm. Comparing with the UV spectrum of the precursor, a large red shift of the Soret band and Q bands was observed. This is due to the formation of J aggregates of the porphyrins present into the nanoparticles. The study of the nanoparticles made by the phthalocyanine precursor (Figure 4b) which present its typical bands at 346, 611, 638 and 675 nm shows a red shift of the photosensitizer present in the nanoparticles and an enlargement of some bands (361, 642 and 693 nm). Like the porphyrin precursor, phthalocyanine can also form J or H aggregates. As the shift is bathochromic, there is a high amount of the precursor disposed in J aggregation (end-to-end stacking).

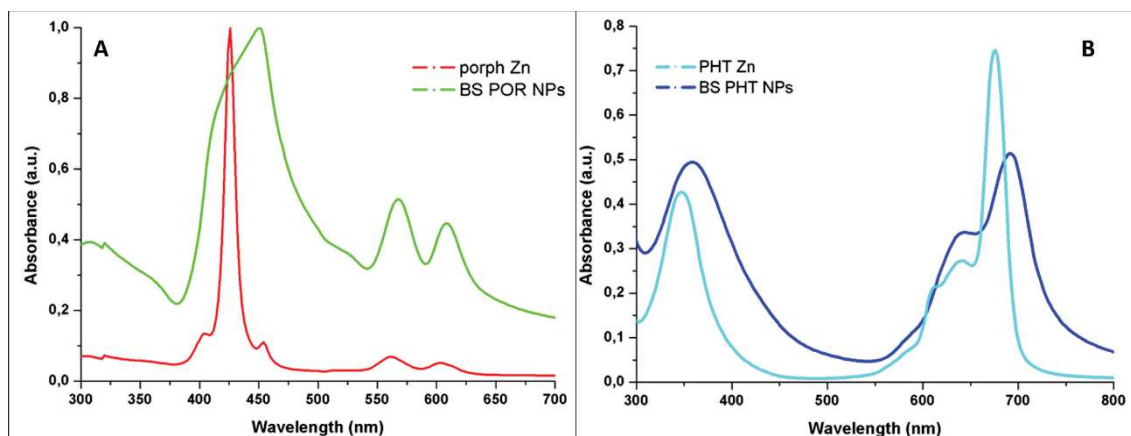


Fig. 4. a) UV-Visible absorption spectra in EtOH of BSPOR NPs and the porphyrin precursor. b) UV-Visible absorption spectra of the BSPHT NPs and the phthalocyanine precursor.

The *in vitro* two-photon imaging studies were performed in MCF-7 breast cancer cells. Nanoparticles were incubated 20 hours with MCF-7 cancer cells. The membranes of cells were stained with a Cell Mask Orange Plasma Membrane during 15 minutes before the imaging experiments. Two-photon imaging (Figure 5) was performed with a Carl Zeiss confocal microscope at low laser power (6%) at 800 nm for BSPOR and 750 nm for BS PHT. The endocytosis of nanoparticles was clearly observed in the merged images and their efficiency for intracellular tracking was demonstrated.

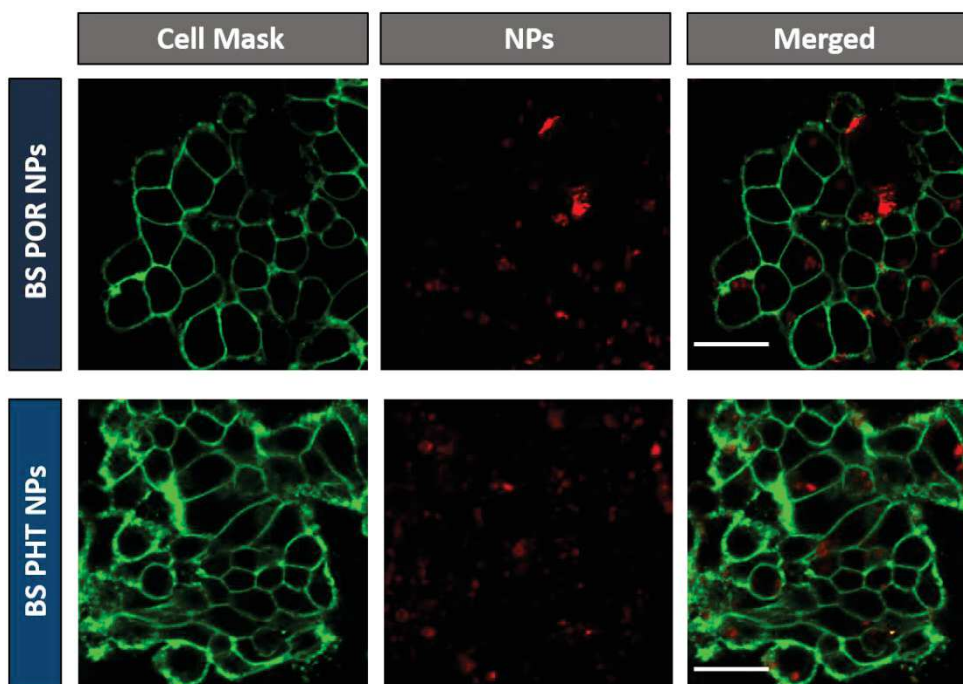


Fig. 5. Two-photon confocal microscopy images of cells at 800 nm. NPs incubated during 20 h with 80 $\mu\text{g}\cdot\text{mL}^{-1}$ of BSPOR or BSPHT. Scale bars of 10 μm .

Finally, the two-photon *in vitro* therapy (Figure 6) was conducted on MCF-7 cancer cells that were incubated with 80 $\mu\text{g}/\text{ml}$ of nanoparticles for 24 hours. After irradiation at 800 nm, the MTT assay (a yellow tetrazole reduced to purple formazan in living cells) was performed after 48 hours. BSPHT caused the 21% of selective cell-killing. Interestingly 86% of death was observed with BS POR NPs.

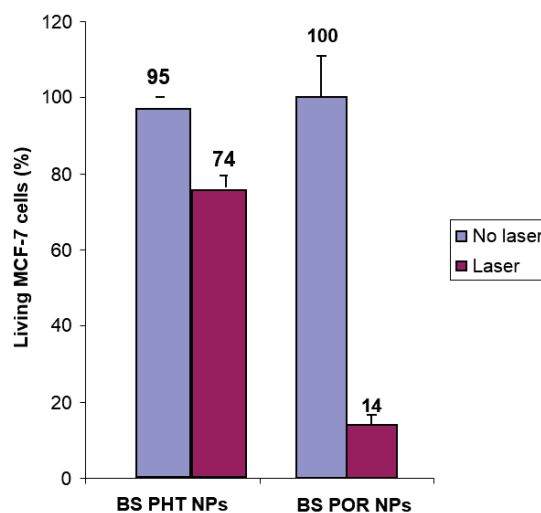


Fig. 6. TPE-triggered cancer cell killing on BSPOR and BSPHT NPs (irradiated at 800 nm).

3.3.3. Conclusions

In summary, we have designed bridged-silsesquioxane nanoparticles from a) tetrasilylated porphyrin and b) phtalocyanine photosensitizers that were obtained by click chemistry. The morphology and compositions were fully characterized by various techniques, which showed the presence of the PS. Besides, the nanoparticles cellular uptake was demonstrated by TPE-fluorescence imaging *in vitro* in MCF-7 breast cancer cells. Two-photon therapy was applied to all nanoparticles and lead to 21 % to 86 % of cancer cell killing. It is envisioned that those nanoparticles, specially the BS POR could be a new promising nanodevice for applications in cancer treatment.

3.3.4. Supporting Information

Experimental section

3.3.4. S1. Materials and procedures

Cetyltrimethylammonium bromide (CTAB) and sodium hydroxide were purchased from Sigma-Aldrich. Absolute ethanol was purchased from Fisher Chemicals. R. Norma Pure. (3-azidopropyl)-trimethoxysilane was obtained from a reported procedure by M. Ortega-Muñoz et al (*Adv. Synth. Catal.* **2006**, 348, 2410).

^1H and ^{13}C NMR spectra were recorded with a Bruker AC 400 spectrometer. Chemical shifts (in δ units, ppm) are referenced to TMS using CHCl_3 ($\delta = 7.26$ ppm) and CDCl_3 ($\delta = 77.0$ ppm) as the internal standards, respectively, for ^1H and ^{13}C NMR spectra. IR spectra were recorded on a Perkin-Elmer 100 FT spectrophotometer. Absorption spectra were recorded on a Hewlett-Packard 8453. Mass spectrometry was carried out at the Laboratoire de Mesures Physiques (Montpellier, France) with a Thermo-Finnigan MAT95 apparatus in electronic impact ionization mode. Dynamic light scattering analyses were performed using a Cordouan Technologies DL 135 Particle size analyzer instrument. ^{29}Si and ^{13}C CP/MAS solid state NMR sequences were recorded with a VARIAN VNMR300, using Q8MH8 and adamantane references respectively. TEM analysis performed on a JEOL 1200 EXII instrument. SEM analysis performed on a FEI Quanta FEG 200 instrument.

Nanomaterial synthesis and characterization

3.3.4. S2. Silylation of POR precursor

A mixture of the tetrapropargylyl porphyrine derivative (100 mg, 1.12×10^{-1} mmol), bromotris(triphenylphosphine)copper(I) ($[\text{CuBr}(\text{PPh}_3)_3]$, 10 mg, 1×10^{-2} mmol), and anhydrous THF (3 mL) was placed in a 10 mL microwave sealable reactor, and (3-azidopropyl)triethoxysilane (150 mg, 0.6 mmol) was added. Then, the tube was flushed with argon and the microwave process was conducted 20 min at 100°C at 200 mW. After evaporation of the solvents, the POR precursor was quantitatively obtained as a purple solid (210 mg, 1.12×10^{-1} mmol). The yield of the reaction was 100 %. ^1H NMR (300 MHz, $\text{DMSO}-d_6$): δ 8.81 (s, 8H, $\underline{\text{H}}_{\text{pyrrole}}$), 8.41 (s, 4H, triazole), 8.09 (d, $^3J = 8.4$

Hz, 8H, $H_{\text{ph-pyrrole}}$), 7.44 (d, $^3J = 8.2$ Hz, 8H, $H_{\text{ph-triazole}}$), 5.43 (s, 8H, N- CH_2 -riazole), 4.45 (t, $^3J = 7.0$ Hz, 8H, triazole- CH_2), 3.77 (q, $^3J = 7$ Hz, 24H, O- CH_2 - CH_3), 1.99 (t, $^3J = 7.8$ Hz, 8H, triazole- CH_2 - CH_2), 1.16 (t, $^3J = 6.9$ Hz, 36H, O- CH_2 - CH_3), 0.60 (t, $^3J = 7.7$ Hz, 8H, CH_2 -Si). ^{13}C NMR (400MHz, DMSO): δ 158.8, 149.9, 143.19, 135.5, 131.8, 129, 125, 120, 113.1, 58.2, 53.3, 52.14, 24.3, 18.5, 7.3. ^{29}Si NMR (400MHz, DMSO): δ -46.4. FTIR (neat KBr) $\nu_{\text{max}}/\text{cm}^{-1} = 3116, 3032, 2977, 2932, 2882, 1596, 1563, 1502, 1435, 1391, 1346, 1296, 1268, 1240, 1174, 1107, 1068, 996, 945, 840, 789, 712, 684, 533, 422$. UV/Vis λ_{max} (EtOH): 426, 561, 604 nm. Emission (EtOH): $\lambda_{\text{max}} = 607, 660$ nm ($\lambda_{\text{excitation}} = 432$ nm). MALDI-TOF: calcd for $\text{C}_{92}\text{H}_{120}\text{N}_{16}\text{O}_{16}\text{Si}_4\text{Zn}$: 1880.690, found 1880.720.

3.3.4. S3. Silylation of PHT precursor

A mixture of the tetrapropargylyd phthalocyanine derivative (85 mg, 7.3×10^{-2} mmol), bromotris (triphenylphosphine) copper (I) ($[\text{CuBr}(\text{PPh}_3)_3]$, 10 mg, 1×10^{-2} mmol), and anhydrous THF (3 mL) was placed in a 10 mL microwave sealable reactor, and (3-azidopropyl) triethoxysilane (72.2 mg, 0.29 mmol) was added. Then, the tube was flushed with argon and the microwave process was conducted 35 min at 100°C at 200 mW. After evaporation of the solvents, the PHT precursor was quantitatively obtained as a blue solid (157 mg, 7.3×10^{-2} mmol). The yield of the reaction was 100%. ^1H NMR (400 MHz, DMSO- d_6): δ 8.87-7.40 (m, H_{aromatic}), 5.27 (d, 8H, O- CH_2 -riazole), 4.32 (t, $^3J = 7.0$ Hz, 8H, triazole- CH_2), 3.66 (q, $^3J = 7.0$ Hz, 24H, O- CH_2 - CH_3), 1.87 (t, $^3J = 7.8$ Hz, 8H, triazole- CH_2 - CH_2), 1.07 (t, $^3J = 7.0$ Hz, 36H, O- CH_2 - CH_3), 0.46 (t, $^3J = 7.5$ Hz, 8H, CH_2 -Si). ^{13}C NMR (400MHz, DMSO): δ 160.31, 158.7, 158.4, 149.9, 139.8, 133.5, 132.5, 131.9, 131.4, 129.3, 129.0, 124.9, 124.2, 120.9, 120.6, 112.3, 111.3, 111.0, 106.9, 61.9, 58.2, 52.1, 24.3, 18.7, 7.3. ^{29}Si NMR (400MHz, DMSO): δ -46.3. UV/Vis λ_{max} (EtOH): 346, 611, 638, 675 nm. MALDI-TOF: calcd for $\text{C}_{109}\text{H}_{124}\text{N}_{20}\text{O}_{20}\text{Si}_4\text{Zn}$: 2151.98, found 2151.8.

3.3.4. S4. Synthesis of BSPOR NPs

A mixture of CTAB (250 mg), distilled water (120 mL), and sodium hydroxide (875 μL , 2 M) was stirred at 80°C during 50 minutes at 750 rpm in a 250 mL three neck round bottom flask. Then, the two-photon photosensitizer (83 mg in a solution of 500 μL of DMSO and 1 mL of absolute ethanol) was added and the condensation process was conducted for 2 h. Afterwards, the solution was cooled to room temperature while

stirring; fractions were gathered in propylene tubes and collected by centrifugation during 20 minutes at 20 krpm. The sample was then washed three times with a solution of NH_4NO_3 in EtOH (6g/L). Each washing was followed by sonication at 40°C and centrifugation collection of the sample. The sample was washed three times with EtOH and collected in the same manner. The as-prepared material was dried under vacuum for few hours. 35.2 mg of product were obtained.

3.3.4. S5. Synthesis of BSPHT NPs

A mixture of CTAB (125 mg), distilled water (60 mL), and sodium hydroxide (437 μL , 2 M) was stirred at 80°C during 50 minutes at 750 rpm in a 250 mL three neck round bottom flask. Then, the two-photon photosensitizer (48 mg in a solution in 2 mL of absolute ethanol) was added and the condensation process was conducted for 2 h. Afterwards, the solution was cooled to room temperature while stirring; fractions were gathered in propylene tubes and collected by centrifugation during 20 minutes at 20 krpm. The sample was then washed three times with a solution of NH_4NO_3 in EtOH (6g/L). Each washing was followed by sonication at 40°C and centrifugation collection of the sample. The sample was washed three times with EtOH and collected in the same manner. The as-prepared material was dried under vacuum for few hours. 27.6 mg of product were obtained.

***In vitro* studies**

3.3.4. S6. Two-photon fluorescence imaging

The day prior to the experiment, MCF-7 cells were seeded onto bottom glass dishes (World Precision Instrument, Stevenage, UK) at a density of 10^6 cells. cm^{-2} . Adherent cells were then washed once and incubated in 1 mL culture medium containing NPs at a concentration of 40 $\mu\text{g}.\text{mL}^{-1}$ for 20 h. Fifteen min before the end of incubation, cells were loaded with Cell Mask TM Orange Plasma Membrane Stains (Invitrogen, Cergy Pontoise, France) for membrane staining at a final concentration of 5 $\mu\text{g}.\text{mL}^{-1}$. Before visualization, cells were washed gently with phenol red-free DMEM. Cells were then scanned with a LSM 780 LIVE confocal microscope (Carl Zeiss, Le Pecq, France), at 760 or 800 nm with a slice depth (Z stack) of 0.62 μm .

3.3.4. S7. TPE-therapy

MCF-7 human breast cancer cells were cultured in Dulbecco's modified Eagle's medium (DMEM) supplemented with 10% fetal bovine serum and 50 $\mu\text{g}\cdot\text{mL}^{-1}$ gentamycin. All cells were allowed to grow in humidified atmosphere at 37°C under 5% CO_2 . For *in vitro* phototoxicity, MCF-7 cells were seeded into a 384 multiwell glass-bottomed plate (thickness 0.17 mm), with a black polystyrene frame, 2000 cells per well in 50 μL of culture medium, and allowed to grow for 24 h. NPs were then dispersed under ultrasounds in PBS at a concentration of 1 $\text{mg}\cdot\text{mL}^{-1}$ and cells were then incubated for 20 h with or without nanoparticles at a final concentration of 40 $\mu\text{g}\cdot\text{mL}^{-1}$ in supplemented DMEM. After incubation with NPs, cells were washed twice, maintained in fresh culture medium, and then submitted (or not) to laser irradiation; with the Carl Zeiss Microscope LSM 780 LIVE confocal microscope (laser power input 3W). Half of the well was irradiated at 760 or 800 nm by three scans of 1.57 s duration in 4 different areas of the well. The laser beam was focused by a microscope objective lens (Carl Zeiss 10x, NA 0.4). After 2 days, the MTT assay was performed and was corrected.

3.4. General conclusions and perspectives

Different photosensitizers were used to prepare bridged silsesquioxane nanoparticles and used for *in vitro* two-photon therapy and imaging. First, biodegradable bridged silsesquioxane nanoparticles were synthesized from a disulfide precursor and a metallated porphyrin. The first precursor provides the ability to be biodegradable because of the S-S bonds and the second one, as a photosensitizer, provides his utility in imaging and PDT. Their PDT effect was studied under irradiation at 800 nm in MCF-7 breast cancer cells, and the best results were obtained for DISP NPs with almost 54% of cell death. Imaging results at 760 nm were also reported for the nanoparticles. The biodegradability of the NPs was assessed in near-physiological conditions, at 37°C in the presence of mercaptoethanol.

Second, two different bridged silsesquioxane nanoparticles were synthesized from either a metallated porphyrin (BSPOR), or from a metallated phthalocyanine (BSPHT). Both precursors were tetrasilylated by click chemistry under CuAAC catalysis. The resulting nanoparticles were analysed by different techniques. BSPOR and BSPHT produced 86% and 21% of cell death respectively. Their efficiency for intracellular tacking was demonstrated by *in vitro* imaging at 750 nm.

In the near future a surface stabilization with PEG could be used to avoid the aggregation of the nanoparticles and to allow their use *in vivo*. Grafting of a targeting moiety can also be envisaged.

3.5. References

1. D. A. Loy and K. J. Shea, *Chemical Reviews*, 1995, 95, 1431-1442.
2. K. J. Shea and D. A. Loy, *Chemistry of Materials*, 2001, 13, 3306-3319.
3. L. Zhao, D. A. Loy and K. J. Shea, *J. Am. Chem. Soc.*, 2006, 128, 14250-14251.
4. L.-C. Hu, M. Khiterer, S.-J. Huang, J. C. C. Chan, J. R. Davey and K. J. Shea, *Chemistry of Materials*, 2010, 22, 5244-5250.
5. J. Della Rocca, R. C. Huxford, E. Comstock-Duggan and W. Lin, *Angewandte Chemie International Edition*, 2011, 50, 10330-10334.
6. L. Fertier, C. Théron, C. Carcel, P. Trens and M. Wong Chi Man, *Chemistry of Materials*, 2011, 23, 2100-2106.
7. L.-C. Hu, Y. Yonamine, S.-H. Lee, W. E. van der Veer and K. J. Shea, *J. Am. Chem. Soc.*, 2012, 134, 11072-11075.
8. X. Li, T. Tang, Y. Zhou, Y. Zhang and Y. Sun, *Microporous and Mesoporous Materials*, 2014, 184, 83-89.
9. J. Croissant, M. Maynadier, A. Gallud, H. P. N'Dongo, J. L. Nyalosaso, G. Derrien, C. Charnay, J.-O. Durand, L. Raehm, F. Serein-Spirau, N. Cheminet, T. Jarrosson, O. Mongin, M. Blanchard-Desce, M. Gary-Bobo, M. Garcia, J. Lu, F. Tamanoi, D. Tarn, T. M. Guardado-Alvarez and J. I. Zink, *Angew. Chem. Int. Ed.*, 2013, 52, 13813-13817.
10. H. M. Kim and B. R. Cho, *Acc. Chem. Res.*, 2009, 42, 863-872.
11. C. Mauriello-Jimenez, J. Croissant, M. Maynadier, X. Cattoen, M. Wong Chi Man, J. Vergnaud, V. Chaleix, V. Sol, M. Garcia, M. Gary-Bobo, L. Raehm and J.-O. Durand, *J. Mater. Chem. B*, 2015, 3, 3681-3684.
12. I. Schick, S. Lorenz, D. Gehrig, A.-M. Schilman, H. Bauer, M. Panthoefel, K. Fischer, D. Strand, F. Laquai and W. Tremel, *J. Am. Chem. Soc.*, 2014, 136, 2473-2483.
13. C. Jiang, T. Zhao, P. Yuan, N. Gao, Y. Pan, Z. Guan, N. Zhou and Q.-H. Xu, *ACS Appl. Mater. Interfaces.*, 2013, 5, 4972-4977.
14. Q. N. Lin, Q. Huang, C. Y. Li, C. Y. Bao, Z. Z. Liu, F. Y. Li and L. Y. Zhu, *J. Am. Chem. Soc.*, 2010, 132, 10645-10647.
15. *Application: WO Pat.*, 2010-EP690352011073054, 2011.
16. J. Croissant, X. Cattoen, M. W. C. Man, A. Gallud, L. Raehm, P. Trens, M. Maynadier and J.-O. Durand, *Adv. Mater.*, 2014, 26, 6174-6178.
17. M. Pawlicki, H. A. Collins, R. G. Denning and H. L. Anderson, *Angew. Chem. Int. Ed.*, 2009, 48, 3244-3266.
18. J. Croissant, M. Maynadier, O. Mongin, V. Hugues, M. Blanchard-Desce, A. Chaix, X. Cattoen, M. Wong Chi Man, A. Gallud, M. Gary-Bobo, M. Garcia, L. Raehm and J.-O. Durand, *Small*, 2015, 11, 295-299.
19. J. Croissant, D. Salles, M. Maynadier, O. Mongin, V. Hugues, M. Banchard-Desce, X. Cattoen, M. W. C. Man, A. Gallud, M. Garcia, M. Gary-Bobo, L. Raehm and J.-O. Durand, *Chemistry of Materials*, 2014, 26, 7214-7220.
20. J.-H. Park, L. Gu, G. von Maltzahn, E. Ruoslahti, S. N. Bhatia and M. J. Sailor, *Nat Mater*, 2009, 8, 331-336.
21. M. Fadel, K. Kassab and D. A. Fadeel, *Lasers Med. Sci.*, 2010, 25, 283-292.
22. M. Gaumet, R. Gurny and F. Delie, *Int. J. Pharm.*, 2010, 390, 45-52.
23. J. Panyam and V. Labhasetwar, *Adv. Drug. Deliv. Rev.*, 2003, 55, 329-347.
24. M. Keeney, S.-G. Ong, A. Padilla, Z. Yao, S. Goodman, J. C. Wu and F. Yang, *ACS Nano*, 2013, 7, 7241-7250.

25. J. M. Silva, M. Videira, R. Gaspar, V. Pr at and H. F. Florindo, *J. Control. Release*, 2013, 168, 179-199.
26. J. Croissant, A. Chaix, O. Mongin, M. Wang, S. Clement, L. Raehm, J.-O. Durand, V. Hugues, M. Blanchard-Desce, M. Maynadier, A. Gallud, M. Gary-Bobo, M. Garcia, J. Lu, F. Tamanoi, D. P. Ferris, D. Tarn and J. I. Zink, *Small (Weinheim an der Bergstrasse, Germany)*, 2014, 10, 1752-1755.
27. G. Bhakta, S. Mitra and A. Maitra, *Biomaterials*, 2005, 26, 2157-2163.
28. J. Li, Y.-C. Chen, Y.-C. Tseng, S. Mozumdar and L. Huang, *J. Control. Release*, 2010, 142, 416-421.
29. K. Burglova, A. Noureddine, J. Hodacova, G. Toquer, X. Cattoen and M. Wong Chi Man, *Chem. Eur. J.*, 2014, 20, 10371-10382.
30. J. D. Rocca, M. E. Werner, S. A. Kramer, R. C. Huxford-Phillips, R. Sukumar, N. D. Cummings, J. L. Vivero-Escoto, A. Z. Wang and W. Lin, *Nanomedicine : nanotechnology, biology, and medicine*, 2015, 11, 31-38.
31. N. Mizoshita, T. Tani and S. Inagaki, *Chem. Soc. Rev.*, 2011, 40, 789-800.
32. L. Zhao, M. Vaupel, D. A. Loy and K. J. Shea, *Chemistry of Materials*, 2008, 20, 1870-1876.
33. M. Khiterer and K. J. Shea, *Nano Lett.*, 2007, 7, 2684-2687.
34. V. Jain, M. Khiterer, R. Montazami, H. M. Yochum, K. J. Shea and J. R. Heflin, *ACS Appl. Mater. Interfaces.*, 2009, 1, 83-89.
35. H. Rathnayake, J. Binion, A. McKee, D. J. Scardino and N. I. Hammer, *Nanoscale*, 2012, 4, 4631-4640.
36. J. L. Vivero-Escoto, W. J. Rieter, H. Lau, R. C. Huxford-Phillips and W. Lin, *Small*, 2013, 9, 3523-3531.
37. X. Catto en, A. Noureddine, J. Croissant, N. Moitra, K. B urglov a, J. Hoda ov a, O. de los Cobos, M. Lejeune, F. Rossignol, D. Toulemon, S. B egin-Colin, B. P. Pichon, L. Raehm, J.-O. Durand and M. Wong Chi Man, *J. Sol-Gel Sci. Technol.*, 2014, 70, 245-253.
38. A.-L. Wirotius, E. Ibarboure, L. Scarpantonio, M. Schappacher, N. D. McClenaghan and A. Deffieux, *Polymer Chem.*, 2013, 4, 1903-1912.
39. N. C. Maiti, S. Mazumdar and N. Periasamy, *The Journal of Physical Chemistry B*, 1998, 102, 1528-1538.
40. M. Shirakawa, S.-i. Kawano, N. Fujita, K. Sada and S. Shinkai, *The Journal of Organic Chemistry*, 2003, 68, 5037-5044.
41. S. Tao and G. Li, *Colloid and Polymer Science*, 2007, 285, 721-728.
42. E. Beaumont, J. C. Lambry, M. Blanchard-Desce, P. Martasek, S. P. Panda, E. E. H. van Faassen, J. C. Brochon, E. Deprez and A. Slama-Schwok, *Chembiochem*, 2009, 10, 690-701.
43. A. C. Robin, S. Gmouh, O. Mongin, V. Jouikov, M. H. V. Werts, C. Gautier, A. Slama-Schwok and M. Blanchard-Desce, *Chem. Commun.*, 2007, 1334-1336.
44. V. Pansare, S. Hejazi, W. Faenza and R. K. Prud'homme, *Chemistry of materials : a publication of the American Chemical Society*, 2012, 24, 812-827.
45. K. Hayashi, M. Nakamura, H. Miki, S. Ozaki, M. Abe, T. Matsumoto and K. Ishimura, *Adv. Funct. Mater.*, 2012, 22, 3539-3546.
46. S.-C. A. Yeh, K. R. Diamond, M. S. Patterson, Z. Nie, J. E. Hayward and Q. Fang, *Theranostics*, 2008, 2, 817-826.
47. M. Gary-Bobo, Y. Mir, C. Rouxel, D. Brevet, I. Basile, M. Maynadier, O. Vaillant, O. Mongin, M. Blanchard-Desce, A. Morere, M. Garcia, J.-O. Durand and L. Raehm, *Angew. Chem. Int. Ed.*, 2011, 50, 11425-11429.

48. M. Gary-Bobo, O. Hocine, D. Brevet, M. Maynadier, L. Raehm, S. Richeter, V. Charasson, B. Looock, A. Morere, P. Maillard, M. Garcia and J.-O. Durand, *Int. J. Pharm.*, 2012, 423, 509-515.
49. K. Bürglová, N. Moitra, J. Hodacová, X. Cattoën and M. Wong Chi Man, *Journal of Organic Chemistry*, 2011, 76, 7326-7333.

CHAPTER 4

Two-photon-actuated photodynamic therapy, imaging, drug and gene delivery *via* periodic mesoporous organosilica nanoparticles in cancer cells

4.1. Introduction

A new type of ordered mesoporous material called periodic mesoporous organosilica (PMOs) were developed for the first time in 1999.¹⁻³ These materials are synthesized by sol-gel process using simultaneously a soft template, where a directing agent is present, and a hydrolysable organosilane that condenses around the template. The organosilane compound presents a structure of the $(XO)_3Si-R-Si(OX)_3$ type where R represents an organic functional linker and X represents an hydrolysable group such as ethoxy or methoxy for example. This molecule can be bis or multisilylated. Like for other mesoporous nanomaterials, a myriad of surfactants and pH conditions (acidic, neutral or basic) can be used⁴. The facility to produce thin films by spin-coating has extended their use in multiple domains such as the microelectronics⁵, adsorption⁶ and catalysis^{7,8,9}.

These materials present a large number of advantages such as a robust porous organic/inorganic framework where the organic groups contribute to the rigidity or flexibility of the walls and the intrinsic properties of the material. Like porous silica materials they present tuneable pore size, pore channels and a high surface area but unlike them, they present hydrophobicity that facilitates the interactions and the high loading of drug molecules and a slower release rate.

Since Stein described for the first time the PMOs materials, multiple works have been presented. Inagaki reported the synthesis of ethylene-PMOs synthesized using OTAC as structuring agent¹. Depending on the molar compositions, he obtained two types of symmetries (2D-hexagonal and 3D-hexagonal). Stein³ synthesized a type MCM-41 material from ethylene or ethenylene using CTAB as surfactant. Once the material realized, he modified the ethenylene groups into dibromoethylene groups. Few years later, Mokaya and co-workers synthesized the first well-ordered hexagonal ethenylene material with a crystal like pore walls¹⁰. The first synthesis of diastereoisomerically pure BTEENE in *trans* configuration was reported by the group of Van der Voort¹¹.

If a variety of PMOs materials have been synthesized from a large number of organosilane precursors (i.e. dendrimers¹², aromatic compounds¹³, etc), the reduction of the size at the nanoscale has been scarcely reported. The first periodic mesoporous organosilica nanoparticles were reported in 2006 by Djojoputro and co-workers¹⁴. They synthesized 100-400 nm ethane-based hollow nanospheres using a mixture of directing agents (the FC-4 fluorocarbon surfactant and the CTAB surfactant). Three years later,

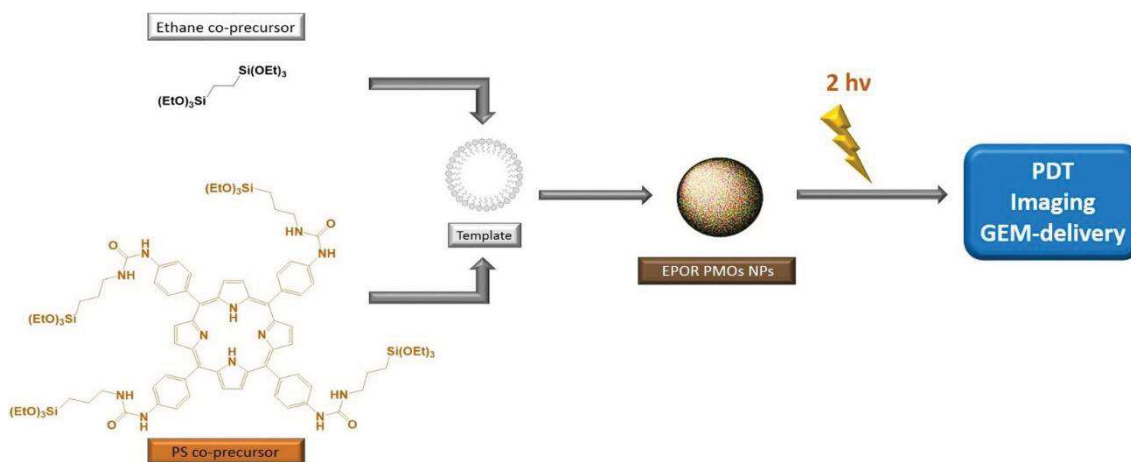
Cho et al. reported the synthesis of worm-like benzene periodic mesoporous organosilica nanoparticles. The synthesis of crystal-like PMOs nanoparticles from methane, ethane, ethylene and benzene organosilanes, under basic conditions and in the presence of CTAB as structuring agent, were reported by Guan and co-workers in 2012¹⁵. Two years later, Croissant et al. synthesized biodegradable ethylene-bis (propyl) disulphide-based PMOs nanorods¹⁶. The biodegradability of the nanoparticles was assessed by disulphide cleavage in the presence of mercaptans.

In biomedical applications, PMOs were first used in the immobilization of cytochrome C. In this case the adsorption was done in ethane-PMO material. Park et al. reported the immobilization of lysozyme in large-pore amine, phenylene and biphenylene PMOs materials^{17, 18}. Due to the hydrophobic interactions the adsorption was higher in phenylene and biphenylene materials than in silica materials. In 2009, Qiao and co-workers described the encapsulation and release of the tetracycline antibiotic on hollow and solid spheres of ethane PMOs particles¹⁹. In 2013, Chen et al. reported the silibinin delivery *in vitro* from hollow phenylene PMOs nanoparticles which produced 88 % of cell killing. Croissant et al. described in 2014 gold NPs core coated with an ethylene-2PS PMO shell where the 2PS was a photosensitizer for two-photon triggered theranostic²⁰. Under irradiation the nanoparticles produced 40 % of cell killing in MCF-7 cancer cells. Loaded with doxorubicin, these nanoparticles produced under irradiation a synergistic cell killing through the PDT and the drug delivery that increased the death of cells up to 75 %.

In this chapter, the syntheses of four different PMOs nanoparticles will be presented. Their use in drug delivery of doxorubicin (hydrophilic) or gemcitabine (hydrophilic), two-photon photodynamic therapy and imaging will demonstrate their efficacy *in vitro* or *in vivo*. First, ethane PMOs nanoparticles encapsulating a free base tetrasilylated porphyrin will be presented for effective *in vitro* synergistic two-photon therapy and gemcitabine delivery. In the second part, nanodiamonds cores were encapsulated into ethane and ethylene PMOs nanoparticles. Their efficacy under two-photon irradiation was demonstrated in MCF-7 cancer cells. Doxorubicin was also loaded into the pores of the nanoparticles and the delivery was demonstrated *in vitro*. The same drug was encapsulated in ethylene-porphyrin PMOs nanoparticles. The effective release and two-photon imaging results are presented in third part. In the last part, pure

porphyrin PMOs are presented. The structure of this novel material was studied by a large number of techniques such as solid NMR, HRTEM tomography and others. Due to the presence of large cavities, siRNA delivery was realized *in vitro*, leading to interesting results. Their efficiency in two-photon imaging and gene delivery was also tested *in vivo* in zebrafish model. The prepared nanoparticles demonstrated are very promising for theranostic applications under two photon irradiation.

4.2. Use of free base porphyrin-functionalized periodic mesoporous organosilica nanoparticles for imaging and synergetic gemcitabine delivery through two-photon therapy



Abstract

Periodic mesoporous organosilica nanoparticles were synthesized *via* co-condensation of bis-silylated ethane precursors and tetrasilylated free base porphyrins. The mesoporosity of the nanoplatforms lead the gemcitabine loading at neutral pH. The drug delivery was tested *in vitro* and a synergetic effect between the photodynamic therapy and the delivery gave rise to high cell killing. The endocytosis of the nanoparticles was also confirmed by two-photon fluorescence imaging of breast cancer cells.

Interdisciplinary collaboration

Nanomaterial synthesis, physic-chemical characterizations and applications in solution: C. Mauriello Jimenez, D. Laurencin, L. Raehm, J-O. Durand.

Synthesis of porphyrin photosensitizer: S. Richeter

Cell studies: M. Maynadier, M. Gary-Bobo, M. Garcia.

➤ N° Patent (France) :1650396

4.2.1. Introduction

Gemcitabine hydrochloride (GEM, dFdC) is a FDA approved chemotherapeutic drug in the treatment of metastized breast and ovarian cancer, non-small cell lung cancer and pancreatic cancer²¹⁻²³. It is an analogue of the de-oxy-cytidine and is metabolized by the nucleosides kinases in three different phosphorylated metabolites: difluorodeoxycytidine monophosphate (dfdCMP), difluorodeoxycytidine diphosphate (dfdCDP) and difluorodeoxycytidine triphosphate (dfdCTP)²⁴. Its phosphorylated derivatives interfere at different steps in the processing DNA pathway and the consequent apoptosis of cancer cells. One way is when the dfdCTP is incorporated into the DNA, replacing the dCTP (deoxycytidine triphosphate) by DNA polymerase epsilon which do not differentiate the two metabolites. Therefore, the polymerase does not induce repair mechanisms and abnormal DNA chains are being formed. Inhibition of DNA synthesis leads to growth inhibition or cell death.

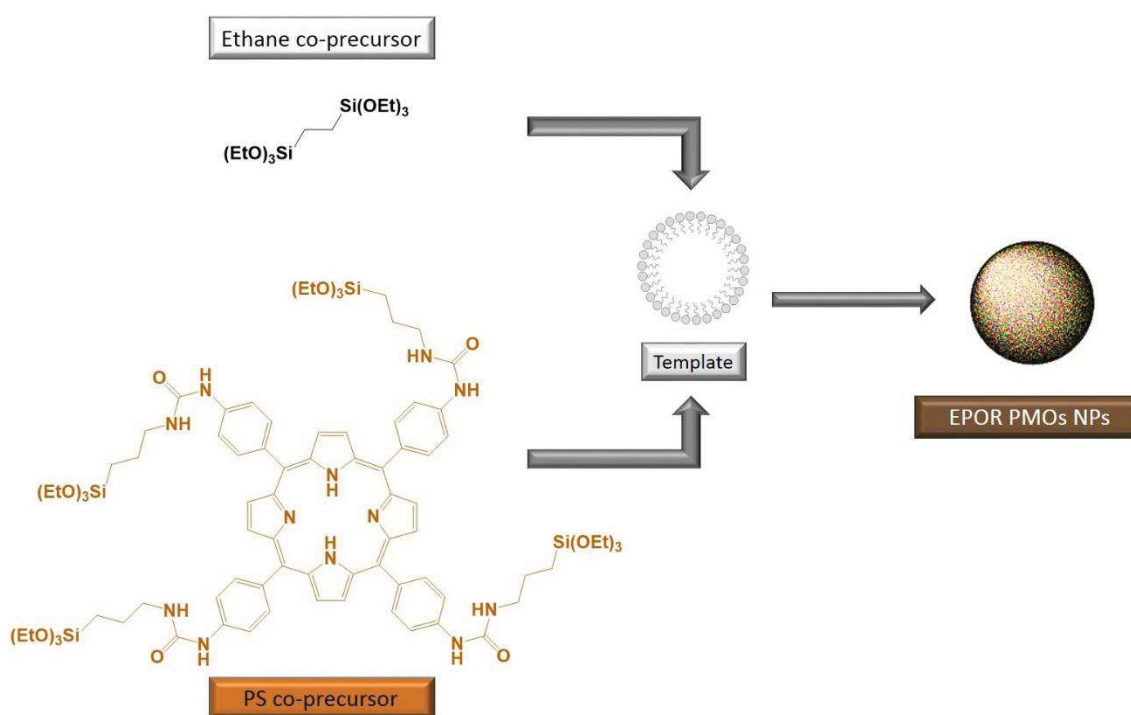
This drug is intravenously injected and due to its short plasma half - life (17 min)²⁵, the dose that is necessary for treatments has to be larger (a standard dose corresponds to 1000 mg/m²) and can induce adverse effects. To overcome these disadvantages, recent works used nanoparticles as gemcitabine delivery carriers²⁶. Hou et al. published in 2009 a work about albumin nanospheres loaded with gemcitabine and their use *in vitro* against human pancreatic cells²⁷. The maximum drug loading that was obtained corresponds to 13 %. Nel and coworkers published recently the synthesis of lipid-coated mesoporous silica nanoparticles for the synergistic delivery of paclitaxel (PTX) and gemcitabine in human pancreatic cancer in mice²⁸. The mesoporous silica nanoparticles were loaded with gemcitabine and coated with a lipid layer containing the paclitaxel drug. The maximum loading capacity of the nanocarriers was 40 %.

Herein, we report the first synergetic cancer cell killing via two-photon-actuated PDT and gemcitabine delivery with periodic mesoporous organosilica nanoparticles. Nanoparticles (EPOR PMOs) were synthesized by sol-gel method, from two silylated precursors: a bis-silylated ethane precursor (E) and a tetrasilylated free base porphyrin (POR) co-precursor used as photosensitizer (PS). The presence of the porphyrin molecule allows to achieve two-photon imaging and two-photon photodynamic therapy. Then, gemcitabine hydrochloride drug was loaded into the pores (92% of drug loading) and nanoparticles were used as delivery nanoplatform *in vitro* in MCF-7 cancer cells. The two-photon therapy was applied and a synergetic effect between the drug delivery

and the PDT was obtained, leading to a 25 % increase of killing effect of the gemcitabine.

4.2.2. Results and discussion

Mesoporous organosilica nanoparticles were produced by co-condensation of bis-(triethoxysilyl) ethane and a tetraalkoxysilylated free base porphyrin (Scheme 1). First, a mixture of CTAB used as surfactant and NaOH used as catalyst was prepared for 2 hours at 80 °C and 750 rpm. Then, a mixture of the ethane precursor and a solution of porphyrin precursor in EtOH was added to the template. The sol-gel process was carried out for 1 h 45 min at 80 °C and 750 rpm.



Scheme 1. Synthesis of EPOR PMOs nanoparticles.

The nanocarrier (EPOR PMOs) morphology was first characterized via transmission electron microscopy (TEM) which showed porous monodisperse nanoparticles with a 381 nm diameter (Figure 1a, 1b). The monodispersity of the size was observed by Dynamic Light Scattering that showed an hydrodynamic diameter at around 666 nm (Supp. Inf. S5).

The presence of the photosensitizer in the nanoparticles was confirmed by the absorption bands (427, 527, 569, 603, 666 nm) in the UV-visible spectra in EtOH

(Figure 1d) and the solid state nuclear magnetic resonance (^{29}Si and ^{13}C CPMAS spectra; Supp. Inf. S10). As it can be observed in the UV spectra, the bands are red-shifted compared to the spectra of the porphyrin precursor (425, 520, 563, 603, 655 nm). The widening of the Soret band and the red shift can be due to the presence of J aggregates of porphyrin. Besides, as shown by the N_2 -adsorption desorption analysis, nanoparticles present a typical IV isotherm and a surface area of $832\text{ m}^2/\text{g}$ (Figure 1c). From the BJH analysis 3 nm (Supp. Inf. S6) was obtained as pore diameter which confirmed the mesoporosity of the nanoparticles. These values are in agreement with the distance of 4 nm between pores deduced from small-angle X-ray diffractogram ($2\sigma = 2.3$) that showed a beginning of structuring of the pores (Supp. Inf. S7).

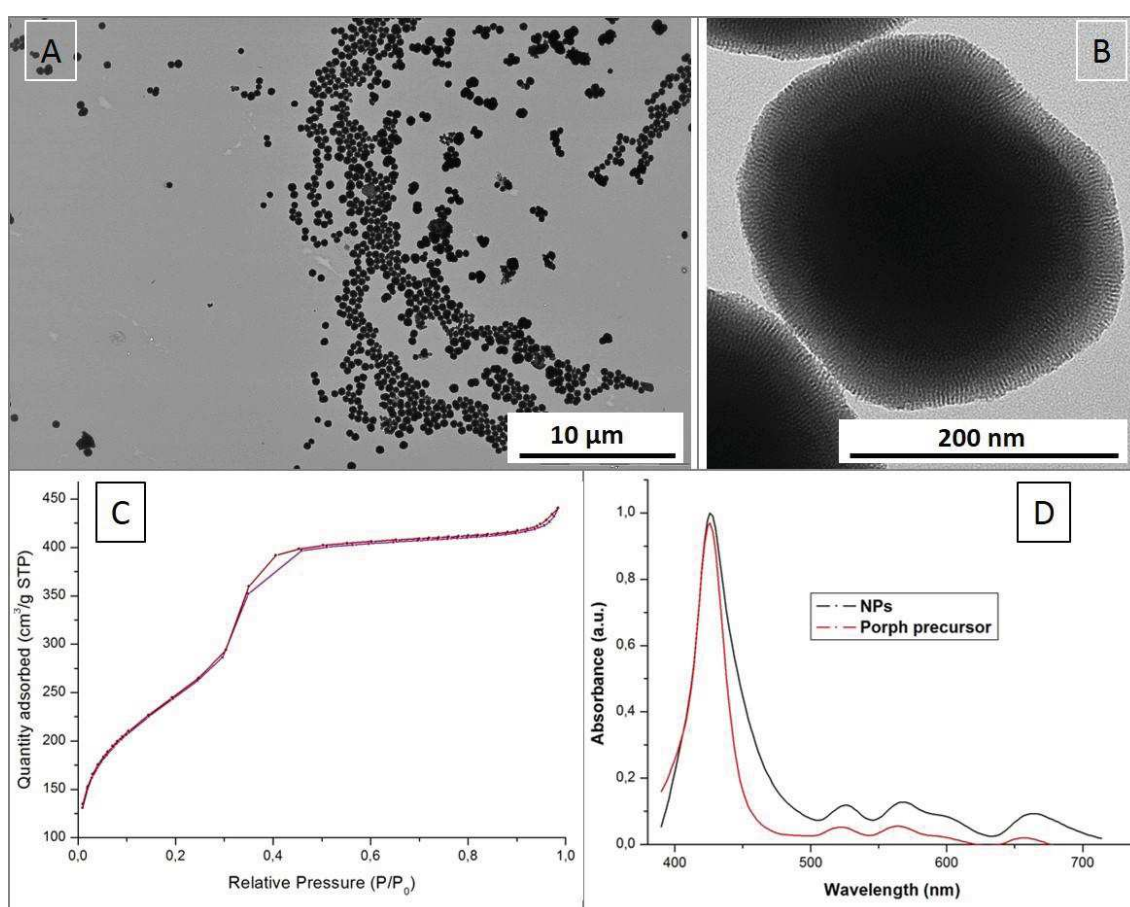


Fig. 1. a) Transmission electron microscopy image of EPOR PMOs nanoparticles (Scale bar: 10 μm). b) TEM image at scale bar 200 nm, where the porosity can be observed. c) N_2 -adsorption desorption analysis. d) UV-visible absorption spectra of the POR precursor and the obtained nanoparticles.

Moreover, gemcitabine (GEM) was loaded at neutral pH into the nanoparticles for 48 hours leading to the formation of GEM-EPOR PMOs. The loading amount of the drug was obtained by UV-Vis absorption spectra of the supernatants and corresponds to 50

wt %. The delivery of GEM without irradiation was examined. Drug delivery was experimented at pH 7 in water and no release of GEM was observed in these conditions due to the important interactions between the drug and the organosilica matrix (Supp. Inf. S11). Then the pH was changed at 5.5 and drug release was observed due to the protonation of the amino group of the gemcitabine ($pK_a = 3.6$). Then, the cargo delivery in solution from GEM-EPOR PMOs nanoparticles was tested in MCF-7 cancer cells using two-photon irradiation.

First, two-photon photodynamic therapy was applied to MCF-7 cancer cells incubated for 20 hours with an 80 $\mu\text{g/mL}$ solution of EPOR PMOs nanoparticles. The two-photon excitation was performed at 6% of laser power at 800 nm. The MTT assay was performed after 48 hours after irradiation. The non-loaded nanoparticles produced 30 % of cell killing under two-photon irradiation and were biocompatible without irradiation. Then, GEM-loaded nanoparticles were incubated in MCF-7 cancer cells. The autonomous delivery of GEM from the EPOR nanoparticles occurred before irradiation via the change of pH from the membrane to the lysosome of the cell (pH 5.5) and produced around 40 % of cell killing. In order to demonstrate a synergistic cancer therapy (drug delivery plus PDT), two-photon irradiation (800 nm) was applied. Irradiated GEM-EPOR nanoparticles caused around 60 % of cell killing, demonstrating the efficiency of organosilica nanoparticles as medical nanocarrier for cancer therapy (Figure 2).

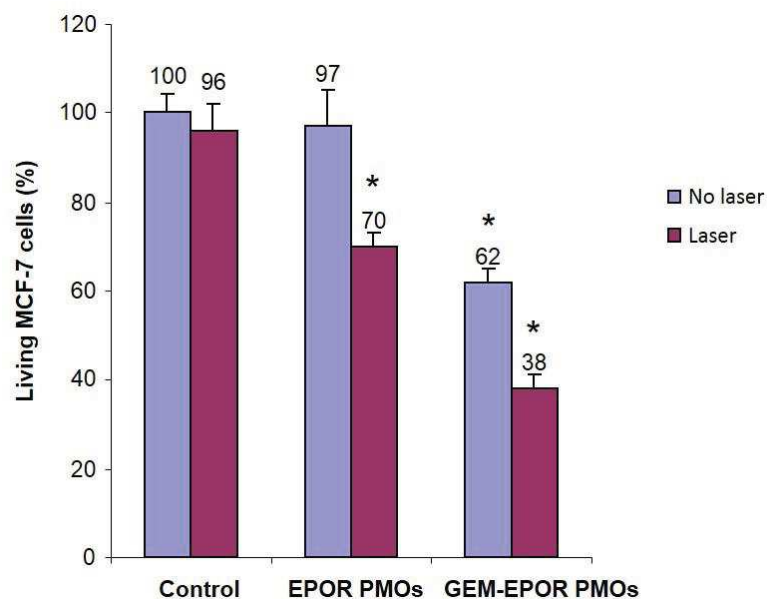


Fig. 2. *In vitro* two-photon photodynamic therapy in MCF-7 breast cancer cells of EPOR PMOs and GEM-loaded EPOR PMOs nanoparticles.

Finally, two-photon fluorescence imaging of EPOR PMOs nanoparticles in MCF-7 cancer cells (Figure 3) confirmed the cellular uptake of the nanoparticles. To assess the endocytosis *in vitro*, cancer cells were incubated during 20 hours with a solution of 80 mg/ml of nanoparticles. Then, membranes were stained with Cell Mask for 15 minutes and irradiation was performed at 750 nm.

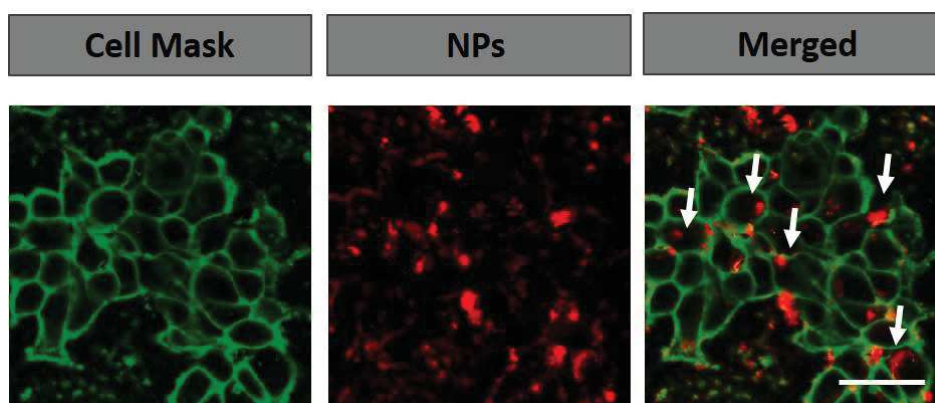


Fig. 3. *In vitro* two-photon fluorescence imaging of EPOR PMOs nanoparticles that confirmed the endocytosis of the nanoplatforms. (Scale bar: 10 μ m)

4.2.3. Conclusions

In summary, periodic mesoporous organosilica nanoparticles were designed from bis-silylated ethane and tetra silylated porphyrin as precursors. The nanoplatform was fully characterized by various techniques. As the material presented a high surface area and mesoporosity and due to its hydrophobicity, gemcitabine hydrochloride was encapsulated into the pores. The efficiency of two-photon irradiation was demonstrated in unloaded nanoparticles and in gemcitabine-loaded nanoparticles. The synergy effect between the photon irradiation and the drug delivery produced an increase of the cell death of 20 % as compared to the delivery without irradiation. The presence of the porphyrin photosensitizer that formed J aggregates into the matrix lead to perform fluorescence imaging that demonstrated the endocytosis of EPOR PMOs nanoparticles in cancer cells. The data demonstrated that EPOR PMOs are a promising nanocarrier for applications in cancer therapy.

4.2.4. Perspectives: biodegradable EPOR PMOs nanoparticles

Owing to this success with periodic mesoporous organosilica nanoparticles, biodegradable PMOs nanoparticles were designed. In order to add a biodegradable character to EPOR PMOs nanoparticles, bis (triethoxysilylpropyl) disulphide was added to the nanopatform. Biodegradable EPOR nanoparticles, were designed *via* co-condensation of the tetrasilylated porphyrin, the bis-silylated ethane and bis-silylated disulphide in 1:55:45 mol proportion. Like the material presented in this chapter, biodegradable nanoparticles (EDISPOR PMOs) were obtained at 80 °C in aqueous media with CTAB as surfactant and NaOH as catalyst.

The structure of the material was then studied via transmission electron microscopy (TEM). Images displayed aggregated porous nanoparticles (Figure 4a). A red shift of the porphyrin bands that corresponds to the J aggregation was observed by UV-Vis (Figure 4b). N₂ adsorption-desorption analysis calculated a surface area of 950 m²/g and the BHJ analysis calculated pore size of 2.2 nm.

Their efficiency in two-photon therapy was tested *in vitro* in MCF-7 cancer cells with different concentrations of nanoparticles (Figure 4c). After 20 hours of incubation with 80 µg / ml of nanoparticles, cells were irradiated at 800 nm. Nanoparticles produced 40 % of cell killing under irradiation. The endocytosis of the nanoparticles was also demonstrated *in vitro* under an irradiation at 800 nm with the same concentration of nanoparticles (Figure 4d).

Due to their high surface area and their biodegradable character, those nanoparticles could be used as drug carrier. The biodegradability, the surface stabilization and the loading of drug is still under investigation.

Chapter 4. Two-photon-actuated photodynamic therapy, imaging, drug and gene delivery *via* periodic mesoporous organosilica nanoparticles in cancer cells

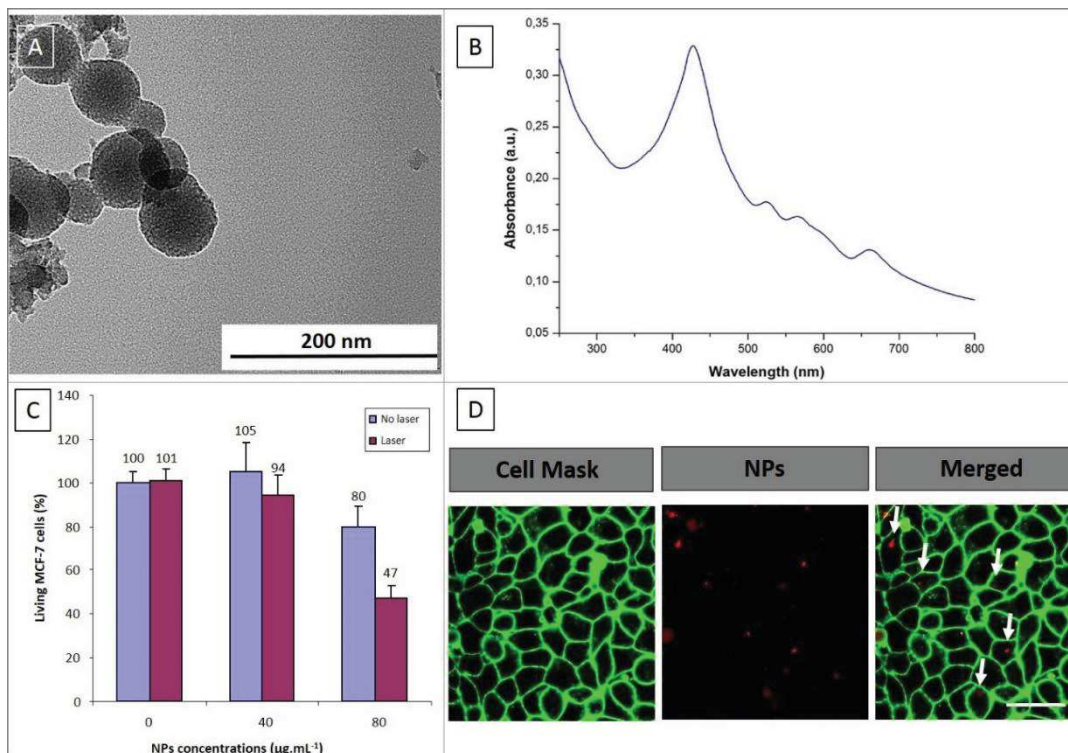


Fig. 4. a) TEM image of EDISPOR PMOs nanoparticles. (Scale bar: 200 nm). b) UV-visible absorption spectra of nanoparticles. c) Two photon PDT in MCF-7 cancer cells. d) Two photon imaging in vitro of the nanoparticles in MCF-7 cancer cells. (Scale bar: 10µm)

4.2.5. Supporting Information

Experimental section

4.2.5. S1. Materials and general procedures

^1H and ^{13}C NMR spectra were recorded on a Bruker AC 400 spectrometer. Chemical shifts (in δ units, ppm) are referenced to TMS using DMSO- d_6 ($\delta = 2.50$ ppm) and DMSO- d_6 ($\delta = 40.6$ ppm) as the internal standards, respectively, for ^1H and ^{13}C NMR spectra. IR spectra were recorded on a Perkin-Elmer 100 FT spectrophotometer. Absorption spectra were recorded on a Hewlett-Packard 8453 spectrophotometer. Dynamic Light scattering analyses were performed using a Cordouan Technologies DL 135 Particle size analyzer instrument. All solid state NMR experiments were performed on a Varian VNMRS 600 MHz (14.1 T) NMR spectrometer. A 3.2 mm Varian T3 HXY magic angle spinning (MAS) probe was used for ^1H and ^{13}C experiments. The operating frequencies for ^1H and ^{13}C were 599.81 and 150.84 MHz, respectively. One-dimensional ^1H - ^{13}C CPMAS NMR spectra were recorded spinning at 18 kHz, using a 90° ^1H excitation pulse of 2.5 μs , followed by a contact time of 3.0–5.0 ms (ramped pulse). Spinal-64 ^1H decoupling²⁹ (100 kHz RF) was applied during acquisition. A recycle delay of 2.0 s was used, and the total number of transients acquired was 3200 (for the porphyrin alone) and 43700 (for the PMO). ^{13}C chemical shifts were referenced externally to adamantane (used as a secondary reference), the high frequency peak being set to 38.5 ppm. BET analyses were performed using a TRISTAR 3000 gas adsorption analyzer instrument. TEM analyses were performed on a JEOL 1200 EXII instrument.

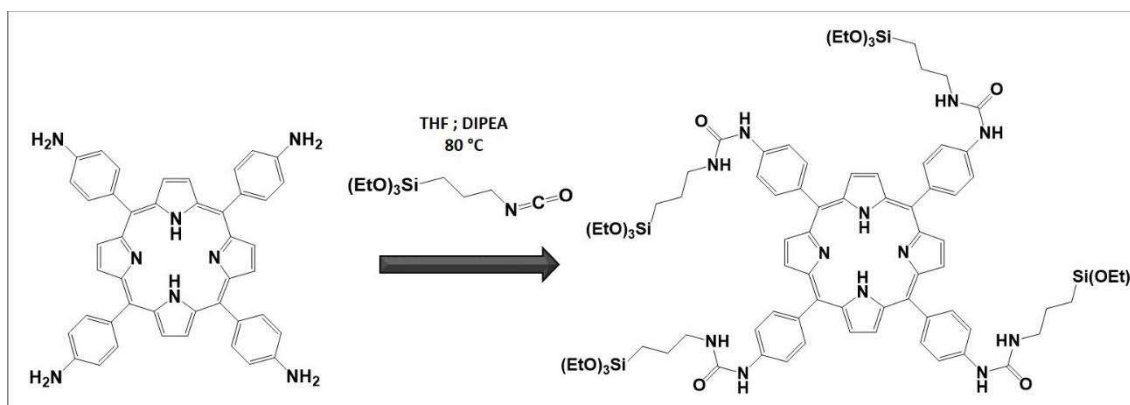
Cetyltrimethylammonium bromide (CTAB), sodium hydroxide, bis (3-triethoxysilylpropyl) ethane and isocyanatepropyltriethoxysilane (IPTS) were purchased from Sigma-Aldrich.

Nanomaterial synthesis and characterization

4.2.5. S2. Synthesis of silylated porphyrin PS

A mixture of the tetraamine porphyrin (100 mg, 1.4×10^{-2} mmol), DIPEA (5.61 mg), isocyanatepropyltriethoxysilane (181.3 mg) and anhydrous THF (5 mL) was placed in

a Schlenk under argon. Then, reaction was conducted at 80 °C and stirred at 750 rpm during 36 hours. After evaporation of the solvent, the POR precursor was washed with AcOEt and recrystallized in hexane. This process was repeated 4 times. Finally, the precursor was dried 24 hours under vacuum. The yield of the reaction was 83 % ^1H NMR (300 MHz, DMSO- d_6): δ (ppm) 8.90 (s, 8H, $\text{H}_{\beta\text{pyrrole}}$), 8.87 (s, 4H, CO-NH-CH_2), 8.06 (d, $^3J = 8.3$ Hz, 8H, $\text{H}_{3,5}$ aryl), 7.83 (d, $^3J = 8.2$ Hz, 8H, $\text{H}_{2,6}$ aryl), 6.40 (t, 4H, $^3J = 5.2$ Hz, CO-NH-Ph), 3.80 (q, $^3J = 7.0$ Hz, 24H, $\text{O-CH}_2\text{-CH}_3$), 1.19 (t, $^3J = 7.0$ Hz, 36H, $\text{O-CH}_2\text{-CH}_3$), 0.60 (t, $^3J = 7.4$ Hz, 8H, $\text{CH}_2\text{-Si}$). ^{13}C NMR (400 MHz, DMSO- d_6): δ 155.9, 141.1, 136.1, 135.3, 134.3, 120.4, 116.5, 113.1, 58.3, 42.4, 23.9, 18.8, 7.9. ^{29}Si NMR (400 MHz, CD_2Cl_2): δ -45.1. FTIR (neat KBr) (cm^{-1}): 2939, 1644, 1589, 1532, 1429, 1345, 1261, 1242, 1139, 1035, 810, 670. UV-Vis (EtOH) λ_{max} , nm: 425, 520, 563, 603, 655. MALDI-TOF: calcd for Formula $\text{C}_{84}\text{H}_{118}\text{N}_{12}\text{O}_{16}\text{Si}_4$: 1662.79, found 1662.8.



Scheme S2. Design of the POR precursor.

4.2.5. S3. Synthesis of EPOR PMOs nanoparticles

250 mg of cetyltrimethylammonium bromide and 875 μl of NaOH (2M) are introduced into a 250 mL three-neck round bottom flask with 120 mL of ultrapure water. The mixture is stirred at 750 rev / min for 50 minutes at 80°C. Porphyrin precursor (23,6 mg in 1 mL of absolute ethanol) is introduced simultaneously by reaction with bis (triethoxysilyl) ethane (10/90 by weight). The reaction is held for 1 hour 45 minutes at 80 °C. Then the obtained nanoparticles are centrifuged. The surfactant is extracted with an ethanolic solution of ammonium nitrate (6g / L). The nanoparticles are suspended in this solution (50 mL) for 30 minutes with ultrasound at 50 ° C and centrifuged at 20000 turn/ min for 20 min. The protocol is repeated three times. Three washings with ethanol

are then made. The nanoparticles are dried under vacuum. 139 mg of nanoparticles were obtained.

4.2.5. S4. GEM loading of nanoparticles

1.6 mg of EPOR PMOs nanoparticles are suspended with 1.9 mg gemcitabine in 2 mL of deionized water and stirred at 25 °C for 24 h. Then the nanoparticles are centrifuged at 10000 rpm during 5 min. Nanoparticles were washed 4 times with water and dried for few hours under vacuum. The loading capacities were deduced by the titration of gemcitabine in the supernatant fractions.

GEM wt (%)	50
-------------------	-----------

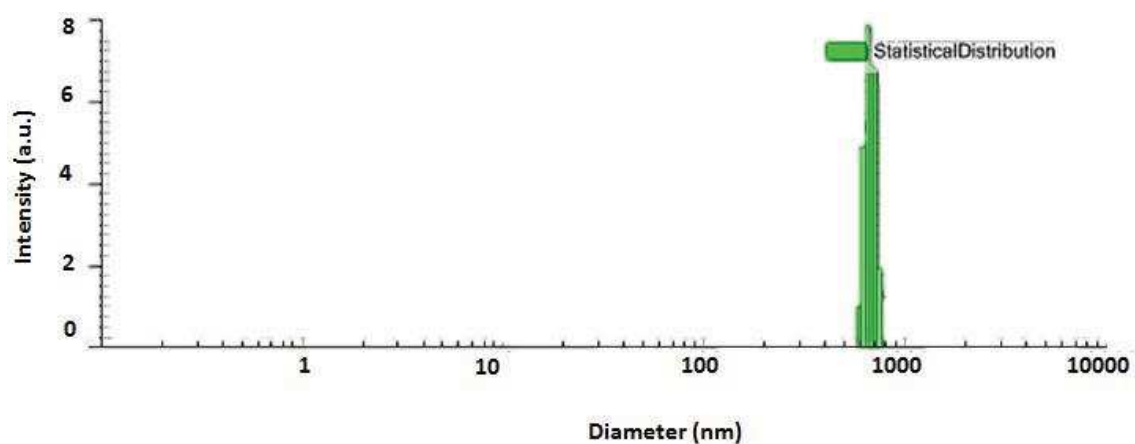


Figure S5. Dynamic light scattering and size distribution of EPOR NPs.

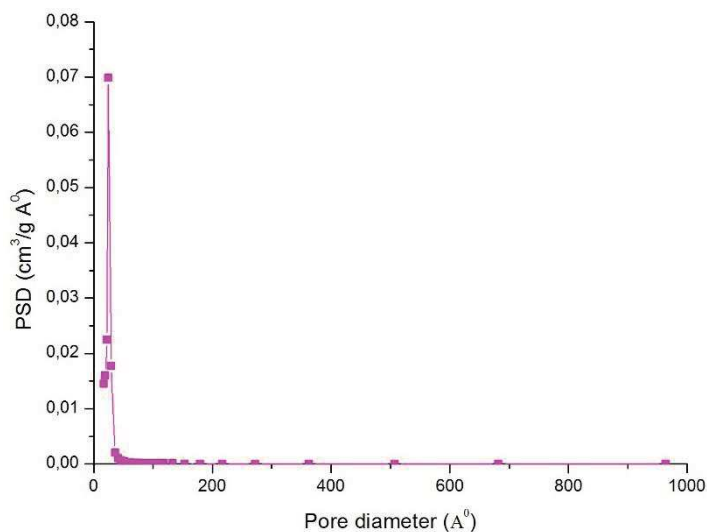


Figure S6. Pore size distribution of EPOR NPs.

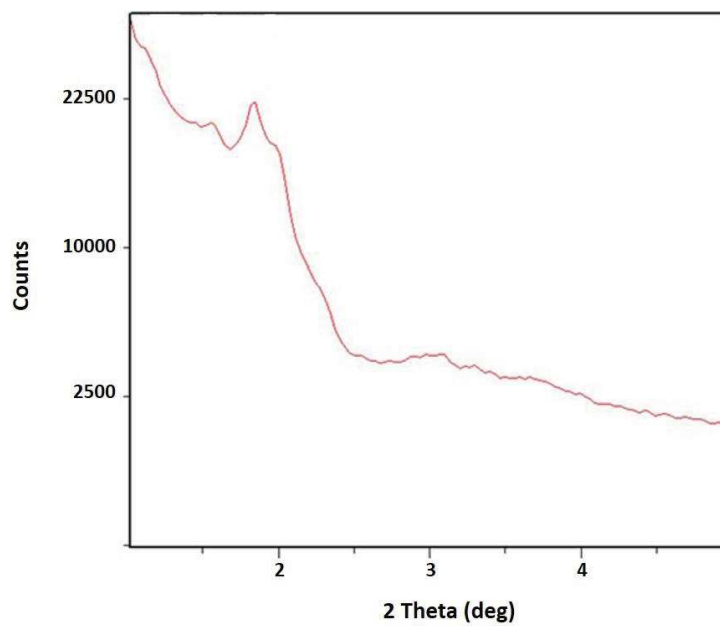


Figure S7. Small angle X-ray diffraction pattern of EPOR NPs (Cu k_{α}).

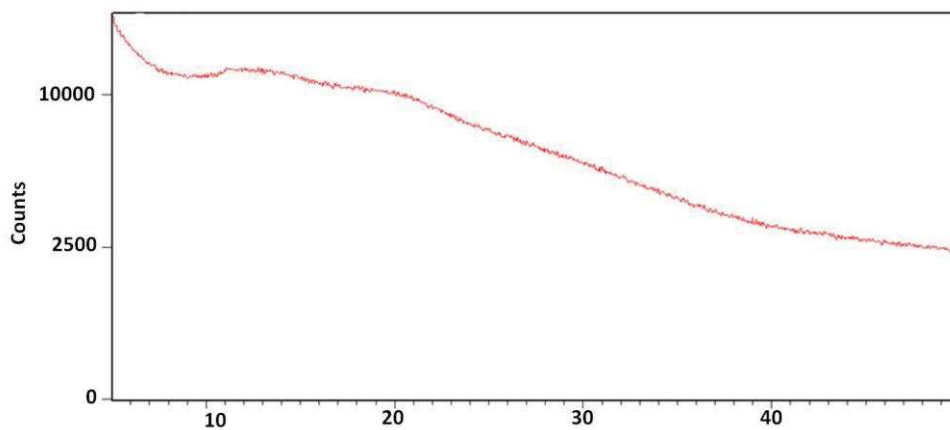


Figure S8. Wide angle X-ray diffraction pattern of EPOR NPs (Cu k_{α}).

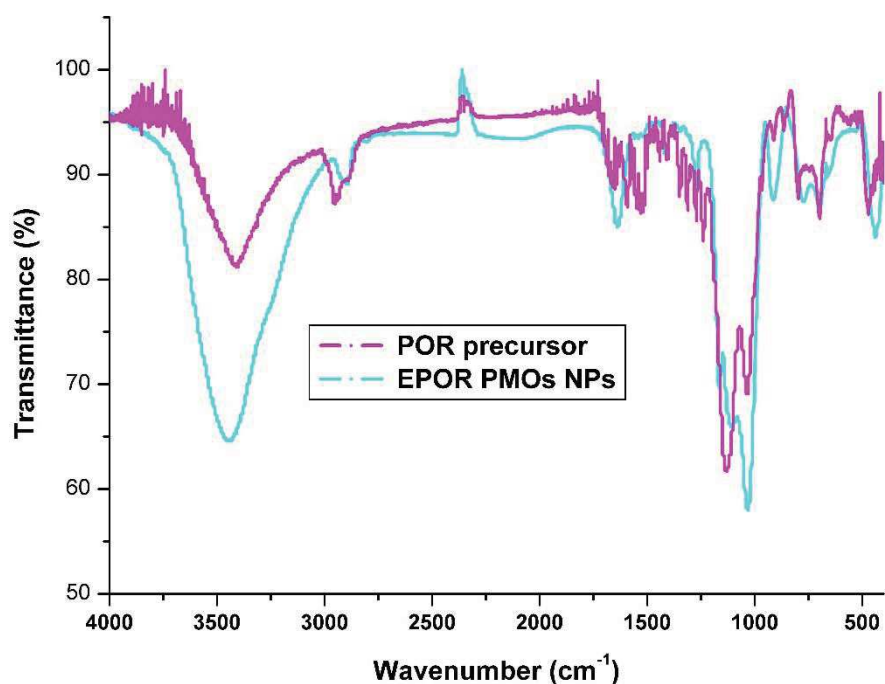


Figure S9. FTIR spectra of the POR precursor, and EPOR NPs confirming the presence of the ETH and POR moieties in the nanomaterials framework.

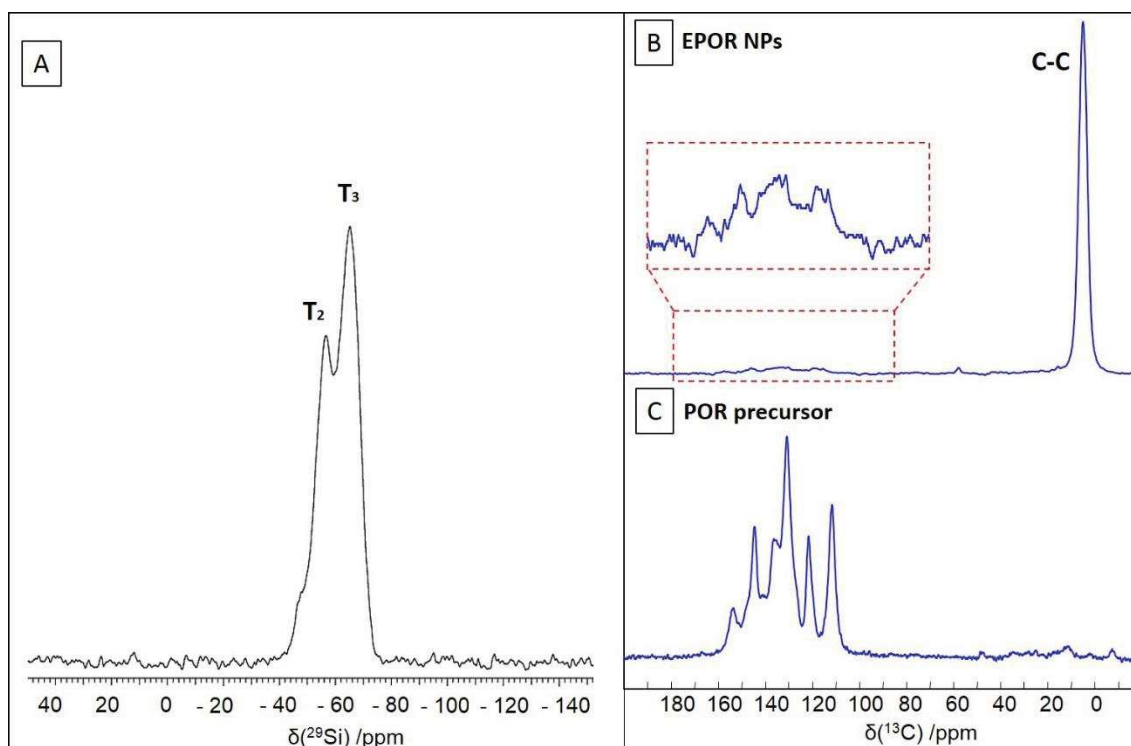
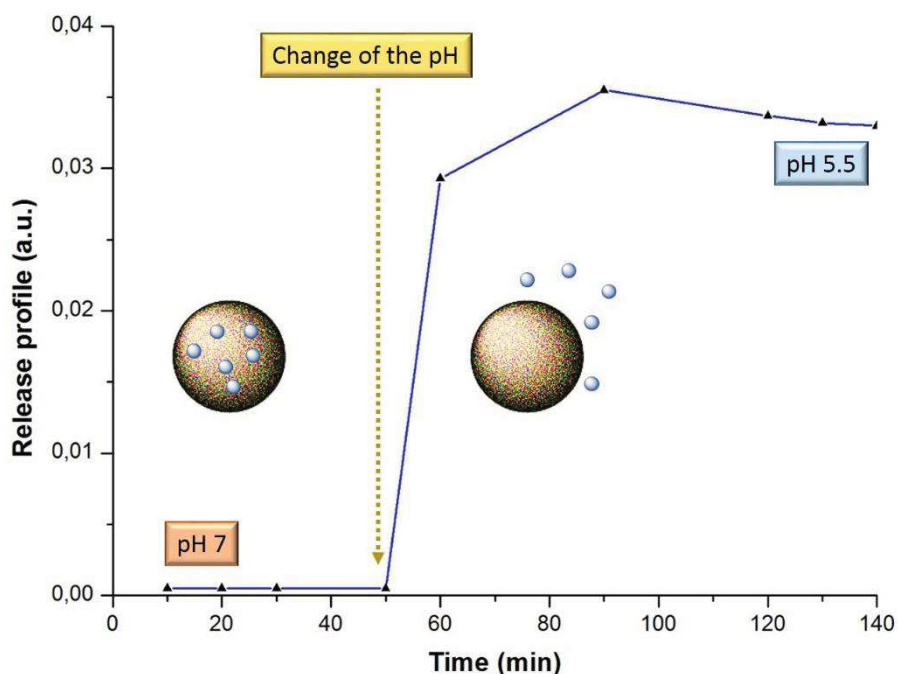


Figure S10. ²⁹Si and ¹³C Solid state CPMAS NMR spectra of EPOR NPs (A and B respectively) and POR precursor (C).

4.2.5. S11. Drug release control in simulated biological media

Release experiment of GEM-loaded EPORNPs was performed in ultrapure water upon addition, after 60 min, of HCl (0.2 M) to obtain a lysosomal pH.



In vitro studies

4.2.5. S12. Two-photon fluorescence imaging

The day prior to the experiment, MCF-7 cells were seeded onto bottom glass dishes (World Precision Instrument, Stevenage, UK) at a density of 10^6 cells.cm⁻². Adherent cells were then washed once and incubated in 1 ml culture medium containing NPs at a concentration of 80 μ g.mL⁻¹ for 20 h. Fifteen min before the end of incubation, cells were loaded with Cell Mask TM Orange Plasma Membrane Stains (Invitrogen, Cergy Pontoise, France) for membrane staining at a final concentration of 5 μ g.mL⁻¹. Before visualization, cells were washed gently with phenol red-free DMEM. Cells were then scanned with LSM 780 LIVE (Carl Zeiss, Le Pecq, France), at 800 nm with a slice depth (Z stack) of 0.62 μ m.

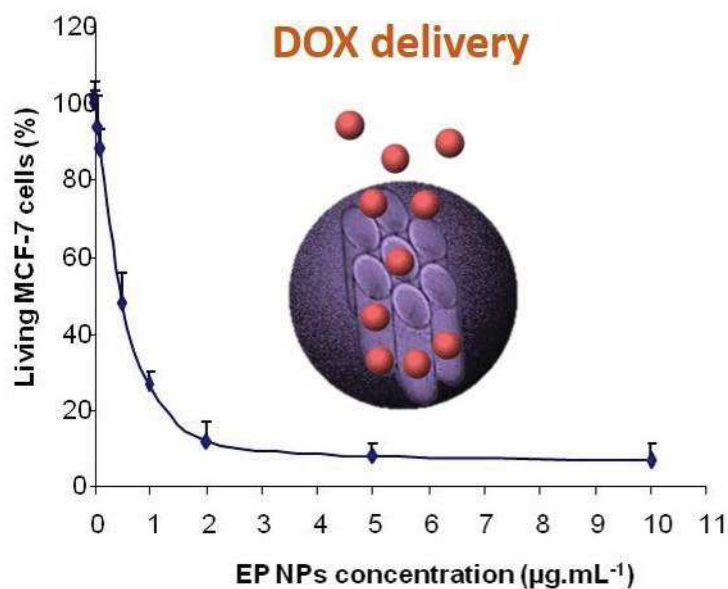
4.2.5. S13. Drug delivery experiments

MCF-7 cells were seeded into 96-well plates at 2000 cells per well in 200 μ L culture medium and allowed to grow for 24 h. Increasing concentrations of EPOR NPs (from 0.01 to 10 μ g.mL⁻¹) dispersed in sterile water, were incubated in culture medium of MCF-7 cells during 72 h and a MTT assay was performed to evaluate the toxicity.

Chapter 4. Two-photon-actuated photodynamic therapy, imaging, drug and gene delivery *via* periodic mesoporous organosilica nanoparticles in cancer cells

Briefly, cells were incubated for 4 h with 0.5 mg.mL^{-1} of MTT (3-(4,5-dimethylthiazol-2-yl)-2,5-diphenyltetrazolium bromide; Promega) in media. The MTT/media solution was then removed and the precipitated crystals were dissolved in EtOH/DMSO (1:1).

4.3. Porphyrin-functionalized mesoporous organosilica nanoparticles for two-photon imaging of cancer cells and drug delivery



Abstract

The synthesis of a zinc porphyrin derivative possessing eight triethoxysilyl groups was performed through a CuAAC-click reaction. This porphyrin was covalently entrapped in ethenylene-bridged mesoporous organosilica nanoparticles which efficiently allowed performing doxorubicin delivery and two-photon imaging of breast cancer cells.

Interdisciplinary collaboration

Nanomaterial synthesis, physic-chemical characterizations and applications in solution: C. Mauriello Jimenez, J. Croissant, X. Cattoën, M. Wong Chi Man, L. Raehm, J-O. Durand.

Synthesis of porphyrin photosensitizer: J. Vergnaud, V. Chaleix, V. Sol

Cell studies: M. Maynadier, M. Gary-Bobo, M. Garcia.

➤ *J. Mater. Chem. B*, 2015, 3, 3681-3684

4.3.1. Introduction

Mesoporous organosilica nanoparticles have very recently attracted much attention for applications in nanomedicine.^{15, 16, 30-34} Such nanoparticles are based on a silsesquioxane framework and an organic fragment which constitutes the structure of the material and which tailors their properties.^{4, 35, 36} These nanoparticles are very promising for cancer theranostics due to their low hemolytic properties,³⁶ high biocompatibility,³³ and high drug uptake and release capacities. Hollow mesoporous organosilica nanoparticles were prepared for pH-triggered drug and gene delivery, high intensity focused ultrasounds imaging and drug delivery.³¹ Glutathione-triggered biodegradation of mesoporous organosilica nanoparticles was also reported.^{16, 34}

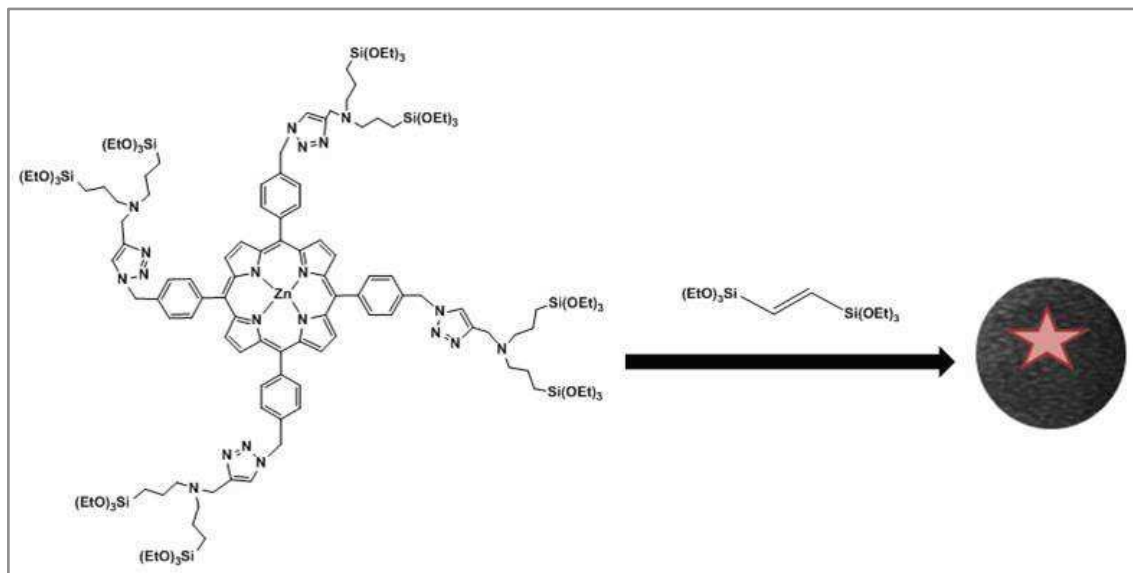
Two-photon excitation of nanoparticles has been demonstrated to be a promising strategy for *in vitro* and *in vivo* biomedical imaging applications.³⁷⁻⁴⁰ Indeed, two-photon excitation provides a tri-dimensional spatial resolution with a typical resolution of a micron, while the combination with near-infrared excitation enhances the tissue penetration with a safer treatment.^{16, 20, 37-39, 41} We have recently described periodic mesoporous organosilica nanoparticles for two photon-imaging, therapy and drug delivery.⁴² These nanoparticles incorporated a photosensitizer designed for two-photon excitation and allowed two-photon fluorescence imaging of breast cancer cells at 760 nm.

As an alternative to a two-photon photosensitizer, we show here that a porphyrin derivative possessing eight trialkoxysilyl groups could be successfully covalently incorporated within ethenylene-bridged mesoporous organosilica nanoparticles (EP NPs) and enabled two-photon fluorescence imaging of cancer cells at low laser power. These nanoparticles, when loaded with doxorubicin, induced very efficiently cancer cell killing at low concentration of nanoparticles.

4.3.2. Results and discussion

To synthesize mesoporous organosilica nanoparticles containing the zinc-porphyrin moiety, a new sol-gel precursor featuring 8 triethoxysilyl groups was designed. It was obtained in high yield from Zn (II)-5,10,15,20-Tetrakis(4-(azidomethyl)-phenyl)porphyrin⁴³ through the CuAAC reaction⁴⁴ with *N,N*-bis(3-triethoxysilylpropyl)prop-2-yn-1-amine in mild conditions, under microwave irradiation (Scheme S4). The preparation of the EP NPs (Scheme 1) was carried out in water at 80

°C, using cetyltrimethylammonium bromide as the structure-directing agent under basic catalysis. Bis (triethoxysilyl) ethene (E) and porphyrin **1** were co-condensed under these conditions. After 2 hours, the nanoparticles were centrifuged and the template extracted with ammonium nitrate.



Scheme 1. Synthesis of EP NPs from bis(triethoxysilyl)ethene and porphyrin **1**.

The morphology and structure of the EP material were then characterized via various techniques. Transmission electron micrographs (TEM) revealed spherical nanoparticle with rough surfaces and diameter ranging from 200 to 600 nm (Figure 1A). Dynamic light scattering (DLS) confirmed the nano-size of the material with an average hydrodynamic diameter of 460 nm (Figure 1B). Nitrogen adsorption-desorption analysis showed that the NPs are mesoporous, with a type IV isotherm. A very high specific surface area of $1400 \text{ m}^2 \cdot \text{g}^{-1}$, with an average pore diameter of 2.5 nm were deduced using the Brunauer-Emmett-Teller (BET) and Barrett, Joyner et Halenda (BJH) theories (Figure S7). A wormlike porosity was observed by TEM at higher magnification (see image on the right in Figure 1A), consistent with the small angle X-ray diffraction pattern which showed a broad peak at 2.2 degrees (Figure S8).

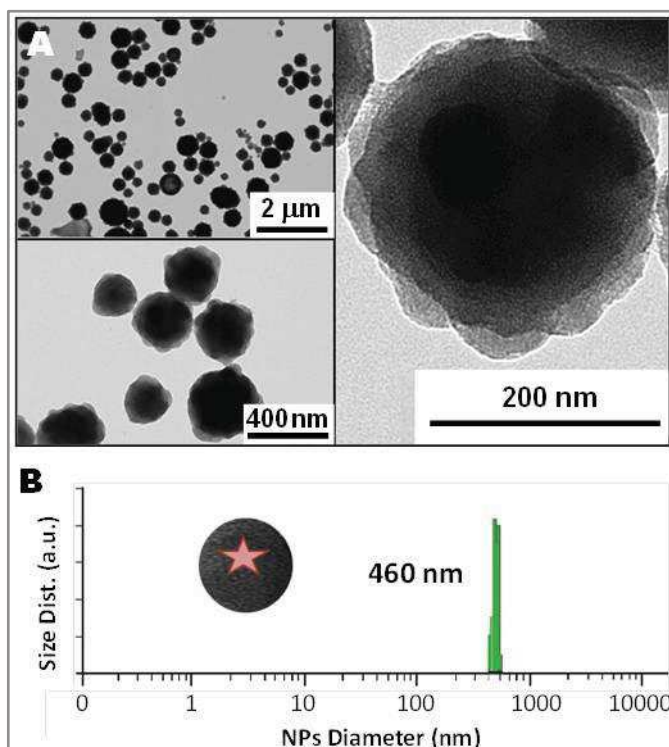


Fig. 1. TEM images (A) and DLS size distribution (B) of the EP NPs.

The composition and photophysical properties of the two-photon-sensitive nanomaterial were then investigated. First, the successful incorporation of the porphyrin fragments was clearly seen from the UV-Vis spectrum of EP NPs with the band at 430 nm (see Figure 2). Elemental analysis of nitrogen was used to determine the porphyrin content in the NPs, which was 0.04 mmol/g (Table S13). The wide angle X-ray diffraction pattern only showed a broad peak at 20°, corresponding to non-regular repetitions within the siloxane framework (Figure S9), without any sharp peak that would evidence regular repetition of organics within the structure. The presence of only R-SiO₃ environments was checked by ²⁹Si CP-MAS NMR (Figure S11). Fourier transform infrared (FTIR) and ¹³C nuclear magnetic resonance (NMR) spectroscopies (see Figures S10 and S11) confirmed the presence of the ethylene and the porphyrin bridges. It is noteworthy that the zeta potential was positive (Figure S12), due to the protonation of the tertiary amines at pH 7.4 and 5.5. Additionally, as shown by the UV-Vis spectrum (Figure 2), the porphyrin moiety was clearly aggregated inside the nanoparticles. Indeed, the Soret band was enlarged and Q bands shifted to the red which suggests the presence of *J* aggregates.⁴⁵ Porphyrins usually have a low two-photon absorption cross-section but *J* aggregation of porphyrin derivatives is known to increase the two-photon absorption cross-section.⁴⁶

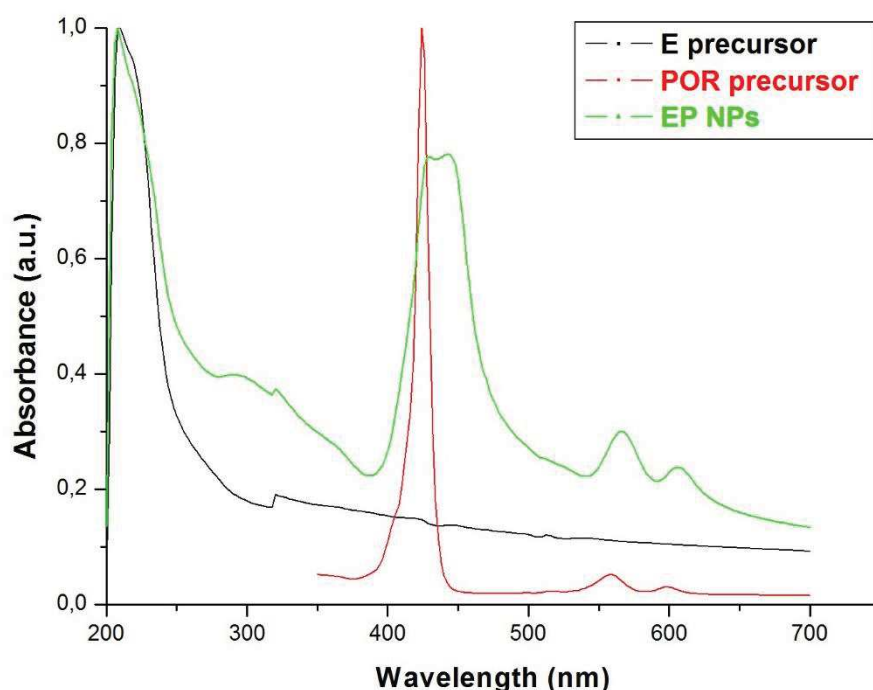


Fig. 2. UV-Vis spectra of POR 1, bis(triethoxysilyl)ethane (E) and EP NPs in EtOH.

Consequently, the two-photon imaging capacity of the EP NPs was assessed in cancer cells. The cytotoxicity of the nanoparticles on MCF-7 breast cancer cells was measured with the MTT assay, and the percentage of living cells was high, up to a concentration of $50 \mu\text{g.mL}^{-1}$ (see Figure S15). Then, the nanomaterial was incubated for 20 h in MCF-7 breast cancer cells. The cellular uptake was determined via two-photon fluorescence imaging (TPEF). The laser excitation was performed with a Carl Zeiss two-photon confocal microscope at low power (2.8% of the input power) at different wavelengths. The cell membranes were stained with Cell Mask 15 min before the imaging experiments. EP NPs were successfully endocytosed by cancer cells as shown by TPEF at 750 and 800 nm (see Figure 3A and B respectively). Thus, these findings demonstrate the suitability of porphyrin-functionalized mesoporous organosilica nanoparticles for two-photon imaging.

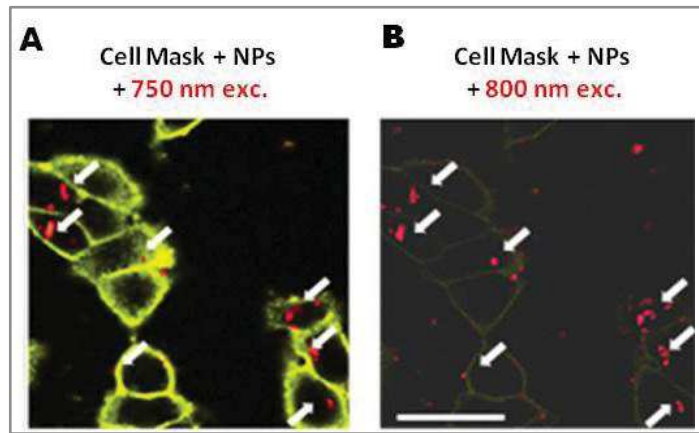


Fig. 3. Two-photon fluorescence imaging of MCF-7 breast cancer cells. Cell membranes were stained with Cell Mask TM Orange Plasma Membrane, EP NPs were incubated and irradiated at 750 (A) and 800 nm (B). Arrows indicate NPs in cells. Scale bar 10 μm .

Owing to their high porosity, the nanoparticles were then applied as drug nano-carriers. EP NPs were loaded with doxorubicin at pH 5.5¹⁶ and the drug loading was 20 wt %. EP NPs were incubated with MCF-7 for 72 h and found to be remarkably efficient to cause cell death as only 25% of cancer cells survived at a concentration of EP NPs of only 1 $\mu\text{g.mL}^{-1}$ (see Figure 4).

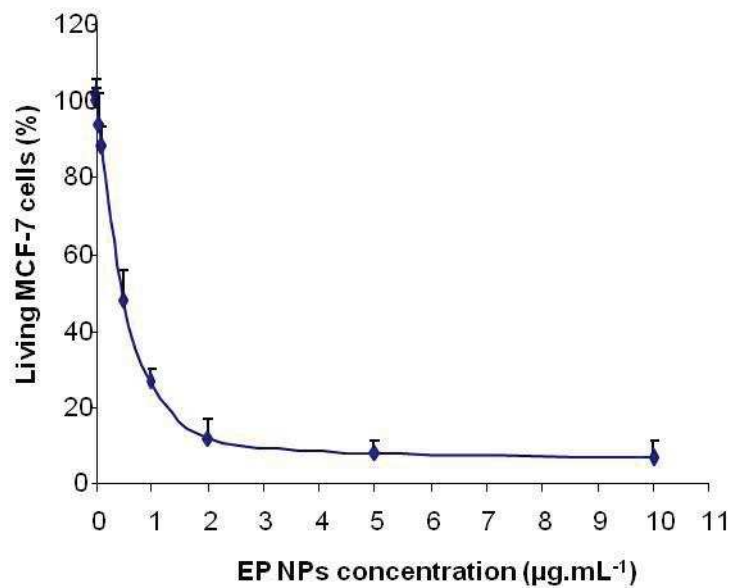


Fig. 4. Doxorubicin delivery in MCF-7 cancer cells via EP NPs.

4.3.3. Conclusions

We have prepared an octa-trialkoxysilane-substituted Zn porphyrin which was successfully covalently incorporated in ethenylene-bridged mesoporous organosilica nanoparticles. The nanoscaled particles displayed a very high specific surface area, enabling drug loading and release. Moreover, the aggregation of the porphyrin derivative within the mesopores enabled potent two-photon fluorescence imaging of breast cancer cells. Furthermore, the doxorubicin-loaded organosilica nanoparticles were very efficient to induce cancer cell killing showing promising potential for theranostic applications.

4.3.4. Supporting Information

Experimental section

4.3.4. S1. Materials and general procedures

Click reaction was performed using a microwave CEM Discover-Explorer. ^1H and ^{13}C NMR spectra were recorded on a Bruker AC 400 spectrometer. Chemical shifts (in δ units, ppm) are referenced to TMS using CH_2Cl_2 ($\delta=5.32$ ppm) or CDCl_3 ($\delta=7.26$ ppm) and CD_2Cl_2 ($\delta=53.6$ ppm) as the internal standards, respectively, for ^1H and ^{13}C NMR spectra. IR spectra were recorded on a Perkin-Elmer 100 FT spectrophotometer. Absorption spectra were recorded on a Hewlett-Packard 8453 spectrophotometer. Dynamic Light scattering analyses were performed using a Cordouan Technologies DL 135 Particle size analyzer instrument. ^{29}Si and ^{13}C solid state NMR sequences were recorded with a VARIAN VNMRS300, using Q8MH8 and adamantane references respectively. BET analyses were performed using a TRISTAR 3000 gas adsorption analyzer instrument. TEM analyses were performed on a JEOL 1200 EXII instrument.

Cetyltrimethylammonium bromide (CTAB), sodium hydroxide, pyrrole, 4-(bromomethyl)benzaldehyde, sodium azide and zinc diacetate were purchased from Sigma-Aldrich. Anhydrous ethanol and propionic acid were purchased from Fischer Chemicals. Pyrrole was distilled over CaH_2 under reduced pressure immediately before use. Methylene chloride and chloroform were distilled over P_2O_5 then CaH_2 . Analytical thin-layer chromatography (TLC) was performed on silica gel (Merck, 60F₂₅₄). Merck precoated plates (silica gel 60, 2 mm) were used for preparative thin-layer chromatography. Column chromatography was carried out with silica gel (60 ACC, 15–40 μm , Merck) Bis (3-triethoxysilylpropyl) ethylene was purchased from ABCR. *N,N*-bis (3-triethoxysilyl) propyl prop-2-yn-1-amine was obtained from a reported procedure by K.Bürglovà et al. (Chem. Eur. J. **2014**, 20, 1-13).

Synthesis of porphyrin precursor

4.3.4. S2. Synthesis of 4-(azidomethyl) benzaldehyde

In a typical procedure,¹ 4-(bromomethyl) benzaldehyde was obtained as white solid crystals in 80% yield. Azidation step was performed as following: 4-(bromomethyl) benzaldehyde (1.6 g, 8 mmol) was dissolved in acetone (15 mL), and then poured into a saturated solution of sodium azide in water (5 equivalents). The reaction was activated under microwave irradiation (300 W, 80 °C, 1 min) until reaction completion checked by TLC. The crude solution was then concentrated under vacuum, and then solubilized in 30 mL of CHCl₃, washed with 10 mL of water to remove salts (three times). The organic layer was dried over MgSO₄, then evaporated under vacuum to give after purification on chromatoflash (CHCl₃ - Petroleum ether) 4-(azidomethyl) benzaldehyde as a pale yellow oil in 95% yield. Spectral data are in accordance with literature.²

4.3.4. S3. Synthesis of Zn(II)-5,10,15,20-Tetrakis(4-(azidomethyl)phenyl)porphyrin

4-(azidomethyl) benzaldehyde (1.1 eq., 377 mg, 2.3 mmol) was dissolved in refluxing propionic acid (75 mL). Then, freshly distilled pyrrole (1 eq., 2.0 mmol, 143 μ L) diluted in 15 mL of propionic acid was dropwise over a period of 30 minutes in a light protected two-neck flask. After removing of solvent, the crude product was purified by chromatography on silica gel (CH₂Cl₂/ Petroleum ether: 7/3) to give 180 mg of tetrakis (4-(azidomethyl) phenyl) porphyrin as a dark purple solid in 37 % yield. Spectral data are in accordance with literature.³ Tetrakis (4-(azidomethyl) phenyl) porphyrin (180 mg, 0.21 mmol) was solubilized in refluxing THF and Zinc diacetate (5 eq., 1.0 mmol, 200 mg) was added. After 2 h of reaction, THF was removed under vacuum. The crude product was solubilized in chloroform and filtered on silica gel to give Zn(II)-5,10,15,20-Tetrakis(4-(azidomethyl)phenyl)porphyrin as a pale purple solid in quantitative yield. ¹H NMR (400 MHz, CDCl₃) δ (ppm): 8.91 (s, 8H, H β _{pyrrole}); 8.22 (d, 8H, ³J = 7.8 Hz, H_{3,5} aryl) ; 7.68 (d, 8H, ³J = 7.8 Hz, H_{2,6} aryl) ; 4.69 (s, 8H, -CH₂-N₃). FITR (neat KBr) (cm⁻¹): 2956 (CH aryl), 2850 (CH alkyl), 2098 (N₃). UV-Vis (CHCl₃): λ_{max} nm ($\epsilon \times 10^{-3}$ L.mol⁻¹.cm⁻¹) 425 (118.5), 555 (6.5), 595 (1.6).

¹ Lin, W.; Peng, D.; Wang, B.; Long, L.; Guo, C.; Yuan, J. *Eur. J. Org. Chem.* **2008**, 5, 793-796.

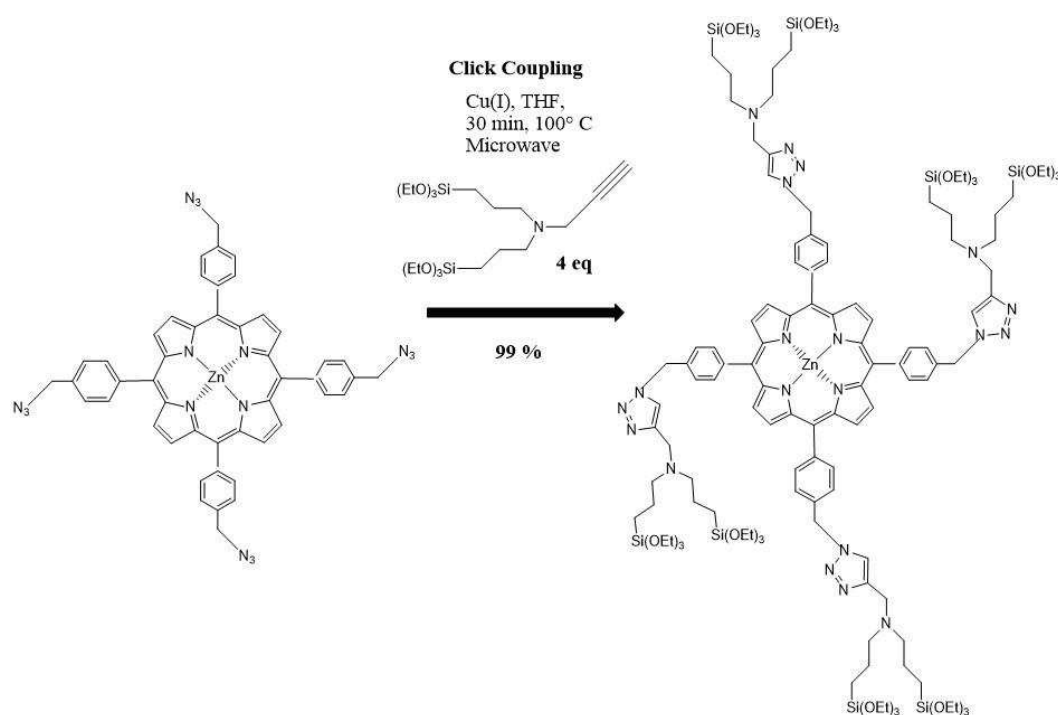
² Barbe, J.-M.; Canard, G.; Brande's, S.; Guillard, R. *Eur. J. Org. Chem.* **2005**, 21, 4601-4611.

³ Eggenpiller, A.; Michelin, C.; Desbois, N. Richard, P.; Barbe, J.-M.; Denat, F.; Licon, C.; Gaidon, C.; Sayeh, A.; Choquet, P.; Gros, C. P. *Eur. J. Org. Chem.* **2013**, 29, 6629-6643.

Nanomaterial synthesis and characterization

4.3.4. S4. Synthesis of silylated porphyrin PS

A mixture of the tetraazido porphyrin derivative (20 mg, 2.2×10^{-2} mmol), bromotris (triphenylphosphine)copper(I) ($[\text{CuBr}(\text{PPh}_3)_3]$), 4 mg, 4×10^{-3} mmol), and anhydrous THF (3 mL) was placed in a 10 mL microwave sealable reactor, and *N,N*-bis(3-triethoxysilyl)propyl)prop-2-yn-1-amine (41.4 mg, 8.92×10^{-2} mmol) was added. Then, the tube was flushed with argon and the microwave process was conducted for 30 min at 100 °C (maximum power 200 W). After evaporation of the solvent, the POR precursor was quantitatively obtained as a purple solid (59.8 mg, 2.2×10^{-1} mmol). The yield of the reaction was 100 %. ^1H NMR (300 MHz, CD_2Cl_2): δ (ppm) 8.79 (s, 8H, $\text{H}_{\beta\text{pyrrole}}$), 8.14(d, $^3J = 7.8$ Hz, 8H, $\text{H}_{3,5}$ aryl), 7.39 (d, $^3J = 7.6$ Hz, 8H, $\text{H}_{2,6}$ aryl), 6.96 (s, 4H, triazole), 5.32 (s, 8H, aryl- CH_2 -triazole), 3.78 (q, $^3J = 6.4$ Hz, 48H, O- CH_2 - CH_3), 3.36 (s, 8H, N- CH_2 -triazole), 2.43 (t, 16H, $^3J = 6$ Hz, $(\text{CH}_2-\text{CH}_2-\text{CH}_2)_2\text{N}-\text{CH}_2$ -triazole), 1.45 (m, 16H, $\text{CH}_2-\text{CH}_2-\text{CH}_2-\text{Si}$), 1.18 (t, $^3J = 7.0$ Hz, 72H, O- CH_2-CH_3), 0.59 (t, $^3J = 7.4$ Hz, 16H, CH_2-Si). ^{13}C NMR (400 MHz, CD_2Cl_2): δ 149.9, 135.8, 131.7, 128.5, 128.3, 125.4, 79.2, 71.9, 67.8, 58.1, 56.4, 41.6, 34.1, 29.6, 25.5, 20.4, 7.7. ^{29}Si NMR (400 MHz, CD_2Cl_2): δ -45.1. FTIR (neat KBr) (cm^{-1}) 3116, 3032, 2977, 2932, 2882, 1596, 1563, 1502, 1435, 1391, 1346, 1296, 1268, 1240, 1174, 1107, 1068, 996, 945, 840, 789, 712, 684, 533, 422. UV-Vis (EtOH) λ_{max} , nm: 424, 559, 598.



Scheme S4. Design of the POR 1 via click CuAAC coupling.

4.3.4. S5. Synthesis of EP nanoparticles

A mixture of CTAB (125 mg), distilled water (60 mL), and sodium hydroxide (437 μ L, 2 M) was stirred at 80 °C for 50 minutes at 750 rpm in a 250 mL three -neck round bottom flask. Then, 1,2 bis(triethoxysilyl)ethylene (350 μ L, 0.92 mmol) was added to the aforementioned solution along with the two-photon photosensitizer (33 mg, 0.012 mmol, in 1 mL of absolute ethanol), and the condensation process was conducted for 2 h. Afterwards, the solution was cooled to room temperature while stirring; fractions were gathered in propylene tubes and collected by centrifugation during 20 minutes at 30 Krpm. The sample was then washed three times with a solution of NH_4NO_3 in EtOH (6 g/ L), water, and ethanol. Each washing was followed by centrifugation collection of the sample in the same manner. The as-prepared material was dried under vacuum for few hours. 112 mg of product were obtained.

4.3.4. S6. DOX loading of nanoparticles

A mixture of NPs (10 mg), DOX (3.2 mg), and deionized water (1 mL) was prepared in an eppendorf tube, sonicated for 5 min in a bath at 45 °C, and 30 μ L of hydrochloric acid (0.02M) were added to reach pH 5.5. Then, the solution was stirred overnight at 25 °C. The solution was neutralized with aliquots of sodium hydroxide and stirred for 30 minutes. Finally, the NPs were collected by centrifugation during 5 min at 10 000 rpm. The sample was washed five times with water, and dried for few hours under vacuum. The loading capacities were deduced by the titration of doxorubicin in the supernatant fractions.

DOX wt (%)	20
-------------------	-----------

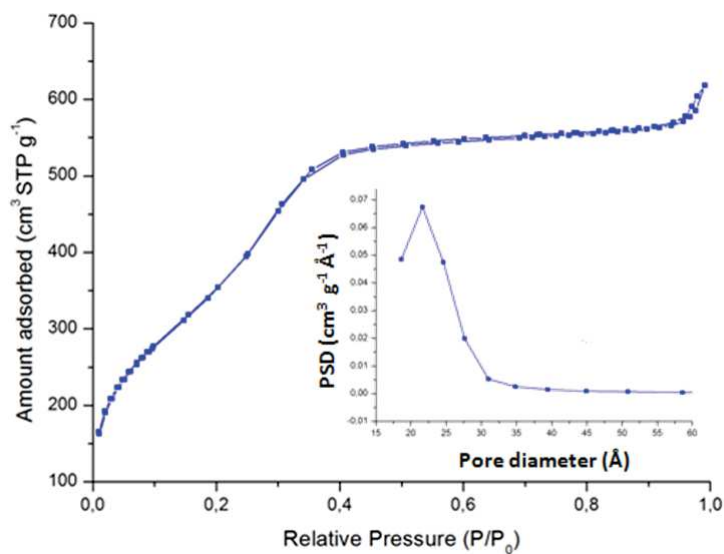


Figure S7. N₂-adsorption-desorption isotherm and pore size distribution of EP NPs.

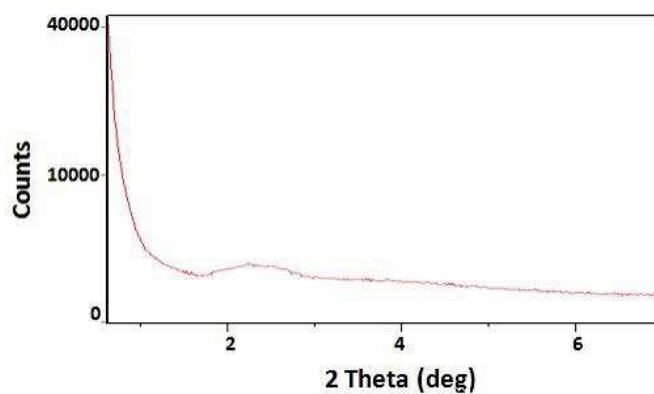


Figure S8. Small angle X-ray diffraction pattern of EP NPs (Cu k_α).

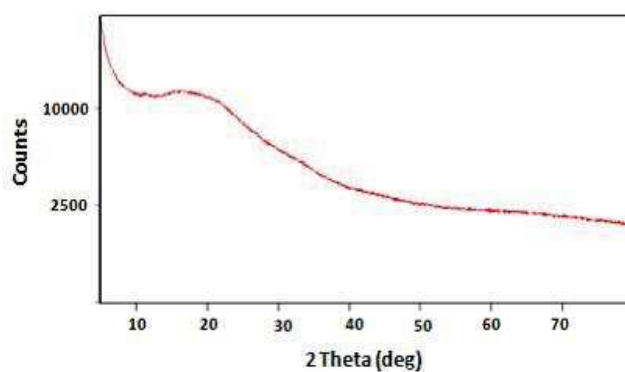


Figure S9. Wide angle X-ray diffraction pattern of EP NPs (Cu k_α).

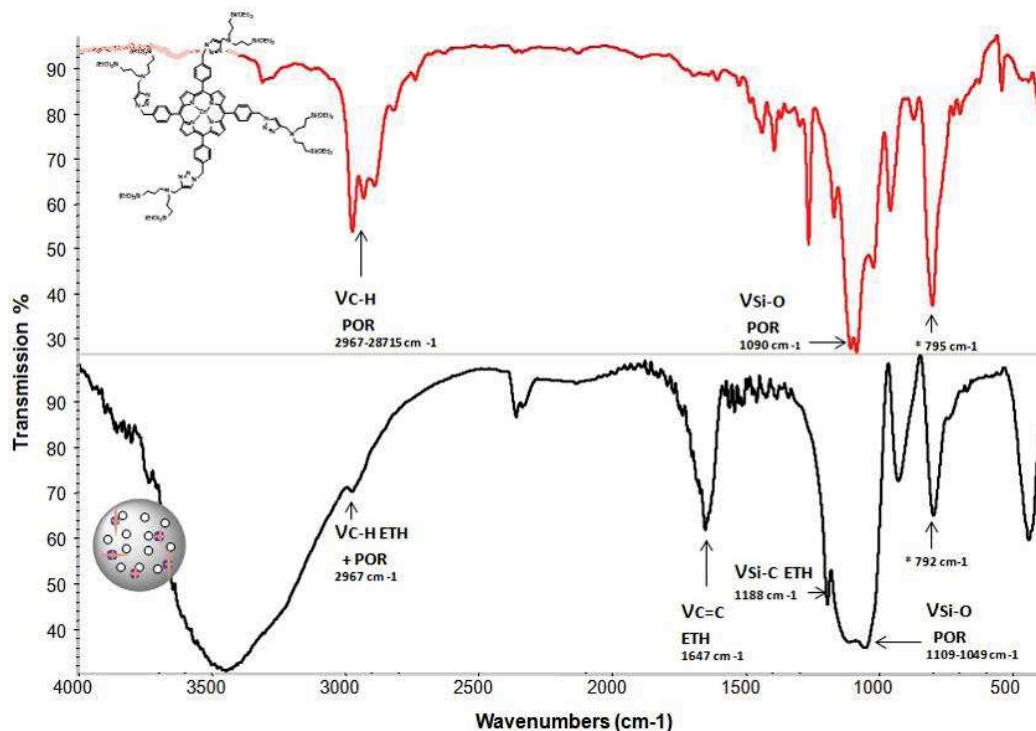


Figure S10. FTIR spectra of the POR 1, and EP NPs confirming the presence of the ETH and POR moieties in the nanomaterials framework. * Out of plan bending of *para*-disubstituted aromatic rings in the POR.

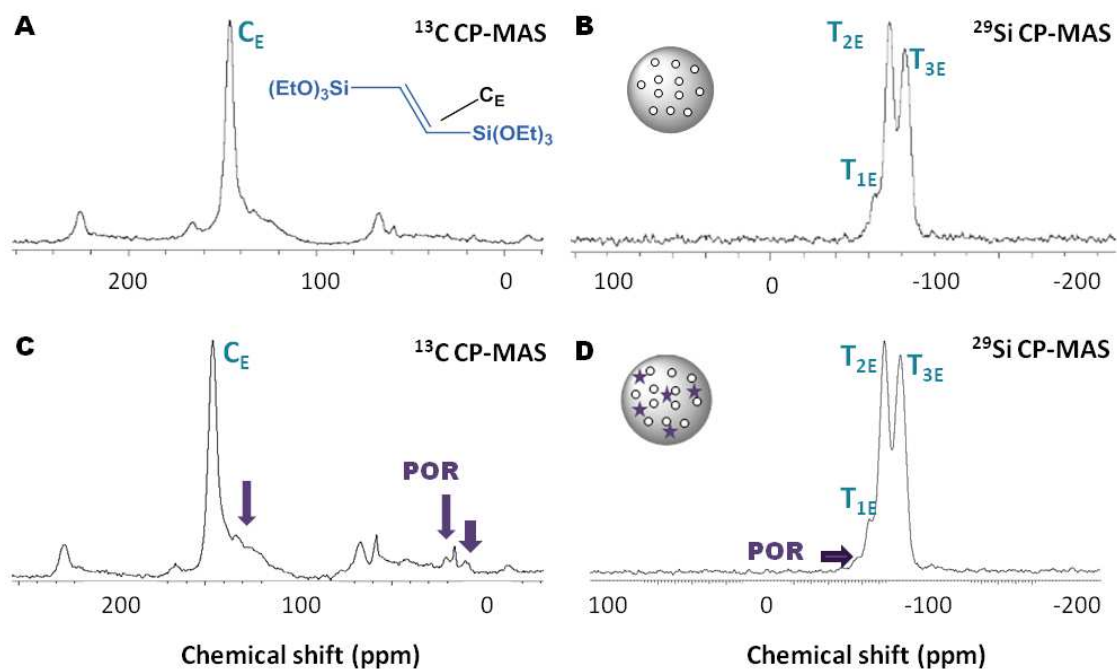


Figure S11. ^{29}Si and ^{13}C Solid state CPMAS NMR spectra of E NPs (A-B) and EP NPs (C-D).

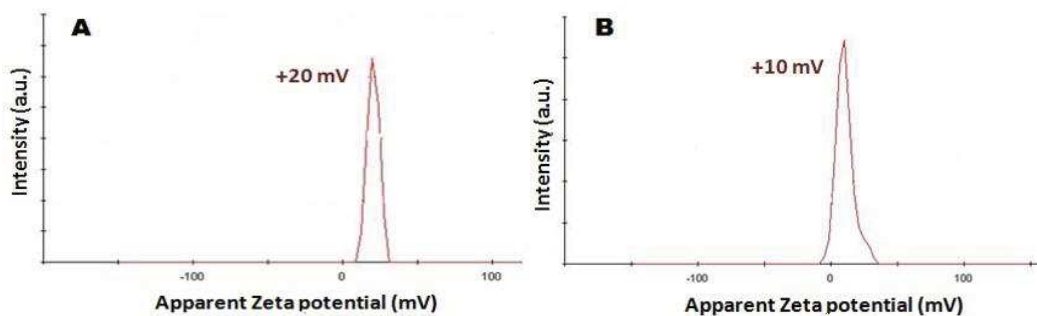


Figure S12. Zeta potential of EP NPs at PH 5.5 (A) and PH 7.4 (B).

Table S13. Photosensitizer weight percent determination in the EP NPs.

NPs N wt% [a]	NPs POR wt% [b]
1.55	11

[a] Elemental analysis by combustion measurements of the EP NPs.

[b] Determination based on the nitrogen wt% in the POR molecules.

***In vitro* studies**

4.3.4. S14. Two-photon fluorescence imaging

The day prior to the experiment, MCF-7 cells were seeded onto bottom glass dishes (World Precision Instrument, Stevenage, UK) at a density of 10^6 cells.cm⁻². Adherent cells were then washed once and incubated in 1 ml culture medium containing NPs at a concentration of 40 $\mu\text{g.mL}^{-1}$ for 20 h. Fifteen min before the end of incubation, cells were loaded with Cell Mask TM Orange Plasma Membrane Stains (Invitrogen, Cergy Pontoise, France) for membrane staining at a final concentration of 5 $\mu\text{g.mL}^{-1}$. Before visualization, cells were washed gently with phenol red-free DMEM. Cells were then scanned with LSM 780 LIVE (Carl Zeiss, Le Pecq, France), at 750 or 800 nm with a slice depth (Z stack) of 0.62 μm .

4.3.4. S15. Unloaded NPs *in vitro* control (cytotoxicity 72 h)

MCF-7 cells were incubated with increasing concentrations of EP NPs (from 5 to 200 $\mu\text{g.mL}^{-1}$). After 72 h treatment, a MTT assay was performed and data are mean \pm SD of 3 experiments.

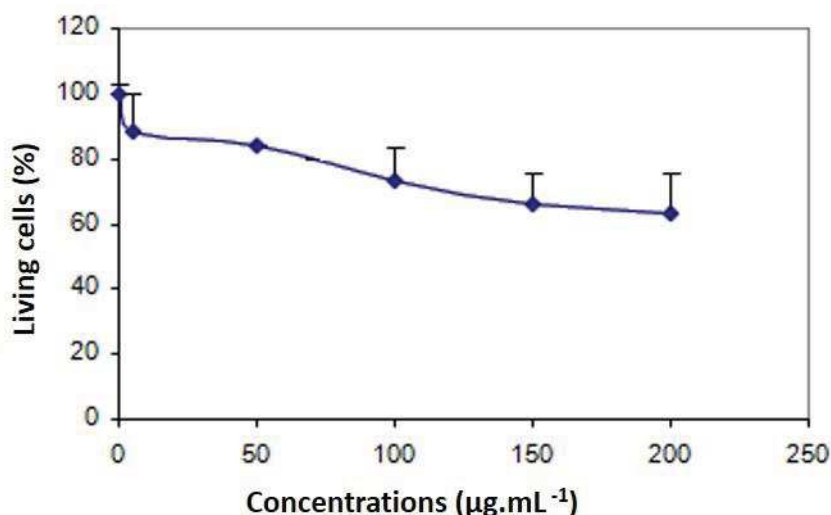
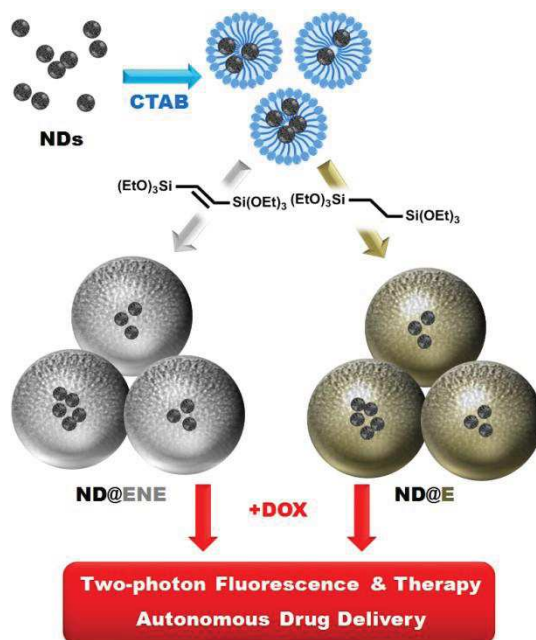


Figure S15. Cytotoxicity of unloaded EP NPs in MCF-7 cells after 72 h of incubation.

4.3.4. S16. Drug delivery experiments

MCF-7 cells were seeded into 96-well plates at 2000 cells per well in 200 μL culture medium and allowed to grow for 24 h. Increasing concentrations of EP NPs (from 0.01 to 10 $\mu\text{g.mL}^{-1}$) dispersed in sterile water, were incubated in culture medium of MCF-7 cells during 72 h and a MTT assay was performed to evaluate the toxicity. Briefly, cells were incubated for 4 h with 0.5 mg.mL^{-1} of MTT (3-(4,5-dimethylthiazol-2-yl)-2,5-diphenyltetrazolium bromide; Promega) in media. The MTT/media solution was then removed and the precipitated crystals were dissolved in EtOH/DMSO (1:1). The solution absorbance was read at 540 nm.

4.4. Core-Shell Nanodiamonds-Periodic Mesoporous Organosilica Nanoparticles for Two-Photon Imaging, Photodynamic Therapy and Synergistic pH-Responsive Drug Delivery



Abstract

Nanodiamonds are a chemically stable, non-toxic and highly fluorescent form of carbon, which make them suitable for medical applications. Herein we report on construction of nanomaterial containing nanodiamonds entrapped in ethylene and ethenylene-bridged periodic mesoporous organosilica nanoparticles for application in delivery of doxorubicin, two-photon imaging and photodynamic therapy of breast cancer cells.

Interdisciplinary collaboration

Nanomaterial synthesis, physic-chemical characterizations and applications in solution: C. Mauriello Jimenez, N. Knezevic, Y. Galán Rubio, O. Hocine, J. Croissant, M. Seric, L. Raehm, J-O. Durand.

Photothermal studies: S. Szunerits, R. Boukherroub, F. Teodorescu

Cell studies: M. Maynadier, V. Stojanovic, M. Gary-Bobo, M. Garcia.

➤ **J. Mater. Chem. B**, 2016, **4**, 5803.

4.4.1. Introduction

Diamond nanoparticles, (nanodiamonds, NDs), have emerged as particularly well-suited nanostructures for biomedical applications. NDs are inert, optically transparent, photoluminescent, biocompatible and can furthermore be functionalized in many ways depending on their intended ultimate application.⁴⁷⁻⁶⁷ Indeed, the presence of negatively-charged nitrogen-vacancy centres ($N^{\cdot-}V^{\cdot-}$) have allowed NDs to be used as markers for bioimaging. Since $N^{\cdot-}V^{\cdot-}$ centers are a deep defect of about 1.80 eV below the conduction band of the NDs, excellent photostability over time with emitted luminescence is observed around 680 nm.⁶⁸⁻⁷¹ However, NDs present a tendency to aggregate and form unstable suspension in physiological environments.^{72, 73} Encapsulation of NDs into shells has been identified as a promising way for the formation of stable ND dispersions in biological media.^{74, 75} A liposome-based encapsulation process was proposed by Bumb *et al.* to improve the colloidal stability of fluorescent NDs.⁷⁶ A core-shell system based on a ND core and a mesoporous silica shell has been proposed lately by Rosenholm *et al.* for bioimaging and efficient drug delivery.^{74, 75}

Periodic mesoporous organosilica (PMO) NPs, obtained from bridged organoalkoxysilanes ($R'O_3Si-R-SiO_3R'$; $R' = Me, Et$; $R =$ organic bridge), are unique hybrid nanomaterials with porous framework.⁷⁷ The organic moiety represents 30 to 80% of the material depending on the size of the organic bridges of the PMO,^{20, 35, 77} and the properties are therefore very different from those of the well-known mesoporous silica nanoparticles (MSN). For drug loading and release, PMO NPs could be advantageous over MSN as these materials have higher loading capacities without drug leakage in the absence of the pore capping due to the hydrophobic silsesquioxane hybrid framework. In addition at the nanoscale, these matrices in addition present higher biocompatibility, for instance ethylene-bridged ($Si-CH_2-CH_2-Si$) PMO are much lower haemolytic nanomaterials than MSN,^{36, 77} and long term blood circulation make them very promising for biomedical applications such as drug delivery for cancer treatment.^{16, 32, 78, 79}

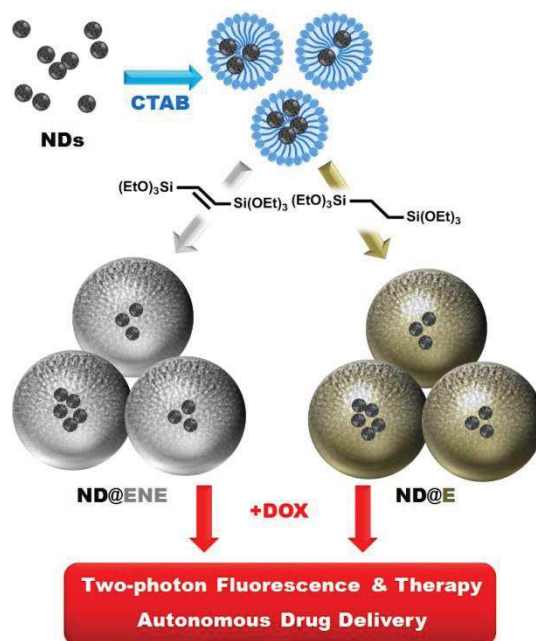
Furthermore, two-photon excitation (TPE) has been demonstrated to be particularly relevant in nanomedicine therapies since it exhibits deeper penetration in tissues and non-invasive three-dimensional spatiotemporally-controlled irradiation with a resolution of a micron.^{80, 81} We have recently described various PMO NPs for TPE-imaging and

pH-triggered drug delivery.^{42, 82} TPE fluorescence resulted from the incorporation of tetrasilylated diphenyl-butadiene or of tetrasilylated porphyrin fluorophores.

Herein, as an alternative to the complex design of silylated absorbers, we describe the first encapsulation of NDs within ethenylene (Si-CH=CH-Si) and ethylene-bridged PMO NPs (ND@ENE, ND@E) for drug delivery, TPE imaging and TPE-PDT applications. The nanomaterials were fully characterized, and found to be highly porous and biocompatible. The TPE-PDT effect with these nanomaterials was not expected as the generation of ROS from NDs upon light irradiation was never described to our knowledge. Moreover, a recent study highlights the skin protective effect of NDs which do not generate ROS upon UVB irradiation compared to other nanomaterials such as TiO₂ which generate ROS in these conditions.⁸³ As a result, multifunctional NDs@PMO NPs loaded with high doxorubicin anticancer drug contents (30-40 wt %) were used for cancer theranostics and synergistic cell killing upon non-invasive two-photon irradiation.

4.4.2. Results and discussion

The synthesis of the ND@ENE NPs was carried out at room temperature, using cetyltrimethylammonium bromide (CTAB) as the porogen agent under basic catalysis (NH₄OH solution) and a trace amount of TEOS to stabilize NDs. A solution of NDs was added and stirred for 30 min. Bis(triethoxysilyl)ethenylene was then condensed overnight under these conditions, after which NPs were centrifuged and the template extracted with ammonium nitrate. In the case of ND@E NPs the synthesis was carried out at 80 °C using the same structure-directing agent and sodium hydroxide as basic catalyst. NDs were then introduced to the mixture and this was stirred for 30 min. Then, bis(triethoxysilyl)ethene was added and the condensation process was conducted for 2 h. Then, NPs were treated as ND@ENE NPs (Scheme 1).



Scheme 1. Templated sol-gel synthesis of ND@ENE and ND@E PMO NPs from 1, 2-bis (triethoxysilyl) ethane or 1, 2-bis (triethoxysilyl) ethylene and NDs, and theranostic applications of doxorubicin-loaded core@shell PMO NPs.

The morphology and structure of the materials were then characterized by various techniques. Transmission electron microscopy (TEM) images revealed spherical ND@ENE NPs with diameters ranging from 170 to 190 nm (Figures 1A and S6) and 80 to 130 nm ND@E NPs (Figures 1B and S6). Dynamic Light Scattering (DLS) confirmed the nanosize of the materials with average hydrodynamic diameters of 160 nm for ND@ENE NPs and 560 nm for ND@E NPs (Figure S5).

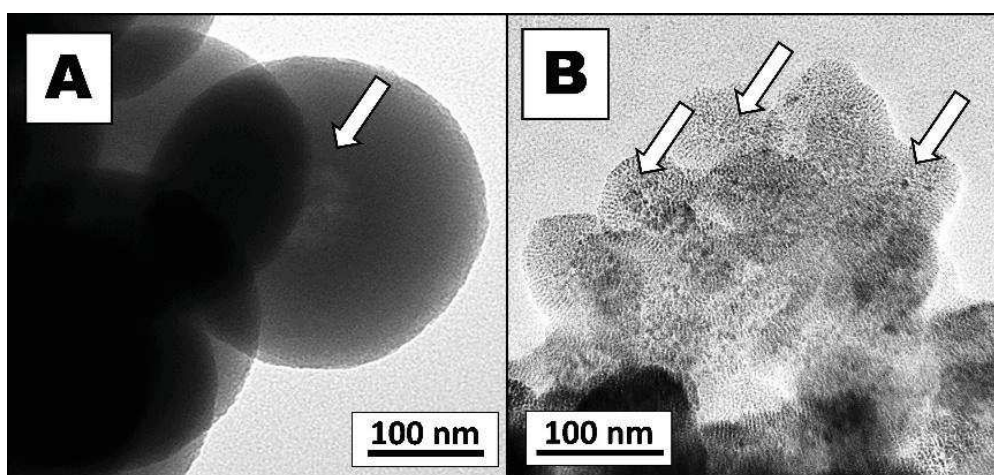


Fig. 1. TEM images of ND@ENE and ND@E NPs (A and B respectively).

Nitrogen adsorption-desorption analyses showed that all NPs were mesoporous since they present type IV isotherms (Figure 2). A very high specific area of $1444 \text{ m}^2 \text{ g}^{-1}$ was

obtained for ND@ENE instead of $890 \text{ m}^2 \text{ g}^{-1}$ for ND@E NPs. Barrett, Joyner and Halenda (BJH) theory confirmed the presence of pores around 2 to 3 nm with a pore volume of 0.51 and $0.55 \text{ cm}^3 \text{ g}^{-1}$ for ND@ENE and ND@E NPs, respectively. Small angle X-ray diffraction (XRD) showed for ND@E NPs a broad peak at 1.5° (2θ instead of a narrower peak for ND@ENE NPs (Figure S7).

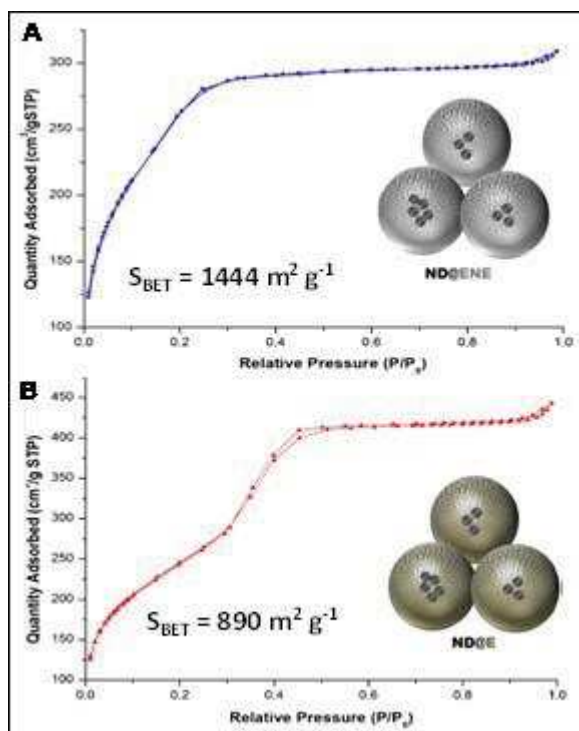


Fig. 2. N_2 -adsorption-desorption isotherms of ND@ENE NPs (a), ND@E NPs (b).

The composition of the material was then studied. The siloxane network was consistent with the broad peak observed in the wide angle XRD patterns of ND@PMO (Figure S8). Fourier transform infrared (FTIR) and ^{13}C nuclear magnetic resonance (NMR) spectroscopies (Figures S9 and S10 respectively) confirmed the presence of ethylene and ethenylene moieties in NPs. The silsesquioxane network was proved by ^{29}Si CP-MAS NMR with the presence of the T bands at -65, -75 and -85 ppm for ENE NPs and -55, -65 ppm for E NPs (Figure S10A-B). In the spectra of ND@ENE NPs, minor Q bands were also observed as a result of the TEOS added to stabilize NDs during the core-shell syntheses. Besides, the carbon corresponding to the ENE moiety was found at 150 ppm (C=C) and the E moiety appeared at 5 ppm (C-C) in the ^{13}C NMR spectra (Figure S10C-D).

We then investigated the biocompatibility of our nanomaterials as well as their capabilities for TPE-imaging of cancer cells. The cytotoxicity of the NPs on MCF-7

breast cancer cells was measured with the MTT assay, and the percentage of living cells was 80%, up to a concentration of $70 \mu\text{g L}^{-1}$ (Figure S15). Then, $80 \mu\text{g L}^{-1}$ of NPs were incubated for 20 h in MCF-7 breast cancer cells. The cellular uptake was determined *via* TPE-fluorescence imaging. The cell membranes were stained with Cell Mask Orange Plasma Membrane 15 min before the imaging experiments. ND@ENE and ND@E NPs were successfully endocytosed by cancer cells as shown by TPE-fluorescence at 800 nm inside the cytosol (see Figure 3A-B).

Eventually, *in vitro* TPE-PDT was performed on breast cancer cells. MCF-7 cells were incubated for 20 h in the presence of $80 \mu\text{g mL}^{-1}$ of ND@ENE and ND@E NPs. When irradiated at 800 nm with 3 scans of 1.56 s at the maximum power (100 %) of the laser, ND@ENE NPs showed 40 % of cancer cell death whereas the cancer killing for ND@E was 7% (Figure 3C). This is probably due to the presence of a higher amount of NDs in ND@ENE NPs (used 10 mg of ND per 0.78 mmol of Si precursor) than in ND@E NPs (used 5 mg of ND for 0.89 mmol of Si precursor), thus leading to a higher PDT activity.

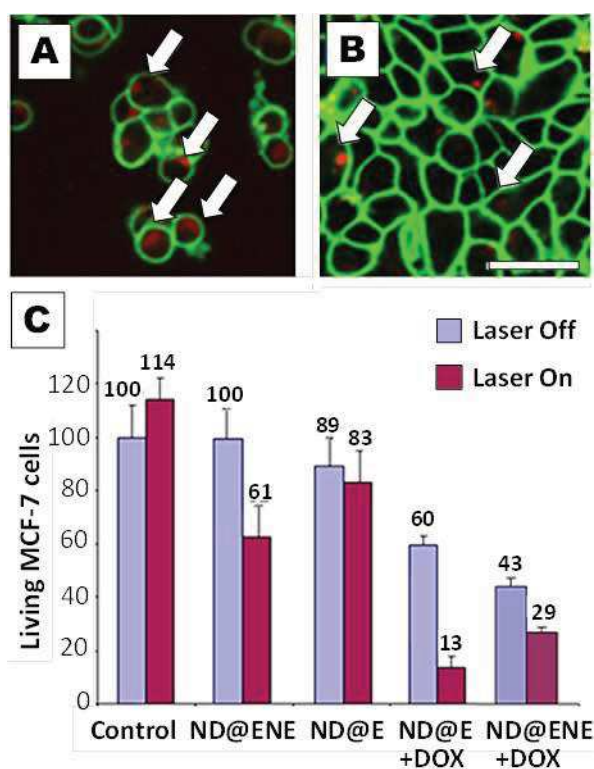


Fig. 3. Two-photon fluorescence imaging (5% of laser power) of MCF-7 breast cancer cells. Cell membranes were stained with Cell Mask, ND@ENE NPs and ND@E NPs were incubated for 20h at $40 \mu\text{g mL}^{-1}$ and irradiated at 800 nm (A, B respectively). Arrows indicate NPs in cells. Scale bar $10\mu\text{m}$. TPE-triggered cancer cell killing with ND@ENE NPs, ND@E NPs (incubation for 20 h at $80 \mu\text{g mL}^{-1}$) and ND@E+DOX, ND@ENE+DOX (incubation for 20 h at $5 \mu\text{g mL}^{-1}$) (C). Lines represent standard deviations of three independent experiments.

Core-shell nanocarriers were then examined as vectors for autonomous doxorubicin (DOX) delivery and synergistic therapy. NPs presented a drug loading of 29 and 40 wt % for ND@ENE and ND@E NPs, respectively. Drug release experiments were first carried out at pH 7 in water, with DOX-loaded ND@ENE and ND@E NPs (Figure S11), and no passive release of the drug was observed under these conditions. The release was then triggered at pH 5.5, which corresponds to the acidity of the lysosomal cellular compartment (Figure S16). [23] Moving on to *in vitro* studies, DOX-loaded ND@PMO NPs were incubated with MCF-7 for 20 h and found to be remarkably efficient at only $5 \mu\text{g } \mu\text{L}^{-1}$, causing 40 and 57 % of cell deaths for ND@E+DOX and ND@ENE+DOX, respectively (see survival without laser in Figure 3C). Combining the autonomous drug delivery feature for PMO NPs and the ND-mediated PDT, synergistic therapies were then performed. Using NPs concentration of $5 \mu\text{g } \mu\text{L}^{-1}$ the carriers induced high cell killing, the synergy reaching up to 87 % of cells killed upon irradiation at 800 nm.

In order to explain the observed results, we monitored the ability of the prepared materials to produce heat and reactive oxygen species (ROS) upon exposure to femtosecond pulsed laser. As revealed on Figure S12, a negligible difference of heat production ($+2 \text{ }^\circ\text{C}$) was observed upon TPE irradiation of ND@PMO when compared to the aqueous control. Therefore photothermal effects are negligible in the cancer cell killing effects. We then examined the generation of ROS in cells (Figure 4) by using the DCFDA kit (dichlorodihydrofluorescein diacetate). In contact with ROS species, non-fluorescent DCFDA is oxidized to the fluorescent dihydrofluorescein (DCF). DCFDA was therefore incubated for 45 min. with cells after endocytosis of the ND@PMO. The experiment revealed no significant fluorescence without irradiation whereas a high fluorescent signal was detected when cells were irradiated, which confirmed the production of ROS upon TPE. The results can be rationalized by the energy profiles of the N^-V^- centers present in NDs (scheme S17).⁸⁴ The zero-phonon line in these centers between the ground state $^3\text{A}_2$ and the excited state ^3E , correspond to 2.20 eV (563 nm). With a two-photon irradiation at 800 nm (1.54 eV) whose selection rules are different from that of monophotonic irradiation, we could have an allowed electronic transition from the ground state $^3\text{A}_2$ to the excited state ^3E . By intersystem crossing the state $^1\text{E}'$ could be reached and in the presence of oxygen, the transition from the metastable state $^1\text{E}'$ and the state $^1\text{A}_1$ (1.19 eV) could lead to the production of $^1\text{O}_2$ (0.98 eV) and reactive oxygen species (ROS).

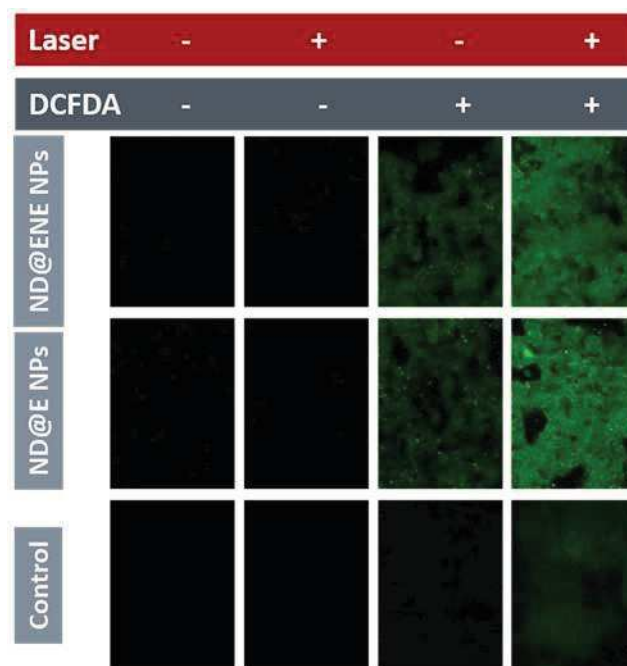


Fig. 4. Detection of intracellular ROS by DCFDA in MCF-7 cancer cells. Cells were incubated 24 h with NPs and ROS production in cells is induced by two-photon irradiation (3 x 1.57 sec) at 800 nm. Green luminescence traduces the generation of ROS detected at 535 nm.

4.4.3. Conclusions

In summary, we have designed nanodiamonds core ethylene- or ethenylene-bridged PMO shell NPs *via* different synthetic processes. The morphology, compositions and functionalities of the nanomaterials were fully characterized by various techniques. TPE-fluorescence imaging *in vitro* was performed to demonstrate the NPs cellular uptake and TPE-PDT led to 40 % of spatiotemporally controlled cancer cell killing. Furthermore, the DOX-loaded organosilica NPs were very efficient to induce cancer cell killing when combined with TPE-PDT affording up to 87 % of synergistic cell death. We also demonstrated for the first time the generation of ROS *via* nanodiamonds. The imaging of ROS species in cells confirmed that cytotoxicity was produced by the presence of the nanodiamonds in PMO NPs under two-photon excitation. Hence, these hybrid nanomaterials exhibit high potential for application as theranostics in cancer treatment.

4.4.4. Supporting Information

Experimental section

4.4.4. S1. Materials and general procedures

IR spectra were recorded on a Perkin-Elmer 100 FT spectrophotometer. Absorption spectra were recorded on a Hewlett-Packard 8453 spectrophotometer. Dynamic Light scattering analyses were performed using a Cordouan Technologies DL 135 Particle size analyzer instrument. ^{29}Si and ^{13}C solid state NMR sequences were recorded with a VARIAN VNMR300, using Q8MH8 and adamantane references, respectively. BET analyses were performed using a TRISTAR 3000 gas adsorption analyzer instrument. TEM analyses were performed on a JEOL 1200 EXII instrument.

Cetyltrimethylammonium bromide (CTAB), sodium hydroxide, ammonium hydroxide (31.2%), 1, 2-bis (triethoxysilyl) ethane, ammonium nitrate (NH_4NO_3), ethanol (EtOH), doxorubicin hydrochloride (DOX), and tetraethylorthosilicate (TEOS) were purchased from Sigma-Aldrich. Anhydrous ethanol was purchased from Fischer Chemicals. 1, 2-bis (triethoxysilyl) ethylene was purchased from ABCR. Hydroxyl-terminated nanodiamonds (ND-OH) were purchased from International Technology Center (Raleigh, NC, USA) and exhibit a primary average particle size of 4.0 nm. They were used as received.

Nanomaterial synthesis and characterization

4.4.4. S2. Synthesis of ND@ENE NPs

A mixture of CTAB (160 mg), distilled water (17.5 mL), absolute ethanol (13 mL) and ammonium hydroxide (150 μL) was stirred at room temperature in a 50 mL three-neck round bottom flask. Immediately after, a solution of NDs in water (10 mL, 1 mg/mL previously sonicated for 2 h) was added dropwise under stirring. TEOS (50 μL) was then added, and after 30 min, 1,2-bis(triethoxysilyl)ethylene (300 μL , 0.78 mmol) was added to the aforementioned solution and the condensation process was conducted overnight at room temperature. Then, fractions were gathered in propylene tubes and collected by centrifugation during 20 min at 20 krpm. The sample was then extracted three times with a solution of NH_4NO_3 in EtOH (6 g L^{-1}) with sonication at 45 °C, and

washed with water, ethanol, and acetone. The as-prepared material was dried under vacuum at 80 °C for 2 h.

4.4.4. S3. Synthesis of ND@E NPs

A mixture of CTAB (125 mg), distilled water (60 mL), and sodium hydroxide (437 μ L, 2 M) was stirred at 80 °C for 50 min at 750 rpm in a 250 mL three-neck round bottom flask. Then, a solution of NDs in water (5 mL, 1 mg/mL previously sonicated for 2 h) was added dropwise under stirring. After 30 min 1,2-bis(triethoxysilyl)ethane (330 μ L, 0.89 mmol) was added to the aforementioned solution and the condensation process was conducted for 2 h. Then, the solution was cooled to room temperature while stirring; fractions were gathered in propylene tubes and collected by centrifugation during 20 min at 20 krpm. Extraction and washings processes were carried out as described for ND@ENE NPs.

4.4.4. S4. DOX loading of ND@ENE and ND@E NPs

A mixture of NPs (10 mg), DOX (3.2 mg), and deionized water (1 mL) was prepared in an eppendorf tube, sonicated for 5 min in a bath at 45 °C, and hydrochloric acid (30 μ L, 0.02 M) were added to reach pH 5.5. Then, the solution was stirred overnight at 25 °C. The solution was neutralized with aliquots of sodium hydroxide and stirred for 30 min. Finally, the NPs were collected by centrifugation during 5 min at 10 krpm. The sample was washed five times with water, and dried under vacuum. The loading capacities were deduced by the titration of DOX in the supernatant fractions.

Loading Capacity (wt %) = [mass of loaded drug/ (mass of loaded drug + mass of NPs)] \times 100

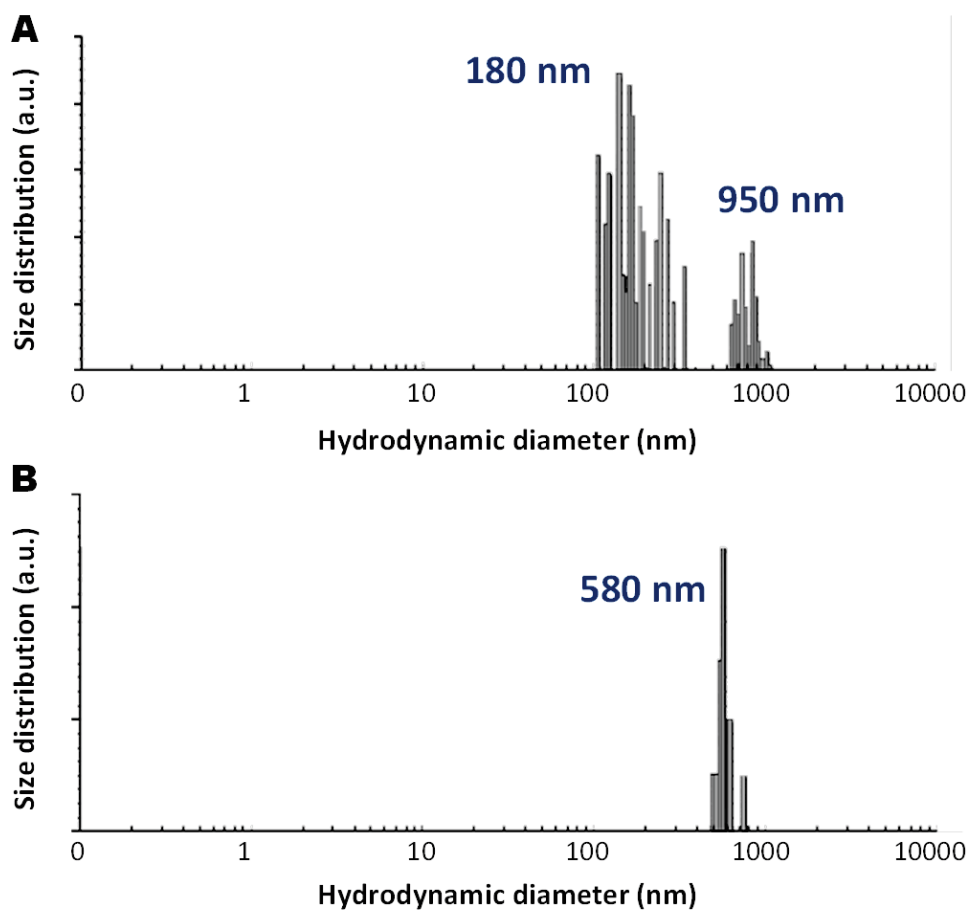


Figure S5. DLS analyses of ND@ENE (A) and ND@E (B). The large diameter arose from the aggregation states of the particles as well as the hydration layers.

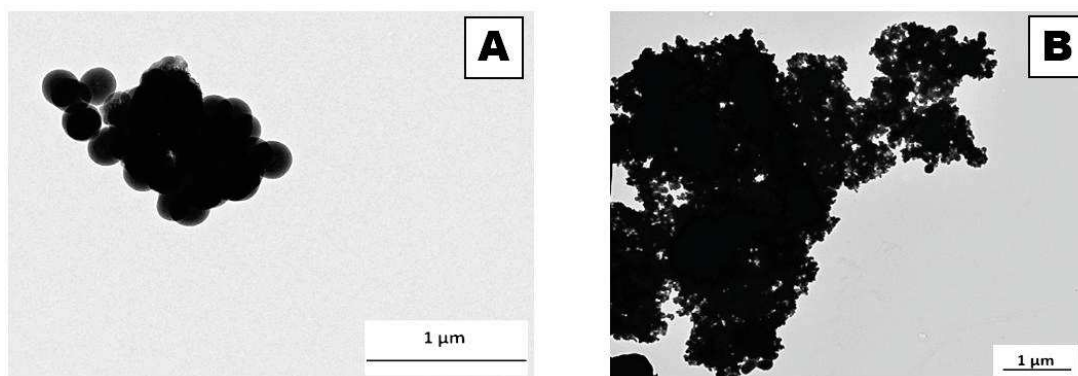


Figure S6. TEM images of ND@ENE and ND@E NPs. (A and B respectively).

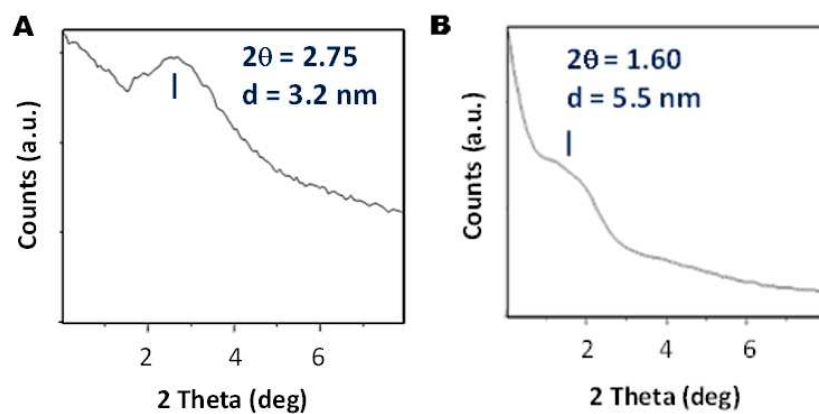


Figure S7. Low angle XRD patterns of ND@ENE (A), ND@E (B), consistent with the porous silsesquioxane frameworks in the materials.

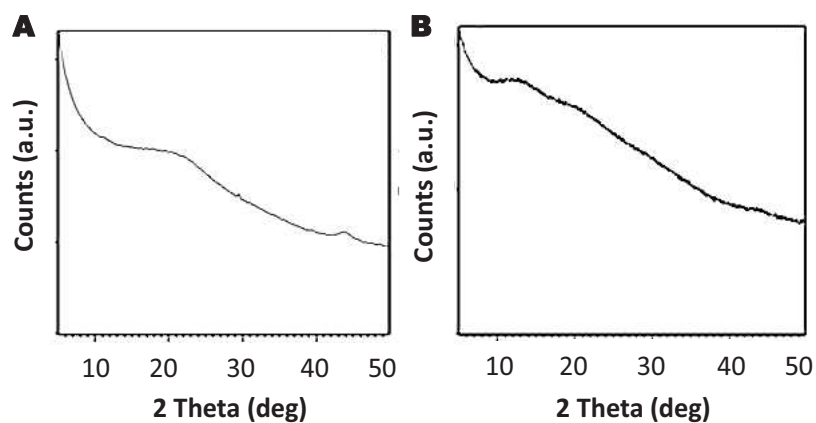


Figure S8. Wide angle XRD patterns of ND@ENE (A), ND@E (B) consistent with the amorphous porous silsesquioxane frameworks.

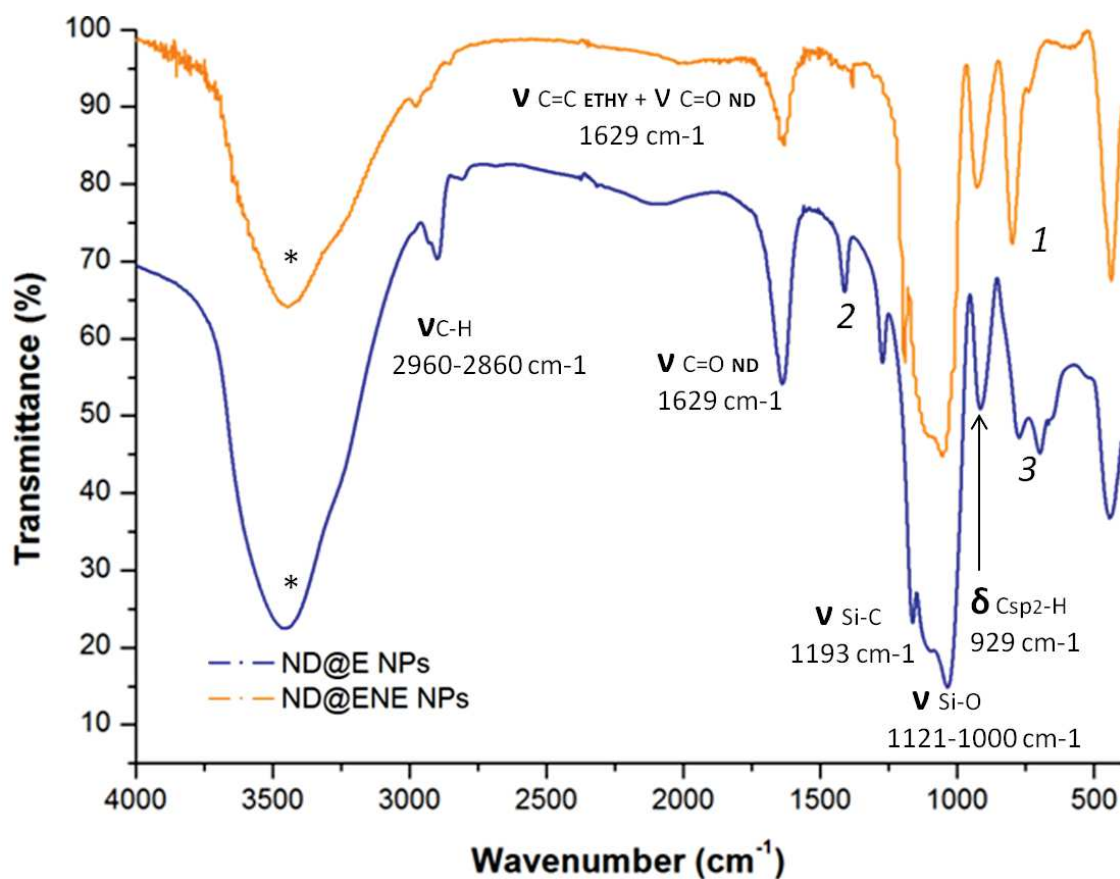


Figure S9. FTIR spectra of ND@ENE NPs and ND@E NPs confirming the presence of the ethylene or ethane and NDs. * Indicates the vibration modes of water. 1 Vibration mode of the ethenylene bridges, likely another $\delta_{\text{Csp}^2\text{-H}}$. 2 Vibration modes of the ethylene bridges, likely a $\delta_{\text{C-C}}$. 3 Vibration modes of the ethylene bridges, likely other $\delta_{\text{Csp}^2\text{-H}}$.

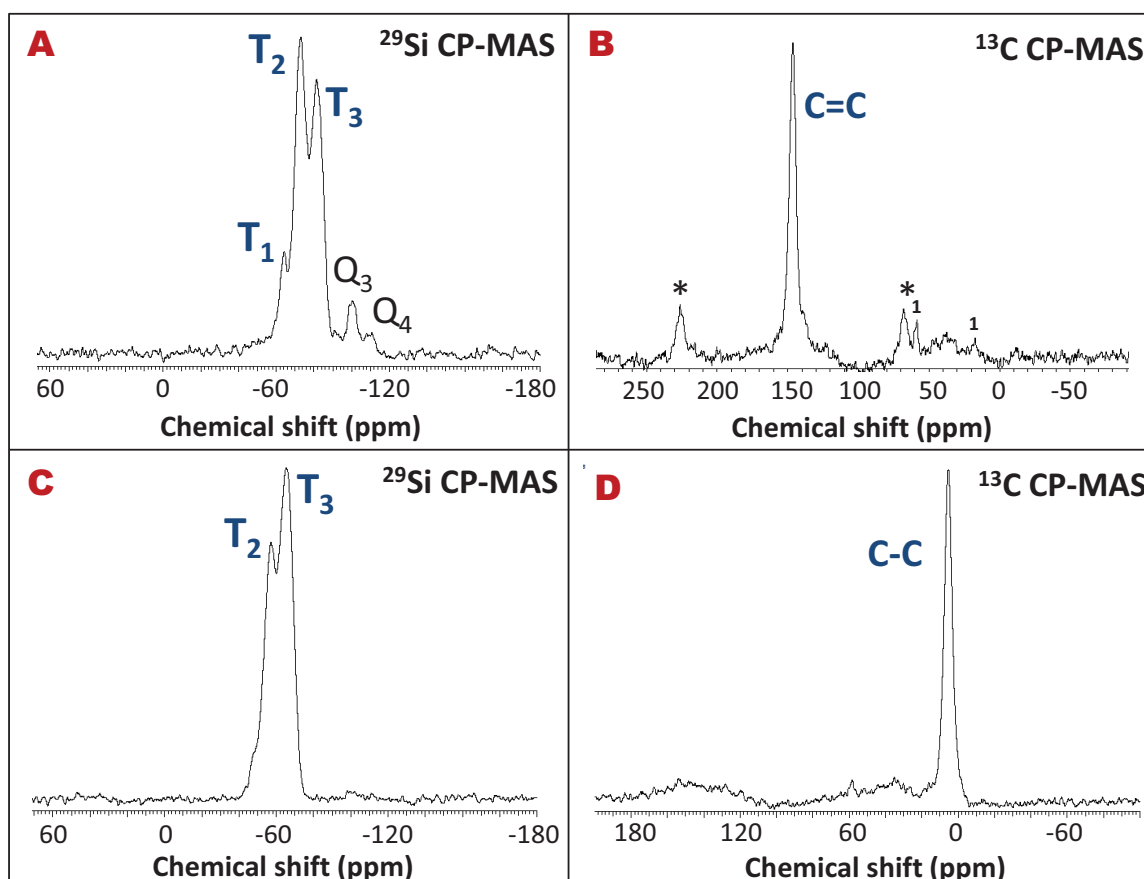


Figure S10. ^{29}Si and ^{13}C Solid state NMR CPMAS spectra of ND@ENE NPs (A-B) and ND@E NPs (C-D). The major proportions of T_2 and T_3 in the silicon spectra correlates a stable silsesquioxane network. The ethenylene and ethylene bridges are clearly distinguished *via* carbon NMR. * Indicates the spinning side bands. / remaining Si-O-CH₂-CH₃.

4.4.4. S11. Drug release control in simulated biological media

Release experiment of DOX-loaded ND@E NPs was performed in ultrapure water upon addition, after 60 min, of HCl (0.2 M) to obtain a lysosomal pH.

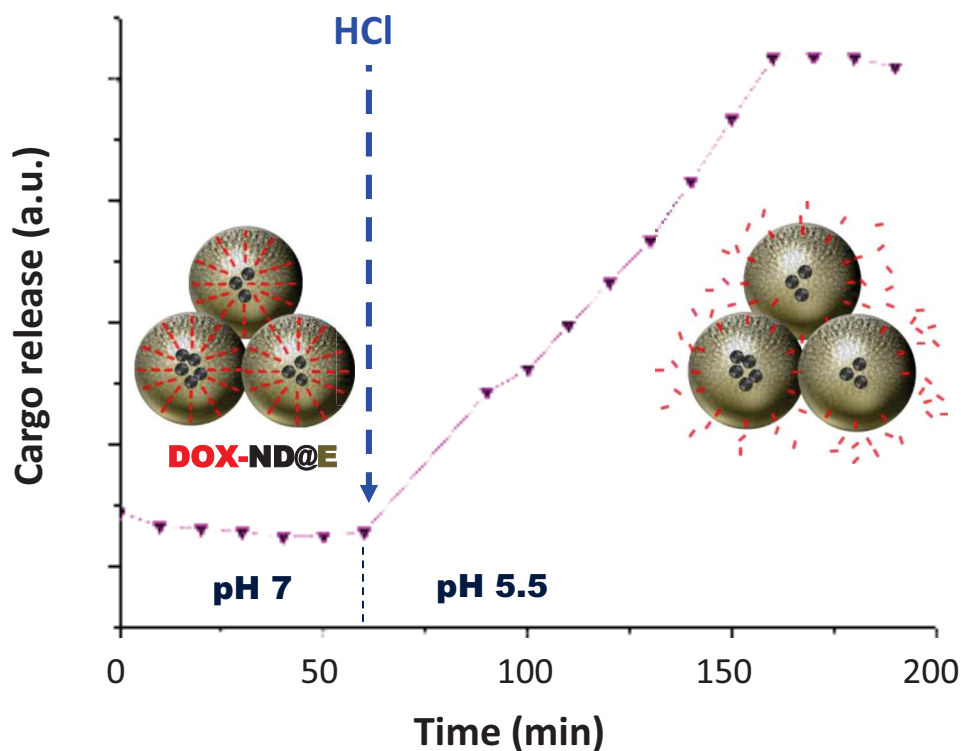


Figure S11. DOX release from DOX-ND@ENE and DOX-ND@E NPs in water upon pH trigger from a neutral condition to pH 5.5.

4.4.4. S12. Photothermal effect

Irradiations were performed in standard 96-well plates with a pulsed titanium: saphir laser (Chameleon model, Coherent). This laser source delivers 100 fs pulses at a repetition rate of 80 MHz and was used for the photothermal experiments. A telescope with a magnification of 4.3 is used to roughly adapt the beam diameter to the wells' one. The beam diameter was previously measured with a Thorlabs DCU224C CCD camera (New Jersey, USA) and the variation in the diameter over the wavelength along with the setup efficiency was corrected with the laser average power in the calculation of the applied intensity. The wavelength used was 810 nm with the laser power intensity of 1 W cm^{-2} . The temperature changes were captured by Infrared Camera (Thermovision A40, FLIR system, USA) and treated using the ThermoCam Researcher Pro 2.9 software.

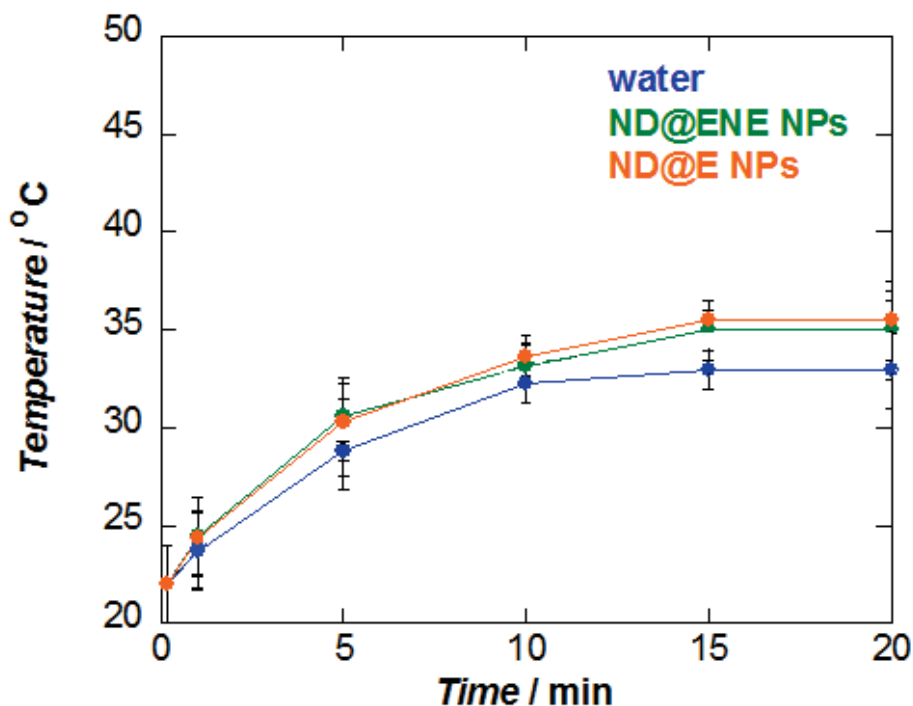


Figure S12. Photothermal effect of the pulsed irradiation for two-photon-excitation of ND@E, ND@ENE NPs, and a water solution control.

In vitro studies

4.4.4. S13. Two-photon fluorescence imaging

The day prior to the experiment, MCF-7 cells were seeded onto bottom glass dishes (World Precision Instrument, Stevenage, UK) at a density of 10^6 cells cm^{-2} . Adherent cells were then washed once and incubated in 1 mL culture medium containing NPs at a concentration of $40 \mu\text{g mL}^{-1}$ for 20 h. Fifteen min before the end of incubation, cells were loaded with Cell Mask TM Orange Plasma Membrane Stains (Invitrogen, Cergy Pontoise, France) for membrane staining at a final concentration of $5 \mu\text{g mL}^{-1}$. Before visualization, cells were washed gently with phenol red-free DMEM. Cells were then scanned with LSM 780 LIVE (Carl Zeiss, Le Pecq, France), at 750 or 800 nm with a slice depth (Z stack) of $0.62 \mu\text{m}$.

4.4.4. S14. TPE-therapy

MCF-7 human breast cancer cells were cultured in Dulbecco's modified Eagle's medium (DMEM) supplemented with 10 % fetal bovine serum and $50 \mu\text{g mL}^{-1}$ gentamycin. All cells were allowed to grow in humidified atmosphere at $37 \text{ }^\circ\text{C}$ under 5 % CO_2 . For *in vitro* phototoxicity, MCF-7 cells were seeded into a 384 multiwell glass-

bottomed plate (thickness 0.17 mm), with a black polystyrene frame, 2000 cells per well in 50 μL of culture medium, and allowed to grow for 24 h. NPs were then dispersed under ultrasounds in PBS at a concentration of 1 mg mL^{-1} and cells were then incubated for 5 h with or without nanoparticles at a final concentration of 80 $\mu\text{g mL}^{-1}$ in supplemented DMEM. After incubation with NPs, cells were washed twice, maintained in fresh culture medium, and then submitted (or not) to laser irradiation. After 2 days, the MTS assay was performed and was corrected.

4.4.4. S15. Unloaded NPs *in vitro* control (cytotoxicity for 72 h)

MCF-7 cells were incubated with increasing concentrations of NPs (from 5 to 200 $\mu\text{g mL}^{-1}$). After 72 h treatment, a MTT assay was performed and data are mean \pm SD of 3 experiments.

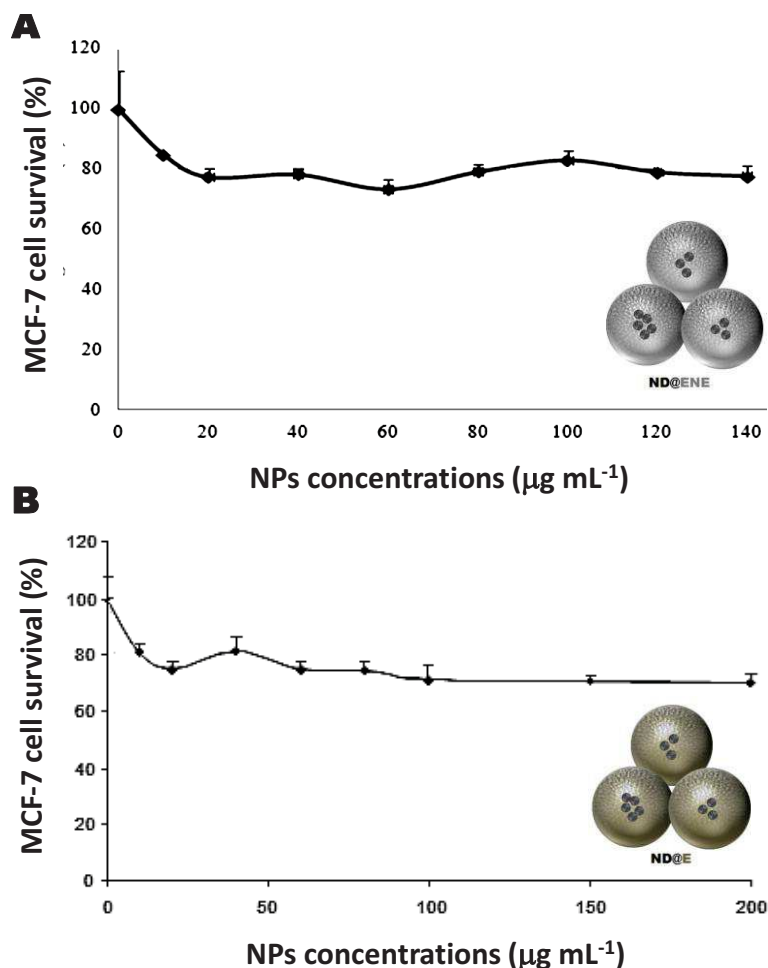


Figure S15. Cytotoxicity of ND@ENE NPs (A) and ND@E NPs (B) on MCF-7 cells after 72 h of incubation.

4.4.4. S16. Drug delivery experiments

MCF-7 cells were seeded into 96-well plates at 2000 cells per well in 200 μL culture medium and allowed to grow for 24 h. Increasing concentrations of DOX ND@E NPs (from 0.01 to 200 $\mu\text{g mL}^{-1}$) dispersed in sterile water, were incubated in culture medium of MCF-7 cells during 72 h and a MTT assay was performed to evaluate the toxicity. Briefly, cells were incubated for 4 h with 0.5 mg mL^{-1} of MTT (3-(4,5-dimethylthiazol-2-yl)-2,5-diphenyltetrazolium bromide, Promega) in media. The MTT medium solution was then removed and the precipitated crystals were dissolved in EtOH/DMSO (1:1). The solution absorbance was read at 540 nm.

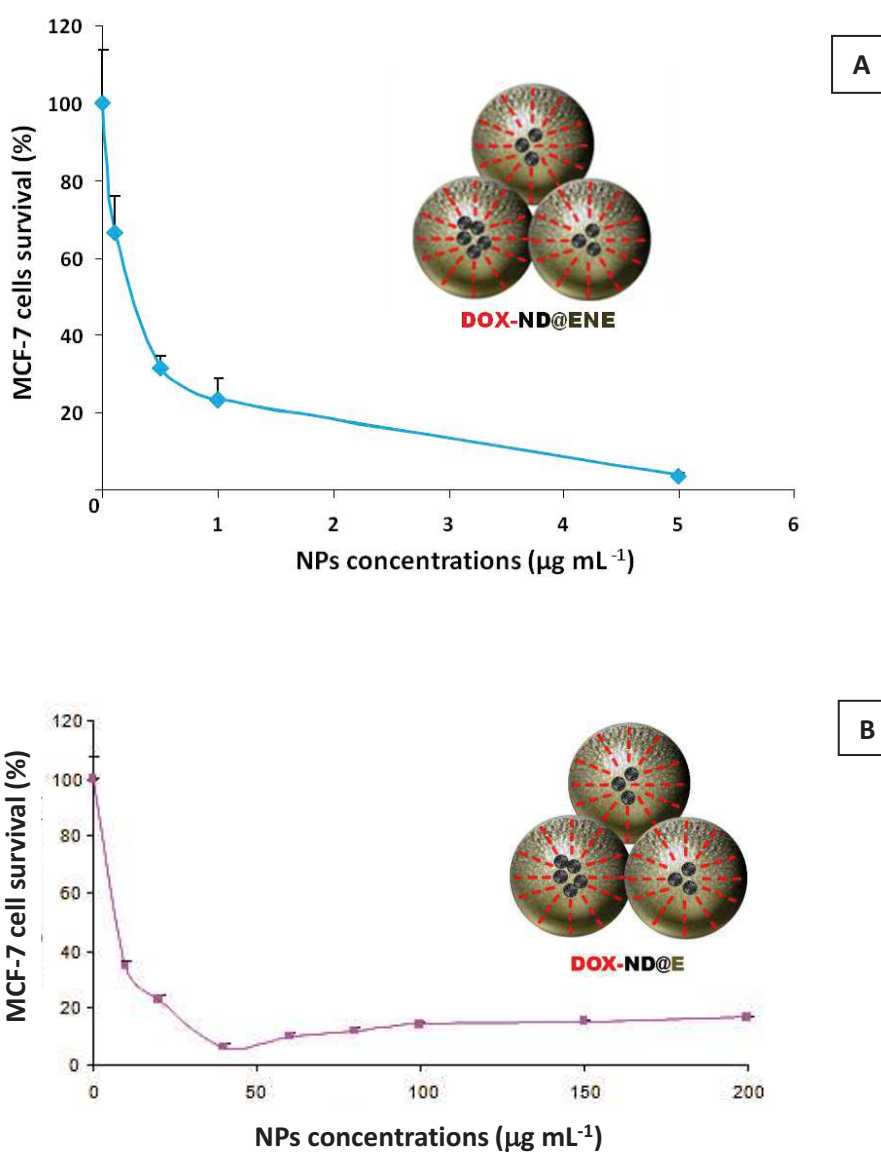


Figure S16. DOX delivery in MCF-7 cancer cells *via* DOX-ND@ENE NPs (A) and DOX-ND@E NPs (B).

4.4.4. S17. ROS imaging

The detection of intracellular reactive oxygen production (ROS) was realized using DCFDA Cellular ROS Detection Assay Kit (abcam). For this, MCF-7 cells were seeded in a glass bottom microplate and treated with $80 \mu\text{g mL}^{-1}$ nanoparticles. After 24 h, cells were rinsed and incubated 45 min at 37°C with DCFDA at $20 \mu\text{M}$. Then, cells were rinsed and irradiated or not with a two-photon microscope ($3 \times 1.57 \text{ sec}$) at 800 nm . Green luminescence traduces the generation of ROS detected at 535 nm .

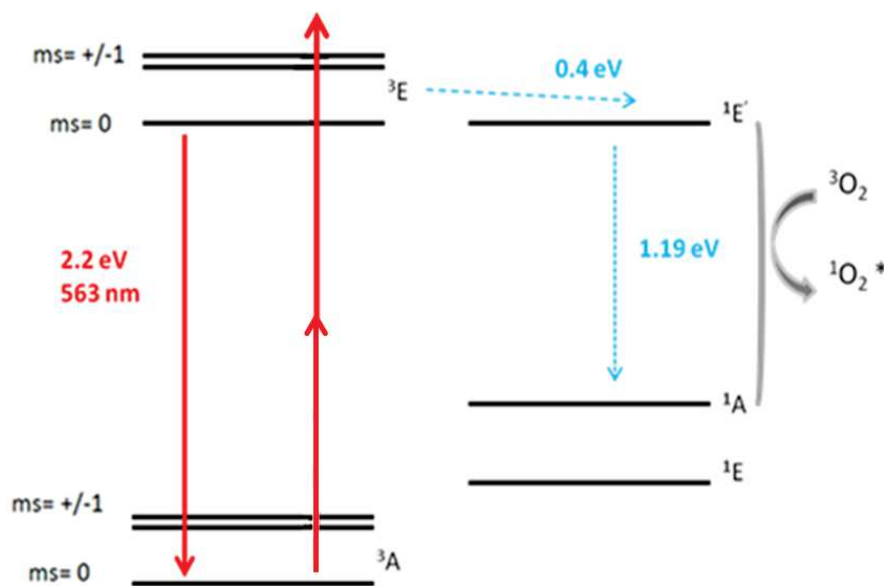
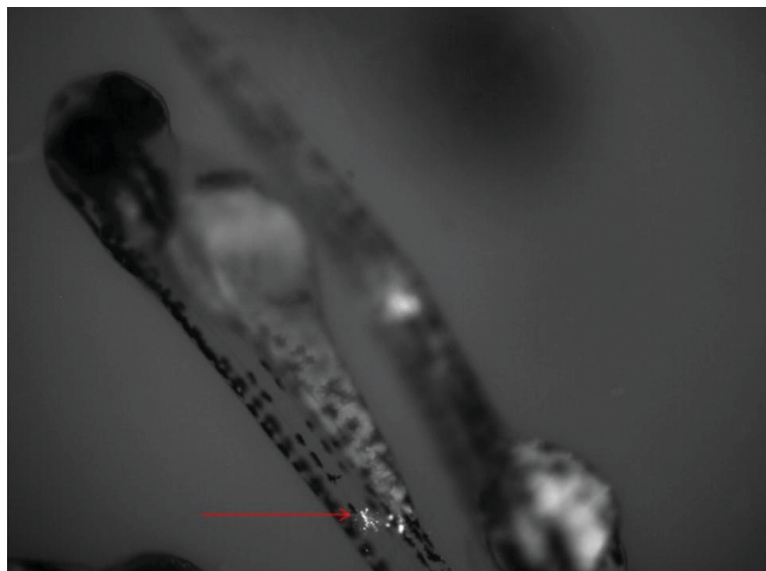


Figure S17. Energy-level diagram for NV centers.

4.5. Design of pure porphyrin mesoporous organosilica nanoparticles for two-photon fluorescence imaging, PDT and gene delivery *in vitro* and *in vivo*



Abstract

We report the synthesis of pure porphyrin organosilica mesoporous nanoparticles produced from a metallated porphyrin (POR). The precursor was octasilylated by click chemistry under CuAAC catalysis. Their efficiency for intracellular tracking was demonstrated by the *in vitro* imaging at 750 nm in MCF-7 cancer cells and their efficiency in photodynamic therapy was demonstrated with the two-photon therapy at 800 nm. Their efficiency as siRNA delivery nanoplatform was tested *in vitro* and *in vivo* in zebrafish model.

Interdisciplinary collaboration

Nanomaterial synthesis, physico-chemical characterizations and applications in solution: C. Mauriello Jimenez, D. Laurencin, J. Croissant, N. Khashab, L. Raehm, J-O. Durand.

Synthesis of porphyrin photosensitizers: V. Chaleix, P. Maillard, S. Richeter

Cell studies: M. Maynadier, M. Gary-Bobo, M. Garcia.

In vivo studies: G. Lutfalla, D. Aggad, N. Bettache, M. Maynadier

4.5.1. Introduction

Since the discovery of gene silencing by Fire and co-workers in 1998,⁸⁵ RNAi interference (an endogenous pathway by which a short piece of RNA is able to induce the destruction of mRNA containing a complementary sequence) has attracted international attention⁸⁵. In eukaryotic cells the double-stranded RNAi is cleaved into small interfering RNA (siRNA) by the Dicer enzyme. Once the siRNA is incorporated and cleaved into the protein complex (RISC), its guide strand degrades complementary mRNA⁸⁶.

In 2001, Tuschl and colleagues demonstrated that *synthetic* siRNA was able to achieve gene knockdown in mammalian cells⁸⁷. Since then, siRNA have been used for the treatment of viral infections^{88, 89}, hereditary disorders^{90, 91} or cancer^{92, 93}. However, the clinical implementation of the siRNA is currently hampered by physiological disadvantages of siRNA. Due to its negative charge and to its size (around 13 kDa) the siRNA cannot cross cellular membranes and is degraded by endogenous nucleases. To overcome these disadvantages effective delivery platforms have been developed¹¹¹. So far, various delivery materials such as lipids (to treat advanced cancers, ebola-virus infection or hypercholesterolemia)^{94, 95} or cyclodextrin nanoparticles (Ewing's sarcoma was inhibited by this delivery system)^{96, 97} have been used. Conjugated delivery systems (i.e. conjugated peptides, antibodies, cholesterol)^{98, 99} were also developed to obtain a single-component system that uses only equimolar amounts of delivery material and siRNA. In 2010, Mark Davis and co-workers developed nanoparticles designed to deliver the siRNA to patients with the skin cancer melanoma. Nanoparticles were made from polyethylene glycol (PEG) molecules which were terminated with adamantane (AD) that form inclusion complexes with surface cyclodextrins.¹⁰⁰

To avoid the degradation of siRNA or other macromolecules in the endolysosomal compartments, a new technology derived from PDT has emerged: the PCI or photochemical internalisation^{101, 102}. PCI leads the release of these macromolecules into the cytosol by inducing the disruption of lysosomal membranes by a photochemical reaction produced by the activation of the PS by light exposure. Following the disruption, the content present into the endocytic vesicle can be released into the cytosol. Several studies demonstrated the enhancement of gene silencing through PCI. Oliveira et al.^{103, 104} described in 2007 and 2008 the increase of the treatment efficacy of a lipid vector of anti-EGF siRNA in neck squamous cells and the gene silencing *in*

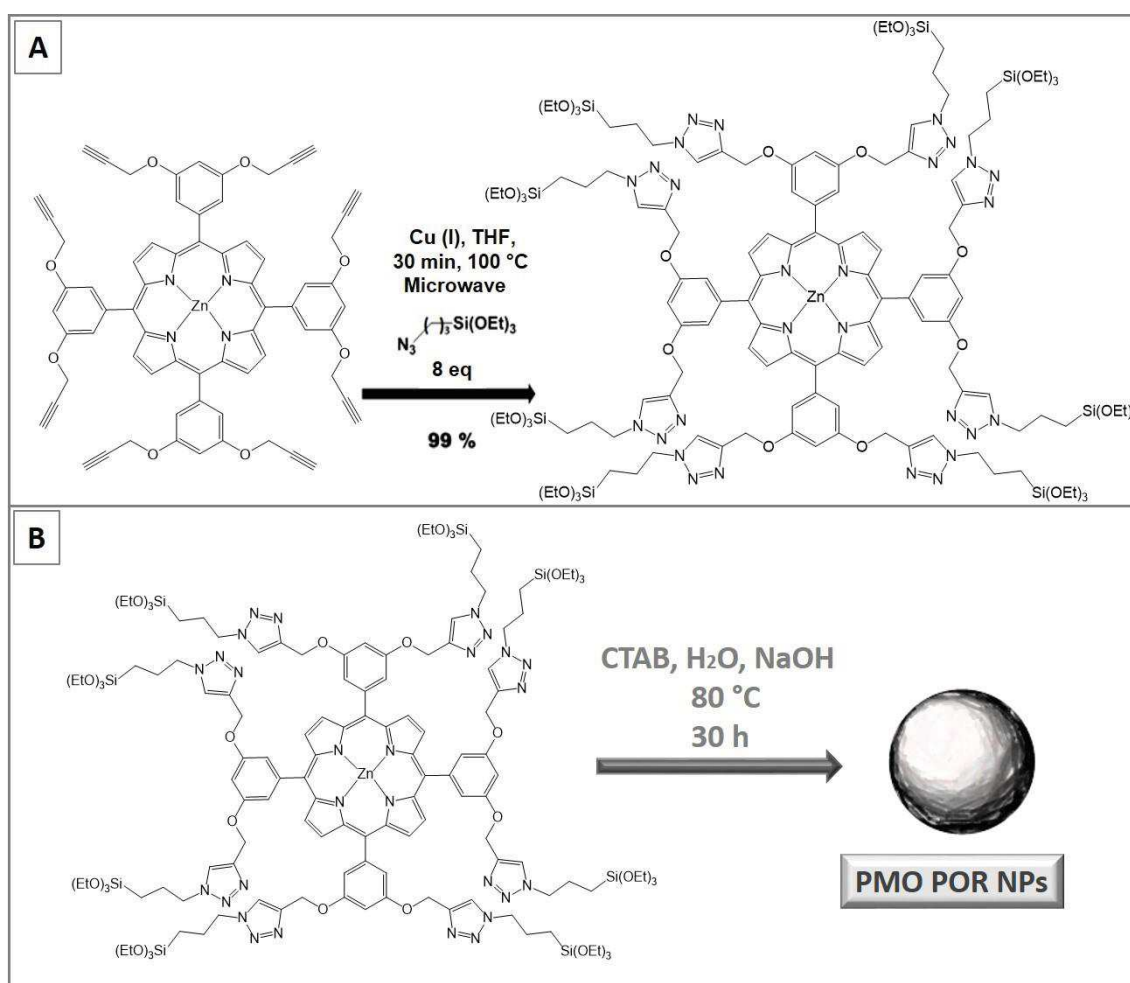
in vivo, using photochemical internalisation. Recently, Smedt et al.¹⁰⁵ described the induced PCI-mediated delivery of siRNA using nanogels as gene vector.

Two-photon near-infrared irradiation has become particularly relevant in the field of nanomedicine since it allows safer and deeper laser penetration in tissues. Due to its non-invasive spatio-temporally-controlled irradiation with a resolution of a micron, it is very promising for PCI¹⁰⁶⁻¹⁰⁸.

In view of these characteristics, two-photon-actuated photochemical internalisation (PCI) for siRNA delivery *via* pure porphyrin mesoporous organosilica nanoparticles is described. Through a sol-gel process, a novel metallated octasilylated porphyrin, obtained by click chemistry, gave rise to 200 nm diameter nanoparticles. The aggregation of the porphyrin molecule was used to apply two-photon near infrared irradiation for *in vitro* fluorescence imaging and PDT in MCF-7 cancer cells. Due to the large porosity of the nanomaterial, siRNA was entrapped and delivered *in vitro* and caused more than 50 % of gene silencing. The positive synergetic effect of the application of two-photon irradiation to deliver siRNA was demonstrated¹⁰⁹. Furthermore, preliminary tests *in vivo* in zebrafish were achieved for the fluorescence imaging and good results were obtained. The nanomaterial was fully characterized using a variety of techniques, including solid state NMR¹¹⁰, allowing the type of aggregation of the photosensitizer molecules to be explained.

4.5.2. Results and discussion

A novel metallated porphyrin, engineered for two-photon excitation (TPE) and possessing eight triethoxysilyl groups, was synthesized by click chemistry (Supp. Inf. S2) from octaalkyne Zn porphyrin and (3-azidopropyl) triethoxysilane at 100° C for 40 min (Scheme 2a). This photosensitizer was used to prepare pure porous porphyrin nanoparticles, in the presence of CTAB as surfactant and NaOH as catalyst. The product (PMOs POR) was obtained after 30 hours of reaction at 80°C (Scheme 2b; Supp. Inf. S3).



Scheme 2. A) Design of the POR precursor via click CuAAC coupling. B) Synthesis of PMO POR NPs.

The composition and properties of the nanoparticles were then characterized. High resolution transmission electron microscopy (HRTEM) analysis revealed 150-250 nm polydisperse NPs (Figure 1a, b). In the images different “slices” of porphyrin that build the material are observed (Figure 1c). Various techniques were used to understand this phenomenon. The distribution size of nanoparticles was determined. The Gaussian analysis gave a mean size at 209 nm (Supp. Inf. S5b). Intensity-averaged Dynamic Light Scattering (DLS) revealed NPs (in an EtOH solution) with a hydrodynamic diameter around 776 nm that reports the aggregation of some nanoparticles (Supp. Inf. S5a).

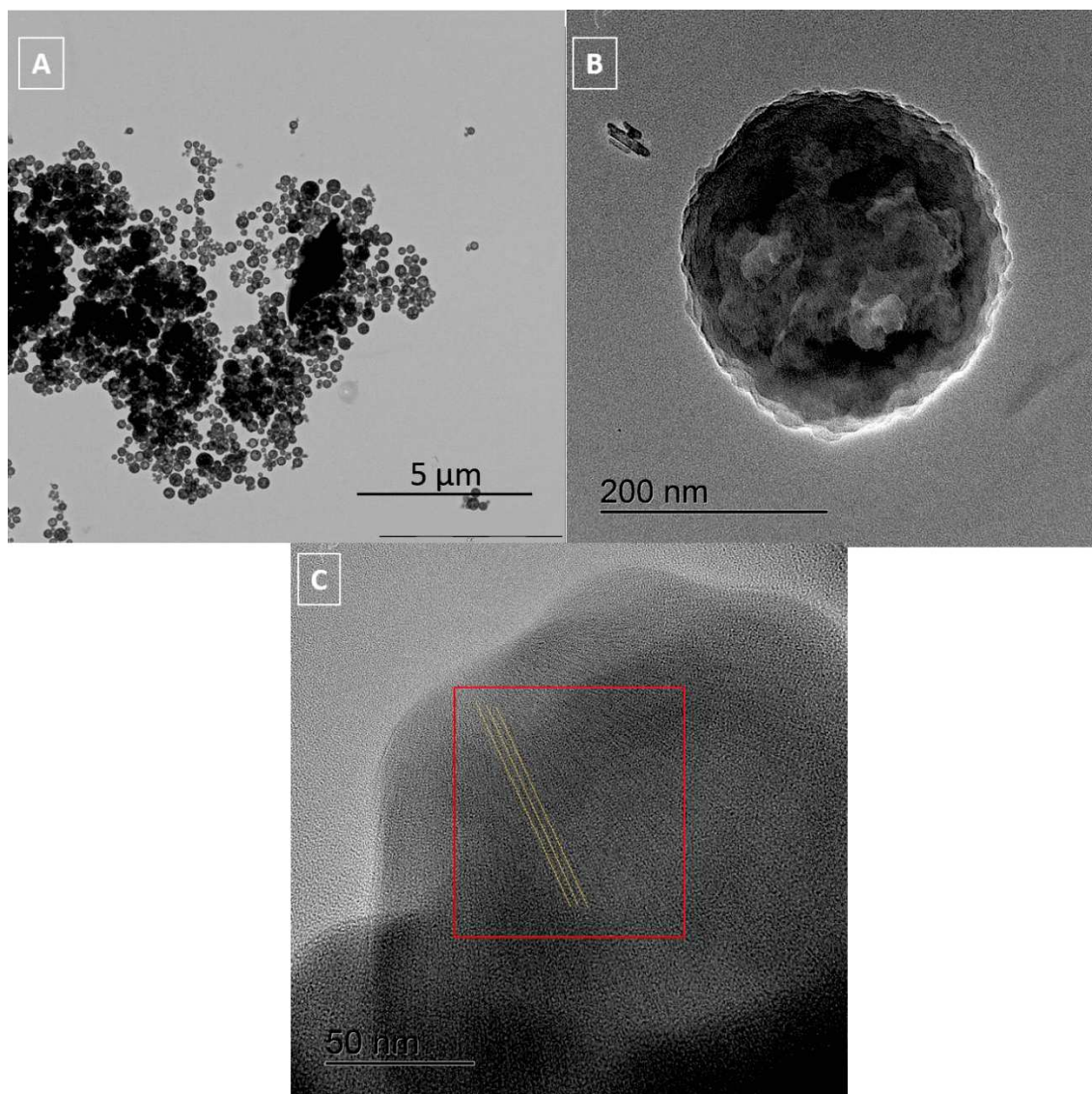


Fig. 1. HRTEM micrographs of as prepared PMOs POR nanoparticles at different magnifications. In yellow, different porphyrin “slices” are represented.

The FTIR spectra of the photosensitizer (Supp. Inf. S6) and the corresponding material confirmed the successful condensation of the nanomaterial (Si-O-Si band at 1050 cm^{-1}). UV-visible spectroscopy of the nanoparticles, in a EtOH solution (Figure 2a), confirmed the formation of the pure metallated porphyrin nanoparticles as shown respectively by the absorption of the intense Soret band at 439 nm and the presence of the two Q bands at 561 and 604 nm. The presence of only two Q bands confirmed that in any case the porphyrin was demetallated during the sol-gel process. Compared to the porphyrin precursor (426, 559, 595 nm) a red shift of the spectra was observed. This can be explained by the formation of J aggregates of porphyrin that are known to increase the two-photon absorption cross-section. The red shift (from 601 and 651 nm for the porphyrin precursor to the 608 and 658 nm for nanoparticles) was also observed by

fluorescence spectroscopy (Figure 2b). A nanoparticle made by stacked porphyrins (as the HRTEM suggested) could explain this type of aggregation.

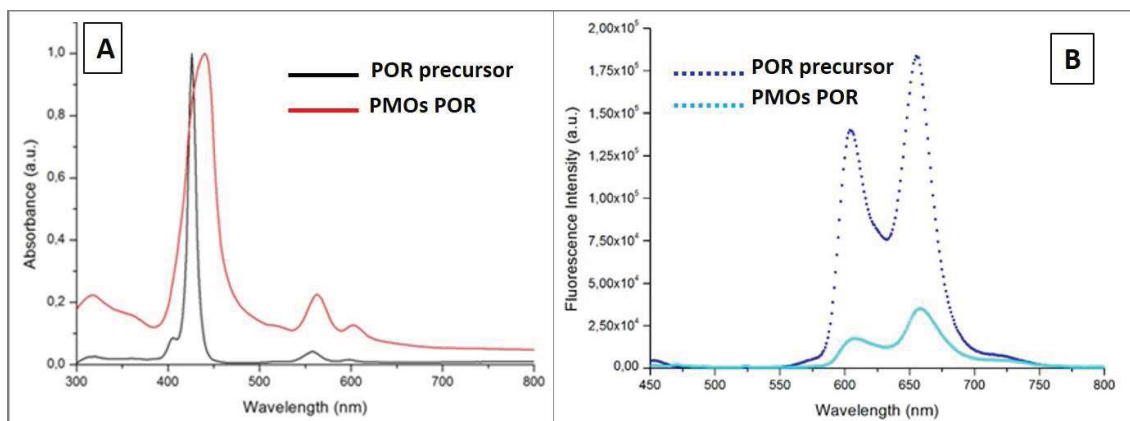


Fig. 2. UV-Visible absorption spectra (A) and fluorescence spectra (B) ($\lambda_{\text{exc}} = 420$ nm) of the porphyrin precursor and PMOs POR NPs (B).

²⁹Si Solid State NMR spectra of PMOs POR (Fig. S9) showed the presence of the siloxane network with a high condensation of the precursor with a T³ resonance at -70 ppm and a small amount of less-condensed material with a T² peak (-52 ppm). Regarding the ¹³C Solid state NMR spectra, an analysis of the material at different contact times (CT, dipolar recoupling pulse of the CPMAS sequence) was carried out to determine with precision the carbons corresponding to each band. At low CT (100 μ s), all the carbons except the quaternary ones were observed. At high CT as 5 ms, the quaternary carbons were observed with high resolution. By comparing the ¹³C NMR spectra of the porphyrin precursor and the spectra of the nanomaterial, and by looking at previous ¹³C NMR studies of porphyrins in the literature, the following attribution of the resonances was derived (Figure 3).

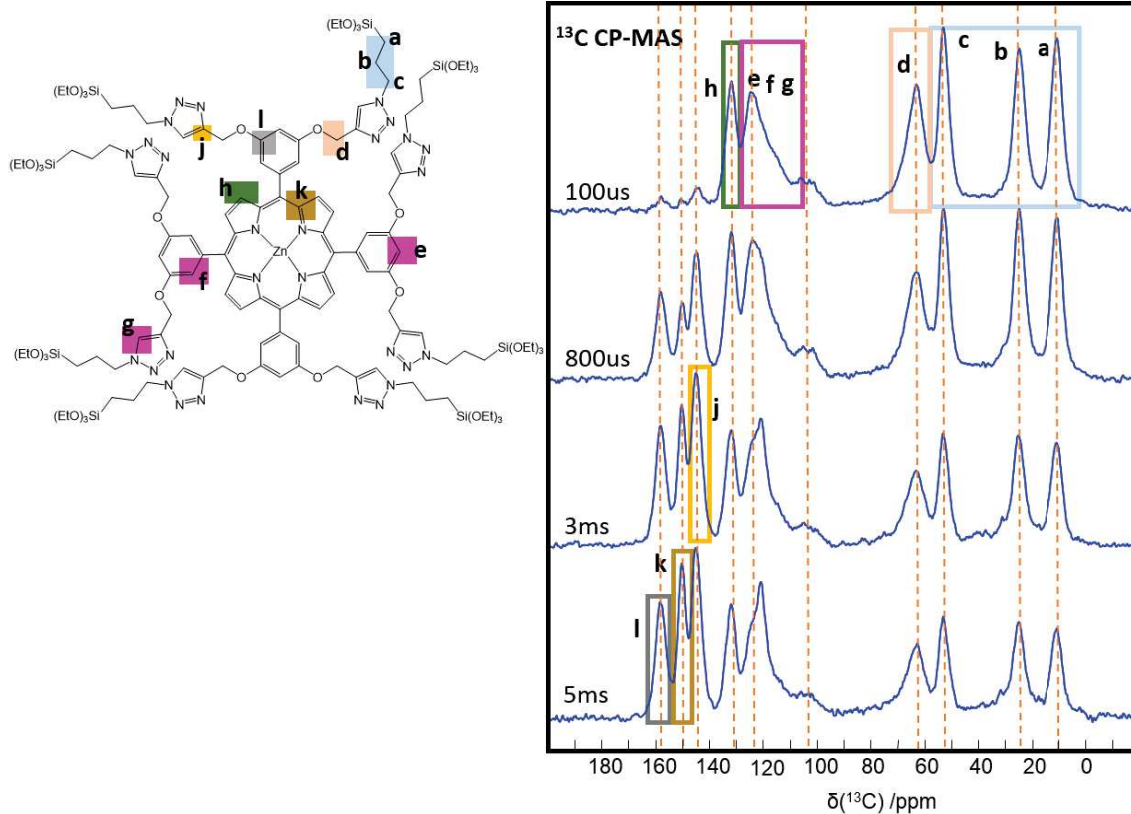
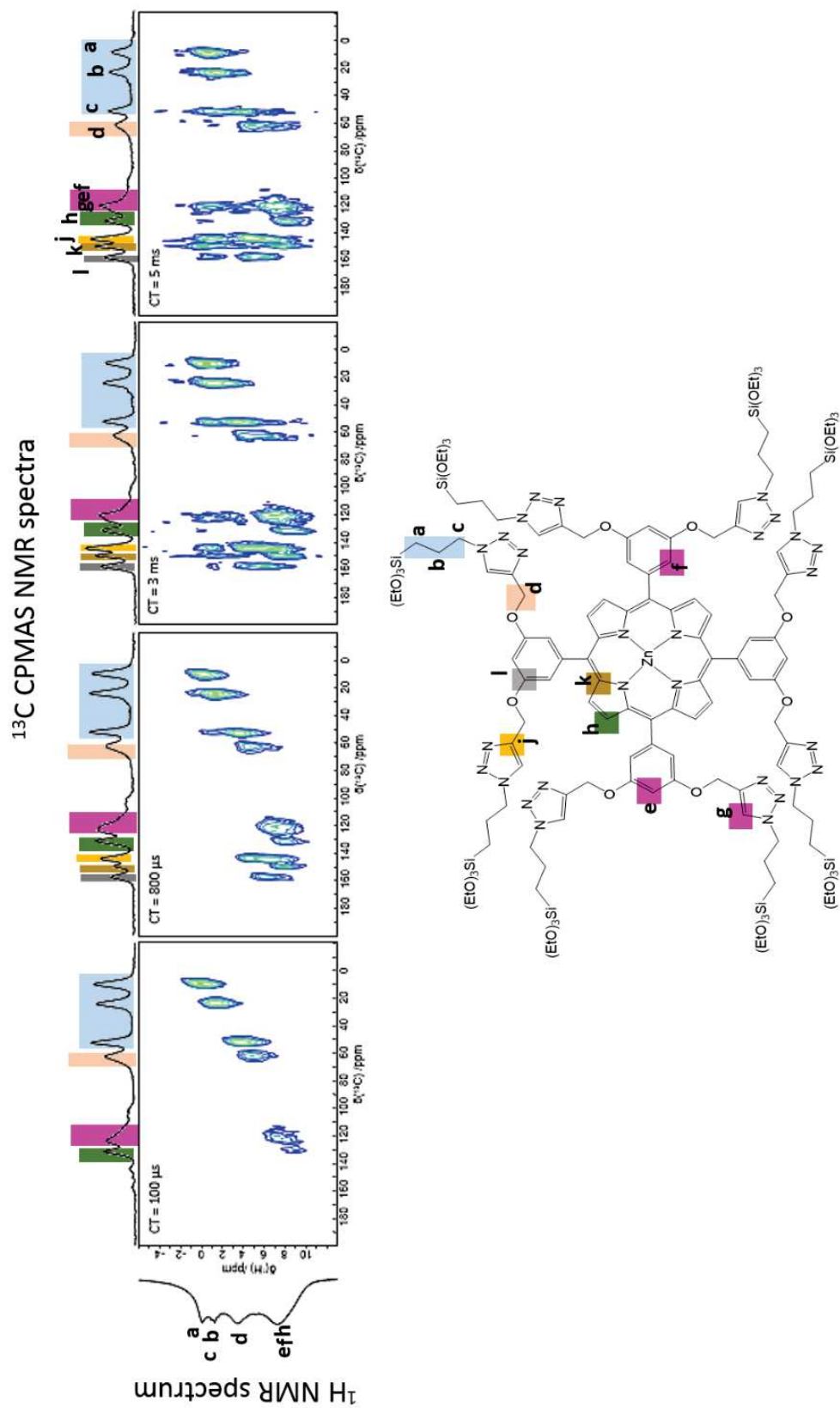


Fig. 3. ^{13}C Solid state CPMAS NMR spectra of POR PMOs NPs. The ^{13}C NMR analysis was done at different contact-times (CT= 100 μs , 80 μs , 3 ms, 5 ms).

A comprehensive study about the aggregation between porphyrin molecules in nanoparticles was realized by 2D ^1H - ^{13}C CPMAS experiments at different CT. With this study it could be observed the proximity between the different functional groups of different porphyrin molecules (Figure 4).

Fig. 4. 2D study NMR of PMOs: correlation between ^1H and ^{13}C resonances at different contact times.



At low CT (100 μ s) only the correlation between the protons and the secondary or tertiary carbons of the porphyrin was detected. The assignment was performed on the basis of the solution ^1H and ^{13}C NMR spectra of the starting silylated porphyrin. The first carbon signal (12.5 ppm) was correlated with the proton at 0.5 ppm that was attributed to $\underline{\text{CH}_2}\text{-Si}$ (**a**). The second and the third carbon signals (27.5 and 52.5 ppm) were correlated with the proton at 1.9 ppm that corresponds to the $\underline{\text{CH}_2}\text{-CH}_2\text{-triazole}$ (**b**) and the proton at 4.4 ppm which corresponds to the $\text{CH}_2\text{-}\underline{\text{CH}_2}\text{-triazole}$ (**c**) respectively. The methylene group of the $\text{O-}\underline{\text{CH}_2}\text{-triazole}$ (**d**; 62.5 ppm) is correlated with the proton signal at 5.4 ppm. Proton signal between 7 and 8 ppm corresponds to the tertiary carbon of triazole (**g**) and the aromatic CH protons of the phenyl (**e**, **f**) which are present in a same large signal at 120 ppm. The last correlation is attributed to the $\underline{\text{CH}}$ of the pyrrole (130 ppm) which is correlated with the proton at 8.9 ppm (**h**).

At CT 800 μ s the quaternary carbon signals come out. The first quaternary signal appeared at 142 ppm and is attributed to the quaternary carbon of the triazole (**j**). As the 2D NMR shows, the carbon is near the protons of the $\text{CH}_2\text{-}\underline{\text{CH}_2}\text{-triazole}$ (**c**) and $\text{O-}\underline{\text{CH}_2}\text{-triazole}$ (**d**) which confirms the attribution of the quaternary carbon signal. At 155 ppm the quaternary carbon of the pyrrole appears (**k**). The signal of the 2D shows that the carbon is not only near to CH of the pyrrole (**h**) and the aromatic of the phenyls (**e**, **f**) but also to the CH of the triazole group (**g**). The last quaternary carbon corresponds to the carbon of the phenyl (**l**). This carbon is near to the $\text{O-}\underline{\text{CH}_2}\text{-triazole}$ (**d**) and the CH of the phenyl (**e**, **f**) and the CH of the pyrrole (**h**). At this CT, it can be proposed that the stacking of the porphyrins explains the proximity between the triazole and pyrrole groups.

At 3 ms the signal of the 2D study are larger, most probably because of the proximities between porphyrin molecules. The quaternary triazole (**j**) is close to the $\underline{\text{CH}_2}\text{-Si}$ (**a**) and the aromatic CH of the phenyl is near the $\underline{\text{CH}_2}\text{-CH}_2\text{-triazole}$ (**b**). At 5 ms the quaternary carbons of the phenyl and the pyrrole groups present a large crosspeak in correlation with the $\underline{\text{CH}_2}\text{-Si}$ (**a**), $\underline{\text{CH}_2}\text{-CH}_2\text{-triazole}$ (**b**) and $\text{CH}_2\text{-}\underline{\text{CH}_2}\text{-triazole}$ (**c**).

The three last CT in the 2D study are consistent with a J-type stacking between the porphyrins molecules as the $\underline{\text{CH}_2}\text{-Si}$ (**a**) and the $\text{CH}_2\text{-}\underline{\text{CH}_2}\text{-triazole}$ (**c**) are close to the pyrrole groups (**h**, **k**).

Besides, the wide angle X-ray diffraction pattern (Supp. Inf. S7) showed a broad peak at 20 °, which corresponds to non-regular repetitions within the siloxane framework. The accessibility of the porous structure of the nanomaterial was demonstrated by N₂-adsorption and desorption technique, presenting a low BET specific surface area at around 230 m².g⁻¹. The BJH pore size analysis (Figure 5b) showed different bands, where 2 nm could correspond to mesoporosity in each slice and 4 and 9 nm could correspond to the separation between each slice. This separation of 4 and 9 nm was also observed by HRTEM that revealed the porosity between two or different slices (Figure 5c). The porosity of 1-2 nm was also observed in one slice (Figure 5d).

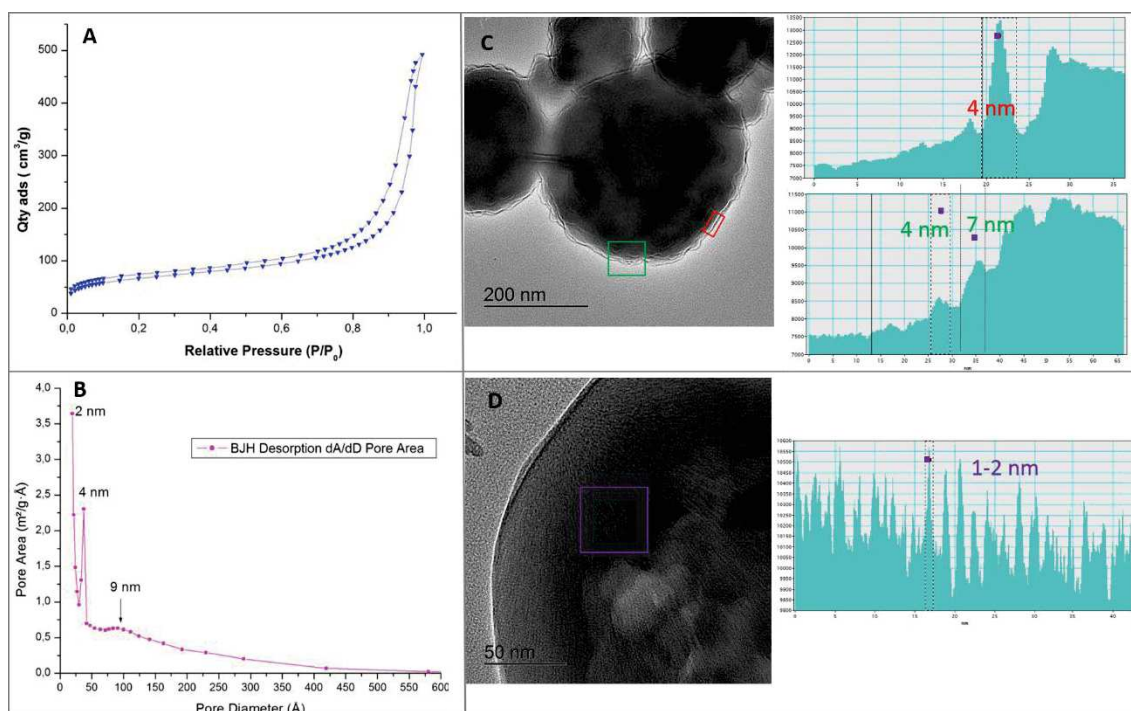


Fig. 5. N₂-adsorption-desorption isotherm (A) and pore size distribution (B) of POR PMO NPs. The study by HRTEM images showed porosity between different slices (C) and porosity in each slice (D).

To confirm the structure and the porosity in the nanoparticles, a tomography study, in which the physical morphology was explored using virtual slices (orthogonal planes), was performed by HRTEM (Figure 6). The image corresponds to the video of the tomogram of the polyamide thin film. In the reconstruction, an xy-orthogonal plane (red) is shown (two simultaneous vantage points) as it travels along the thickness of the thin film (z-axis) from the front to the back surface (and back) revealing how the internal morphology changes at different depths. The thickness of these virtual slices is approximately 2 nm. As it is shown in the image, the nanoparticles present 3D interconnected cavities and different slices constitute the nanoparticles. The strong

attraction between porphyrin molecules which has formed J aggregates and the rapid condensation have given rise to a slices of J aggregates that curve in the presence of surfactant.

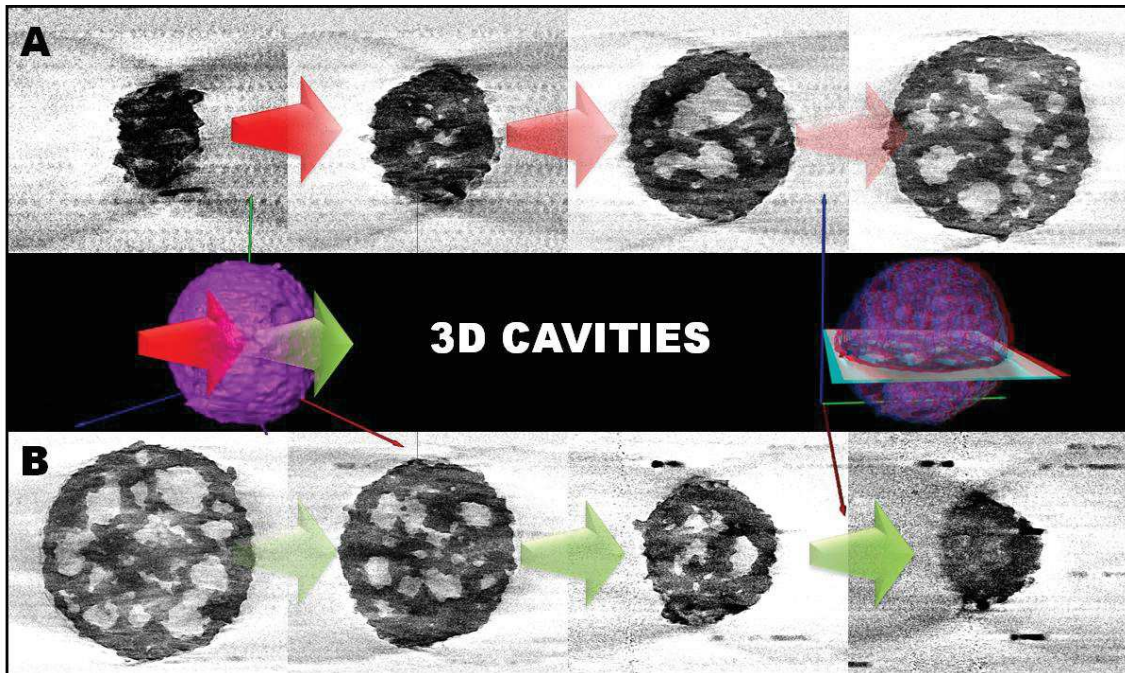


Fig. 6. Video images of the tomogram of the PMOs POR NPs.

The endocytosis of the nanomaterial was evaluated by the two-photon imaging on MCF-7 breast cancer cells (Figure 7). Nanoparticles ($80 \mu\text{g}/\text{mL}$) were incubated in cancer cells for 20 h. The membranes of cells were stained with a Cell Mask Orange Plasma Membrane during 15 minutes before the imaging experiments. Two-photon imaging was performed with a Carl Zeiss confocal microscope at low laser power (6%) at 750 nm. The endocytosis of nanoparticles was clearly seen with the merged images and their efficiency for intracellular tracking was demonstrated.

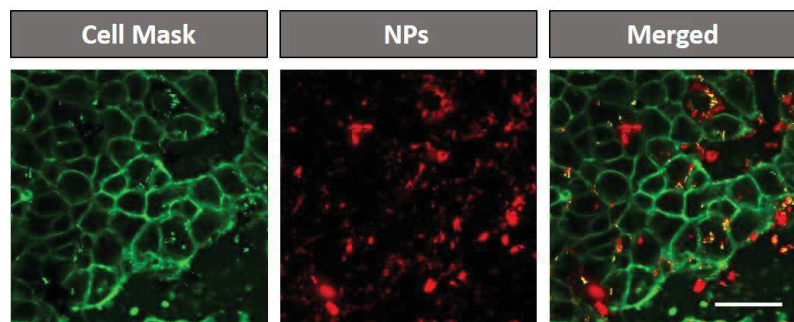


Fig. 7. Two-photon confocal microscopy images of cells NPs incubated during 20 h with $80 \mu\text{g}\cdot\text{mL}^{-1}$ of PMOs POR NPs. Scale bars of 10 μm .

Two-photon *in vitro* therapy was conducted on MCF-7 cancer cells that were incubated with 80 $\mu\text{g/ml}$ of nanoparticles for 24 hours (Supp. Inf. S11). After irradiation at 800 nm, the MTT assay was performed after 48 hours. The nanoparticles caused 37% of selective cell-killing. The siRNA delivery *in vitro* in MCF-7 cancer cells was finally assessed via TPE stimuli. As the nanoparticles showed a negative zeta potential (-33.2 mV), a surface functionalization with APTES was done to change the charge (+5.3 mV) and increase the affinity with the siRNA. The siRNA sequence targeting the luciferase gene (siLuc 5'- AACGTACGCGGAATAACTTCGA-3') was chosen to be encapsulated into the nanoparticles, and the silencing efficiency was tested in stable luciferase-expressing MCF-7 cells. siRNA-NPs were incubated for 20 h at 40 $\mu\text{g/ml}$ with cells. Then, cells were irradiated or not with a confocal Carl Zeiss two-photon microscope at 800 nm. After irradiation, MTT assay was performed after 48 hours. siRNA and nanoparticles alone did not significantly affect the luciferase expression (Figure 8). On the contrary, when the functionalized NPs were mixed in 1/30 weight ratio with siRNA, it led to 50 % of gene silencing effect.

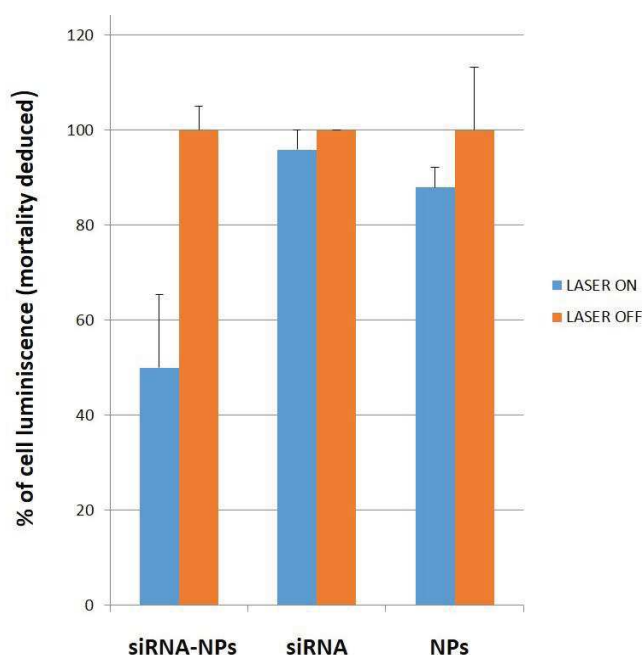


Fig. 8. TPE-gene delivery of NPs (40 $\mu\text{g/ml}$) complexed with siRNA (irradiated at 800 nm).

To perform the efficiency analysis of gene delivery by PMOs nanoparticles *in vivo*, zebrafish larva was chosen as an animal model.

To evaluate the biological activities of the nanoparticles, the GFP mRNA was transcribed from the PCS2 expression vector containing the eGFP ORF. The mRNA

was injected at the one-cell stage and successfully injected embryos were sorted using the green fluorescence driven by the injected GFP mRNA. Embryos were concomitantly injected with siRNA-GFP or empty NPs or NPs functionalized with siRNA-GFP. In this system, the injected GFP mRNAs accumulate to a significant level at 6 hours post-fertilization (hpf). Thus RNAs were prepared at 6 hpf to quantify expression level of the GFP.

As shown in Figure 9, empty nanoparticles did not affect GFP expression. In contrast the siRNA targeting GFP mRNA clearly suppressed the GFP expression ($\approx 75\%$) compared with the injected control with the GFP mRNA alone. Importantly, we observed a significant reduction in the rate of GFP expression in embryos treated with nanoparticles complexed with siRNA-GFP ($\approx 64\%$), suggesting that NPs release siRNA-GFP, which is available to reduce the GFP expression.

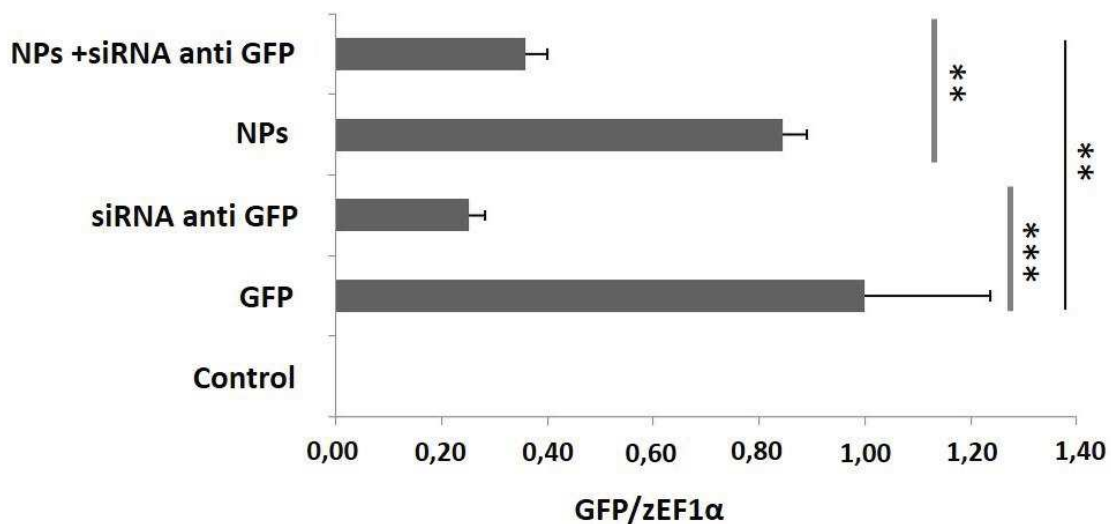


Fig. 9. Effects of NPs complexed to siRNA anti GFP on GFP expression. Quantification by quantitative RT-PCR of GFP mRNA relative to zebrafish EF1 α in 6 hours post-fertilization larvae. Embryos at one-cell stage were not injected (control) or injected with GFP mRNA, siRNA anti GFP, empty NPs or NPs + siRNA anti GFP. RNA was extracted from whole animals (40 larvae per sample) at 6 hours post-injection.

Results are displayed as mean values Crossing point (Cp) with error bars showing 95% confidence intervals in a Student *t* test of three independent experiments. ****p* = 0.001 for GFP vs siRNA anti GFP; ^{NS}*p* = 0.3435 for GFP vs NPs; ***p* = 0.01 for GFP vs NPs+siRNA anti GFP; ***p* = 0.04 for empty NPs vs NPs+siRNA anti GFP.

Two-photon excited photodynamic therapy was also performed on injected embryos. The irradiation at 800 nm did not improve the release from nanoparticles, probably

because they were directly injected into the cytoplasm at the one-cell stage, which was already enough to effectively release the siRNA. However this data demonstrate the strong potential of such PMO for gene delivery.

To confirm the effects of the NPs and to visualize their distribution we used confocal microscopy imaging of fixed whole injected zebrafish larvae at 28 hpf.

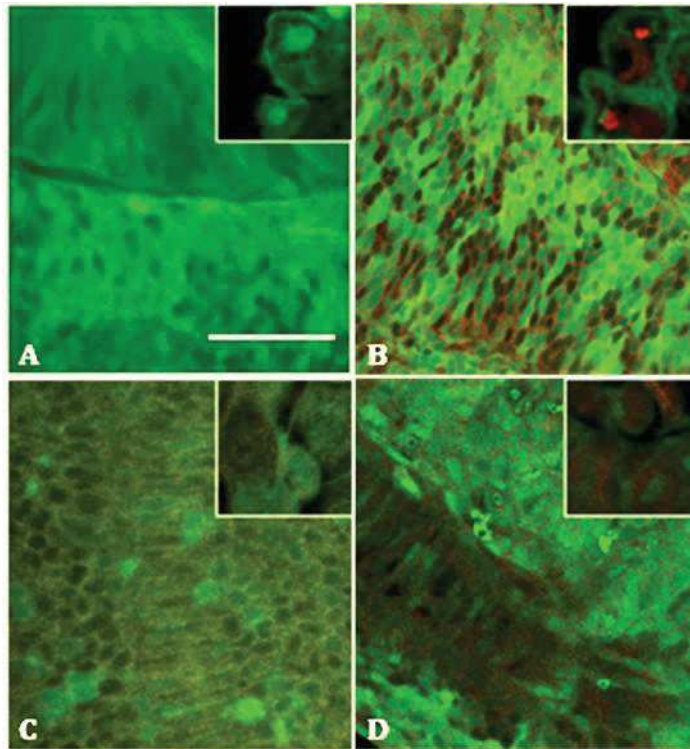


Fig. 10. SiRNA delivery in vivo from nanoparticles. Confocal fluorescence microscopy of 28 h post-fertilization fixed larvae. All panels represent the overlays for green channel (GFP) and red channel (siRNA anti GFP coupled to Cy3 fluorochrome and/or nanoparticles). (A) Transient GFP expression in injected GFP mRNA larvae. (B) The siRNA anti GFP reduces effectively the GFP expression. (C) Nanoparticles colocalize with the GFP expression inducing a yellow staining. (D) The PMOs nanoparticle releases the siRNA anti GFP, which in turn reduces the GFP expression. Scale bar represents 100 μm for all photos. Inset: magnification to show the siRNA anti GFP effect at cellular level.

As shown in Figure 10, a diffuse distribution of GFP expression could be observed in injected control with the GFP mRNA alone (Figure 10a). Multiple yellow dots were visible when GFP mRNA was injected with empty NPs, indicating a consistently colocalization between GFP and nanoparticles (Figure 10c). The capacity of the siRNA targeting GFP mRNA to interfere with GFP expression is visualized by a loss of green signal. A black spot surrounding a red dot were observed when the GFP mRNA was injected either with siRNA anti GFP alone or complexed with NPs (Figure 10b and d,

respectively). The fluorescent micrograph images are consistent with the results from the quantification.

4.5.3. Conclusions

In summary, we have designed organosilica mesoporous nanoparticles from an octasilylated porphyrin that was obtained by click chemistry. The morphology and compositions were fully characterized by various techniques, which showed the presence of the PS. Besides, the J aggregation of porphyrin molecules in the nanoparticle was studied by solid state NMR. Nanoparticles cellular uptake was demonstrated by TPE-fluorescence imaging *in vitro* in MCF-7 breast cancer cells. Two-photon therapy was applied to nanoparticles and lead to 31 % of cancer cell killing. siRNA delivery was demonstrated *in vitro* in MCF-7 cancer cells and produced 50% of gene silencing effect. The gene delivery was also demonstrated *in vivo* in zebrafish model. The confocal fluorescence microscopy showed the reduction of the GFP expression done by the complexed PMOs - siRNA anti GFP. Results concluded that the complex is a promising nanoplatform for theranostics.

4.5.4. Supporting Information

Experimental section

4.5.4. S1. Materials and general procedures

Click reaction was performed using a microwave CEM Discover-Explorer. ^1H and ^{13}C NMR spectra were recorded on a Bruker AC 400 spectrometer. Chemical shifts (in δ units, ppm) are referenced to TMS using CH_2Cl_2 ($\delta= 5.32$ ppm) or CHCl_3 ($\delta= 7.26$ ppm) and CD_2Cl_2 ($\delta=53.6$ ppm) as the internal standards, respectively, for ^1H and ^{13}C NMR spectra. IR spectra were recorded on a Perkin-Elmer 100 FT spectrophotometer. Absorption spectra were recorded on a Hewlett-Packard 8453 spectrophotometer. Dynamic Light scattering analyses were performed using a Cordouan Technologies DL 135 Particle size analyzer instrument. BET analyses were performed using a TRISTAR 3000 gas adsorption analyzer instrument. TEM analyses were performed on a JEOL 1200 EXII instrument.

Cetyltrimethylammonium bromide (CTAB), sodium hydroxide, were purchased from Sigma-Aldrich. (3-azidopropyl) triethoxysilane was obtained from a reported procedure by M.Ortega-Munoz et al. (*Adv. Synth. Catal.* **2006**, 348, 2410).

Wild-type AB zebrafish were purchased from the Zebrafish International Resource Center (ZIRC) as embryos and raised to adulthood in Roussel (ou Verdier) lab's facilities. Only fish directly from ZIRC or their F1 offspring were used as egg producers to avoid inbreeding effects. Embryos were obtained from pairs of adult fish by natural spawning and raised at 28.5°C in tank water.

Nanomaterial synthesis and characterization

4.5.4. S2 Silylation of POR precursor

A mixture of the octapropargyld porphyrine derivative (100 mg, 9.0×10^{-2} mmol), bromotris (triphenylphosphine)copper(I) ($[\text{CuBr}(\text{PPh}_3)_3]$, 13 mg, 1.5×10^{-2} mmol), and anhydrous THF (3 mL) was placed in a 10 mL microwave sealable reactor, and (3-azidopropyl)triethoxysilane (178.1 mg, 7.1×10^{-1} mmol) was added. Then, the tube was flushed with argon and the microwave process was conducted for 30 min at 100 °C (maximum power 200 W). After evaporation of the solvent, the POR precursor was

quantitatively obtained as a purple solid (276.0 mg, 8.9×10^{-2} mmol). The yield of the reaction was 99 %. ^1H NMR (400 MHz, DMSO- d_6): δ (ppm) 8.94 (s, 8H, $\text{H}_{\beta\text{pyrrole}}$), 8.35 (t broad, 4H, H_4aryl), 7.53 (d, $^3J = 1.5$ Hz, 8H, $\text{H}_{2,6\text{aryl}}$), 7.28 (s, 8H, triazole), 5.41 (s, 16H, aryl- CH_2 -triazole), 4.42 (t, 16H, $^3J = 6.9$ Hz, CH_2 - CH_2 -triazole), 3.76 (q, $^3J = 7.0$ Hz, 48H, O- CH_2 - CH_3), 1.95 (m, 16H, CH_2 - CH_2 - CH_2 -Si), 1.15 (t, $^3J = 7.0$ Hz, 72H, O- CH_2 - CH_3), 0.58 (t, $^3J = 8$ Hz, 16H, CH_2 -Si). ^{13}C NMR (400 MHz, DMSO- d_6): δ 157.3, 149.1, 144.8, 142.6, 131.9, 131.5, 128.6, 128.4, 124.5, 119.9, 114.6, 100.8, 61.6, 57.6, 51.7, 23.9, 17.8, 6.9. ^{29}Si NMR (400 MHz, DMSO- d_6): δ -46.5. FTIR (neat KBr) (cm^{-1}) 2973, 2931, 2900, 1600, 1446, 1402, 1357, 1183, 1165, 1125, 1100, 990, 940, 790, 709, 682. UV-Vis (EtOH) λ_{max} , nm: 426, 559, 595. Emission (EtOH): $\lambda_{\text{max}} = 601$, 651 nm ($\lambda_{\text{excitation}} = 420$ nm). MALDI-TOF: calcd for $\text{C}_{140}\text{H}_{212}\text{N}_{28}\text{O}_{32}$ Si_8Zn :3089.440, found 3089.329.

4.5.4. S3. Synthesis of porphyrin periodic mesoporous organosilica nanoparticles (PMOs)

A mixture of CTAB (125 mg), distilled water (60 mL), and sodium hydroxide (437 μL , 2 M) was stirred at 80 °C for 2 h at 750 rpm in a 250 mL three-neck round bottom flask. Then, the two-photon photosensitizer (55 mg, 0.017 mmol, in 1 mL of absolute ethanol) was added to the aforementioned solution, and the condensation process was conducted for 30 h. Afterwards, the solution was cooled to room temperature while stirring; fractions were gathered in propylene tubes and collected by centrifugation during 20 minutes at 20 Krpm. The sample was then washed three times with a solution of NH_4NO_3 in EtOH (6 g/ L), water, and ethanol. Each washing was followed by centrifugation collection of the sample in the same manner. The as-prepared material was dried under vacuum for a few hours. 33.5 mg of product were obtained.

4.5.4. S4. Functionalization of porphyrin periodic mesoporous organosilica nanoparticles (PMOs-NH₂).

20 mg of NPs were put in suspension in 200 μL of EtOH for 10 min. Then 480 μL of deionized water and 31.2 μL of APTS were added. The suspension was neutralized to pH 6 by addition of HCl 0.2M. The reaction was stirred at 750 rpm at RT for 20 h. The sample was then gathered in eppendorf tubes and collected by centrifugation during 12 minutes at 10 Krpm and washed three times with EtOH. NPs were dried under vacuum for few hours.

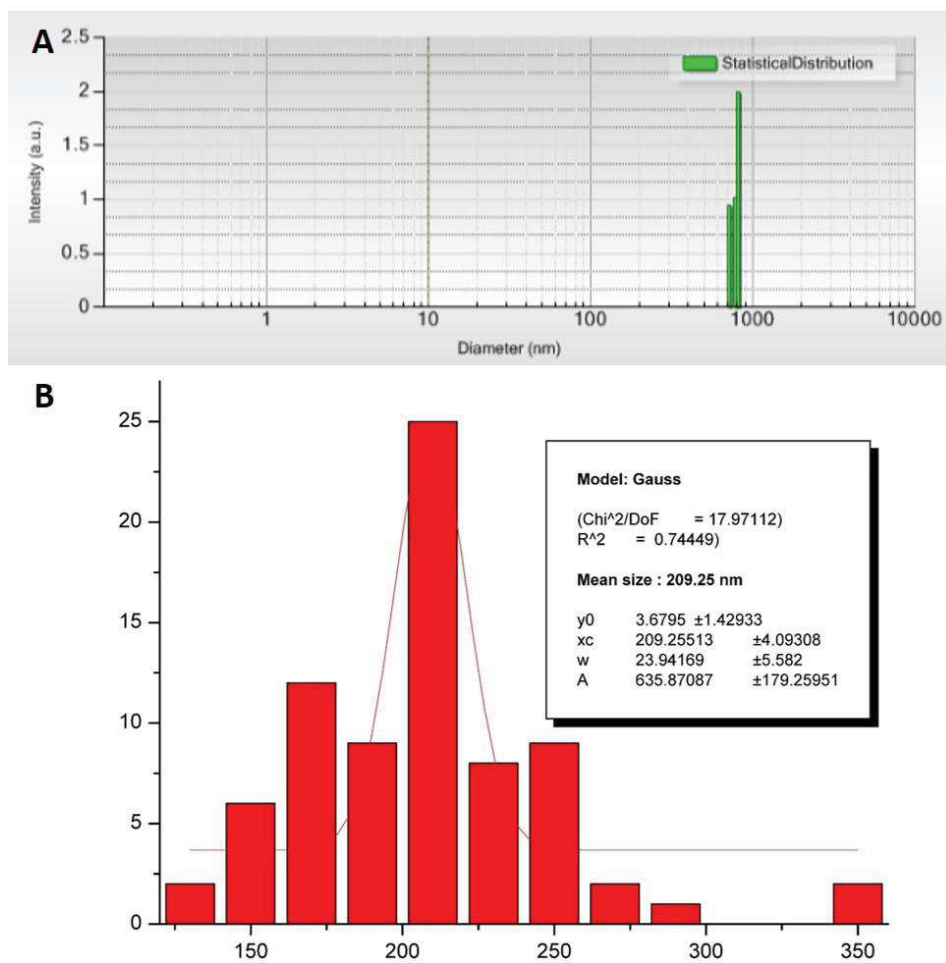


Figure S5. Intensity - Dynamic Light Scattering of nanoparticles (A) and size distribution determined from TEM images (B).

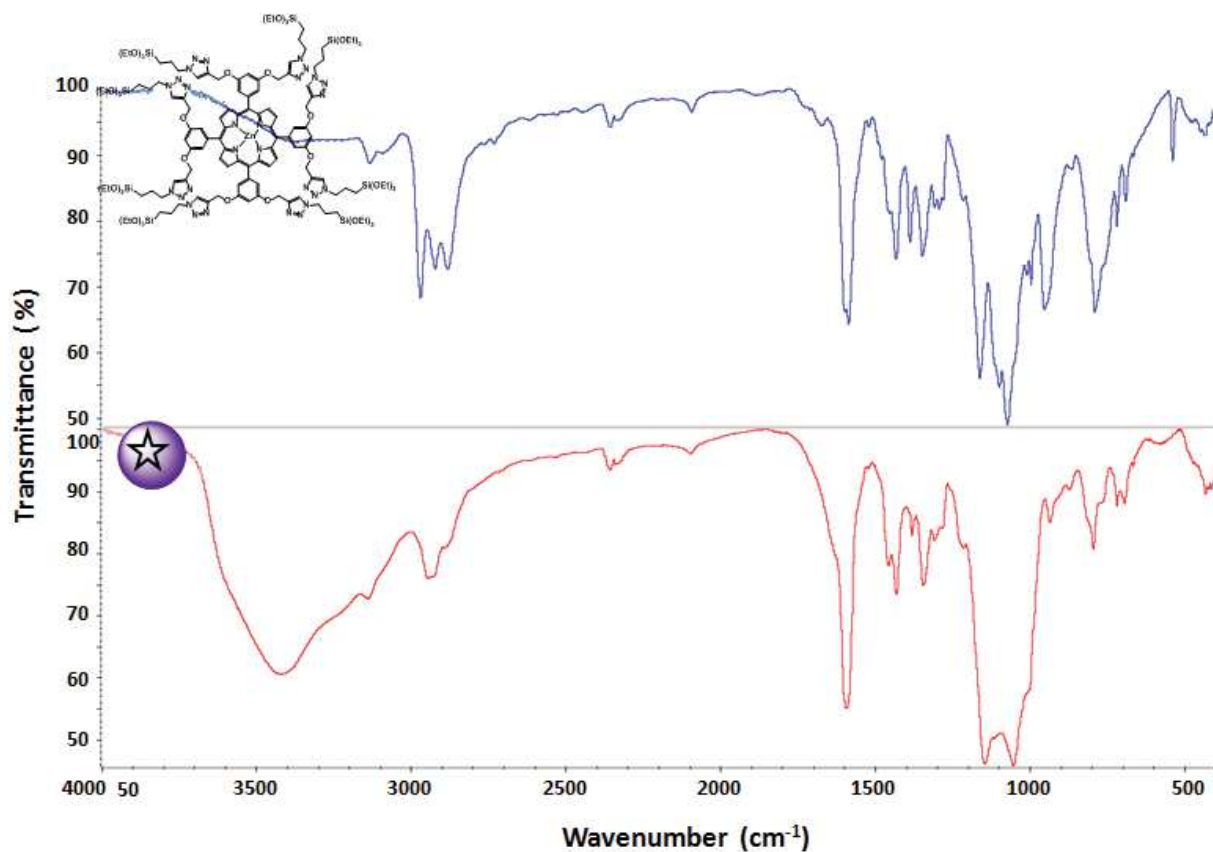


Figure S6. FTIR spectra of the POR precursor and PMOs POR NPs confirming the presence of the ETH and POR moieties in the nanomaterials framework.

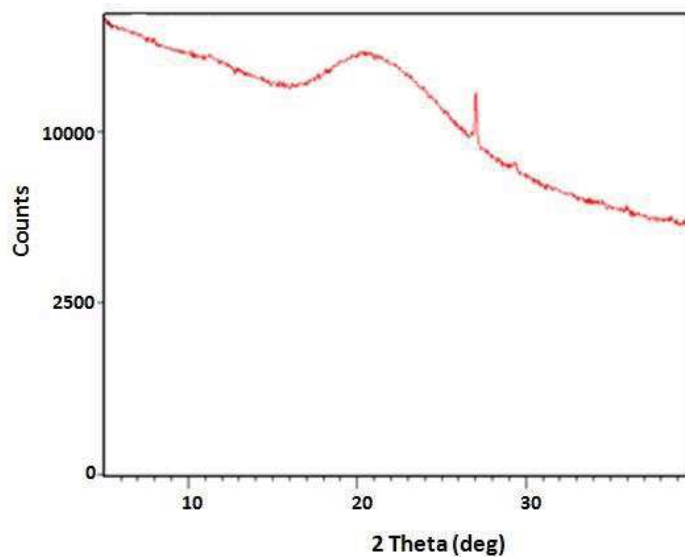


Figure S7. Wide angle X-ray diffraction pattern of POR NPs (Cu k_α). Narrow peaks correspond to the presence of Cu catalyst.

4.5.4. S8. Solid state NMR studies

^{29}Si solid state NMR spectra were recorded with a VARIAN VNMRS300, using Q8MH8 as a reference (low frequency peak at -109.2 ppm). ^{13}C solid state NMR experiments were performed on a Varian VNMRS 600 MHz (14.1 T) NMR spectrometer. A 3.2 mm Varian T3 HXY magic angle spinning (MAS) probe was used for ^1H and ^{13}C experiments. The operating frequencies for ^1H and ^{13}C were 599.81 and 150.84 MHz, respectively.

^1H -MAS experiments were carried out at a spinning speed of 18 kHz. The 90° excitation pulse was set to 2.5 μs . 4 transients were acquired, with a recycle delay of 0.5 to 16 s, depending on the sample. ^1H chemical shifts were referenced externally to adamantane at 1.8 ppm (used as a secondary reference).

One-dimensional ^1H - ^{13}C CPMAS NMR spectra were recorded spinning at 18 kHz, using a 90° ^1H excitation pulse of 2.5 μs , followed by a contact time of 0.1, 0.8, 3.0 or 5.0 ms (ramped pulse). Spinal-64 ^1H decoupling 29 (100 kHz RF) was applied during acquisition. A recycle delay of 0.5 to 8.0 s was used, depending on the sample, and the total number of transients acquired ranged from 950 to 12000. ^{13}C chemical shifts were referenced externally to adamantane (used as a secondary reference), the high frequency peak being set to 38.5 ppm. Two-dimensional ^1H - ^{13}C CP heteronuclear correlation experiments were also recorded under similar conditions and at the same contact times, using an FSLG (frequency-switched Lee-Goldburg) homonuclear decoupling scheme during the t_1 evolution period.

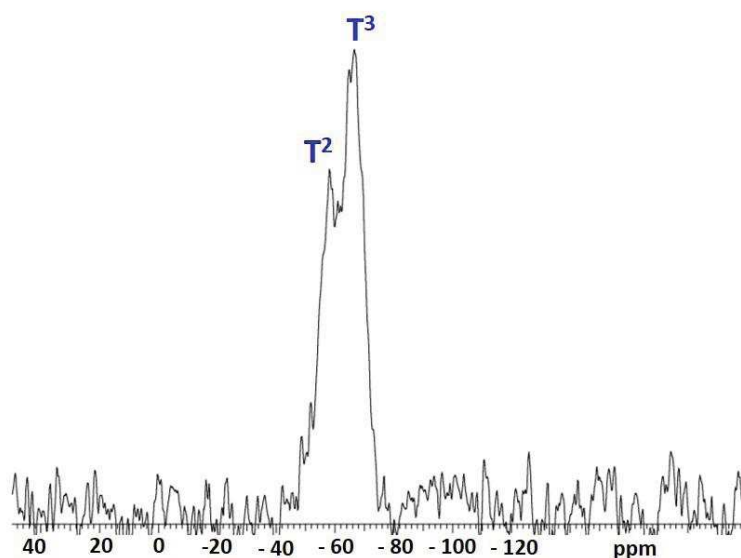


Figure S9. ^{29}Si CPMAS solid state NMR.

***In vitro* studies**

4.5.4. S10. Two-photon fluorescence imaging

The day prior to the experiment, MCF-7 cells were seeded onto bottom glass dishes (World Precision Instrument, Stevenage, UK) at a density of 10^6 cells.cm⁻². Adherent cells were then washed once and incubated in 1 ml culture medium containing NPs at a concentration of 80 $\mu\text{g.mL}^{-1}$ for 20 h. Fifteen min before the end of incubation, cells were loaded with Cell Mask (Invitrogen, Cergy Pontoise, France) for membrane staining at a final concentration of 5 $\mu\text{g.mL}^{-1}$. Before visualization, cells were washed gently with phenol red-free DMEM. Cells were then scanned with LSM 780 LIVE (Carl Zeiss, Le Pecq, France), at 750 nm with a slice depth (Z stack) of 0.62 μm .

4.5.4. S11. TPE-therapy

MCF-7 human breast cancer cells were cultured in Dulbecco's modified Eagle's medium (DMEM) supplemented with 10% fetal bovine serum and 50 $\mu\text{g.mL}^{-1}$ gentamycin. All cells were allowed to grow in humidified atmosphere at 37°C under 5% CO₂. For *in vitro* phototoxicity, MCF-7 cells were seeded into a 384 multiwell glass-bottomed plate (thickness 0.17 mm), with a black polystyrene frame, 2000 cells per well in 50 μL of culture medium, and allowed to grow for 24 h. NPs were then dispersed under ultrasounds in PBS at a concentration of 1 mg.mL^{-1} and cells were then incubated for 20 h with or without nanoparticles at a final concentration of 80 $\mu\text{g.mL}^{-1}$ in supplemented DMEM. After incubation with NPs, cells were washed twice, maintained in fresh culture medium, and then submitted (or not) to laser irradiation; with the Carl Zeiss Microscope LSM 780 LIVE confocal microscope (laser power input 3W). Half of the well was irradiated at 800 nm by three scans of 1.57 s duration in 4 different areas of the well. The laser beam was focused by a microscope objective lens (Carl Zeiss 10x, NA 0.4). After 2 days, the MTT assay was performed and was corrected.

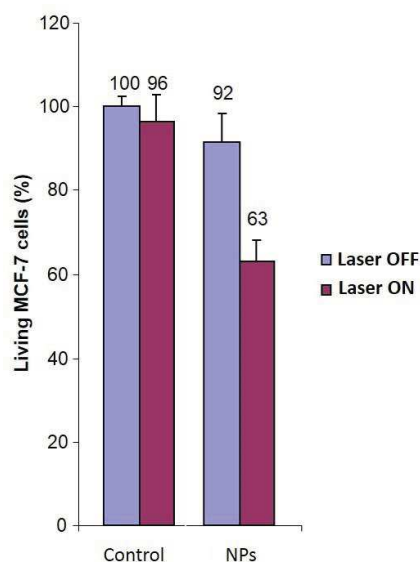


Fig. S11. TPE-triggered in MCF-7 cancer cells incubated with 80 $\mu\text{g/ml}$ NPs (irradiated at 800 nm).

***In vivo* studies**

4.5.4. S12. GFP mRNA transcription

10 μg of the PCS2-eGFP expression plasmid was linearised by NotI and then purified using Invitrogen kit. 1 μg of linearised plasmid was transcribed using the RNA polymerase DNA dependant: Sp6 (Roche) and then treated with 1 μl of turbo DNase. Finally the GFP mRNA was purified using Marcherey-Nagel Nucleospin RNA Kit.

4.5.4. S13. Injection in zebrafish

PMOs nanoparticles alone are diluted to 100 $\mu\text{g/ml}$ in water containing 1% phenol red and 300 pg GFP mRNA. 100 $\mu\text{g/ml}$ of nanoparticles are complexed with 250 nM siRNA (against GFP mRNA) in water containing 1% phenol red and 300 pg GFP mRNA for 30 min. Each solution is injected (1 nl) in the cytoplasm at the one cell stage. Developing embryos were observed at 3 hours post fertilization (hpf) under an Olympus MVX10 epifluorescence microscope and poorly fluorescent embryos were discarded. For each condition, the injected (or not) embryos were divided into 2 sets: one that will be irradiated and the other not.

4.5.4. S14. Two-photon excited photodynamic therapy

For Two-photon excited irradiation, zebrafish larvae were placed into multi-well glass bottom (thickness 0.17 mm) and submitted to laser irradiation.

Two-photon irradiation was performed on a confocal microscope equipped with a mode-locked Ti-sapphire laser generating 100 fs wide pulses at a 80 MHz rate. The laser beam is focused by a microscope objective lens (10×, NA 0.4). The wells were irradiated at 800 nm by 3 scans of 1.25 s each and the surface of the scanned areas was $1.5 \times 1.5 \text{ mm}^2$, with a slice depth of 0.67 μm .

4.5.4. S15. RNA extraction and qRT-PCR

Total RNA from 40 pooled zebrafish embryos were prepared using Marcherey-Nagel Nucleospin RNA Kit and were OligodT primed reverse transcribed using M-MLV reverse transcriptase. Quantitative RT-PCRs were performed on a LightCycler 480 system (Roche, France), following manufacturer's instructions (SYBR Green format, Roche Applied Science, Meylan, France). PCR conditions were as follows: 3 min denaturation at 95°C, 45 cycles of 95°C for 4 sec, 65°C for 14 sec and 72°C for 19 sec. The *zEF1a* gene was used as internal control.

4.5.4. S16. Fluorescence imaging

Zebrafish larvae of 24 hpf were manually dechorionated and then treated with 1-phenyl 2-thiourea (PTU), leading to generating transparent zebrafish (to improve signal detection by confocal microscopy). The embryos were fixed at 28 hpf in 4% PFA, washed in PBS, manually deyolked and then mounted flat onto transparent slides with a coverslip (using Dako fluorescent mounting medium). Confocal fluorescence microscopy was performed using a Leica DM2500CSQ upright microscope with a Leica TCS SPE confocal scan head, differential interference contrast (DIC) optics and a SuperZGalvo SPE z-step controller.

Fixed embryos were observed with a 40X Leica Apo oil 1.15 NA or objective. Overlays of fluorescent images were processed and assembled using LAS-AF software. Final image analysis and visualization were performed using ImageJ-win32 to adjust levels and brightness and to remove out-of-focus background fluorescence.

4.6. General conclusions and perspectives

Different porphyrin photosensitizers were silylated to be used as precursors for the synthesis of periodic mesoporous organosilica nanoparticles. Their use *in vitro* for two-photon therapy, fluorescence imaging and drug and gene delivery was demonstrated. First, PMOs nanoparticles were synthesized by sol-gel process *via* co-condensation between the bis-silylated ethane precursor and a tetrasilylated free base porphyrin. Their PDT effect was studied under an irradiation at 800 nm in MCF-7 breast cancer cells, with almost 30% of death. Imaging results at 750 nm were also reported for the nanoparticles and the endocytosis in cells was confirmed. Gemcitabine was loaded into the porous structure, obtaining a drug loading of 50 wt %. The synergetic effect between the two-photon irradiation and the drug delivery was demonstrated *in vitro* in MCF-7 cancer cells. The combination of both phenomena gave rise to 60 % of cell death.

PMOs nanoparticles were also synthesized by sol-gel process *via* co-condensation between the bis-silylated ethylene precursor and an octasilylated metallated porphyrin. The porphyrin precursor was silylated quantitatively by click chemistry using a copper catalyst. The internalisation of the nanoparticles in cancer cells was confirmed by two-photon fluorescence imaging at 750 nm and 800 nm. Doxorubicin was loaded into the porous structure and was delivered *in vitro* obtaining 75 % of cell killing with a concentration of loaded-NPs of only 1 µg/ml.

In a third part, nanodiamonds were encapsulated in a periodic mesoporous organosilica structure made from a bis-silylated ethane or ethylene precursor. Under two-photon irradiation, nanodiamonds could produce ROS species that was confirmed by ROS imaging using DCFDA detection assay. The systems were used as doxorubicin nanovehicle producing around 40 % of cell killing. The combination with two-photon irradiation leads to increase the mortality to 87 % of cell killing.

In the last part of the chapter, pure porphyrin PMOs were synthesized from an octasilylated porphyrin obtained by click chemistry. The characterization by different techniques as solid NMR, UV-visible or HRTEM explained the presence of J aggregation between the porphyrin molecules and the presence of interconnected cavities. siRNA gene delivery was performed *in vitro* in MCF-7 breast cancer cells and the synergetic application of two-photon therapy leads to 50 % of gene silencing effect. The gene delivery was also performed *in vivo* in zebrafish model. Finally, the extinction

of the GFP gene present in zebrafish by the anti-GFPsiRNA loaded in the nanoparticles was established by confocal fluorescence imaging.

In a near future, the functionalization of the nanoparticles with targeting molecules could be envisaged to improve their internalisation in cells. Xenografted tumour could be used for the *in vivo* test in zebrafish to demonstrate the potential of these new nanoplatforms in cancer treatment.

4.7. References

1. S. Inagaki, S. Guan, Y. Fukushima, T. Ohsuna and O. Terasaki, *J. Am. Chem. Soc.*, 1999, **121**, 9611-9614.
2. T. Asefa, M. J. MacLachlan, N. Coombs and G. A. Ozin, *Nature*, 1999, **402**, 867-871.
3. B. J. Melde, B. T. Holland, C. F. Blanford and A. Stein, *Chemistry of Materials*, 1999, **11**, 3302-3308.
4. P. Van der Voort, D. Esquivel, E. De Canck, F. Goethals, I. Van Driessche and F. J. Romero-Salguero, *Chem. Soc. Rev.*, 2013, **42**, 3913-3955.
5. M. Ikai, Y. Maegawa, Y. Goto, T. Tani and S. Inagaki, *Journal of Materials Chemistry A*, 2014, **2**, 11857-11865.
6. M. Ide, E. De Canck, I. Van Driessche, F. Lynen and P. Van Der Voort, *RSC Adv.*, 2015, **5**, 5546-5552.
7. J. Huang, F. Zhang and H. Li, *Applied Catalysis A: General*, 2012, **431-432**, 95-103.
8. S. S. Park, M. S. Moorthy and C.-S. Ha, *Korean Journal of Chemical Engineering*, 2014, **31**, 1707-1719.
9. S. Shylesh and A. P. Singh, *Microporous and Mesoporous Materials*, 2006, **94**, 127-138.
10. Y. Xia and R. Mokaya, *The Journal of Physical Chemistry B*, 2006, **110**, 3889-3894.
11. C. Vercaemst, M. Ide, B. Allaert, N. Ledoux, F. Verpoort and P. Van Der Voort, *Chem. Commun.*, 2007, 2261-2263.
12. K. Landskron and G. A. Ozin, *Science*, 2004, **306**, 1529-1532.
13. Y. Li, F. Auras, F. LÄbermann, M. DÄblingler, J. Schuster, L. Peter, D. Trauner and T. Bein, *J. Am. Chem. Soc.*, 2013, **135**, 18513-18519.
14. H. Djojoputro, X. F. Zhou, S. Z. Qiao, L. Z. Wang, C. Z. Yu and G. Q. Lu, *J. Am. Chem. Soc.*, 2006, **128**, 6320-6321.
15. B. Guan, Y. Cui, Z. Ren, Z.-a. Qiao, L. Wang, Y. Liu and Q. Huo, *Nanoscale*, 2012, **4**, 6588-6596.
16. J. Croissant, X. Cattoen, M. W. C. Man, A. Gallud, L. Raehm, P. Trens, M. Maynadier and J.-O. Durand, *Adv. Mater.*, 2014, **26**, 6174-6178.
17. M. Park, S. S. Park, M. Selvaraj, I. Kim and C.-S. Ha, *J. Porous Mater.*, 2011, **18**, 217-223.
18. M. Park, S. S. Park, M. Selvaraj, D. Zhao and C.-S. Ha, *Microporous and Mesoporous Materials*, 2009, **124**, 76-83.
19. C. X. Lin, S. Z. Qiao, C. Z. Yu, S. Ismadji and G. Q. Lu, *Microporous and Mesoporous Materials*, 2009, **117**, 213-219.
20. J. Croissant, D. Salles, M. Maynadier, O. Mongin, V. Hugues, M. Banchard-Desce, X. Cattoen, M. W. C. Man, A. Gallud, M. Garcia, M. Gary-Bobo, L. Raehm and J.-O. Durand, *Chemistry of Materials*, 2014, **26**, 7214-7220.
21. L. H. R. a. P. Couvreur, *Current Pharmaceutical Design*, 2008, **14**, 1124-1137.
22. R. Hill, M. Rabb, P. A. Madureira, D. Clements, S. A. Gujar, D. M. Waisman, C. A. Giacomantonio and P. W. K. Lee, *Cell Death Dis*, 2013, **4**, e791.

23. S. Adachi, S. Kokura, T. Okayama, T. Ishikawa, T. Takagi, O. Handa, Y. Naito and T. Yoshikawa, *International Journal of Hyperthermia*, 2009, **25**, 210-219.
24. M. Y. Jiang PH, Sawabu N, Minamoto T., *World J Gastroenterol* 2006, **12**, 1597-1602.
25. A. RP, *Anti-Cancer Drugs*, 1995, **6**, 63-64.
26. R. Khaira, J. Sharma and V. Saini, *The Scientific World Journal*, 2014, **2014**, 560962.
27. J.-m. Li, W. Chen, H. Wang, C. Jin, X.-j. Yu, W.-y. Lu, L. Cui, D.-l. Fu, Q.-x. Ni and H.-m. Hou, *Acta Pharmacol Sin*, 2009, **30**, 1337-1343.
28. H. Meng, M. Wang, H. Liu, X. Liu, A. Situ, B. Wu, Z. Ji, C. H. Chang and A. E. Nel, *ACS Nano*, 2015, **9**, 3540-3557.
29. B. M. Fung, A. K. Khitrin and K. Ermolaev, *Journal of Magnetic Resonance*, 2000, **142**, 97-101.
30. M. Wu, Y. Chen, L. Zhang, X. Li, X. Cai, Y. Du, L. Zhang and J. Shi, *J. Mater. Chem. B*, 2015, **3**, 766-775.
31. X. Qian, W. Wang, W. Kong and Y. Chen, *RSC Adv.*, 2014, **4**, 17950-17958.
32. X. Li, L. Zhou, Y. Wei, A. M. El-Toni, F. Zhang and D. Zhao, *J. Am. Chem. Soc.*, 2014, **136**, 15086-15092.
33. Y. Chen, P. Xu, H. Chen, Y. Li, W. Bu, Z. Shu, Y. Li, J. Zhang, L. Zhang, L. Pan, X. Cui, Z. Hua, J. Wang, L. Zhang and J. Shi, *Adv. Mater.*, 2013, **25**, 3100-3105.
34. Y. Chen, Q. Meng, M. Wu, S. Wang, P. Xu, H. Chen, Y. Li, L. Zhang, L. Wang and J. Shi, *J. Am. Chem. Soc.*, 2014, **136**, 16326-16334.
35. J. Croissant, X. Cattoen, M. Wong Chi Man, P. Dieudonne, C. Charnay, L. Raehm and J.-O. Durand, *Adv. Mater.*, 2015, **27**, 145-149.
36. C. Urata, H. Yamada, R. Wakabayashi, Y. Aoyama, S. Hirose, S. Arai, S. Takeoka, Y. Yamauchi and K. Kuroda, *J. Am. Chem. Soc.*, 2011, **133**, 8102-8105.
37. J. Dimitrijevic, L. Krapf, C. Wolter, C. Schmidtke, J.-P. Merkl, T. Jochum, A. Kornowski, A. Schueth, A. Gebert, G. Huettmann, T. Vossmeier and H. Weller, *Nanoscale*, 2014, **6**, 10413-10422.
38. D. Ding, C. C. Goh, G. Feng, Z. Zhao, J. Liu, R. Liu, N. Tomczak, J. Geng, B. Z. Tang, L. G. Ng and B. Liu, *Adv. Mater.*, 2013, **25**, 6083-6088.
39. *Application: WO Pat.*, 2010-EP690352011073054, 2011.
40. V. Leuret, L. Raehm, J. O. Durand, M. Smahhi, M. H. V. Werts, M. Blanchard-Desce, D. Methy-Gonnod and C. Dubernet, *J. Biomed. Nanotechnol.*, 2010, **6**, 176-180.
41. J. Croissant, M. Maynadier, A. Gallud, H. P. N'Dongo, J. L. Nyalosaso, G. Derrien, C. Charnay, J.-O. Durand, L. Raehm, F. Serein-Spirau, N. Cheminet, T. Jarrosson, O. Mongin, M. Blanchard-Desce, M. Gary-Bobo, M. Garcia, J. Lu, F. Tamanoi, D. Tarn, T. M. Guardado-Alvarez and J. I. Zink, *Angew. Chem. Int. Ed.*, 2013, **52**, 13813-13817.
42. J. Croissant, A. Chaix, O. Mongin, M. Wang, S. Clement, L. Raehm, J.-O. Durand, V. Hugues, M. Blanchard-Desce, M. Maynadier, A. Gallud, M. Gary-Bobo, M. Garcia, J. Lu, F. Tamanoi, D. P. Ferris, D. Tarn and J. I. Zink, *Small (Weinheim an der Bergstrasse, Germany)*, 2014, **10**, 1752-1755.
43. A. Eggenspiller, C. Michelin, N. Desbois, P. Richard, J. M. Barbe, F. Denat, C. Licon, C. Gaidon, A. Sayeh, P. Choquet and C. P. Gros, *Eur. J. Org. Chem.*, 2013, **2013**, 6629-6643.

44. K. Burglova, A. Nouredine, J. Hodacova, G. Toquer, X. Cattoen and M. Wong Chi Man, *Chem. Eur. J.*, 2014, **20**, 10371-10382.
45. R. Giovannetti, *Macro to Nano Spectroscopy*, 2012.
46. P. C. Ray and Z. Sainudeen, *J. Phys. Chem. A*, 2006, **110**, 12342-12347.
47. A. Barras, J. I. Lyskawa, S. Szunerits, P. Woisel and R. Boukherroub, *Langmuir*, 2011, **27**, 12451-12457.
48. A. Barras, S. Szunerits, L. Marcon, N. Monfilliette-Dupont and R. Boukherroub, *Langmuir*, 2010, **26**, 13168-13172.
49. Y.-R. Chang, H.-Y. Lee, K. Chen, C.-C. Chang, D.-S. Tsai, C.-C. Fu, T.-S. Lim, Y.-K. Tzeng, C.-Y. Fang, C.-C. Han, H.-C. Chang and W. Fann, *Nat Nano*, 2008, **3**, 284-288.
50. S. A. Dahoumane, M. N. Nguyen, A. Thorel, J.-P. Boudou, M. M. Chehimi and C. Mangeney, *Langmuir*, 2009, **25**, 9633-9638.
51. A. Krüger, *Angew. Chem. Int. Ed.*, 2006, **45**, 6426-6427.
52. A. Krüger, *Chem. Eur. J.*, 2008, **14**, 1382-1390.
53. Y. Liang, M. Ozawa and A. Krueger, *ACS Nano*, 2009, **3**, 2288-2296.
54. V. N. Mochalin, O. Shenderova, D. Ho and Y. Gogotsi, *Nat. Nanotechnol.*, 2012, **7**, 11-23.
55. V. Vijayanthimala, D. K. Lee, S. V. Kim, A. Yen, N. Tsai, D. Ho, H.-C. Chang and O. Shenderova, *Expert Opin. Drug Delivery*, 2015, **12**, 735-749.
56. D. Passeri, F. Rinaldi, C. Ingallina, M. Carafa, M. Rossi, M. L. Terranova and C. Marianecchi, *J. Nanosci. Nanotechnol.*, 2015, **15**, 972-988.
57. M. Montalti, A. Cantelli and G. Battistelli, *Chem. Soc. Rev.*, 2015, **44**, 4853-4921.
58. L. Lai and A. S. Barnard, *J. Nanosci. Nanotechnol.*, 2015, **15**, 989-999.
59. M. I. Kanyuk, *Biotechnol. Acta*, 2015, **8**, 9-25.
60. D. Chen, C. A. Dougherty, K. Zhu and H. Hong, *J. Control. Release*, 2015, **210**, 230-245.
61. H. M. Chaudhary, A. S. Duttagupta, K. R. Jadhav, S. V. Chilajwar and V. J. Kadam, *Curr. Drug Delivery*, 2015, **12**, 271-281.
62. R. Lam and D. Ho, *Expert Opin. Drug Delivery*, 2009, **6**, 883-895.
63. H. B. Man and D. Ho, *J. Lab. Autom.*, 2013, **18**, 12-18.
64. H. Man, J. Sasine, E. K. Chow and D. Ho, *RSC Nanosci. Nanotechnol.*, 2014, **31**, 151-169.
65. D. Ho, *Cancer Treat Res*, 2015, **166**, 85-102.
66. X.-Q. Zhang, R. Lam, X. Xu, E. K. Chow, H.-J. Kim and D. Ho, *Adv. Mater.*, 2011, **23**, 4770-4775.
67. X. Zhang, S. Wang, C. Fu, L. Feng, Y. Ji, L. Tao, S. Li and Y. Wei, *Polymer Chem.*, 2012, **3**, 2716-2719.
68. J. Slegerova, M. Hajek, I. Rehor, F. Sedlak, J. Stursa, M. Hruby and P. Cigler, *Nanoscale*, 2015, **7**, 415-420.
69. Y. Y. Hui, B. Zhang, Y.-C. Chang, C.-C. Chang, H.-C. Chang, J.-H. Hsu, K. Chang and F.-H. Chang, *Opt. Express*, 2010, **18**, 5896-5905.
70. Y. Y. Hui, C.-L. Cheng and H.-C. Chang, *J. Phys. D: Appl. Phys.*, 2010, **43**, 374021/374021-374021/374011.
71. S. N. Mikov, A. V. Igo and V. S. Gorelik, *Physics of the Solid State*, 1999, **41**, 1012-1014.

72. A. Pentecost, S. Gour, V. Mochalin, I. Knoke and Y. Gogotsi, *ACS Appl. Mater. Interfaces.*, 2010, **2**, 3289-3294.
73. T. Takimoto, T. Chano, S. Shimizu, H. Okabe, M. Ito, M. Morita, T. Kimura, T. Inubushi and N. Komatsu, *Chemistry of Materials*, 2010, **22**, 3462-3471.
74. E. von Haartman, H. Jiang, A. A. Khomich, J. Zhang, S. A. Burikov, T. A. Dolenko, J. Ruokolainen, H. Gu, O. A. Shenderova, I. I. Vlasov and J. M. Rosenholm, *J. Mater. Chem. B*, 2013, **1**, 2358-2366.
75. N. Prabhakar, T. Naereoja, E. von Haartman, D. S. Karaman, H. Jiang, S. Koho, T. A. Dolenko, P. E. Haenninen, D. I. Vlasov, V. G. Ralchenko, S. Hosomi, I. I. Vlasov, C. Sahlgren and J. M. Rosenholm, *Nanoscale*, 2013, **5**, 3713-3722.
76. A. Bumb, S. K. Sarkar, N. Billington, M. W. Brechbiel and K. C. Neuman, *J. Am. Chem. Soc.*, 2013, **135**, 7815-7818.
77. J. G. Croissant, X. Cattoen, M. W. C. Man, J.-O. Durand and N. M. Khashab, *Nanoscale*, 2015, **7**, 20318-20334.
78. N.-T. Chen, K.-C. Tang, M.-F. Chung, S.-H. Cheng, C.-M. Huang, C.-H. Chu, P.-T. Chou, J. S. Souris, C.-T. Chen, C.-Y. Mou and L.-W. Lo, *Theranostics*, 2014, **4**, 798-807.
79. C. Chen, L. Zhou, J. Geng, J. Ren and X. Qu, *Small*, 2013, **9**, 2793-2800.
80. J. Croissant, M. Maynadier, O. Mongin, V. Hugues, M. Blanchard-Desce, A. Chaix, X. Cattoen, M. Wong Chi Man, A. Gallud, M. Gary-Bobo, M. Garcia, L. Raehm and J.-O. Durand, *Small*, 2015, **11**, 295-299.
81. J. G. Croissant, O. Mongin, V. Hugues, M. Blanchard-Desce, X. Cattoen, M. Wong Chi Man, V. Stojanovic, C. Charnay, M. Maynadier, M. Gary-Bobo, M. Garcia, L. Raehm and J.-O. Durand, *J. Mater. Chem. B*, 2015, **3**, 5182-5188.
82. C. Mauriello-Jimenez, J. Croissant, M. Maynadier, X. Cattoen, M. Wong Chi Man, J. Vergnaud, V. Chaleix, V. Sol, M. Garcia, M. Gary-Bobo, L. Raehm and J.-O. Durand, *J. Mater. Chem. B*, 2015, **3**, 3681-3684.
83. M.-S. Wu, D.-S. Sun, Y.-C. Lin, C.-L. Cheng, S.-C. Hung, P.-K. Chen, J.-H. Yang and H.-H. Chang, *J. Nanobiotech.*, 2015, **13**, 35.
84. Y. Ma, M. Rohlfing and A. Gali, *Physical Review B*, 2010, **81**, 041204.
85. A. Fire, S. Xu, M. K. Montgomery, S. A. Kostas, S. E. Driver and C. C. Mello, *Nature*, 1998, **391**, 806-811.
86. P. J. F. Leuschner, S. L. Ameres, S. Kueng and J. Martinez, *EMBO Reports*, 2006, **7**, 314-320.
87. S. M. Elbashir, J. Harborth, W. Lendeckel, A. Yalcin, K. Weber and T. Tuschl, *Nature*, 2001, **411**, 494-498.
88. F. L. Tan and J. Q. Yin, *Cell Res*, 2004, **14**, 460-466.
89. K.-T. Jeang, *BMC Biology*, 2012, **10**, 1-6.
90. G. Daniel, *Recent Patents on DNA & Gene Sequences*, 2008, **2**, 40-43.
91. S. A. Leachman, R. P. Hickerson, P. R. Hull, F. J. D. Smith, L. M. Milstone, E. B. Lane, S. J. Bale, D. R. Roop, W. H. I. McLean and R. L. Kaspar, *Journal of Dermatological Science*, 2008, **51**, 151-157.
92. G. R. Devi, *Cancer Gene Ther*, 2006, **13**, 819-829.
93. W. Guo, W. Chen, W. Yu, W. Huang and W. Deng, *Chinese Journal of Cancer*, 2013, **32**, 488-493.
94. D. V. Morrissey, J. A. Lockridge, L. Shaw, K. Blanchard, K. Jensen, W. Breen, K. Hartsough, L. Machemer, S. Radka, V. Jadhav, N. Vaish, S. Zinnen, C. Vargeese,

Chapter 4. Two-photon-actuated photodynamic therapy, imaging, drug and gene delivery *via* periodic mesoporous organosilica nanoparticles in cancer cells

- K. Bowman, C. S. Shaffer, L. B. Jeffs, A. Judge, I. MacLachlan and B. Polisky, *Nat Biotech*, 2005, **23**, 1002-1007.
95. Y. Y. C. Tam, S. Chen and P. R. Cullis, *Pharmaceutics*, 2013, **5**, 498-507.
96. J. Guo, J. R. Ogier, S. Desgranges, R. Darcy and C. O' Driscoll, *Biomaterials*, 2012, **33**, 7775-7784.
97. B. M. D. C. Godinho, J. R. Ogier, R. Darcy, C. M. O'Driscoll and J. F. Cryan, *Mol. Pharm.*, 2013, **10**, 640-649.
98. S.-K. Lee, A. Siefert, J. Beloor, T. M. Fahmy, P. Kumar, K. D. Wittrup and L. V. Gregory, in *Methods in Enzymology*, Academic Press, Editon edn., 2012, vol. Volume 502, pp. 91-122.
99. S.-S. Kim, S. Subramanya, D. Peer, M. Shimaoka and P. Shankar, in *Antiviral RNAi: Concepts, Methods, and Applications*, Humana Press, Totowa, NJ, Editon edn., 2011, pp. 339-353.
100. M. E. Davis, J. E. Zuckerman, C. H. J. Choi, D. Seligson, A. Tolcher, C. A. Alabi, Y. Yen, J. D. Heidel and A. Ribas, *Nature*, 2010, **464**, 1067-1070.
101. P. K. Selbo, A. Weyergang, A. Hogset, O.-J. Norum, M. B. Berstad, M. Vikdal and K. Berg, *J. Control. Release*, 2010, **148**, 2-12.
102. Berg K, Berstad M, Prasmickaite L, Weyergang A, Selbo PK, Hedfors I and H. A, *Top Curr Chem*, 2010, **296**, 251-281.
103. S. Oliveira, A. Hogset and G. Storm, *Current Pharmaceutical Design*, 2008, **14**, 3686-3697.
104. S. Oliveira, M. M. Fretz, A. Hogset, G. Storm and R. M. Schiffelers, *Biochimica et Biophysica Acta (BBA) - Biomembranes*, 2007, **1768**, 1211-1217.
105. K. Raemdonck, B. Naeye, A. Hogset, J. Demeester and S. C. De Smedt, *J. Control. Release*, 2010, **145**, 281-288.
106. S. Brown, *Nat Photon*, 2008, **2**, 394-395.
107. O. Kazuya and K. Yoshiaki, *Anti-Cancer Agents in Medicinal Chemistry*, 2008, **8**, 269-279.
108. K. Ogawa and Y. Kobuke, *BioMed Research International*, 2013, **2013**, 11.
109. Y. Yang, F. Liu, X. Liu and B. Xing, *Nanoscale*, 2013, **5**, 231-238.
110. M. Strohmeier, A. M. Orendt, J. C. Facelli, M. S. Solum, R. J. Pugmire, R. W. Parry and D. M. Grant, *J. Am. Chem. Soc.*, 1997, **119**, 7114-7120.
111. Midoux, P., Pichon, C., Yaouanc, J.-J. & Jaffrès, P.-A. *Br. J. Pharmacol*, 2009, **157**, 166-178.

5. General conclusions

During this work the elaboration of nanomaterials for the diagnostic and the therapy of low size cancers through photodynamic therapy (PDT) was achieved. This new therapy involves the activation of a photosensitizer molecule (PS) with specific wavelengths of light giving rise to energy transfer cascades that yield cytotoxic reactive oxygen species leading to apoptotic and necrotic cell death.

Different photosensitizers (porphyrin, phthalocyanine and nanodiamonds) were used to be covalently encapsulated in mesoporous silica nanoparticles, for example, or to co-condensed with organosilica precursors. Their use for *in vitro* one and two photon therapy was demonstrated. The endocytosis of the nanomaterials was confirmed through fluorescence imaging *in vitro*. For two-photon nanomaterials, drug and gene delivery was also performed *in vitro* and *in vivo*.

First, MCM-41 nanoparticles were synthesized by sol-gel process at room temperature and functionalized by four novel analogues of the membrane lectin overexpressed in prostate cancer cells, the mannose-6-receptor. Their PDT effect was studied under irradiation at 650 nm in LNCaP prostate cancer cells, and better results were obtained for di-substituted analogues with almost 75% of death. Second, 20 nm-sized MSNs were synthesized. Three different porphyrins were encapsulated and the resulting nanoparticles were used in one photon photodynamic therapy producing 30% of death *in vitro*.

Two type of two photon nanomaterials were synthesized. First, biodegradable bridged silsesquioxane nanoparticles were synthesized from a disulfide precursor and a metallated porphyrin. The first precursor provides the ability to be biodegradable because of the S-S bonds and the second one, as a photosensitizer, provides his utility in imaging and PDT. Their PDT effect was studied under irradiation at 800 nm in MCF-7 breast cancer cells, with almost 54% of cell death. The biodegradability of the NPs was assessed in near-physiological conditions. Second, two different bridged silsesquioxane nanoparticles were synthesized from either a metallated porphyrin (BSPOR), or from a metallated phthalocyanine (BSPHT). BSPOR and BSPHT produced 86% and 21% of cell death respectively. Their efficiency for intracellular tacking was demonstrated by *in vitro* imaging at 750 nm.

General conclusions

Then, periodic mesoporous organosilica nanoparticles were synthesized. Their use *in vitro* for two-photon therapy, fluorescence imaging and drug and gene delivery was demonstrated. First, PMOs nanoparticles were synthesized by sol-gel process *via* co-condensation between the bis-silylated ethane precursor and a tetrasilylated free base porphyrin. Their PDT effect was studied under an irradiation at 800 nm in MCF-7 breast cancer cells, with almost 30% of death. Gemcitabine was loaded into the porous structure, obtaining a drug loading of 50 wt %. The synergetic effect between the two-photon irradiation and the drug delivery was demonstrated *in vitro* in MCF-7 cancer cells. PMOs nanoparticles were also synthesized by sol-gel process *via* co-condensation between the bis-silylated ethylene precursor and an octasilylated metallated porphyrin. The internalisation of the nanoparticles in cancer cells was confirmed by two-photon fluorescence imaging at 750 nm and 800 nm. Doxorubicin was loaded into the porous structure and was delivered *in vitro* obtaining 75 % of cell killing with a concentration of loaded-NPs of only 1 µg/ml.

In a third part, nanodiamonds were encapsulated in a periodic mesoporous organosilica structure made from a bis-silylated ethane or ethylene precursor. Under two-photon irradiation, nanodiamonds could produce ROS species that was confirmed by ROS imaging using DCFDA detection assay. The systems were used as doxorubicin nanovehicle producing 87 % of cell killing in combination with two-photon irradiation.

To conclude, pure porphyrin PMOs were synthesized from an octasilylated porphyrin obtained by click chemistry. The characterization by different techniques as solid NMR, UV-visible or HRTEM explained the presence of J aggregation between the porphyrin molecules and the presence of interconnected cavities. siRNA gene delivery was performed *in vitro* in MCF-7 breast cancer cells and the synergetic application of two-photon therapy leads to 50 % of gene silencing effect. Finally, nanoparticles were used *in vivo* in a zebrafish animal model.

In a near future drug delivery of camptothecin or doxorubicin could be envisaged for the one photon nanoparticles. Test in zebrafish will be done to demonstrate the capacity of these targeted nanoparticles for *in vivo* imaging and PDT. In the near future a surface stabilization with PEG could be used to avoid the aggregation of the nanoparticles and to allow their use *in vivo*. Grafting of a targeting moiety can also be envisaged. In the case of two photon nanoparticles, the functionalization of the nanoparticles with targeting molecules could be envisaged to improve their internalisation in cells.

General conclusions

Xenografted tumour could be used for the *in vivo* test in zebrafish to demonstrate the potential of these new nanoplateforms in cancer treatment.

Resumé. Nanoparticules théranostiques pour le traitement du cancer à travers la
thérapie photodynamique à un ou deux photons

**NANOPARTICULES À VISÉES
THÉRANOSTIQUES POUR LE TRAITEMENT DU
CANCER PAR THÉRAPIE PHOTODYNAMIQUE À
UN OU DEUX PHOTONS**

6.1. Introduction

L'emploi de la nanotechnologie dans la santé a conduit à une nouvelle discipline appelée nanomédecine. Cette branche vise principalement le développement d'outils pour diagnostiquer, prévenir et traiter les maladies de façon plus efficace et rapide ce qui se traduirait dans une meilleure qualité de vie pour l'homme. De nombreux nanosystèmes sont en cours de développement pour le traitement d'une maladie qui tue chaque année près huit millions de personnes dans le monde: le cancer.

Pour traiter cette maladie, de nombreuses techniques médicales sont actuellement mises en place comme la chimiothérapie, la radiothérapie ou la chirurgie. Le traitement des tumeurs par ces techniques efficaces mais très invasives provoquent souvent des effets indésirables chez le patient et vu leur manque de sélectivité, elles peuvent s'attaquer aux cellules saines qui entourent la tumeur.

Pour traiter les petites tumeurs, une technique a été développée : la thérapie photodynamique (PDT). Elle fait appel à l'action simultanée 1) d'une molécule photoactivable, le photosensibilisateur (PS), 2) de lumière de longueur d'onde appropriée et 3) d'oxygène présent naturellement dans le milieu biologique. Les photosensibilisateurs, non toxiques en absence d'excitation lumineuse, absorbent l'énergie lumineuse ce qui les conduit à un état vibrationnel excité. Á ce point deux transitions peuvent se produire : la fluorescence, une transition radiative si la molécule retourne à l'état vibrationnel fondamental ou la conversion intersystème (ISC), une transition non-radiative qui conduit la molécule à un état triplet excité (Fig.1). Á ce stade, en présence d'oxygène, un transfert d'énergie se produit vers l'oxygène créant une cascade de réactions amenant à la formation d'espèces oxygénées réactives (ROS), dont l'oxygène singulet, responsables de la destruction cellulaire.

L'excitation de la molécule photoactivable peut se faire à travers l'irradiation à un ou deux photons. Le premier type d'irradiation est plus facile à mettre en place mais l'excitation à un photon fournit une thérapie par la lumière visible qui ne peut pas pénétrer profondément dans les tissus et où l'activation du PS se produit par un faisceau laser, ce qui peut provoquer des dommages collatéraux. Le deuxième type d'irradiation, par contre, est limité au point focal du laser, ce qui permet une résolution de l'ordre du micromètre. Réalisée dans le proche-infrarouge, elle bénéficie d'un maximum de pénétration dans les tissus biologiques et permet de travailler dans la fenêtre

Resumé. Nanoparticules théranostiques pour le traitement du cancer à travers la thérapie photodynamique à un ou deux photons

thérapeutique (700-1400 nm), où le flux de photons est moins perturbé par l'absorption des tissus biologiques (paramètres qui influent sur l'imagerie par fluorescence). La sélectivité de la PDT permet grâce à une irradiation lumineuse localisée d'éradiquer les cellules tumorales tout en préservant les cellules saines. Grâce aux propriétés de fluorescence des PS, ces molécules permettent aussi de visualiser les tissus malades au cours de leur traitement par PDT.

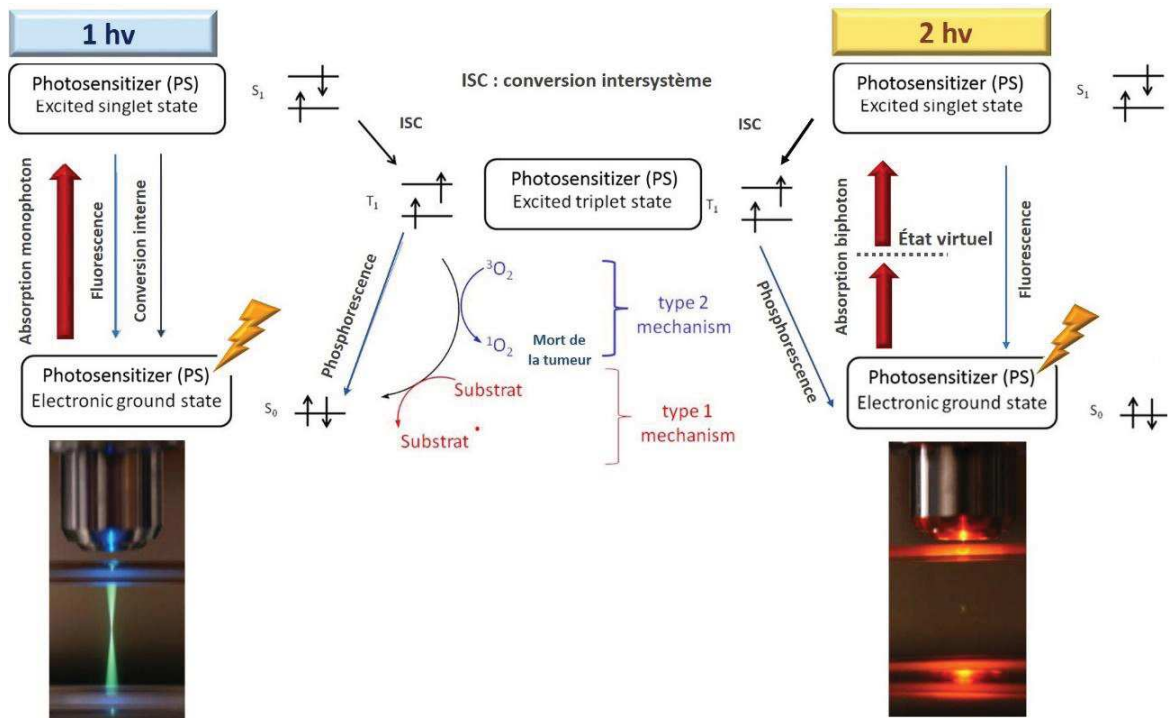


Fig. 1. Diagramme de Jablonski montrant les transitions énergétiques issues de l'irradiation à un ou deux photons. Comme le montrent les photos du microscope, en comparaison à l'absorption à un photon, l'absorption simultanée de deux photons limite la thérapie au point focal du laser.

Un enjeu majeur en thérapie anti-cancéreuse réside dans le fait de tromper les mécanismes de défense de l'organisme pour apporter le médicament à sa cible biologique. La question est de limiter les effets non spécifiques tout en assurant une concentration élevée au niveau de la tumeur. De nouveaux composés, obtenus par la conjugaison d'un PS à une molécule d'adressage tumoral (sucres, peptides, ligands) sont à l'étude. Cependant l'un des problèmes des PS reste leur hydrophobie qui favorise leur agrégation dans les milieux biologiques et limite leur biodisponibilité. Des stratégies d'encapsulation dans des nanoparticules ont été développées. Elles présentent l'avantage d'augmenter la pénétration tissulaire et cellulaire des PS ainsi que l'efficacité de la PDT. Ces nano-vecteurs sont à l'origine du développement de plateformes

théranostiques rassemblant au sein d'une même nanoparticule un PS et un agent de diagnostic. Cette combinaison d'un médicament et d'un test diagnostique est appelée le théranostic.

6.2. Nanosystèmes développés

Cette thèse contient un certain nombre d'expériences qui démontrent l'efficacité de l'utilisation de nanoparticules de silice ou organosilice pour l'imagerie médicale, la délivrance de médicaments et de gènes et pour le traitement PDT. Chaque nanosystème potentiel encapsule un agent photosensibilisant de la famille des porphyrines ou phtalocyanines (Fig. 2).

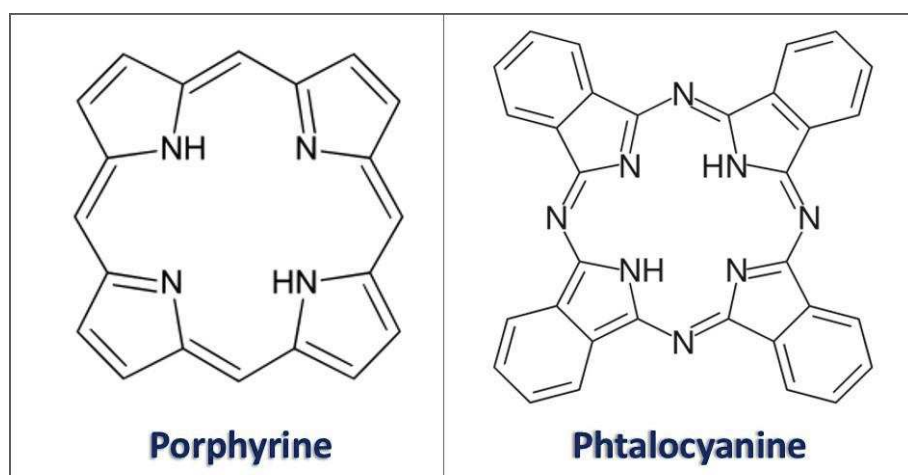


Fig. 2. Structure d'une porphyrine et d'une phtalocyanine.

En premier lieu, des nanoparticules de silice mésoporeuses (MSN) seront décrites pour une utilisation en imagerie par fluorescence et en thérapie photodynamique (PDT). Tout d'abord, des hydrates de carbone et phosphonates, analogues du mannose-6 phosphate ont été utilisés en tant que ligands de ciblage potentiels pour la photothérapie dans les cellules cancéreuses de la prostate. Au début, des nanoparticules de type MCM-41, encapsulant de manière covalente un photosensibilisateur de type porphyrine ont été synthétisées (Fig.3). Leur surface a ensuite été fonctionnalisée avec quatre analogues différents et les nanoparticules ont été testées *in vitro* dans des cellules cancéreuses de la prostate LNCaP. Postérieurement, des nanoparticules de silice mésoporeuse contenant trois photosensibilisateurs différents de type porphyrine ont été synthétisées et testées *in vitro* pour la thérapie à un photon. Ces nanoparticules ont été conçues pour traiter le rétinoblastome. Pour passer à travers la barrière hémato-rétinienne (BRB), l'une des

Resumé. Nanoparticules théranostiques pour le traitement du cancer à travers la
thérapie photodynamique à un ou deux photons

parties de la barrière hémato-oculaire, ces nanoparticules devaient présenter une taille inférieure à 20 nm.

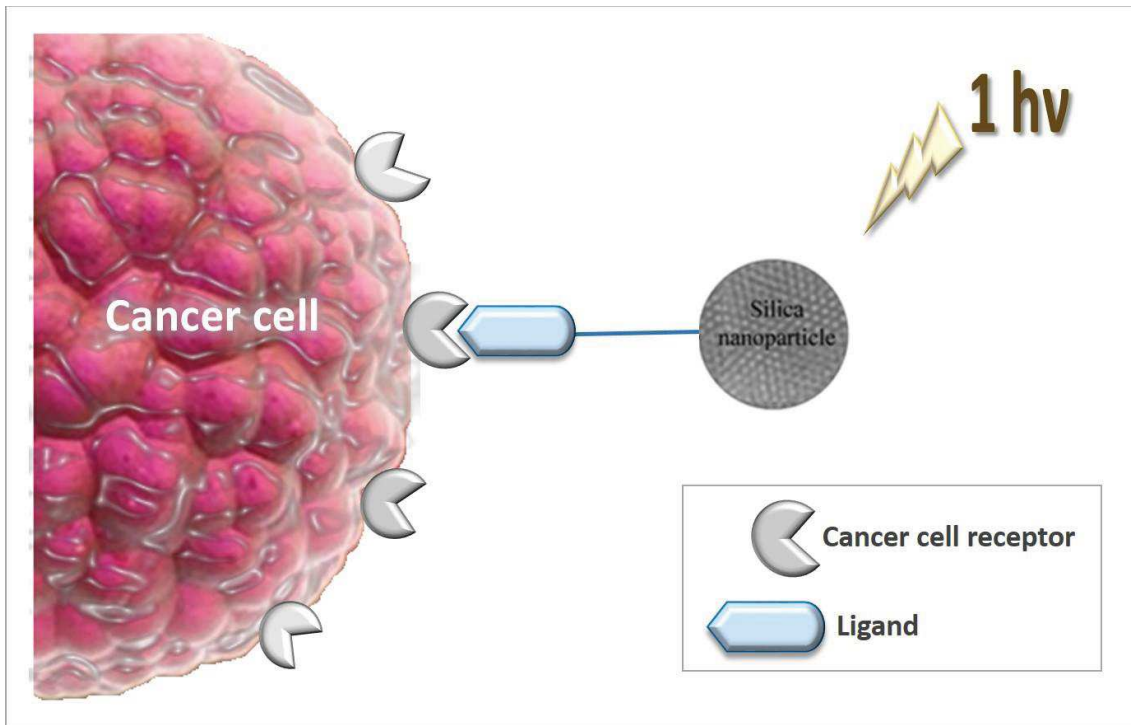


Fig. 3. Représentation des nanoparticules de silice mésoporeuse.

En outre, deux nouveaux nanomatériaux ont été conçus pour la thérapie à deux photons et l'imagerie par fluorescence: les polysilsesquioxanes pontés (BS) d'une part et les nanoparticules d'organosilice mésoporeuse (PMO) de l'autre (Fig.4). Ces nanomatériaux sont exclusivement synthétisés à partir d'organoalcoxysilanes qui fournissent des nanoparticules avec de nombreuses caractéristiques intéressantes par rapport aux nanoparticules de silice.

Tout d'abord, non poreuses, les nanoparticules de silsesquioxanes pontés ont été synthétisées à partir d'une porphyrine métallée ou d'une phthalocyanine. Ces nanoparticules ont été testées *in vitro* dans des cellules MCF-7 du cancer du sein pour un traitement à deux photons.

Afin d'ajouter au système la biodégradabilité, des BS ont été synthétisées à partir d'un précurseur de type disulfure ainsi que d'une porphyrine métallée. La biodégradabilité a été évaluée dans des conditions quasi-physiologiques et les NPs ont été utilisés pour tester leur efficacité en photothérapie *in vitro*.

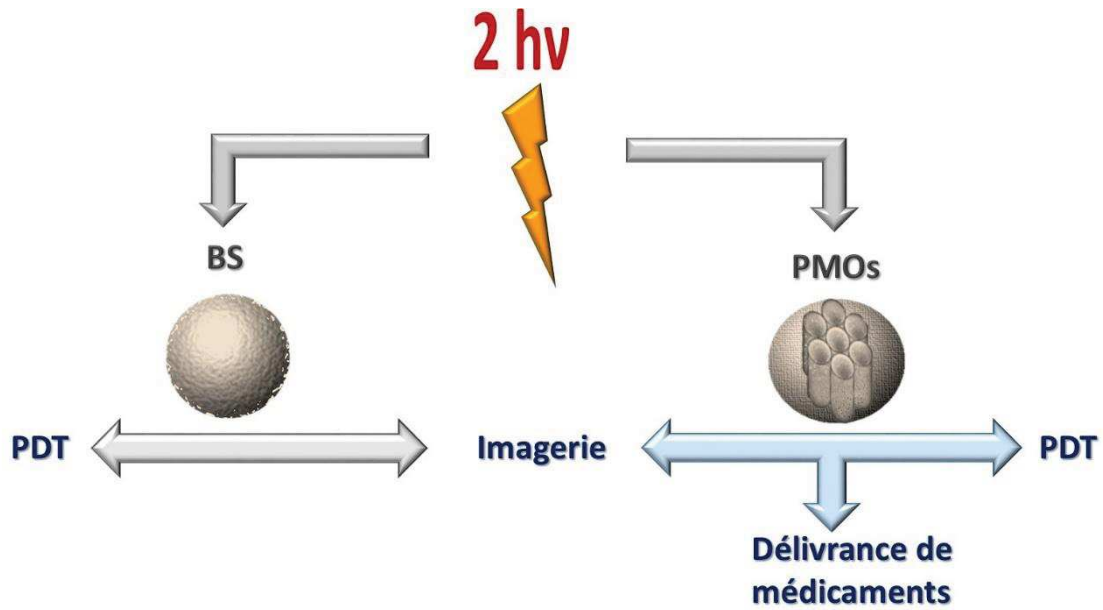


Fig. 4. Applications des nanoparticules pour la PDT à deux photons. Dans le cas de polysilsesquioxane pontés (BS), les nanoparticules seront utilisées pour l'imagerie médicale et la thérapie. Grâce à leur porosité, les PMOs sont aussi utilisés pour faire de la délivrance de médicaments comme la doxorubicine (DOX) ou la gemcitabine (GEM).

Enfin, des nanoparticules PMO ont été synthétisées pour délivrer des médicaments. Quatre différents types de nanoparticules sont présentés. Tout d'abord, les PMO formées à partir de précurseur éthane et de précurseur porphyrine base libre ont été décrits et testés *in vitro* à deux photons pour la thérapie et l'imagerie par fluorescence. Ces nanoparticules ont également été utilisées pour délivrer des gemcitabine (GEM). La charge de médicament élevée et l'effet de synergie entre la délivrance et l'application du traitement PDT ont démontré une efficacité prometteuse dans le domaine de la nanomédecine. Deuxièmement, des nanoparticules à base d'éthylène et de porphyrine ont été présentées pour la délivrance de la doxorubicine (DOX) et l'imagerie de fluorescence à deux photons. Troisièmement, des nanodiamants ont été utilisés comme PS et ont été encapsulés dans des PMOs d'éthane et d'éthylène. L'imagerie de fluorescence, la délivrance de la doxorubicine et l'effet PDT ont été obtenus *in vitro*. Enfin, des nanoparticules PMOs à base de porphyrine ont été synthétisées à partir d'une porphyrine métallée. En raison de leur grande porosité, de délivrance de gène a pu être réalisée *in vitro* et *in vivo*. L'imagerie par fluorescence a également été réalisée avec succès *in vitro* et *in vivo* chez le poisson zèbre.

Resumé. Nanoparticules théranostiques pour le traitement du cancer à travers la
thérapie photodynamique à un ou deux photons

Le résumé de ces travaux sera divisé en trois parties principales : l'élaboration et les applications des nanoparticules de silice mesoporeuse (MSN) pour le traitement du cancer de la prostate et du rétinoblastome à travers la thérapie à un photon, puis la synthèse des nanoparticules BS et enfin celle des PMOs pour la thérapie à deux photons.

6.3. Nanoparticules de silice mesoporeuses (MSN) : synthèse et applications

6.3.1. MSN pour le traitement par PDT 1 hv du cancer de prostate

Des nanoparticules MSN ont été synthétisées par la méthode décrite par Brevet et al. (*Chemical Communications*, 2009, 1475-1477). Ces nanoparticules encapsulant un photosensibilisateur de type porphyrine « base libre » ont été caractérisées par différentes techniques analytiques telles que l'UV-Vis, le FTIR ou la microscopie électronique à transmission. Pour cibler les cellules cancéreuses de la prostate exprimant le récepteur mannose-6-phosphate, quatre nouveaux analogues ont été synthétisés : deux de type carboxylate et deux de type phosphonate. Chaque type présente le correspondant mono et bi-mannoside. Afin de tester *in vitro* l'efficacité du ciblage sur des cellules cancéreuses de la prostate (LNCaP), les nanoparticules ont été fonctionnalisées avec ces quatre analogues, conduisant ainsi à la formation de quatre type de nanoparticules.

Pour prouver l'efficacité du ciblage l'application de la thérapie à un photon à été mise en place *in vitro* (Fig. 5). Entre les analogues mono et bi-mannoside, les seconds se sont révélés plus efficaces provoquant un taux de mort cellulaire autour de 73 % à seulement 6 heures d'incubation. Entre les analogues carboxylates et les analogues phosphonates ce sont ces derniers qui provoquent une plus haute mort cellulaire. Cette affinité pour les analogues de type phosphonate a été démontrée aussi par l'imagerie. En effet on observe une plus grande quantité de nanoparticules internalisées au sein des cellules.

Resumé. Nanoparticules théranostiques pour le traitement du cancer à travers la thérapie photodynamique à un ou deux photons

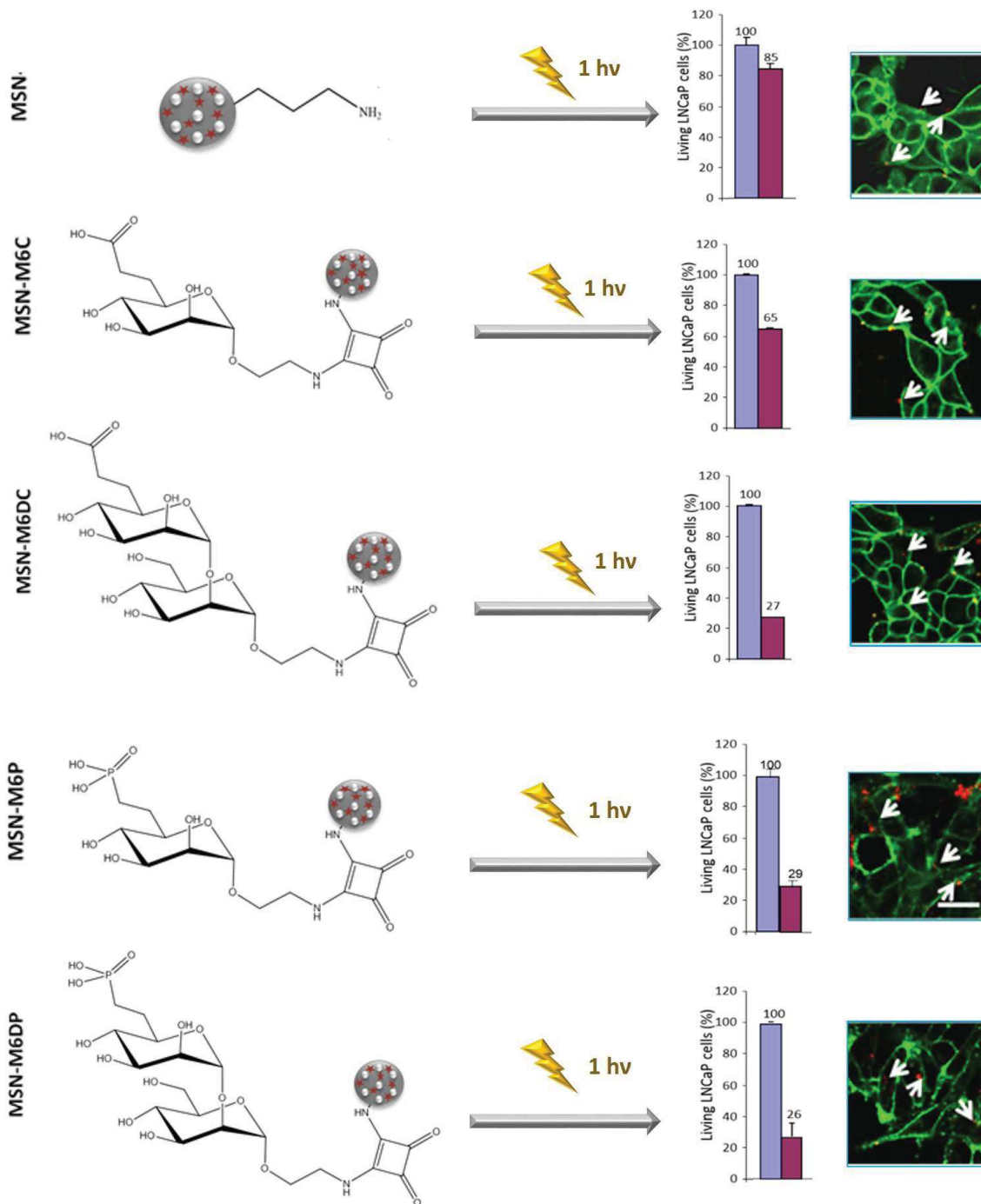


Fig. 5. Thérapie et imagerie médicale à un photon des nanoparticules « nues » et fonctionnalisées par les quatre ligands. À mesure que l'affinité entre le ligand et le récepteur des cellules cancéreuses augmente, la mortalité cellulaire provoquée par la thérapie à un photon augmente.

6.3.2. MSN pour le traitement par PDT 1 hv du rétinoblastome

La réduction de taille des MSN a été ensuite réalisée afin de traverser les membranes biologiques comme la barrière hémato-rétinienne présente dans l'œil. L'élaboration de nanoparticules de 20 nm de diamètre encapsulant une porphyrine a été réalisée par voie sol-gel en conditions basiques et en présence du CTAB comme agent porogène. Trois types de porphyrines ont été encapsulés et analysés par diverses techniques. En vue de l'instabilité colloïdale des nanoparticules, leur surface a été fonctionnalisée par des chaînes PEG. Afin d'être internalisées plus facilement, les nanoparticules ont été fonctionnalisées par du squarate mannose. La stabilisation des nanoparticules a été démontrée dans le milieu biologique et les premiers résultats en PDT à un photon présentés pour les nanoparticules contenant une porphyrine de type maleimide. Ces résultats obtenus à 5 heures d'incubation sont plutôt encourageants.

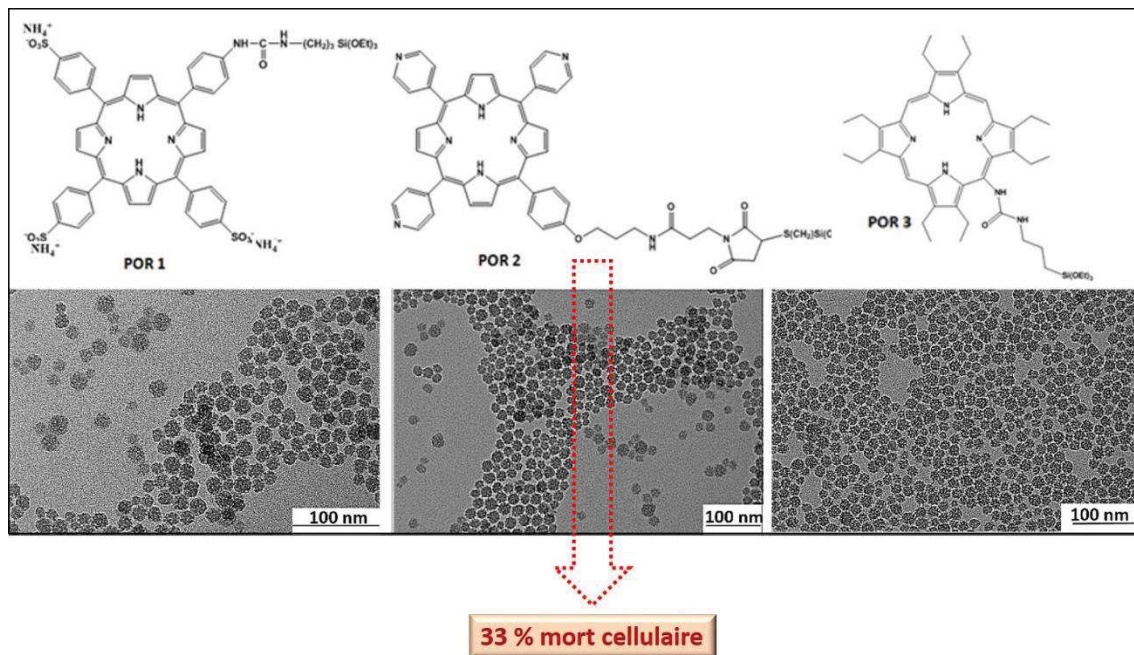


Fig. 6. Trois différentes porphyrines ont été encapsulées dans les nanoparticules de silice mésoporeuses. Les images de microscopie à transmission électronique (TEM) montrent des nanoparticules poreuses de 18 nm de diamètre. Seule la porphyrine 2 a été testée en PDT à un photon, causant 33 % de mort cellulaire.

6.4. Nanoparticules de polysisquioxanes pontés (BS) : imagerie et PDT à deux photons

Ce type de nanomatériaux ainsi que les PMOs ont été synthétisés sans ajout de précurseur de silice (TEOS) et seulement en présence de précurseurs organoalkoxysilane.

6.4.1. BS biodégradables pour le traitement par PDT à deux photons

Pour pouvoir être utilisé pour la PDT à deux photons un photosensibilisateur type porphyrine métallée tétra-alcyne a été silylée par chimie click au microonde en présence d'un catalyseur de cuivre. En co-condensant le PS avec le précurseur 1,2-bis(triéthoxysilylpropyl)-disulfure le caractère biodégradable des nanoparticules est développé (Fig. 7). En effet, les ponts disulfures sont clivés en thiols en présence de la glutathionne .

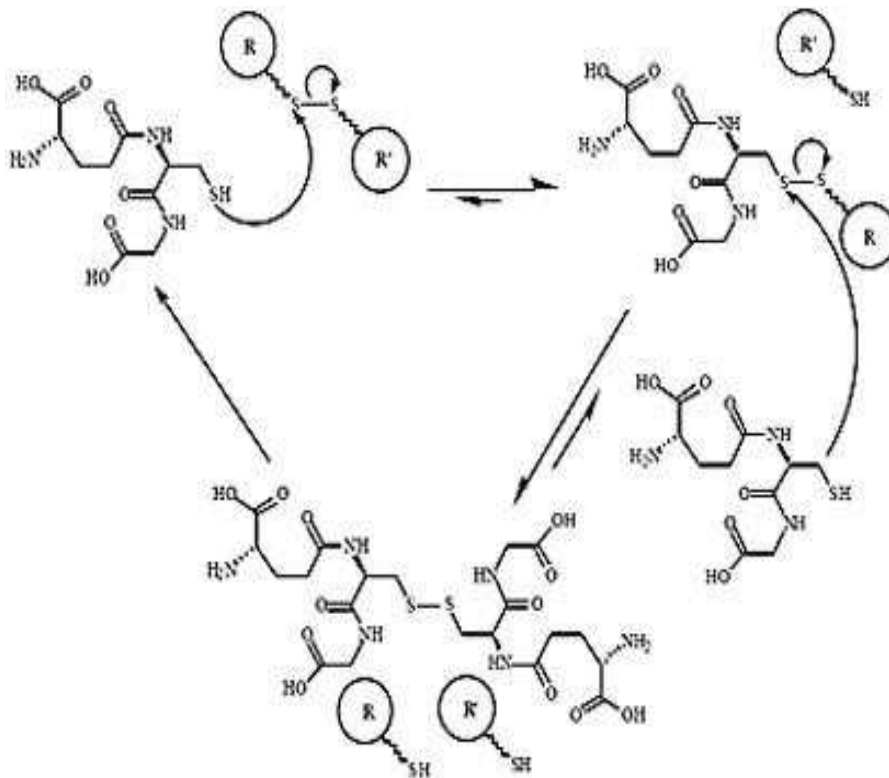


Fig. 7. Réduction des ponts disulfure par la glutathionne. (Image obtenue de l'article de G. Saito et al, *Advanced Drug Delivery Reviews* 55 (2003), pp 199-215)

Les nanoparticules synthétisées (Fig. 8) ne présentent pas de porosité mais leur taille peut être modulée en modifiant la concentration de précurseur disulfure. La

Resumé. Nanoparticules théranostiques pour le traitement du cancer à travers la thérapie photodynamique à un ou deux photons

biodégradabilité a été étudiée dans des conditions similaires à celles du milieu physiologique et confirmé par diverses techniques d'analyse. L'internalisation de ces nanoparticules dans des cellules MCF-7 a été démontrée *in vitro* par imagerie. Leur efficacité en tant que systèmes pour la thérapie à deux photons a été démontrée en obtenant 54% de mort cellulaire sous irradiation.

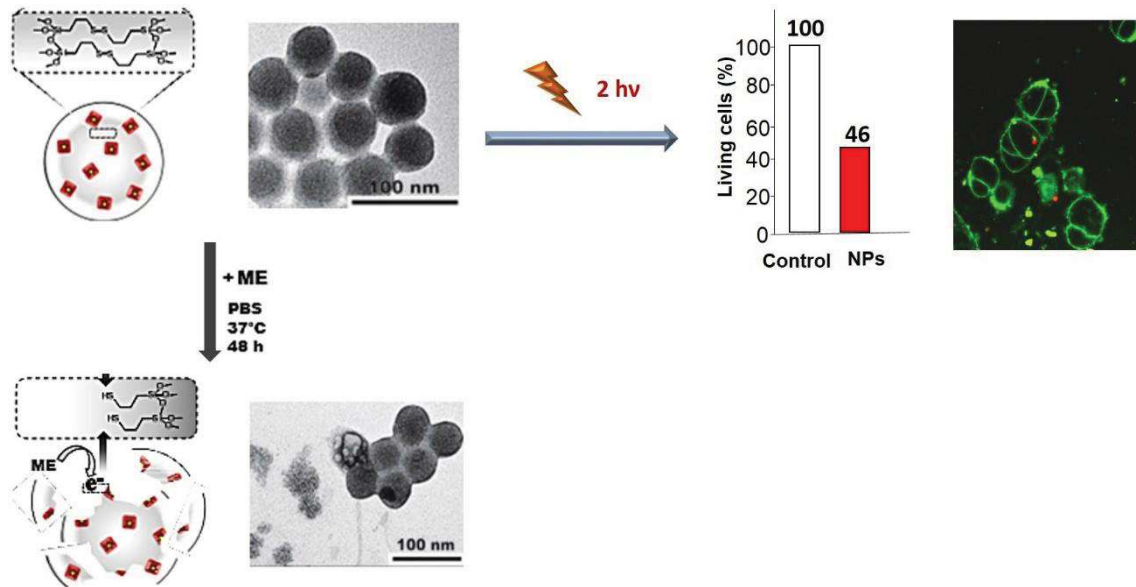


Fig. 8. Les nanoparticules, incubées pendant 20 h dans les cellules MCF-7 du cancer du sein, ont produit sous irradiation à deux photons une mort cellulaire correspondant à 54 %. L'endocytose est confirmée par imagerie. La biodégradabilité a été démontrée dans des conditions similaires aux conditions physiologiques.

6.4.2. BS pour le traitement par PDT à deux photons

Deux types de BS ont été synthétisés à partir seulement du précurseur porphyrine mentionné précédemment et d'une phthalocyanine métallée tétra-alcyne qui a été aussi silylée par chimie click. Les PS présents dans la nanoparticule forment des agrégats de type J comme observé par analyse UV (Fig. 9). Les spectres sont décalés vers le rouge ce qui fait que ces nanoparticules ont pu être utilisées en thérapie à deux photons *in vitro* donnant de très bons résultats avec une mort cellulaire de 86% pour les BS porphyrine et de 21% pour les BS phthalocyanine.

Resumé. Nanoparticules théranostiques pour le traitement du cancer à travers la thérapie photodynamique à un ou deux photons

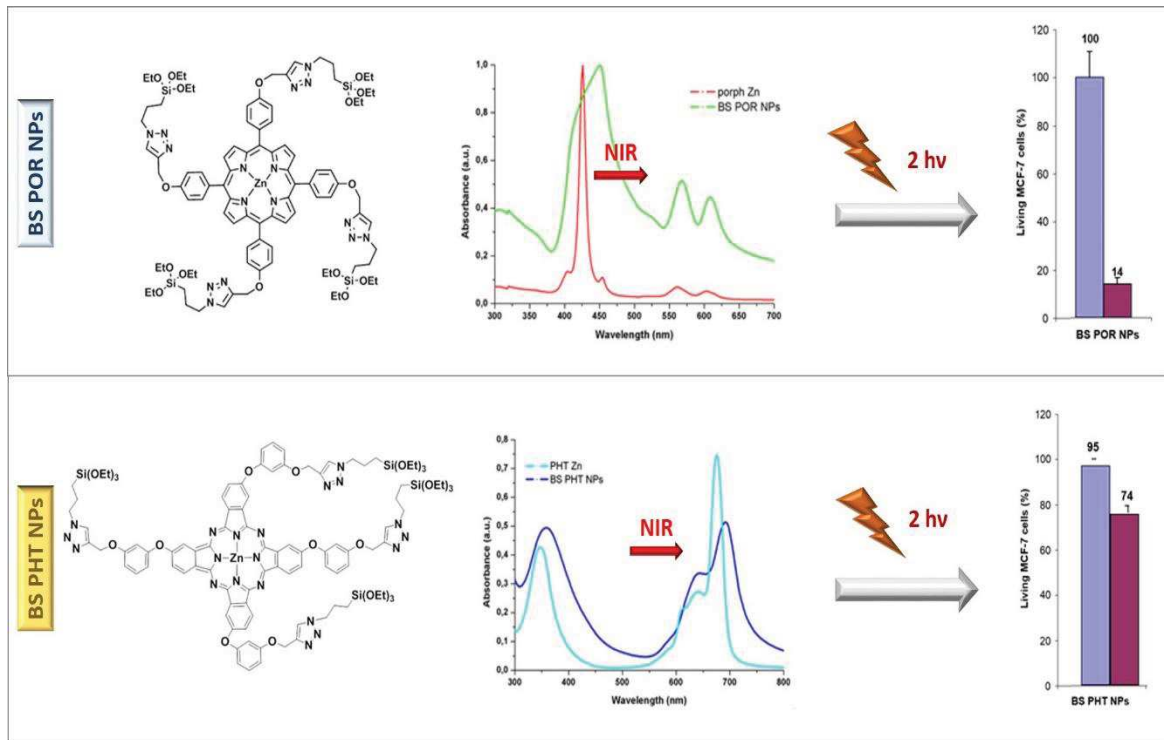


Fig. 9. Les nanoparticules à base de porphyrine et de phthalocyanine analysées par UV montrent que les PS forment des agrégats J au sein des NPs permettant la thérapie à deux photons. Incubées pendant 20 h dans les cellules MCF-7 du cancer du sein elles ont produit entre 25 et 85 % de mort cellulaire.

6.5. Nanoparticules d'organosilice mésoporeuse (PMOs) : nanosystèmes pour la théranostique à deux photons

Enfin, des nanoparticules d'organosilices mésoporeuses (PMOs) ont été synthétisées pour des applications en thérapie à deux photons, l'imagerie médicale et la délivrance de médicaments ou de gènes.

6.5.1. PMOS à base bis (triéthoxysilylpropyl) éthane ou éthylène

Pour obtenir des nanoparticules type PMOs pour des applications à deux photons trois type d'agents photoactivables ont été utilisés : une porphyrine tétrasilylée « base libre », une porphyrine métallée octa-azido et des nanodiamants. Par co-condensation avec des précurseurs éthane ou éthylène en conditions basiques et en présence de CTAB, quatre types de nanoparticules ont été obtenus.

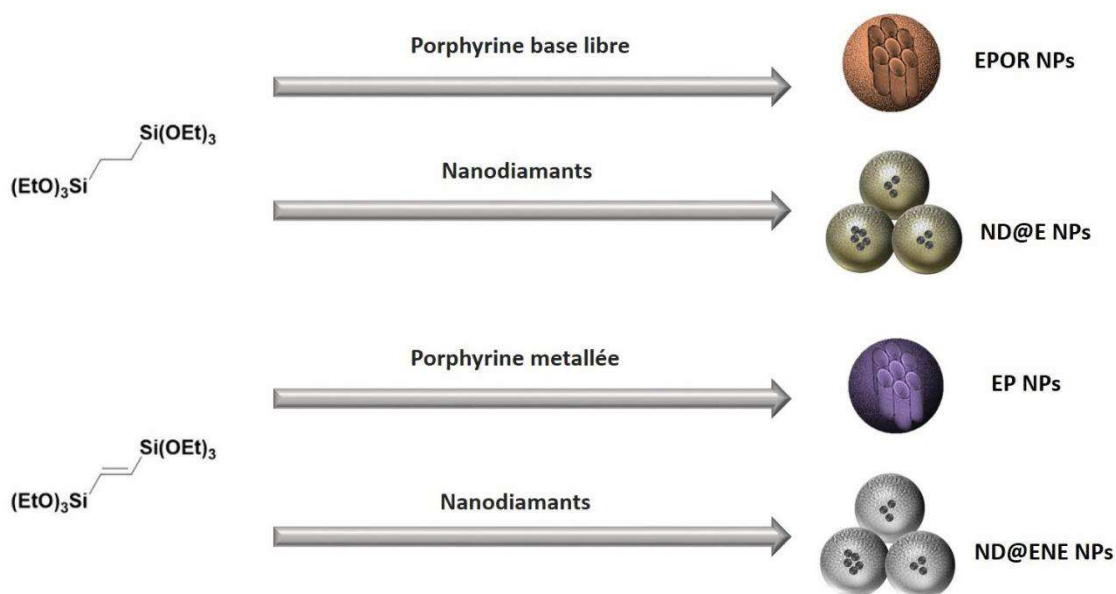


Schéma 1. Représentation des différents matériaux à base de précurseur éthane ou éthylène.

Les premières ont été élaborées à partir de la porphyrine « base libre » en co-condensant avec le précurseur éthane. Ces nanoparticules de 160 nm présentent des pores de 2 nm aptes pour l'encapsulation de médicaments. Dans ce cas l'encapsulation de gemcitabine a été mise en place, conduisant à un grand pourcentage d'encapsulation. La thérapie à deux photons ainsi que la délivrance du médicament a été ensuite menée *in vitro*. La combinaison de la gemcitabine avec l'irradiation à deux photons permet un effet thérapeutique synergétique ce qui permet d'améliorer les résultats de mort

Resumé. Nanoparticules théranostiques pour le traitement du cancer à travers la
thérapie photodynamique à un ou deux photons

cellulaire produit par une délivrance indépendante de l'irradiation. L'endocytose a été
démontrée grâce à la fluorescence du PS.

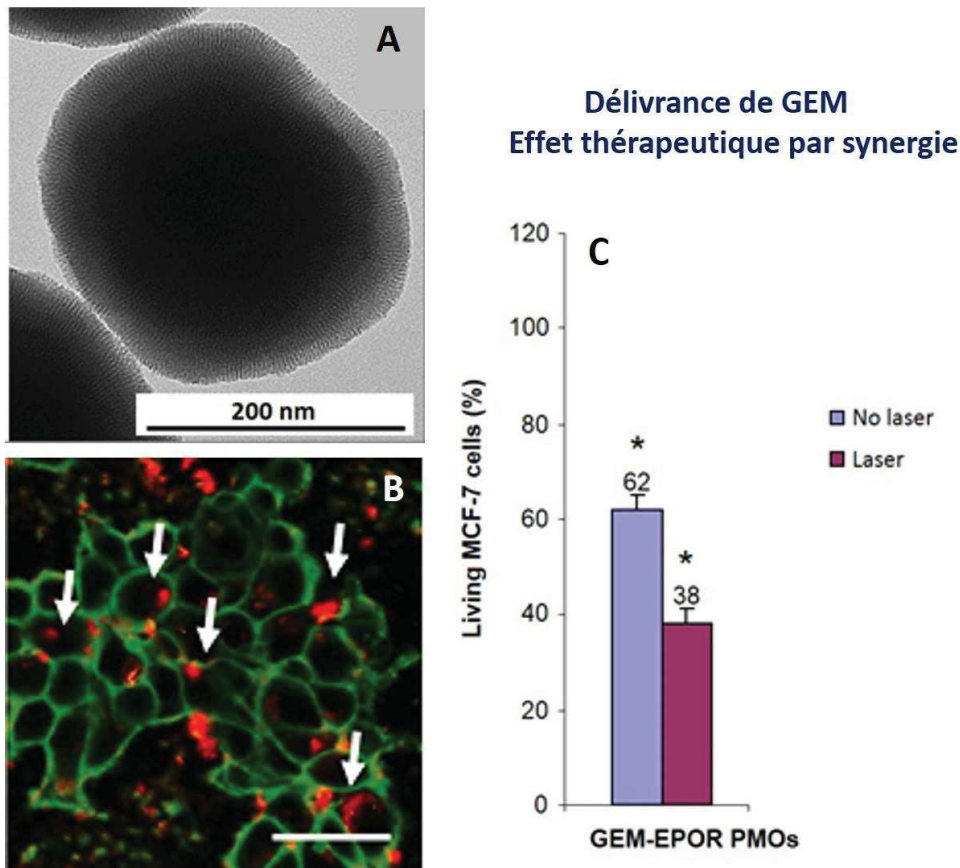


Fig. 10. A) Image TEM montrant des nanoparticules poreuses de 150-200 nm. B) L'imagerie à deux photons montre l'endocytose des nanoparticules dans les cellules. C) Résultats de la thérapie à deux photons. La combinaison de la gemcitabine avec l'irradiation à deux photons permet un effet thérapeutique synergétique.

En ce qui concerne les nanoparticules à base éthylène et porphyrine octasilylée, celles-ci présentent un diamètre de 200 nm. En présence de l'éthylène, l' $^1\text{O}_2$ est « quenché » et la thérapie à deux photons n'a pas pu être mise en oeuvre. Par contre l'endocytose des NPs a été confirmée par la fluorescence intracellulaire produite par le PS. Le chargement des pores avec la doxorubicine (DOX) a permis le relargage autonome des principes actifs dans les cellules MCF-7.

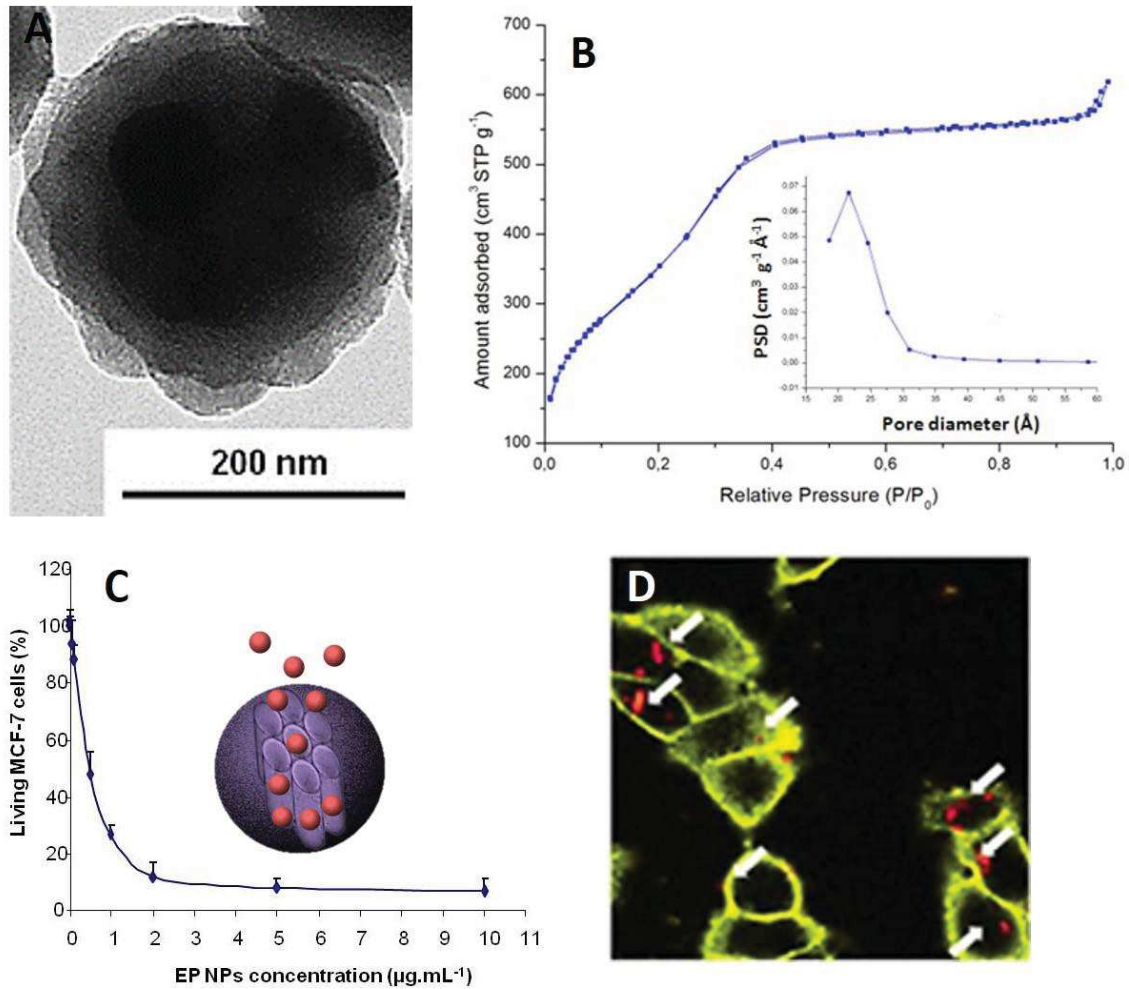


Fig. 11. A) Image TEM montrant des nanoparticules poreuses de 200 nm. B) L'analyse à adsorption et désorption d'azote (BET) montre une courbe de type matériau mesoporeux. C) Délivrance de doxorubicine provoquant 70% de mort cellulaire à faible concentrations de nanoparticules. D) L'imagerie à deux photons montre l'endocytose des nanoparticules dans les cellules.

Des nanodiamants ont été aussi encapsulés dans des PMOS à base d'éthane et d'éthylène pour être utilisés en tant qu'agents photoactivables. En effet, l'imagerie des ROS a permis démontrer que ce type de nanoparticules peut être utilisé en thérapie à deux photons, grâce aux transitions énergétiques des nanodiamants. La délivrance de médicament anticancéreux (DOX) a aussi été prouvée *in vitro*.

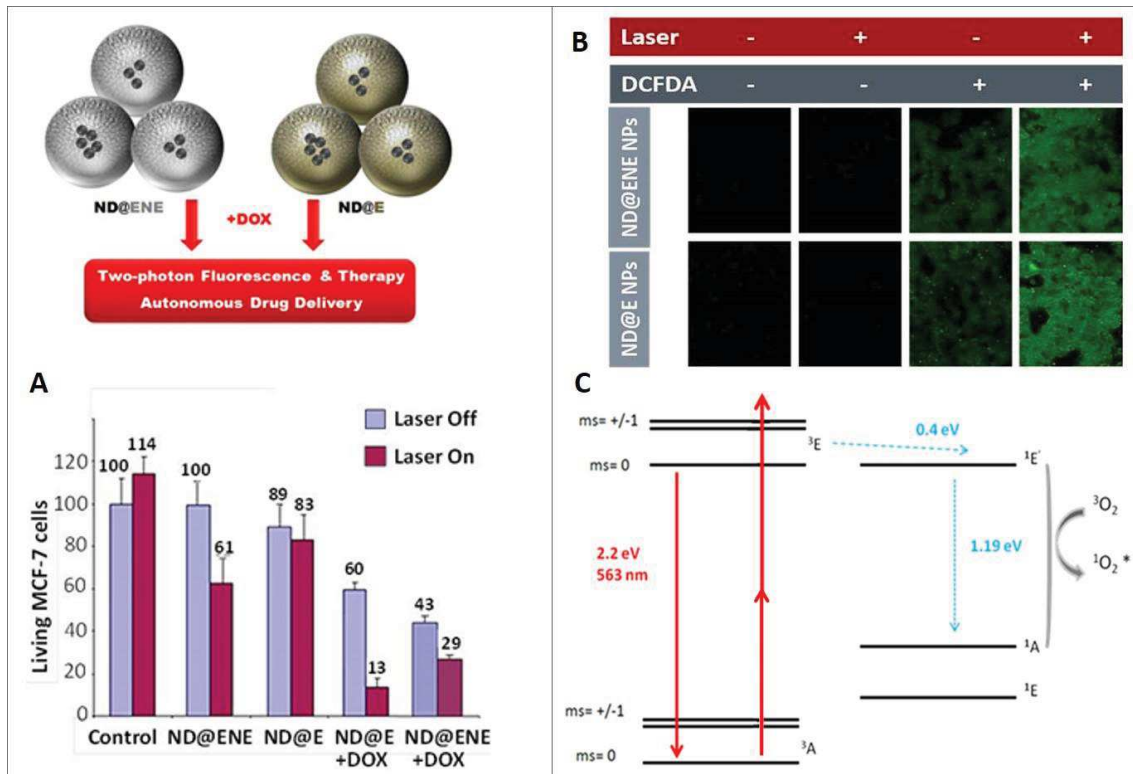


Fig. 12. A) Résultats de la thérapie à deux photons. La combinaison de la doxorubicine avec l'irradiation à deux photons permet un effet thérapeutique synergétique. B) L'imagerie des ROS confirme la production d'espèces oxygénées à partir des nanodiamants irradiés à deux photons. C) Diagramme d'énergie pour les nanodiamants.

6.5.2. PMOS à base de porphyrine pour la délivrance de siRNA

La synthèse de nanoparticules d'organosilice mésoporeuses produites à partir d'une porphyrine métallée (POR) a été élaborée. Le précurseur octasilylé par chimie click a permis de former des nanoparticules creuses avec des cavités 3D interconnectées. La présence d'agrégats J de porphyrines qui forment la nanoparticule a été étudiée par résonance magnétique nucléaire (RMN) du ^{13}C à l'état solide. Des analyses par microscopie de transmission à haute résolution ont été réalisées et montrent une nanoparticule composée de plusieurs couches et la présence de cavités d'environ 12 nm ce qui est aussi confirmé par analyse d'adsorption et désorption d'azote (BET).

Resumé. Nanoparticules théranostiques pour le traitement du cancer à travers la thérapie photodynamique à un ou deux photons

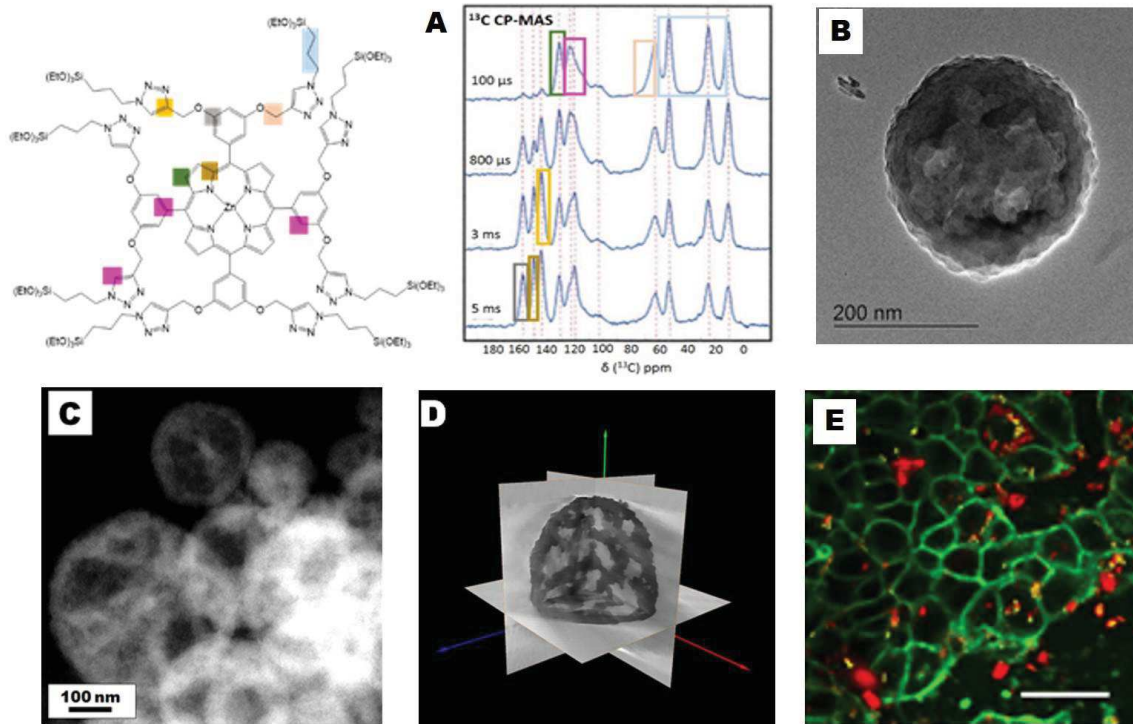


Fig. 13. A) Spectre RMN solide du ^{13}C à différents temps de contact. B) Image TEM montrant des nanoparticules de 200 nm formées par des couches de porphyrine. C) Image STEM montre les cavités des nanoparticules. D) Reconstruction 3D par tomographie montre les cavités interconnectés des PMOs. E) L'imagerie à deux photons montre l'endocytose des nanoparticules dans les cellules.

Leur efficacité pour le suivi intracellulaire a été démontrée par l'imagerie *in vitro* à 750 nm dans les cellules MCF-7. Leur efficacité dans la thérapie photodynamique a été démontrée avec la thérapie à deux photons à 800 nm. Leur efficacité en tant que nanosystèmes pour la délivrance de siRNA a été testée *in vitro* et *in vivo* dans le modèle du poisson zèbre. Les résultats *in vitro* montrent le phénomène appelé photochemical internalisation où grâce à l'irradiation à deux photons les membranes cellulaires sont déstabilisées et le siRNA peut être délivré à l'intérieur du cytosol. Enfin, du siRNA antiGFP a été encapsulé dans les nanoparticules et testé dans des poissons qui exprimaient le gène GFP. Comme le démontrent les images, en présence de nanoparticules chargées et irradiées, le gène GFP (en vert) s'éteint démontrant ainsi l'efficacité de ce type de nanoplateformes pour la thérapie génétique du cancer.

Resumé. Nanoparticules théranostiques pour le traitement du cancer à travers la
thérapie photodynamique à un ou deux photons

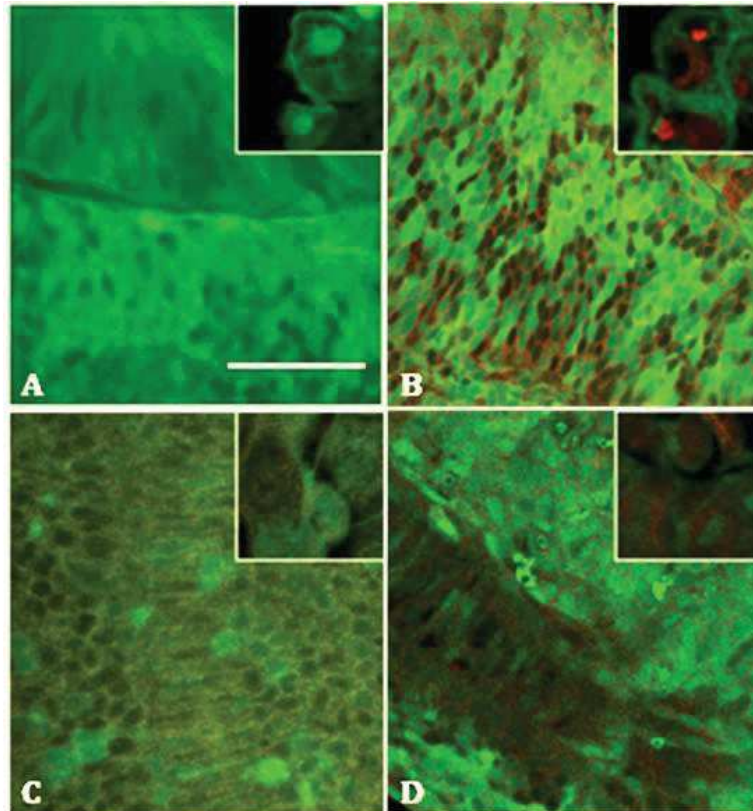


Fig. 14. Délivrance de siRNA in vivo. (A) La couleur verte montre l'expression de LA GFP transitoire injecté dans l'ARNm deS larves. (B) L'activité du siRNA antiGFP réduit efficacement l'expression de la GFP. (C) Nanoparticules colocalisées avec l'expression de la GFP induisant une coloration jaune. (D) Les nanoparticules PMO libèrent le siRNA antiGFP, qui à son tour réduit l'expression de la GFP. La barre d'échelle représente 100 μm pour toutes les photos.

Abstract

Nowadays, the increase of the number of low-size cancers in the world has prompted the development of novel multifunctional nanomaterials applied to new non-invasive therapies. These new therapies are expected to selectively eradicate the tumor, decreasing or suppressing the side effects induced in healthy tissues by current treatments. This study describes the elaboration of nanomaterials for the diagnostic and the therapy of low size cancers through a novel therapy: photodynamic therapy (PDT). This new technique involves the activation of a photosensitizer molecule (PS) with specific wavelengths of light giving rise to energy transfer cascades that yield cytotoxic reactive oxygen species leading to apoptotic and necrotic cell death.

First, the elaboration of mesoporous silica nanoparticles (MSN) containing a porphyrin photosensitizer are presented for the treatment *in vitro* of prostate cancer and retinoblastoma through one-photon therapy. Functionalized nanoparticles with new ligands were synthesized to target the nanoparticles to prostate cancer cells. The decrease of the nanoparticle size to 20 nm was elaborated to cross the blood-retinal barrier and treat retinoblastomas.

On the other hand, two new types of nanomaterials were designed for two-photon nanomedicine which leads to a deeper penetration in tissues. Bridged silsesquioxane (BS) and periodic mesoporous organosilica (PMOs) nanoparticles were designed from different types of tetra or octasilylated-photosensitizers and bis-organoalkoxysilanes such as ethane, ethylene or disulphide. Pure PS bridged silsesquioxane nanoparticles lead to efficient two-photon imaging and photodynamic therapy which were demonstrated *in vitro*. Disulfide-based BS nanoparticles were designed as biodegradable nanomaterials.

Finally, in addition to the imaging and therapy, PMOs nanoparticles were tested *in vitro* as nanocarriers for drug delivery due to their mesoporosity. Gemcitabine or doxorubicin were encapsulated into the pores leading to high drug loadings. Beside the classical photosensitizers, nanodiamonds core-shells PMOs were tested as PDT agent. In addition, pure porphyrin nanoPMOs are presented for gene delivery *in vitro* and *in vivo* in a zebrafish model.

Résumé

L'augmentation du nombre de cancers de faible taille dans le monde a incité le développement de nouveaux nanomatériaux multifonctionnels appliqués à de nouvelles thérapies non invasives. Ces nouvelles thérapies peuvent éliminer sélectivement la tumeur en réduisant ou en supprimant les effets secondaires induits dans les tissus sains par les traitements actuels, tels que la chimiothérapie ou la radiothérapie, qui présentent une efficacité élevée mais une faible sélectivité. Ce travail décrit l'élaboration de nanomatériaux pour le diagnostic et le traitement des cancers de faible taille grâce à une nouvelle thérapie: la thérapie photodynamique (PDT). Cette nouvelle technique, implique l'activation d'une molécule photosensibilisatrice (PS) grâce à des longueurs d'onde spécifiques. Cette activation conduit à des cascades de transfert d'énergie qui produisent des espèces oxygénées réactives cytotoxiques provoquant la mort cellulaire.

Dans un premier temps, l'élaboration de nanoparticules de silice mésoporeuses (MSN) contenant un agent photosensibilisant de type porphyrine est présentée pour le traitement *in vitro* du cancer de la prostate et du rétinoblastome grâce à la thérapie photodynamique à un photon. Des nanoparticules fonctionnalisées avec de nouveaux ligands ont été essayées pour cibler les nanoparticules vers les cellules cancéreuses de la prostate. La diminution de la taille des nanoparticules à 20 nm a été élaborée pour traverser la barrière hémato-rétinienne et traiter les rétinoblastomes.

D'autre part, deux nouveaux types de nanomatériaux ont été conçus pour le traitement à deux photons qui conduit à une pénétration plus profonde dans les tissus. Des nanoparticules polysilsesquioxane pontés (BS) et des nanoparticules d'organosilice mésoporeuses (PMO) ont été conçues à partir de différents types de molécules photosensibilisatrices tétra-silylées ou octa-silylées et de bis-organo-alcoxysilanes comme l'éthane, l'éthylène ou le disulfide. L'efficacité des BS en imagerie à deux photons en thérapie photodynamique a été démontrée *in vitro*. Des nanoparticules de BS à base de disulfides ont été conçues comme nouveaux nanomatériaux biodégradables.

Enfin, en plus de l'imagerie et la thérapie, les PMO ont été testés *in vitro* pour la délivrance de médicaments en raison de leur mésoporosité. La gemcitabine et doxorubicin ont été encapsulées dans les pores obtenant des charges élevées en médicaments. Outre les photosensibilisateurs classiques, des PMO cœur-coquille contenant des nanodiamants ont été testés en tant que PS. Pour finir, des PMO à base de porphyrines sont présentés pour la délivrance de gènes *in vitro* et *in vivo* utilisant le poisson-zébre comme modèle.